

NEUTRON AND MUON STUDIES OF SPIN DYNAMICS IN MAGNETIC SYSTEMS

By
Kevin John Ellis

*A thesis submitted to the University of Huddersfield
in partial fulfilment of the requirements
for the degree of Doctor of Philosophy*

*The University of Huddersfield
June 2013*

Acknowledgements

I wish to thank Professor Cywinski for this opportunity and more importantly for the valuable guidance, advice, and encouragement he has given during my studentship. Likewise all the staff from the School of Applied Sciences, especially Professor Brown and Professor Kilcoyne - it has been a wonderful place to work.

I also wish to express my sincere thanks and acknowledge my debt to the following colleagues and friends. For a multitude of reasons I thank Mark Telling (QEVP!). For helpful and illuminating conversations, technical support and guidance I thank Pascale Deen (now at ESS), Bela Farago, and Peter Fouquet at ILL, Adrian Hillier, Francis Pratt, and Ross Stewart at ISIS. I also thank the office rabble who made my time in Huddersfield so enjoyable and truly unforgettable.

Above all I thank my family for their tireless love and support.

Abstract

In this thesis I present an investigation on the spin dynamics observed during moment localisation, non-ergodic magnetic phase transitions, and weak itinerant electron magnetism.

The pseudo-binary compound $Y(\text{Mn}_{1-x}\text{Al}_x)_2$ has been investigated under the influence of equivalent opposing chemical and mechanical pressures using Muon Spin Relaxation. The results reveal the application of external mechanical pressure (4.5 kbar) to destabilise the manganese moment, and produce a ground state distinctly different to that seen under ambient pressure conditions. Short-range nuclear and spin correlations have been studied *via* diffuse neutron scattering, and through a combination of analysis techniques I have mapped the temperature dependence of these correlations and their evolution due to the substitution of manganese for aluminium.

Applying new models of hierarchical relaxation and non-extensive entropy I have studied the slow relaxation dynamics of the spin glass phase using Neutron Spin Echo spectroscopy. The results are developed further by applying the same analysis to a variety of glassy magnetic phenomena: spin glass freezing ($Y(\text{Mn}_{1-x}\text{Al}_x)_2$ and $Y(\text{Al}_{1-x}\text{Fe}_x)_2$), speromagnetic freezing ($(\text{La}_{1-x}\text{Er}_x)\text{Al}_2$), and superparamagnetic blocking ($\text{Cr}_{1-x}\text{Fe}_x$). I have shown that within this framework the underlying freezing mechanisms result in distinctly different responses, and that in the case of spin glass relaxation an apparently universal scaling relationship is present.

Finally the results of a Muon Spin Relaxation study on the moment fluctuations in Au_4V above the Curie temperature are reported. The temperature dependence of the muon spin relaxation rate is found to be similar to that of the archetypal weak itinerant helimagnet, MnSi .

TABLE OF CONTENTS

Acknowledgements.....	i
Abstract.....	ii
Table of Contents.....	iii
List of Figures.....	vi
List of Tables.....	xiv

Introduction.....	1
--------------------------	----------

Chapter 1 **Magnetism**

1.1 Introduction.....	4
1.1.1 Symmetry.....	4
1.1.2 A Phenomenological Description.....	4
1.2 Theories of Magnetism.....	6
1.2.1 The Exchange Interaction.....	7
1.2.2 Localised Electron Model.....	8
1.2.3 Itinerant Electron Model.....	12
1.2.4 A Unified Theory.....	17

Chapter 2 **The Spin Glass Phase**

2.1 Introduction.....	21
2.1.1 Spin Glass Properties.....	23
2.1.2 The Frustration Effect.....	24
2.1.3 Mean-Field Theories.....	26
2.2 Spin Glass Dynamics.....	29
2.2.1 Non-exponential Relaxation.....	30
2.2.2 A Probabilistic Mechanism.....	34
2.2.3 Non-Extensive Entropy.....	36
2.2.4 Summary.....	42

Chapter 3

Experimental Techniques & Instruments

3.1	Introduction to Neutron scattering.....	45
3.1.1	The Production of Neutrons for Science	48
3.1.2	Kinematics Approximation	50
3.1.3	Scattering & Pair Correlation Functions	54
3.1.4	Nuclear Scattering	55
3.1.5	Magnetic Scattering.....	56
3.1.6	Polarisation Analysis	60
3.1.7	Polarisation Techniques	62
3.2	Neutron Spin Echo Spectroscopy	64
3.2.1	Principles of NSE: A Classical Description	65
3.2.2	Effects of Sample Scattering	70
3.2.3	Implementation and Practicalities	74
3.3	The D7 Spectrometer.....	77
3.3.1	General Requirements	77
3.3.2	D7 Overview	78
3.3.3	Data Corrections.....	79
3.4	Muon Spectroscopy	81
3.4.1	The Muon	82
3.4.2	Pion (Muon) Production.....	83
3.4.3	Behaviour of Muons Inside Condensed Matter.....	85
3.4.4	Muon Spin Relaxation.....	88
3.4.5	Muon Spin Relaxation Functions	89
3.5	Sample Preparation.....	94

Chapter 4

Laves Phase Spin Glasses

4.1	Introduction to AB_2 Intermetallic Compounds.....	97
4.2	Characteristics of YMn_2	101
4.2.1	Spin Glass Behaviour in $Y(Mn_{1-x}Al_x)_2$	104
4.2.2	Sample Preparation.....	106
4.3	Pressure Dependence of Topological Frustration.....	106
4.3.1	Longitudinal Field μ SR Measurements.....	108
4.4	Short-range Order in the Spin Glass Phase	113
4.4.1	Introduction to Diffuse Scattering	114
4.4.2	Nuclear Diffuse Scattering	115
4.4.3	Magnetic Short-range Order.....	121
4.5	NSE Measurements of $Y(Mn_{1-x}Al_x)_2$	133
4.5.1	Evaluating the Weron Parameters	136
4.6	Spin Dynamics in the Concentrated Spin Glass $Y(Al_{1-x}Fe_x)_2$	139
4.6.1	The $Y(Al_{1-x}Fe_x)_2$ System	139
4.6.2	Sample Preparation.....	142
4.6.3	DC Magnetisation.....	143
4.6.4	Spin Dynamics in $Y_{1.05}(Al_{0.35}Fe_{0.65})_2$	146

Chapter 5

RAM: Random Anisotropy Magnets

5.1	Introduction to Random Anisotropy.....	150
5.2	Introduction to $(La_xEr_{1-x})Al_2$	153
5.2.1	Sample Preparation.....	155
5.2.2	NSE Study of $(La_{0.70}Er_{0.30})Al_2$	155

Chapter 6

Superparamagnetic Relaxation in $Cr_{1-x}Fe_x$

6.1	Superparamagnetism	160
6.2	The Chromium-Iron System.....	161
6.2.1	Sample Preparation.....	164
6.2.2	NSE Measurements of $Cr_{1-x}Fe_x$	164

Chapter 7

Spin Fluctuations in Weak Itinerant Electron Magnets

7.1	The Gold-Vanadium System	171
7.1.1	Sample Preparation.....	173
7.1.2	Muon Spin Relaxation in Zero-Field.....	174
7.1.3	Muon Spin Relaxation in Applied Longitudinal Fields.....	178

Conclusion	181
-------------------------	------------

Appendix: Publications	190
-------------------------------------	------------

References	210
-------------------------	------------

WORD COUNT 44527

LIST OF FIGURES

Figure 1:1	Variation of the Landau free energy for a ferromagnet, $F(M)$ for decreasing values of temperatures starting above the Curie temperature, (T_C).	6
Figure 1:2	The result of Hund's rules applied to the lanthanide series, where n represents the number of electrons in the $4f$ subshell.	11
Figure 1:3	The density of states in k -space is calculated by considering the volume of k -space between wavevector (\mathbf{k}) and ($\mathbf{k} + d\mathbf{k}$).	12
Figure 1:4	The density of states, $g(E)$, showing a spontaneous splitting of the spin bands.	14
Figure 1:5	Top: the Stoner parameter as a function of atomic number Z . Middle: the density of states as a function of atomic number. Bottom: The Stoner criterion given by the product of the density of states and the Stoner parameter. It can be seen that only the elements iron, cobalt, and nickel are capable of spontaneous ferromagnetism, however calcium, scandium, and palladium are very close. Recreated from <i>Solid-State Physics</i> , Ibach & Lüth ¹²	16
Figure 1:6	The Rhodes-Wohlfarth plot recreated from <i>Spin Fluctuations in Itinerant Electron Magnetism</i> , Tôru Moriya ¹⁴	18
Figure 1:7	Possible examples of the temperature variation of $S_L^2(T)$, taken from <i>Moriya</i> ¹⁴ . Line a is the local moment case where the mean-square local amplitude of spin fluctuations is constant. Lines b and c represent intermediate vales of stiffness constant, large and small respectively, and line d is for weakly ferromagnetic metals. The vertical arrows represent the position of T_C	20
Figure 2:1	Left: A basic representation of magnetic moments placed at random on a non-magnetic cubic lattice. Right: the RKKY exchange (J_{ij}) plotted as a function of distance (R).	23
Figure 2:2	Left: A frustrated plaquette where single and double bonds represent a ferromagnetic interaction, and an anti-ferromagnetic interaction, respectively. Right: Square lattice where the contour (bold line) represents two possible paths between A and B.	25
Figure 2:3	Left: Topological frustration for near-neighbour Ising spins on a triangular lattice with anti-ferromagnetic interactions. Right: Topological frustration in tetrahedral coordination.	25
Figure 2:4	The Sherrington and Kirkpatrick phase diagram for infinite ranged Ising spins, with a mean and variance exchange interaction \mathbf{J}_0 and \mathbf{J} , respectively. Note, for $1 \leq \mathbf{J}_0 / \mathbf{J} \leq 1.25$ the system exhibits three distinct phases upon cooling: paramagnetic, ferromagnetic and finally a so-called re-entrant spin glass phase, indicated by the shaded region. Recreated from Sherrington & Kirkpatrick ²⁷	28
Figure 2:5	Schematic plot of the free energy density as a function of a phase space coordinate for a spin glass at low temperature; partially recreated from ³⁵ . Note there are many equivalent components or "valleys", each of which corresponds to a ground state, $ \Phi_j^{(i)} $, or low-lying excited state.	29

Figure 2:6	The time dependence of the stretched exponential formula, Eq.(2:5), with $\tau = 1$ s, calculated for several (β) values, plotted on a logarithmic time axis.....	31
Figure 2:7	Simulated dynamic autocorrelation function above T_f taken from <i>Ogielski</i> ⁴⁹ . From right to left, the temperatures are $T = 2.50, 2.00, 1.80, 1.70, 1.60, 1.50, 1.45, 1.40, 1.35,$ and 1.30 . The solid lines represent least square fits to the data using Eq. (2:6).....	33
Figure 2:8	2D representation of the cluster geometry used by the Weron Model, possessing both intra- and inter-cluster interactions.	35
Figure 2:9	Values of the entropy for typical values of q^* extensivity parameter (shown with curve). It can be seen that S_q/k diverges if $q^* \leq 1$, and saturates at $S_q = k_B / (q^* - 1)$ when $q^* > 1$, in the limit $W \rightarrow \infty$	38
Figure 2:10	Simulated results for the Tsallis relaxation function. Each plot reveals the variation of $Q(t)$ with extensivity parameter for $\alpha = 1.0, 0.6$ and 0.33 ; top, middle and bottom respectively.	41
Figure 2:11	The Tsallis non-extensivity parameter obtained by NSE measurements a range of spin glass systems; Recreated form the thesis of <i>Pickup</i> ⁸¹	44
Figure 2:12	The Tsallis non-extensivity parameter for Random Anisotropy Magnets (RAM). Recreated form the thesis of <i>Pickup</i> ⁸¹	44
Figure 3:1	Non-systematic variation of the coherent scattering length with atomic number ^{88, 89}	47
Figure 3:2	Non-systematic variation of the absorption cross section with atomic number in units of brns ($1 \times 10^{-24} \text{cm}^{-2}$) ^{88, 89}	47
Figure 3:3	The scattering geometry in a generic neutron experiment; the incident beam, travelling in the x-direction, interacts with a scattering system located at the origin. A detector counts the number of neutrons scattered into the solid angel $d\Omega$	50
Figure 3:4	Scattering triangles for elastic and inelastic scattering events.	51
Figure 3:5	The magnetic form factor squared, $f(Q)^2$ of a free manganese atom, as well as several of its ions calculated using equation (3:28). It is clear the magnetic form factor falls sharply with scattering vector, and can vary significantly between ionisation states.	59
Figure 3:6	Schematic illustration of the relationship between the scattering vector, \mathbf{Q} and the magnetic interaction operator, \mathbf{D}	60
Figure 3:7	Polarised neutron reflectivity measurements for both parallel and anti-parallel spin states of a 900 layer Fe-Si supermirror on a borofloat glass substrate, taken from <i>Courtois</i> ¹⁰⁹ . Angular separation of parallel and anti-parallel spin states is evident, with a critical angle ($\sim 3^\circ$) four times that of Nickel ($m = 4$).	63
Figure 3:8	Larmor precession for a magnetic moment (μ) placed at an angle (θ) to a magnetic field (\mathbf{B}). The direction in which the moment rotates is shown by the blue arrow... ..	65
Figure 3:9	Mezei flipper coil.....	67

Figure 3:10	The polarisation direction of the neutron beam as it exits the first supermirror is parallel to the field direction of the precession coils (\mathbf{B}). Changing its orientation so that it is perpendicular to z is performed <i>via</i> the first of two $\pi/2$ -flipper coils. Its field (\mathbf{B}_π) and that of the precession coils (\mathbf{B}) generate a resultant field (\mathbf{B}_r) orientated at 45° in the y - z plane. The neutrons precess 180° about (\mathbf{B}_r), and so are perpendicular to (\mathbf{B}) as they exit. Note however, that since the beam is polychromatic a distribution of angles is observed (indicated by the blue region).	69
Figure 3:11	Unwinding α_i after scattering is not as simple as reversing the direction of (\mathbf{B}) in the second coil. This approach would generate a zero-field point at the sample position, quickly depolarising the beam. The neutron spin must be rotated 180° about the y -axis using a π -flipper close to the sample. In this way the field in the second precession coil does not need to be altered, and the neutrons precess in the same direction.	69
Figure 3:12	A simplified picture of IN11 to emphasise the major components for paramagnetic or disordered studies.....	73
Figure 3:13	Representation of the spin echo group as a function of precession coil (symmetric scan) and symmetry coil (asymmetric scan): image created to <i>Cywinski</i> ¹²⁴	74
Figure 3:14	Representation of an echo measurement indicating the four measuring points (E_n), average (<i>Aver</i>), and maximum amplitude determined by flipper on (up) and flipper off (down) measurements.	75
Figure 3:15	D7 has four banks of detectors which have in total over 5000 supermirrors and 132 ^3He detector tubes. Furthermore, the banks rotate about the sample position using pressure pads to give an angular range of ($5^\circ \leq 2\theta \leq 150^\circ$). This image has been taken from <i>Schäpf</i> ¹²⁶	78
Figure 3:16	Image from the CERN 2m bubble chamber: the incoming beam collides with a hydrogen atom, expelling an electron, spiralling anti-clockwise, and a pion (π^+). The pion decays to a muon (μ^+), which travels ~ 1 cm (red line) before it decays into a positron (e^+), spiralling clockwise.	81
Figure 3:17	Positive pion decay - the relationship between muon and neutrino, propagation vector and spin polarization.....	84
Figure 3:18	Schematic of the three states adopted by muons within the atomic lattice of a sample: a) Bound (μ^-) muonic atom, b) Muonium (μ^+), c) Free muon (μ^+).....	85
Figure 3:19	Positive muon decay emitting neutrino, anti-neutrino and high energy positron (e^+) preferentially along its spin direction.....	86
Figure 3:20	Angular distributions of positron emission for: a) the most energetic particles (solid), and b) all energies (dashed), with respect to the muon spin direction (arrow).....	87
Figure 3:21	The geometry of a typical longitudinal field μSR experimental: (T) is the target for muon production, the sample (S) is positioned centrally between two anular detector rings, one upstream, and one downstream of the muon beam.	88
Figure 3:22	Gaussian Kubo-Toyabe relaxation function.....	91
Figure 3:23	Lorentzian Kubo-Toyabe relaxation function.....	91

Figure 3:24	Longitudinal field muon spin relaxation spectra for a Gaussian distribution of isotropic random local fields.....	93
Figure 3:25	The dynamic Gaussian Kubo-Toyabe function, where $R = \sigma/v$	93
Figure 3:26	Simplified cross-section of an archetypal helium reservoir cryostat used for neutron and muon studies at the ILL and ISIS with labelling of the salient features.	96
Figure 4:1	This 3D unit cell model illustrates the diamond-like configuration of the A lattice in the cubic C15 Laves Phase. These atoms occupy the $8a$ site at $(\frac{1}{8}, \frac{1}{8}, \frac{1}{8})$, but for clarity only the 1 st nearest neighbours, at typical interatomic distance $\sim 3.5 \text{ \AA}$ are included....	99
Figure 4:2	The smaller B atoms form a complicated array of staggered polyhedron constructed between 1 st and 2 nd nearest neighbour B atoms at typical interatomic distances of $\sim 2.7 \text{ \AA}$ and $\sim 4.7 \text{ \AA}$ respectively. These atoms occupy the $16d$ site at $(\frac{1}{2}, \frac{1}{2}, \frac{1}{2})$ in the unit cell.	99
Figure 4:3	The complete MgCu_2 crystal structure, also known as the C15 or cubic Laves phase. The larger Mg sites on the A lattice are shown in blue, and the smaller Cu atoms on the B sub-lattice in orange. Again, the tetrahedral structure has been extended outside the unit cell boundary in order to give a fuller representation of the B sub-lattice.....	99
Figure 4:4	The thermal expansion curve of YMn_2 . The original measurements (black) ¹⁵⁴ are presented for comparison with more recent high-resolution measurements (white) ¹⁵⁸ .	102
Figure 4:5	Concentration and temperature dependent magnetic susceptibility of $\text{Y}(\text{Mn}_{1-x}\text{Al}_x)_2$ indicating the appearance of Curie Weiss-like behaviour with increasing Al concentration. These results are taken from Shiga ¹⁷²	105
Figure 4:6	Thermal expansion curves suggest a gradual shift towards a 2 nd order transition in the range $(0.03 \leq x \leq 0.05)$ and that for concentrations $(x \geq 0.10)$ the volume anomaly is fully suppressed. These results are taken from Shiga ¹⁷⁵	105
Figure 4:7	Typical instrument calibration measurement performed in a 20 G transverse field. Solid line is a damped cosine fit to the data.	109
Figure 4:8	Suppression of the background nuclear dipole relaxation from the empty pressure cell <i>via</i> the application of 110 G longitudinal field.	109
Figure 4:9	The observed muon spin relaxation spectra at 4.5kbar, with 110G longitudinal field; the solid lines represent least square fit to the data.	110
Figure 4:10	Temperature dependence of the muon spin depolarisation rate under ambient and applied pressure conditions with $(x = 0.05)$. The $(x = 0.10)$ data is from Cywinski ¹⁷⁶ , and is included for comparison. All solid lines are least square fits to equation (4:2), with vertical dashed lines indicating the position of T_g	111
Figure 4:11	Temperature dependence of the stretching parameter (β) under ambient and applied pressure for $(x = 0.05)$, with previous measurements for $(x = 0.10)$ included for comparison. Solid lines are a guide to the eye.	111

Figure 4:12	Diffuse coherent cross section taken at 10 K for $Y(Mn_{1-x}Al_x)_2$, where $x = 0.05, 0.10, \& 0.30$. Each line represents a least square fit of equation (4:8) to the data. ...	118
Figure 4:13	The calculated Warren-Cowley short-range order parameter for each aluminium concentration from the fits shown in Figure 4:12. The dashed lines are a guide to the eye; the dotted line indicates the first unit cell distance.....	119
Figure 4:16	Variation in both nuclear coherent (open) and magnetic (closed) neutron scattering cross sections as a function of aluminium concentration measured at 10 K.	122
Figure 4:17	The temperature dependence of diffuse magnetic cross section for $x = 0.10$	123
Figure 4:18	The temperature dependence of diffuse magnetic cross section for $x = 0.30$. ..	123
Figure 4:19	Temperature variation of the magnetic diffuse scattering intensities between $(0.6 \leq Q \leq 3.7) \text{ \AA}^{-1}$ for compounds with $(x = 0.10)$ and $(x = 0.30)$ represented by closed and open circles respectively. The intensity is seen to gradually decrease as the temperature increases.	124
Figure 4:20	Least square fit of equation (4:11), with 32 near-neighbour shells, to sample of concentration $(x = 0.05)$	125
Figure 4:21	Least square fit of equation (4:11), with 32 near-neighbour shells, to sample of concentration $(x = 0.10)$	126
Figure 4:22	Least square fit of equation (4:11), with 32 near-neighbour shells, to sample of concentration $(x = 0.30)$	127
Figure 4:23	Variation of the spin-spin correlation values as a function of radial distance at 10 K.	128
Figure 4:24	Variation of the spin-spin correlation values as a function of radial distance at 75 K.	129
Figure 4:25	Variation of the spin-spin correlation values as a function of radial distance at 180 K.	130
Figure 4:29	Neutron spin echo measurements revealing the temperature dependence of spin dynamics in $Y(Mn_{0.90}Al_{0.10})_2$ over the momentum transfer range $(0.781 \leq Q \leq 1.213) \text{ \AA}^{-1}$. The solid lines indicate fitting of the data to the Weron-Tsallis relaxation function.....	134
Figure 4:30	Weron parameters for the NSE spectra of $Y_{1.05}(Mn_{0.90}Al_{0.10})_2$ a) temperature dependence of (τ) , solid line is fit to the Vogel-Fulcher law: $\tau = (1.56 \pm 0.83) \times 10^{-4} \text{ ns}$, $E_a/k_B = (134.60 \pm 42.18) \text{ K}$ and $T_0 = (35.95 \pm 4.54) \text{ K}$. b) fractal parameter, where dashed line is linear fit to data c) the interaction parameter, (k)	135
Figure 4:31	Linear concentration dependence of the lattice parameter in the <i>C15</i> cubic phase of $Y(Al_{1-x}Fe_x)_2$; data taken from <i>Besnus</i> ¹⁹³	140

Figure 4:32	The magnetic phase diagram of $Y(\text{Al}_{1-x}\text{Fe}_x)_2$ where T_g (white circles) and T_C (black circles) were determined <i>via</i> DC magnetisation and Mössbauer spectroscopy ¹⁹⁴ . T_g (diamonds) were determined <i>via</i> μSR ¹⁹⁵	140
Figure 4:33	Molar magnetic susceptibility against temperature for $Y_{1.05}(\text{Al}_{1-x}\text{Fe}_x)_2$, where ($x = 0.65$) and ($x = 0.25$). Samples were cooled in zero field and measurements were taken upon warming in fields up to 0.1 T. T_f for the iron-rich sample is approximately 25K. ...	144
Figure 4:34	Temperature dependence of $1/\chi_m$ for the aluminium-rich ($x = 0.25$) sample fields of 0.02 and 0.10 T. The data has been binned to aid inspection. Lines indicate fits to the Curie-Weiss Law at high temperatures.....	145
Figure 4:35	Temperature dependence of $1/\chi_m$ for the iron-rich ($x = 0.65$) sample in a 0.1 T field. Solid line indicates Curie-Weiss behaviour at high temperature. Moreover, the predicted upturn at low temperatures and freezing peak are clearly visible.....	145
Figure 4:36	Neutron spin echo measurements revealing the temperature dependence of spin dynamics in $Y_{1.05}(\text{Al}_{0.35}\text{Fe}_{0.65})_2$ over the momentum transfer range ($0.2 \leq Q \leq 0.7$) \AA^{-1} . The solid lines represent least square fit to the data using the Weron-Tsallis relaxation function.	147
Figure 4:37	The calculated Weron parameters for $Y_{1.05}(\text{Al}_{0.35}\text{Fe}_{0.65})_2$. a) Temperature dependence of τ , solid line is fit to the Vogel Fulcher law: $\tau_0 = (3.71 \pm 7.05) \times 10^{-6}$ ns, and $E_a/k_B = (112.75 \pm 74.33)$ K, and $T_0 = (9.12 \pm 6.00)$ K. b) Fractal parameter, where dashed line is linear fit to data. c) The interaction parameter, (k); the dashed line is included to guide the eye.	148
Figure 5:1	Schematic phase diagram of the possible magnetic states in the presence of RAM with average exchange J_0 and exchange fluctuations ΔJ . The axis are defined by $\delta = \Delta J / J_0$, $d = D / J_0$ and $t = k_B T / J_0$	151
Figure 5:2	Schematic representations of the correlated speromagnetic phase (<i>left</i>) and speromagnetic phase (<i>right</i>).....	152
Figure 5:3	The temperature and frequency dependence of χ' (Top) and χ'' (Bottom) for $\text{La}_{0.70}\text{Er}_{0.30}\text{Al}_2$. <i>Pottinger</i> ²¹⁸	154
Figure 5:4	The temperature dependence of the total magnetic cross section at various momentum transfer values. This graph has been taken from <i>Mezei</i> ²¹⁶	156
Figure 5:5	Neutron spin echo measurements performed during this investigation ($T = 3.5, 5.0, 7.0$) K, and by <i>Mezei</i> ($T = 10, 15, 20$) K on $(\text{La}_{0.70}\text{Er}_{0.30})\text{Al}_2$. The solid lines indicate fits to the data using the Weron-Tsallis relaxation function.....	157
Figure 5:6	Weron parameters for the NSE spectra of $(\text{La}_{0.70}\text{Er}_{0.30})\text{Al}_2$ (a) temperature dependence of τ , solid line is a fit to the Vogel Fulcher law: $\tau_0 = (3.58 \pm 2.14) \times 10^{-3}$ ns, $T_K = (29.29 \pm 7.91)$ K and $T_0 = (1.17 \pm 0.68)$ K, b) fractal parameter; the dashed lines are included to guide the eye c) the interaction parameter, k	158
Figure 6:1	Magnetic phase diagram of $\text{Cr}_{1-x}\text{Fe}_x$ alloys reproduced from ²²⁷ . Ferromagnetic boundary determined by <i>Burke & Cywinski</i> (filled circle); <i>Loegel</i> (open circle); <i>Aldred & Kouvel</i> (open triangle); <i>Shull & Beck</i> (filled triangle). Anti-ferromagnetic boundary is a compilation of work by <i>Burke & Rainford</i> . The spin glass transition	

temperature was determined by *Burke & Cywinski*. Curved lines are to guide the eye, and the hatching indicates a region of complex magnetic properties. 163

Figure 6:2 Neutron Spin Echo spectra of $\text{Cr}_{0.865}\text{Fe}_{0.135}$; the solid lines are least square fit of a Weron-Tsallis function modified to include a background term, the dashed lines ($T = 20, 11, \text{ and } 7.5 \text{ K}$) represent least square fit to the Weron-Tsallis function..... 165

Figure 6:3 Neutron Spin Echo spectra of $\text{Cr}_{0.825}\text{Fe}_{0.175}$; solid lines represent least square fit to the data using the Weron-Tsallis relaxation function..... 166

Figure 6:4 The calculated Weron parameters of least square fitting NSE measurements of $\text{Cr}_{0.865}\text{Fe}_{0.135}$. a) the temperature dependence of (τ) where the solid line is fit to the Arrhenius law: $\tau_0 = (9.46 \pm 1.66) \times 10^{-4} \text{ ns}$, $E_a/k_B = (33.51 \pm 2.80) \text{ K}$, b) fractal parameter (circle) and background term (triangle), c) the Weron interaction parameter (k); the dashed curve is to guide the eye..... 167

Figure 6:5 The Weron parameters calculated for $\text{Cr}_{0.825}\text{Fe}_{0.175}$. a) the temperature dependence of (τ) where the solid line is fit to the Arrhenius law: $\tau_0 = (7.42 \pm 0.86) \times 10^{-3} \text{ ns}$, $E_a/k_B = (33.42 \pm 6.08) \text{ K}$, b) fractal parameter (α), c) the Weron interaction parameter (k); the dashed curve is to guide the eye. 168

Figure 7:1 Magnetic susceptibility measurements taken from *Creveling*²³⁰, corresponding to a sample which underwent 45 day of annealing at 500 °C followed by 15 days at 300 °C. The solid line is a least square fit to Eq.(6:2); $\chi_0 = 95 \times 10^{-6} \text{ emu gram}$, $C = 79.7 \times 10^{-3} \text{ emu gram}$, and $\theta = 53 \text{ K}$ 172

Figure 7:2 Instrument calibration measurement performed in a homogeneous 20 G transverse field. The solid line is a fit to a damped cosine function. 174

Figure 7:3 The structure of ordered Au_4V in which vanadium atoms are black and gold atoms silver. The isosurface indicates the positions within the unit cell where the nuclear depolarisation rate, $\sigma = 0.34\mu\text{s}^{-1}$. Labels 1 & 2 indicate the likely muon position. 175

Figure 7:4 The observed zero-field muon spin relaxation spectra of Au_4V ; the solid lines represent least square fits using equation (7:2). 176

Figure 7:5 Parameter temperature dependence of equation (7:2) from least square fit of the zero-field data; a) the relaxing asymmetry, (a_1) b) the fluctuation rate, (ν) c) the muon spin relaxation rate, (λ)..... 177

Figure 7:6 The longitudinal field muon spin relaxation spectra form Au_4V observed at 46 K in several applied fields. Eq (7:2) was used to fit both the 0 G and 10 G data. The application of 100 G fully decouples the nuclear dipole fields such that it can be fitted with a single exponential term. 179

Figure 7:7 The scaled inverse muon spin relaxation rate (τ_∞ / λ) versus reduced temperature for Au_4V (closed circles) and MnSi (open circles). The solid line represents the fit of Eq (7:4) to the data. The experimental points for MnSi are taken from *Hayano*²³⁴. Insert: The temperature dependence of relaxing asymmetry in Au_4V 179

Figure 8:1 Tsallis' non-extensivity parameter calculated from Weron analysis of NSE spectra. 184

Figure 8:2 Tsallis' non-extensivity parameter for RAM systems investigated using NSE spectroscopy. 186

Figure 8:3 Tsallis' non-extensivity parameter for superparamagnetic systems; solid lines are guides to the eye..... 186

LIST OF TABLES

Table 1:1	The spin, orbital, and total angular momentum quantum numbers derived from the use of Hund's rules.....	11
Table 3:1	The spin and orbital coefficients calculated by Brown ⁸⁹ used to produce Figure 3:5.	59
Table 3:2	The NSE configurations required for the study of different sample scattering types.	72
Table 3:3	Currently accepted values of the fundamental muon properties ¹³²⁻¹³⁵	82
Table 4:1	Listed here are the Strukturbericht designations, space group and crystal symmetry, as well as the AB stacking sequences for each of the founding systems studied by Friauf and Laves circa 1930.....	98
Table 4:2	The calculated aluminium concentrations within the first unit cell i.e. the first seven near-neighbour shells, where x_{nom} is the nominal sample concentration.....	120

INTRODUCTION

During the last century our understanding of real magnetic systems has improved greatly, due to both significant theoretical advances and a constant improvement of the experimental techniques available. Consequently convergence between prediction and observation has grown, especially since the inclusion of interactions enhanced by, and in addition to, the exchange between spins. Despite this however our understanding of the dynamics of exchange coupled spins, specifically how paramagnetic spin dynamics relate to the magnetic ground state, remains decidedly poor. Fortunately the simultaneous improvement of experimental techniques has led not only to increased accuracy but crucially opened a vast region of momentum and frequency space over which scientists can investigate. Motivated by this I present several investigations in to the spin dynamics of several evolving magnetic systems using neutron scattering and muon spectroscopic techniques.

In YMn_2 the manganese moments, which are separated by distances close to that of the pure metal, are found to localise at low temperature and adopt a complex anti-ferromagnetic spin arrangement alongside a remarkably large lattice expansion. The dynamics associated with this magnetic phase transition have previously been studied using a range of experimental techniques. Partial substitution of aluminium for manganese not only counteracts this lattice expansion but also promotes Curie-Weiss-like behaviour, collapses the long-range magnetic order, and ultimately leads to a spin glass phase at low temperatures. The first question addressed in this thesis is whether using the application of external mechanical pressure the resulting change in spin dynamics can be reversed, leading to a magnetic ground state comparable to

that of the undoped parent compound. To do this muon spin relaxation measurements have been performed and the divergence in the relaxation rate modelled using self-consistent spin fluctuation theory. This investigation is then extended using neutron diffraction to study the evolution in nuclear and spin correlations across the transition temperature as a function of aluminium concentration.

As stated, in this system the addition of non-magnetic aluminium promotes a low temperature spin glass phase largely due to the inherent geometric frustration of the crystallographic structure. A spin glass phase is a disordered magnetic state characterised by the slowing, and eventual freezing, of magnetic moments in random orientation. The dynamics associated with this process follow an unexplained but nonetheless apparently universal non-exponential form - hence this *glassy relaxation* has intrigued scientists for many decades. Noble prize laureate *Philip Anderson* has stated,

*“The deepest and most interesting unsolved problem
in solid state theory is the nature of glass and the
glass transition”¹*

Close analogy can be made between the relaxation dynamics of structural and spin glasses, leading many scientists to believe a deeper understanding of the glass transition should first be sought by establishing a theory for the spin glass transition. Attempts to do so have had unforeseen implications in many fields of research: neural networks, sociology, biological evolution, computer algorithms, artificial intelligence, and economics, all of which to a greater or lesser extent fall under the umbrella of what are known as complex evolving systems and as such the spin glass problem is therefore often considered to be a precursor to the study of complexity itself.

In the context of this research, it has recently been discovered a degree of universality exists between the relaxation dynamics of several dilute spin glass systems studied within the framework of Tsallis' non-extensive entropy. Continuing

this work I present further investigations of this possibly universal relaxation response *via* the Neutron Spin Echo technique.

Finally, discovered in the 1960s, weak itinerant magnetic systems are a fascinating class of material which obey the Curie-Weiss law very precisely, yet have an ordered moment significantly lower than the effective moment calculated for the Curie constant. The intermetallic compound Au_4V is extremely unusual in that it is found to be ferromagnetic despite neither gold nor vanadium carrying a magnetic moment, yet has characteristics of both localised and itinerant electron systems. To resolve this issue a Muon Spin Relaxation study has been performed of the spin fluctuations above the Curie temperature, and comparison made to the archetypal weak itinerant system MnSi using *Moriya's* unified theory as the framework.

Chapter 1

MAGNETISM

1.1 Introduction

Our understanding of magnetism, despite it being ubiquitous in modern day life, is far from complete. This opening chapter will introduce several key concepts such as symmetry, localised and itinerant models, and present a modern-day description.

1.1.1 Symmetry

Transition to a low temperature ordered magnetic phase is accompanied by a reduction of *symmetry*. A simple way to envisage this is by considering the transition from liquid to solid state in condensed matter. A liquid has complete translational and rotational symmetry, that is to say each point is identical averaged over time. However when cooled below the melting point the resulting solid state must sacrifice much of this symmetry. For example, a regular square lattice has only four-fold rotational symmetry, and translational symmetry of integer combinations of its lattice parameter. Similarly, during a ferromagnetic phase transition a reduction in symmetry occurs due to the spins choosing a unique direction along which to align (up or down). This can be illustrated by *Landau's* theory.

1.1.2 A Phenomenological Description

The Landau theory is a phenomenological model which calculates the free energy of a system as a function of its magnetisation, (M). For a ferromagnet in the absence of an external magnetic field the free energy is written as a polynomial series,

$$F(\mathbf{M}) = F_0 + a(T)M^2 + bM^4 \quad (1-1)$$

where (F_0) and (b) are positive constants and [$a(T) = a_0(T - T_C)$] is a temperature dependant parameter allowed to change sign passing the transition temperature, (T_C). By minimising the free energy, ($\delta F / \delta \mathbf{M} = 0$), we find the ground state solutions,

$$\mathbf{M} = 0 \quad \text{or} \quad \mathbf{M} = \pm \left[\frac{a_0(T - T_C)}{2b} \right]^{1/2} \quad (1-2)$$

Clearly the first condition is true for all temperatures but produces an unstable equilibrium position with ($T < T_C$), shown in Figure 1:1. This instability is known as *spontaneous symmetry breaking*. The second result is strictly only valid when ($T < T_C$), thus the magnetisation is zero at all temperatures above the ferromagnetic transition, since we cannot take the root of a negative number, and then proportional to $(T_C - T)^{1/2}$. In this case there are two so-called *broken symmetry* solutions which have the same free energy, one where the spins are aligned in the up direction and the other where they are aligned down.

In a general sense the high temperature disordered paramagnetic phase is analogous to the liquid state in the previous example, where each spin is equivalent average over time, ($\mathbf{M} = 0$), and like the solid state the low temperature ordered phase has a reduced symmetry once the magnetisation adopts a non-zero value. Magnetisation is therefore the *order parameter** of the ferromagnetic phase transition.

Unfortunately, the predictions of the Landau Theory ultimately fail when applied to real systems. Experimental results are often more accurately described by the relationship [$\mathbf{M} \propto (T_C - T)^\beta$], where the exponent takes a value in the range ($0.2 \leq \beta \leq 0.4$); significantly lower than that predicted.

* A parameter associated with a phase transition that indicates the existence of a particular symmetry. Above the transition temperature it takes a value of zero and below a non-zero value.

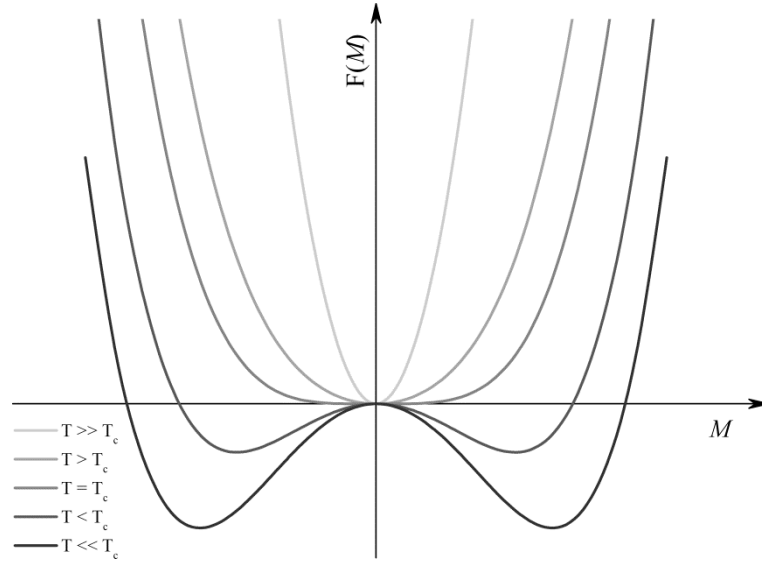


Figure 1:1 Variation of the Landau free energy for a ferromagnet, $F(M)$ for decreasing values of temperatures starting above the Curie temperature, (T_c).

It is important to mention that the susceptibility, specific heat, and correlation length are found to diverge at the critical point, meaning that each of these physical properties tend towards infinity at (T_c). In an analogous way so does the reciprocal of magnetisation. To model this critical behaviour simple power laws are usually applied, such as the derivation above, where the indices are known as *critical exponents*. These exponents not only contain valuable information on the nature of the phase transition under investigation, but also reveal systematic trends between microscopically different systems. The term *universality* is used to describe circumstances where apparently different systems yield the same critical exponent.

1.2 Theories of Magnetism

The modern theory of magnetism started with the advent of quantum mechanics, which from the outset lead to two distinct models: one initiated by *Heisenberg* based on a picture of localised electrons ², the other by *Bloch* based on band theory in which the itinerant electrons are so-called magnetic carriers ³. These mutually opposite models caused considerable controversy and ultimately although the localised electron picture was able to describe the magnetism of Rare earth metals and alloys both had limited success in accounting for the magnetic properties

of $3d$ metallic metals. Subsequently an alternative was developed in 1973 with the aim of interoperating between these extremes of fully localised or itinerant electron descriptions known as the *Self-Consistent Renormalisation Theory*, abbreviated to simply SCR theory ⁴.

1.2.1 The Exchange Interaction

Consider the simple case of a two electron system. The total eigenfunction must be described by the following linear combinations,

$$\Psi_S = \frac{1}{\sqrt{2}} [\psi_\alpha(1)\psi_\beta(2) + \psi_\beta(1)\psi_\alpha(2)]$$

and

$$\Psi_A = \frac{1}{\sqrt{2}} [\psi_\alpha(1)\psi_\beta(2) - \psi_\beta(1)\psi_\alpha(2)]$$
(1-3)

where (ψ_α) and (ψ_β) describe the space and spin quantum states of the particle (1) and particle (2), respectively. The first is called the symmetric and the second anti-symmetric total eigenfunctions, which despite taking different forms both describe the same eigenvalue, a phenomenon called *exchange degeneracy*. However if both particles were in the same quantum state the anti-symmetric expression would be identical to zero.

$$\Psi_A = \frac{1}{\sqrt{2}} [\psi_\alpha(1)\psi_\alpha(2) - \psi_\alpha(1)\psi_\alpha(2)] \equiv 0$$
(1-4)

This is in fact the basis of the Exclusion Principle which states indistinguishable[†] fermions cannot occupy the same quantum state, and by implication must be anti-symmetric under particle exchange.

In this brief explanation labels (1) and (2) contained both the space and spin variables of the electrons; three space and one spin quantum numbers. In a very general way however it is possible to express the anti-symmetric total eigenfunction as the product of these separate factors ⁵,

[†] Particles such as electrons cannot be distinguished between if their wave functions overlap.

$$(\text{total eigenfunction}) = (\text{space eigenfunction}) \times (\text{spin eigenfunction})$$

Due to the spin quantum number being a discrete variable there are subsequently three valid symmetric spin eigenfunctions (triplet state), but still just one anti-symmetric spin eigenfunction (singlet state) for non-interacting electrons. Since the total eigenfunction must be anti-symmetric with exchange of particle labels this leads to a coupling between the spin and space variables; they must have opposite symmetry. There is no classical analogy for this *exchange interaction*; it is simply an electrostatic force driven by quantum mechanical effects which manifests in several ways.

This is called *direct* exchange, which occurs when electronic wave functions overlap. However, when such overlap is negligible exchange interactions may still be mediated *via indirect* mechanisms. For the purposes of this work only the *Rudderman-Kittel-Kasuya-Yosida* (RKKY) interaction⁶⁻⁸ need be discussed. The RKKY exchange interaction is important when considering well localised magnetic moments such as those of the Rare earth metals, or in situations where magnetic impurities are well separated. Briefly, such magnetic moments have a polarising effect on the surrounding sea of *6s*- and *5d*-conduction electrons leading to an excess of spin-up electrons close to the magnetic moment. The spin density thus extends in an oscillatory fashion away from the magnetic moment throughout the lattice, polarising the surrounding magnetic moments, the magnitude and direction of which subsequently varies with separation.

1.2.2 Localised Electron Model

An atom has an eigenstate defined by its spin and orbital angular momenta given by the sum of its individual electrons: $[\mathbf{S} = \sum \mathbf{s}_i]$ and $[\mathbf{L} = \sum \mathbf{l}_i]$, illustrated in Figure 1:2. Assuming the electrons of the atom in question are fully localised the ground state configuration can be determined by Hund's empirically formulated rules which state:

1. The spin quantum number (S) is maximised in a way to minimise the Coulomb energy consistent with the Pauli Exclusion Principle.
2. The orbital quantum number (L) is maximised in a way that is compatible with rule 1. Hence minimising energy further by making it easier for the electrons to avoid one other.
3. For shells less than half full the magnitude of the total angular momentum quantum number [$J = |L - S|$], whilst for shells more than half full [$J = |L + S|$]. This final rule attempts to minimise the spin-orbit energy.

The total angular momentum can then be used to determine the local magnetic moment of the atom,

$$\mathbf{m} = g_J \mu_B \mathbf{J} \quad (1-5)$$

where (g_J) is the *Landé g-factor* and μ_B is the Bohr magneton ($= e\hbar / 2m_e$). To derive the paramagnetic susceptibility we must consider a system of (N) non-interacting local moments under the influence of an external magnetic field (\mathbf{B}) which will tend to align the direction in which they point. Thus each atom will possess a potential energy equal to,

$$E = -g_J \mu_B \mathbf{M}_J \mathbf{B} \quad (1-6)$$

where (\mathbf{M}_J) is the magnitude of (\mathbf{J}) projected along the direction of the applied field. The probability of an atom being in state with energy (E) at temperature (T) is given by Boltzmann statistics, which through a lengthy derivation leads to susceptibility of the form,

$$\chi_{para} = \frac{N g_J^2 \mu_0 \mu_B J(J+1)}{3k_B T} = \frac{C}{T} \quad (1-7)$$

where (C) is the Curie constant. This is the well known Curie Law which often incorporates an effective moment, [$\mu_{eff} = g_J^2 [J(J+1)] \mu_B$] per magnetic atom.

In 1928 *Heisenberg* introduce a model to account for direct exchange interactions taking place between neighbouring atomic spins. In his model the energy of the system is given by the Hamiltonian,

$$\mathcal{H} = - \sum_{ij} J_{ij} \mathbf{S}_i \cdot \mathbf{S}_j \quad (1-8)$$

where (\mathbf{J}) is now the so-called exchange integral which is positive for ferromagnetic alignment and negative for anti-ferromagnetic alignment ². The sum is taken over all nearest neighbour spins, (\mathbf{S}) located on lattice sites i and j . It is important to note that these spins are three-dimensional vectors allowed to point in any direction, ($D = 3$), however the dimensionality of the lattice on which they sit may be ($d = 1, 2, 3 \dots n$).

The most frequently used spin model is perhaps the Ising model ⁹, where the spin operator is one-dimensional and is therefore restricted to point only up or down ($D = 1$). However, regardless of the model chosen equation (1-8) presents a many-body problem which is extremely difficult to solve exactly. In general we resort to an amalgamated mean-field approach where the exchange between a finite number of spins are solved whilst the remaining lattice interactions are replaced by an effective field, (\mathbf{B}_{eff}).

This is highly analogous to the first successful theory of ferromagnetism developed some 20 years earlier by *Weiss* ¹⁰. Here it is assumed that the interactions responsible for magnetic ordering of atomic moments can be wholly represented by an effective mean-field given by,

$$\mathbf{B}_{eff} = \lambda \mathbf{M} \quad (1-9)$$

where the constant (λ) is called the molecular field coefficient.

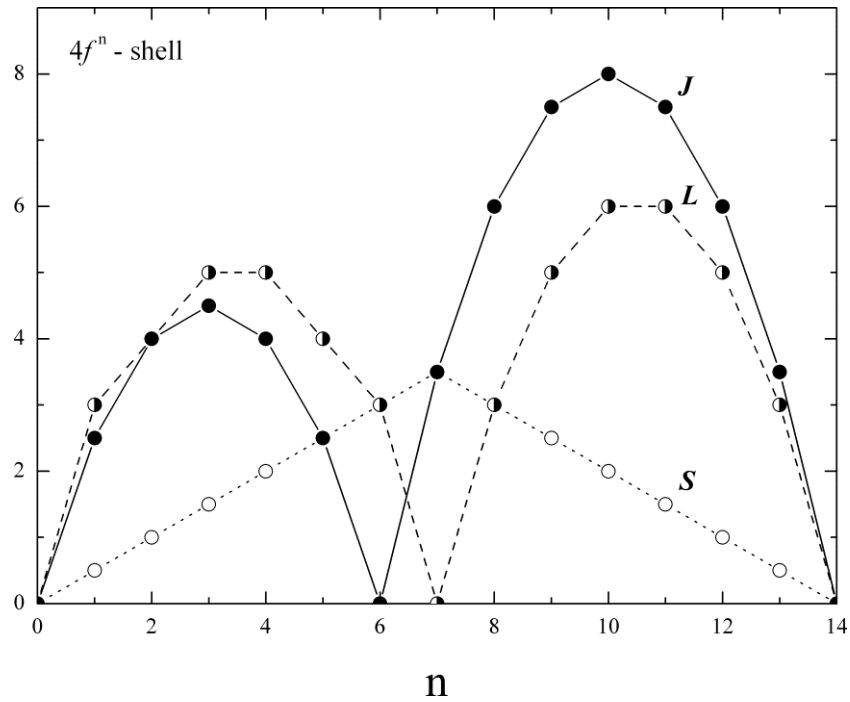


Figure 1:2 The result of Hund's rules applied to the lanthanide series, where n represents the number of electrons in the $4f$ subshell.

	shell	$l=3$	2	1	0	-1	-2	-3	S	L	J
Ce	$4f^1$	↓							1/2	3	5/2
Pr	$4f^2$	↓	↓						1	5	4
Nd	$4f^3$	↓	↓	↓					3/2	6	9/2
Pm	$4f^4$	↓	↓	↓	↓				2	6	4
Sm	$4f^5$	↓	↓	↓	↓	↓			5/2	5	5/2
Eu	$4f^6$	↓	↓	↓	↓	↓	↓		3	3	0
Gd	$4f^7$	↓	↓	↓	↓	↓	↓	↓	7/2	0	7/2
Tb	$4f^8$	↓↑	↓	↓	↓	↓	↓	↓	3	3	6
Dy	$4f^9$	↓↑	↓↑	↓	↓	↓	↓	↓	5/2	5	15/2
Ho	$4f^{10}$	↓↑	↓↑	↓↑	↓	↓	↓	↓	2	6	8
Er	$4f^{11}$	↓↑	↓↑	↓↑	↓↑	↓	↓	↓	3/2	6	15/2
Tm	$4f^{12}$	↓↑	↓↑	↓↑	↓↑	↓↑	↓	↓	1	5	6
Yb	$4f^{13}$	↓↑	↓↑	↓↑	↓↑	↓↑	↓↑	↓	1/2	3	7/2
Lu	$4f^{14}$	↓↑	↓↑	↓↑	↓↑	↓↑	↓↑	↓↑	0	0	0

Table 1:1 The spin, orbital, and total angular momentum quantum numbers derived from the use of Hund's rules.

In this case the susceptibility follows the Curie-Weiss form,

$$\chi = \frac{C}{T - \theta} \quad (1-10)$$

where (θ) is the Weiss constant which defines the position of a transition below which spontaneous magnetic ordering occurs. In the case ($\theta > 0$) the moments adopt ferromagnetic alignment, and when ($\theta < 0$) anti-ferromagnetic alignment. However, being prior to the arrival of quantum mechanics this phenomenological model could not provide an explanation as to the origin of this internal molecular field.

1.2.3 Itinerant Electron Model

The nearly-free electron model offers a simple description of metals and states at ($T = 0$) eigenstates are filled up to the Fermi wavevector (\mathbf{k}_f). If we take the points in k-space to be separated by ($2\pi / L$), where (L^3) is the volume, and the number of states between (\mathbf{k}) and ($\mathbf{k} + d\mathbf{k}$) to be equal to $[4\pi k^2 dk]$,

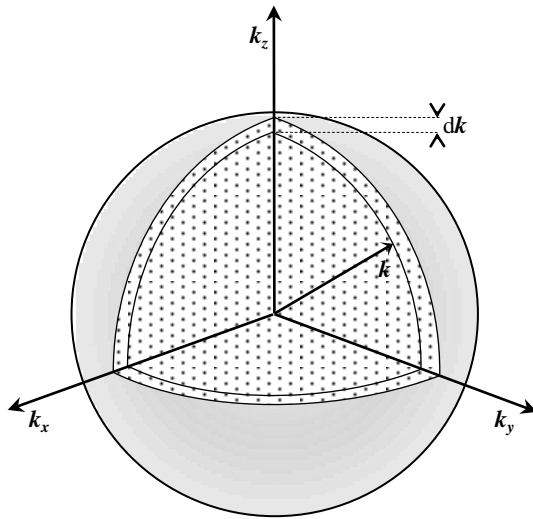


Figure 1:3 The density of states in k-space is calculated by considering the volume of k-space between wavevector (\mathbf{k}) and ($\mathbf{k} + d\mathbf{k}$).

The density of states can be easily derived;

$$g(\mathbf{k})d\mathbf{k} = \frac{V\mathbf{k}^2 d\mathbf{k}}{\pi^2} \quad (1-11)$$

Thus, the number of electrons (N) filling eigenstates up to the Fermi wavevector is,

$$N = \int_0^{k_f} g(\mathbf{k})d\mathbf{k} = \frac{V\mathbf{k}_f^3}{3\pi^2} \quad (1-12)$$

However, the occupancy of these states is governed by the Fermi-Dirac statistics,

$$f(E) = \frac{1}{\exp((E - E_f)/k_B T) + 1} \quad (1-13)$$

where E is the energy of a given eigenstate and (E_f) the Fermi energy. From this equation it can be seen at absolute zero $f(E)$ reduces to a step function, taking the value of unity when ($E < E_f$) and 0 when ($E > E_f$).

Eigenstates with different spin quantum number have the same energy, meaning in the absence of an external field there exists a two-fold degeneracy. When an external magnetic field is applied the electron's energy is either lifted or lowered depending on its relative spin alignment. In the first instance this gives rise to Pauli paramagnetism; the largely temperature independent susceptibility of the electron gas.

This spontaneous splitting of the spin states may also explain the non-integer μ_B measurements of the magnetic moment per atom in metals such as iron ($\sim 2.2 \mu_B$). By analogy with the Weiss model, Stoner¹¹ proposed that electron-electron exchange interactions may be described using a molecular mean-field where each spin experiences an average exchanged field generated by all its neighbouring spins, taking the form,

$$\mathbf{B}_S = \gamma \mathbf{M} \quad (1-14)$$

This molecular field magnetises the electron gas due to Pauli paramagnetism, which in turn causes the molecular field. This feedback mechanism is however strictly dependent on both the molecular field constant (γ) and the Pauli susceptibility (χ_0) being large enough for the system as a whole to save energy by becoming ferromagnetic.

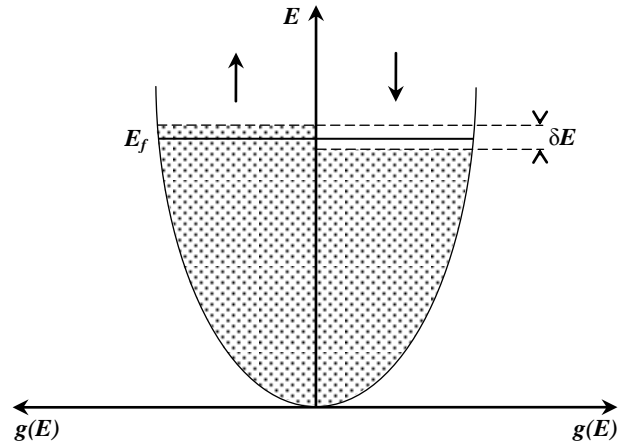


Figure 1:4 The density of states, $g(E)$, showing a spontaneous splitting of the spin bands.

The model is as follows: in the absence of an external field a number of spin-down electrons are elevated by a small amount (δE) from the Fermi energy, changing spin state as they do so. Hence spin-down electrons between $(E_f - \delta E)$ and (E_f) now occupy eigenstates between (E_f) and $(E_f + \delta E)$ in the spin-up band. The number of electrons moved is equal to the density of states at the Fermi energy multiplied by half the energy change, $[g(E_f) \delta E / 2]$. The energy costs is therefore given by,

$$\Delta E_{KE} = \frac{1}{2} g(E_f) \delta E^2 \quad (1-15)$$

However the interaction between the magnetisation and molecular field may give an energy reduction greater than (ΔE_{KE}) . To illustrate this first the magnetisation is written in terms of the number density of up and down spins respectively,

$$\mathbf{M} = \mu_B(n_\uparrow - n_\downarrow) \quad (1-16)$$

Note that the magnetic moment predicted by this equation is not necessarily an integer value of the Bohr magneton. The change in molecular field energy is therefore,

$$\begin{aligned} \Delta E_M &= - \int_0^M \mu_0 \gamma \mathbf{M} d\mathbf{M} \\ &= - \frac{1}{2} \mu_0 \mu_B^2 \gamma (n_\uparrow - n_\downarrow)^2 \\ &= - \frac{1}{2} U (g(E_f) \delta E)^2 \end{aligned} \quad (1-17)$$

with $[U = \mu_0 \mu_B^2 \gamma]$ essentially a measure of the mean exchange per electron driving the molecular field. Figure 1:5 shows the calculated values of (U) and $g(E_f)$ as a function of atomic number. The total energy exchange (ΔE) is therefore the sum of the kinetic and molecular field energies:

$$\Delta E = \Delta E_{KE} + \Delta E_M = \frac{1}{2} g(E_f) \delta E^2 (1 - U g(E_f)) \quad (1-18)$$

Clearly with $[U g(E_f) \geq 1]$ the change in energy given by this equation is negative, implying that spontaneous ferromagnetism is possible since it is energetically favourable for the system as a whole. This condition not only requires strong Coulomb interactions but a high density of states at the Fermi energy, and is referred to as the *Stoner Criterion*. With this in mind it is apparent that, at least for *3d* transition metals, the band structure close to the Fermi energy is vital in determining the magnetic properties of the material.

Thus under the influence of an applied external magnetic field the paramagnetic susceptibility is given by,

$$\chi = \frac{\mathbf{M}}{\mathbf{H}} \approx \frac{\mu_0 \mathbf{M}}{\mathbf{B}} = \frac{\mu_0 \mu_B^2 g(E_f)}{1 - U g(E_f)} = \frac{\chi_0}{1 - U g(E_f)} \quad (1-19)$$

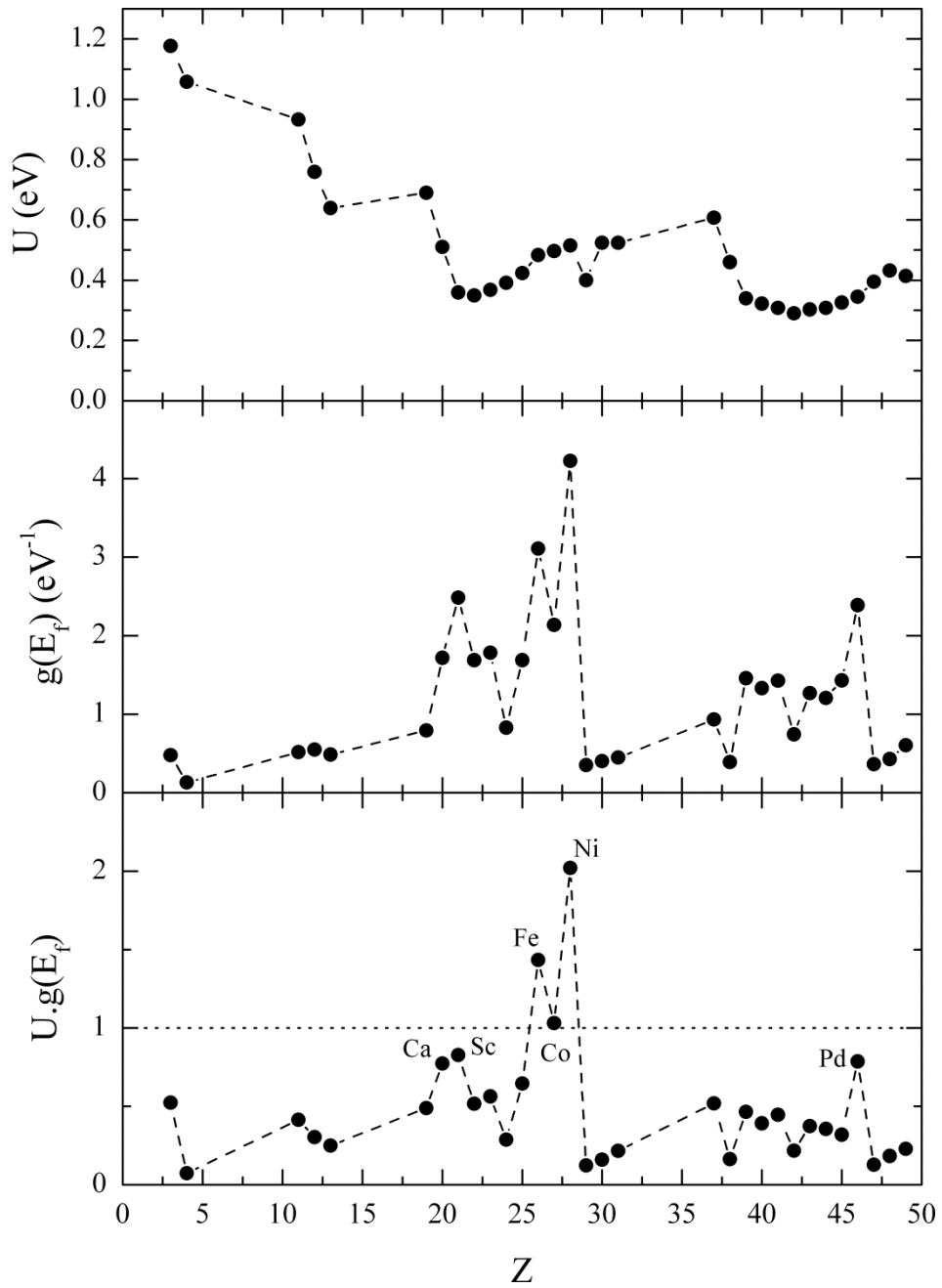


Figure 1:5 Top: the Stoner parameter as a function of atomic number Z . Middle: the density of states as a function of atomic number. Bottom: The Stoner criterion given by the product of the density of states and the Stoner parameter. It can be seen that only the elements iron, cobalt, and nickel are capable of spontaneous ferromagnetism, however calcium, scandium, and palladium are very close. Recreated from *Solid-State Physics*, Ibach & Lüth¹².

and so the Pauli susceptibility is enhanced by the denominator if ($U < 1$), a phenomenon called the Stoner enhancement which is especially evident in systems which are close to ferromagnetism such as palladium and platinum.

1.2.4 A Unified Theory

The localised electron model holds true at least for isolated atoms or for substances where the unpaired electrons are not perturbed too greatly by interatomic interactions, for example insulators and 4f-metals. However its predictions are not consistent with empirical evidence, which reveals the saturation moment, (μ_s), of many metal's does not take an integer value of the Bohr magneton despite obeying the Curie-Weiss Law, equation (1-10). This is largely because the localised electron model does not account of the way chemical bonding significantly alters the electronic structure of atoms in the solid state, i.e. alters the conduction band.

On the other hand, the itinerant electron model successfully predicts that spontaneous ferromagnetism exists only for three elements: iron, cobalt, and nickel which fulfil the *Stoner criterion*, and furthermore accounts for the observed saturation moment per atom being a non-integer value of the Bohr magneton. However compared with experimental results it fails in determining the susceptibility of transition metals above absolute zero, and predicts transition temperatures which are several orders of magnitude too high. Most importantly it is unable to explain the Curie-Weiss Law.

Insight as to a system's degree of itinerancy was provided by the *Rhodes & Wohlfarth*¹³, who by plotting the ratio between the effective and saturation moment (μ_{eff} / μ_s) as a function of the Curie temperature obtained the plot recreated in Figure 1:6. Since under a localised picture the moment does not change greatly across the transition temperature this ratio should be close to one (dashed line). The itinerant limit is realised where ($\mu_{eff} \gg \mu_s$) since the saturation moment is independent of the Curie constant. The plot clearly implies that the vast majority of systems are neither fully localised nor itinerant in nature but instead evolve continuously between the two mutually opposite extremes.

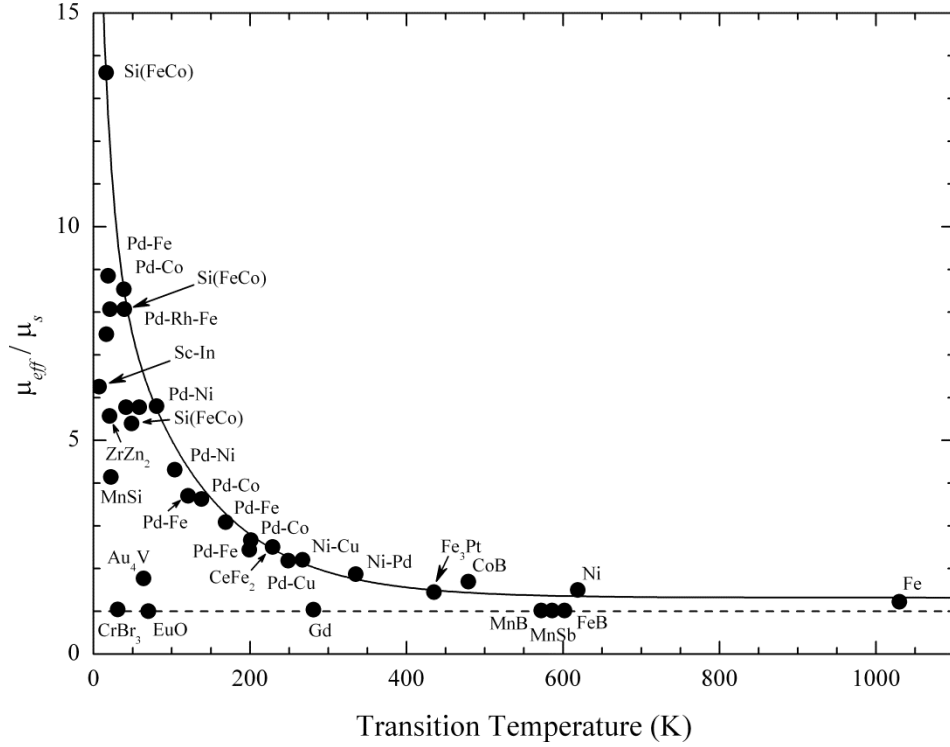


Figure 1:6 The Rhodes-Wohlfarth plot recreated from *Spin Fluctuations in Itinerant Electron Magnetism*, Tôru Moriya ¹⁴.

Subsequently Stoner's theory was extended to include thermally induced spin flip excitations at the Fermi surface in the hope it would extend the model to finite temperatures ¹⁵. By definition a spin flip excitation occurs when an electron is elevated above the Fermi energy, resulting in an electron-hole pair of opposite spin. This mechanism causes a smearing at the Fermi surface and an imbalance between the spin-up and spin-down bands, commonly referred to as a spin density fluctuations or Stoner excitations. However, even with the inclusion of spin density fluctuations the model still fails when compared to experimental observations. Significant improvements arrived in the 1970s when theoreticians began to consider exchange-enhanced spin fluctuations[‡], which were known to greatly enhance Stoner excitations.

Moriya developed a *unified* theory of spin density fluctuations for itinerant electron systems incorporating exchange-enhanced effects which, by calculating the equilibrium state and spin density spectrum in a self-consistent manner, allows both

[‡] The scattering of electron-hole pairs by exchange interaction.

local and itinerant magnetism to exist within the same framework and has greatly improved our current understanding of magnetism^{4, 16}. A detailed discussion of SCR theory is beyond the scope of this work but a comprehensive account may be found in reference¹⁴. Perhaps the most significant results are the prediction of Curie-Weiss susceptibility without a local moment, and reasoning for the disparity between effective and saturation moment observed in weakly ferro- and anti-ferromagnetic metals is also accounted for.

According to SCR theory the magnetic properties of a system are determined *via* the nature of their spin density fluctuations. In the local electron limit the amplitude of the spin density is fixed and fluctuations are regarded as local in real space. Alternatively, in the itinerant electron limit the average spin density amplitude of spin fluctuation at low temperature is localised in reciprocal space, therefore extended in real space. However, as shown in Figure 1:6 many magnetic materials occupy an intermediate range. A general theory of Curie-Weiss susceptibility is developed in terms of a stiffness constant for spin fluctuations, (T_0), which is a measure of the stiffness against a change in amplitude of the spin fluctuation.

$$\frac{1}{\chi_0} = \frac{4U^2}{NT_0} \sum_q \left(\frac{T}{1/\chi_0 + 2V(0) - 2V(q)} - \frac{T_C}{2V(0) - 2V(q)} \right) \quad (1-20)$$

where $V(q) = [U / S_L^2(q)]$. In the local limit ($T_0 \rightarrow 0$) and thus the general expression for magnetic susceptibility reduces to,

$$\chi_0 = \frac{NS_L^2}{3(T - T_C)} \quad (1-21)$$

In the opposite limit (T_0) is large, indicating that the spin fluctuations are “soft”, and,

$$\frac{1}{\chi_0} = \frac{4NU^2S_L^2(T)}{3T_0T_C} (T - T_C) \quad (1-22)$$

In this case the susceptibility arises due to the linear increase of the squared spin density fluctuation amplitude $S_L^2(T)$.

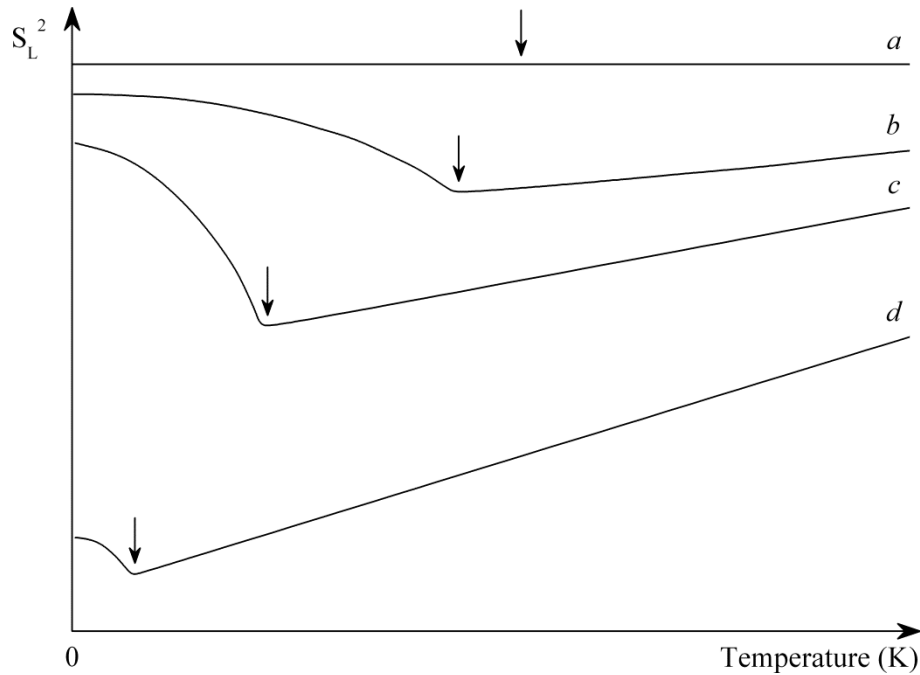


Figure 1:7 Possible examples of the temperature variation of $S_L^2(T)$, taken from *Moriya*¹⁴. Line *a* is the local moment case where the mean-square local amplitude of spin fluctuations is constant. Lines *b* and *c* represent intermediate values of stiffness constant, large and small respectively, and line *d* is for weakly ferromagnetic metals. The vertical arrows represent the position of T_C .

For weak itinerant ferromagnets the theory predicts a Curie temperature far lower than those of the Stoner theory, moreover Curie-Weiss behaviour is predicted above. The spontaneous magnetic moment per atom is dependent on the band structure at the Fermi surface, and is independent of the Curie constant. Finally, it is expected that the spontaneous magnetisation follows the relationship,

$$\mathbf{M} \propto \left(T_C^{4/3} - T^{4/3} \right) \quad (1-23)$$

Chapter 2

THE SPIN GLASS PHASE

In this, the second preliminary chapter, a chronological account along with the salient properties of the spin glass phase are presented. Key concepts are highlighted in order to aid inspection of several attempts to establish a general mean-field theory in the limit of static moments, before finally the dynamics of these systems are discussed in the wider context of non-exponential relaxation, emphasising two ‘new’ and analogous relaxation functions derived independently in recent years from the works of Weron and Tsallis.

2.1 Introduction

Louis Néel first investigated the materials which, some 40 years later, led to the discovery of the spin glass phase¹⁷. He hoped that by studying dilute alloys of transition metal impurities suspended in a noble metal matrix he could better understand the nature of magnetism in the pure transition metal itself. By the 1950s, advancements in cryogenics made it possible to reach much lower temperatures, revealing unusual magnetic behaviour unlike that of a ferromagnet or anti-ferromagnet¹⁸. Most early interpretations did not consider the existence of a phase transition, however the name ‘spin-glass’ was coined at the end of the 1960s to represent a new class of random magnetic alloy in which the magnetic structure is unrecognisable from that of the pure metal¹⁹. In 1971, at a conference on magnetism and magnetic materials, *Cannella, Mydosh & Budnick* revealed the

discovery of a sharp cusp in the susceptibility of dilute AuFe alloys ^{20, 21}. Thus interest in these new novel materials grew. In 1975 the first attempt at establishing a theory behind the spin glass phase was proposed by *Edwards & Anderson* ^{22, 23}, which will be discussed in more detail in the following sections.

Subsequently many hundreds of different magnetic systems have been identified as having spin-glass-like properties. This is perhaps not unexpected since almost all physical systems possess different types of interactions which compete to adopt different ordered states. In a general sense, such competition is uncovered when due to a change in an external parameter (temperature, pressure, or magnetic field) the system undergoes a phase transition, indicating that the external impulse favours one interaction type over the others. It is therefore not surprising that systems displaying spin glass properties are often fundamentally different, which prompted *Mydosh* to construct a broad scheme by which several discrete *families* could be identified ²⁴.

Spin glass family	Example
Noble metal – Transition metal alloys	<u>Au</u> Fe, <u>Cu</u> Mn, <u>Ag</u> Mn
Transition metal – Transition metal alloys	<u>Pb</u> Mn, <u>Mo</u> Mn, <u>Rh</u> Mn, <u>V</u> Fe
Rare earth alloys	La _{1-x} Gd _x Al ₂ , La _{1-x} Ce _x Ru ₂ , La ₈₀ Th ₂₀ Ce
Rare earth compounds	Y(Mn _{1-x} M _x) ₂ , (La _{1-x} Er _x)Al ₂ , (Ti _{1-x} V _x)O ₃
Amorphous semiconducting	(Sb ₂ S ₃) _x (SbI ₃) _y Fe _z
Crystalline insulating and semiconducting	Eu _x Sr _{1-x} S, Eu _{1-x} Gd _x S, Fe _{1-x} Mg _x Cl ₂

The following sections are not intended to give an exhaustive account of this vast field, but instead present a general overview in order to highlight the most important concepts relevant to this work.

2.1.1 Spin Glass Properties

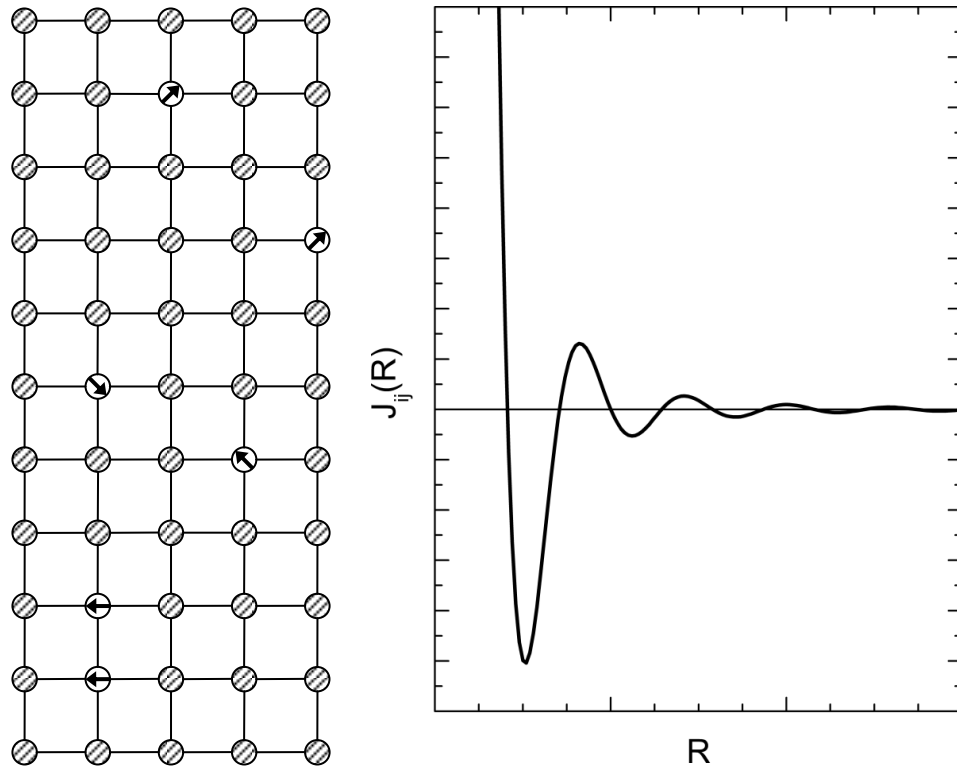


Figure 2:1 Left: A basic representation of magnetic moments placed at random on a non-magnetic cubic lattice. Right: the RKKY exchange (J_{ij}) plotted as a function of distance (R).

Communication between randomly located impurity spins is mediated indirectly through the conduction electrons *via* the RKKY interaction, illustrated above, and due to the long-range oscillatory nature of this exchange some spin-spin interactions are positive, therefore favouring parallel alignment, whilst others are negative and favour anti-parallel alignment. Subsequently, there is no mean ferromagnetic or anti-ferromagnetic order across the sample. On the contrary, upon cooling to sufficiently low temperature the spins freeze in random orientations, and a disordered ground state is entered below a critical temperature (T_f). As mentioned, the dynamics of this freezing process are analogous to those of structural glasses, and it is therefore hoped that in developing a model to understand the transition to the spin glass state a better understanding of the transition from supercooled fluid to amorphous structural glasses might be realised.

On a qualitative level at least, the physical behaviour of the different spin glass families is quite universal despite the diversity of mechanisms involved. The aforementioned cusp in the low temperature susceptibility is commonly accepted to be the hallmark behaviour of a spin glass material, and its position is considered to identify (T_f). In a small static field, the temperature dependence of susceptibility obeys the Curie-Weiss Law, indicating the spins are weakly coupled. In the paramagnetic phase, above (T_f), the magnetisation responds rapidly to changes in magnetic field, whereas in the spin glass phase the response is extremely slow.

Other measurements, such as Muon Spin Relaxation (§ 3.4), also shown similar sharp anomalies. Surprisingly however specific heat, a common indicator of a phase transitions, shows no distinct anomalies but only a broad peak at temperatures above the freezing point together with a low temperature linear term similar to that of a structural glass. This ‘smeared behaviour’ is also present in resistivity measurements ²⁵.

2.1.2 The Frustration Effect

It has been said that extensive investigation on so-called spin systems only began in earnest with the introduction of a new concept called *frustration*, circa 1977. In his seminal paper *Gérard Toulouse* presented an analysis of disorder in the context of spin-glasses, identifying that the spin glass phase is a consequence of “serious disorder” borne of “frustration effects”, as opposed to simply a flipping of interaction signs on sites chosen at random on a regular lattice ²⁶.

Here the term frustration denotes a situation where a spin, or ensembles of spins, cannot orientate in a way to satisfy all the neighbouring interactions. The plaquette, shown Figure 2:2, is perhaps the simplest example, where a single and double bond represent ferromagnetic and anti-ferromagnetic interaction, respectively. Clearly, no configuration of orientations exists whereby all the

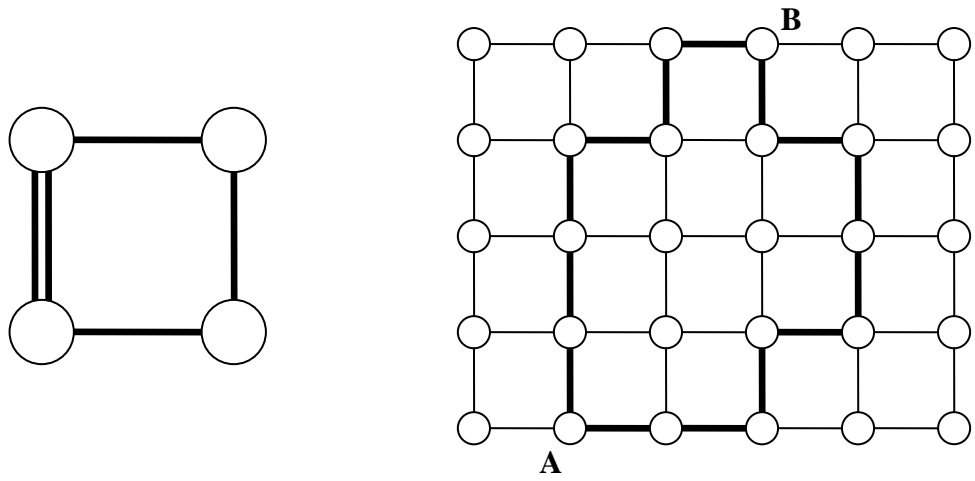


Figure 2:2 Left: A frustrated plaquette where single and double bonds represent a ferromagnetic interaction, and an anti-ferromagnetic interaction, respectively. Right: Square lattice where the contour (bold line) represents two possible paths between A and B.

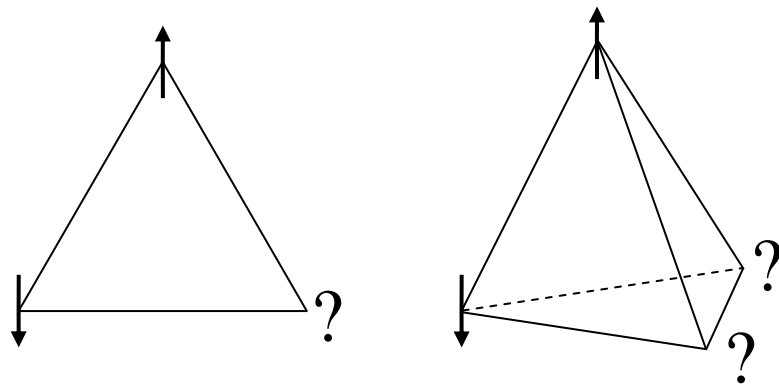


Figure 2:3 Left: Topological frustration for near-neighbour Ising spins on a triangular lattice with anti-ferromagnetic interactions. Right: Topological frustration in tetrahedral coordination.

interactions can be satisfied. Furthermore, a parameter to measure the effect can be defined on any closed contour across a lattice (c), Figure 2:2.

By taking ($J_{ij} = + 1$) to denote ferromagnetic alignment, and ($J_{ij} = - 1$) anti-ferromagnetic alignment, the frustration parameter is defined,

$$\Theta = \prod_{i \neq j}^c J_{ij} \quad (2:1)$$

Hence, when it is possible to orient the spins between points (A) and (B) ($\Theta = + 1$), and the system is not frustrated. If however (A) sends contradictory signals to (B) along the two paths ($\Theta = - 1$), and the system is frustrated. In this simple example it should be noted that the frustration is established solely by competition between ferromagnetic and anti-ferromagnetic exchange interactions, since the inherent geometry of a regular square lattice is bipartite or unfrustrated.

In contrast, a triangular plaquette with only anti-ferromagnetic near-neighbour interactions exhibits geometrical frustration, Figure 2:3. As a result an anti-ferromagnetic triangular lattice is fully frustrated since each individual plaquette has a negative frustration parameter. The ground state must therefore be a compromise, which often gives rise to complicated non-collinear magnetic structures (§ 4.2).

2.1.3 Mean-Field Theories

As previously mentioned, the first attempts to construct a spin glass model were made by *Edwards & Anderson*, who in 1975 proposed a mean-field approach to the spin glass problem ²². To characterise the onset of spin glass *order* they proposed the following parameter,

$$Q(t) = [\langle \mathbf{S}_i(t) \cdot \mathbf{S}_i(0) \rangle^2]_{avg} \quad (2:2)$$

where the angular brackets denote the thermal average of spin (\mathbf{S}_i), and the average of this square over the distribution of interactions (J_{ij}) is given by the square brackets. It simply states that in the spin glass phase there is a non-vanishing

probability that the orientation of a spin remains unchanged after time (t). Assuming classical spins and a Gaussian distribution of exchange interactions it was shown that with ($T \geq T_f$) the order parameter $Q(t) = 0$, whilst for $T = 0$, $Q(t) = 1$ ²³. As will be discussed (§ 3.1.3), such correlation functions can be equated to the intermediate scattering function, $S(\mathbf{Q}, \tau)$, which is attained *via* neutron spin echo spectroscopy (§ 3.2). *Edwards* and *Anderson* further obtained expressions for the zero-field magnetic susceptibility and specific heat, predicting sharp cusps at the freezing temperature. Again, this has only ever been observed in magnetic susceptibility data; however their model did correctly identify the linear dependence in specific heat at low temperatures.

Further progress was made by *Sherrington & Kirkpatrick* who applied the Edwards-Anderson theory to an infinite ranged Ising square (hyper-cubic) model²⁷. To begin, they took a regular lattice of sites, labelled i ,

$$\mathcal{H} = \sum_{i \neq j} J_{ij} (\mathbf{s}_i \cdot \mathbf{s}_j), \quad \mathbf{s}_i = \pm 1 \quad (2:3)$$

where the sum is taken over all spin pairs, interacting *via* exchange (\mathbf{J}) given a priori from the same Gaussian probability distribution,

$$\mathcal{P}(J_{ij}) = \frac{1}{\sqrt{2\pi J^2}} \exp\left(-\frac{(J_{ij} - J_0)^2}{(2J^2)}\right) \quad (2:4)$$

Thus, by means of the so-called replica symmetry method (RS), they were able to find an exact solution, and by evaluating the average partition function of n identical replicas, discovered a *re-entrant* region of the magnetic phase diagram, so named since the system appears to re-enter a less magnetically ordered state upon cooling between the limits ($1 \leq \mathbf{J}_0 / \mathbf{J} \leq 1.25$), shown in the figure below.

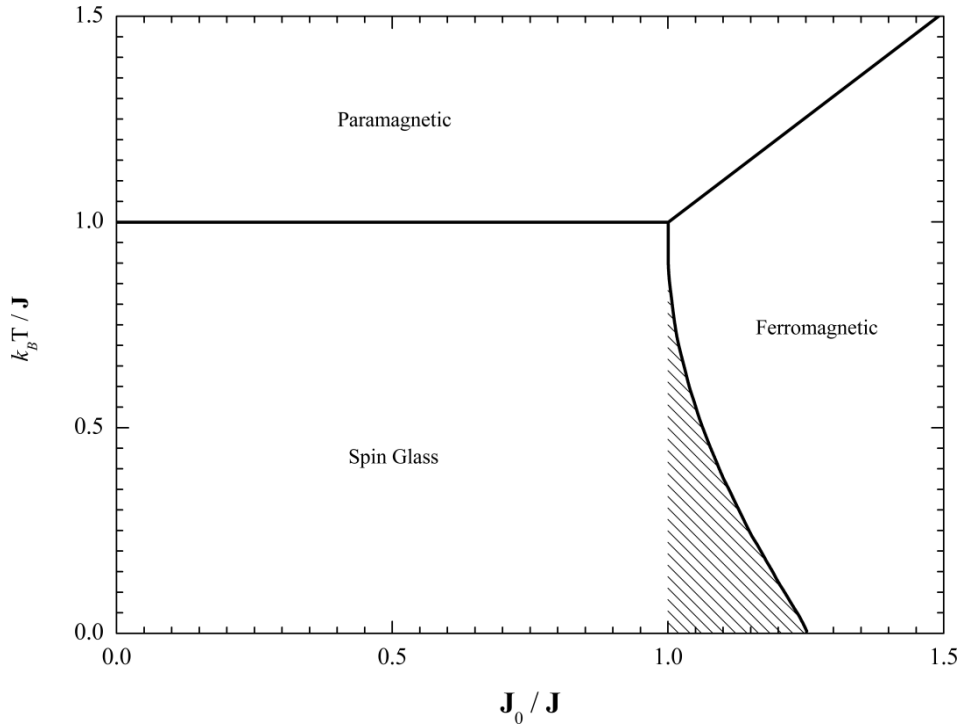


Figure 2:4 The Sherrington and Kirkpatrick phase diagram for infinite ranged Ising spins, with a mean and variance exchange interaction J_0 and J , respectively. Note, for $1 \leq J_0 / J \leq 1.25$ the system exhibits three distinct phases upon cooling: paramagnetic, ferromagnetic and finally a so-called re-entrant spin glass phase, indicated by the shaded region. Recreated from Sherrington & Kirkpatrick²⁷.

Unfortunately at $(T = 0)$ the calculated entropy was negative, violating the third law of thermodynamics. *Thouless* later avoided use of the replica method²⁸ and found the Sherrington-Kirkpatrick model to be correct close to or above the transition temperature; although the solution was still unstable at low temperatures even in the presence of an external magnetic field²⁹.

This instability was crucial as it suggested a breaking of symmetry between replicas. This brought about several attempts to construct a low temperature solution *via* so-called replica symmetry breaking (RSB), the most comprehensive of which was offered in a series of papers by Parisi³⁰⁻³². In short, provided the necessary restrictions are applied, Parisi's model yields seemingly realistic results in the static limit, however the legitimacy and necessity for these restrictions is still not fully understood³³.

2.2 Spin Glass Dynamics

Bantilan & Palmer introduced the term *broken ergodicity* in 1980 to portray the onset of the spin glass state as a sequence of bifurcations in phase space, resulting in many similar but mutually inaccessible microstates³⁴. This is shown schematically in Figure 2:5. It can be seen that as the temperature is reduced distinct valleys appear, separated by infinitely high energy barriers. Once trapped in a branch of the bifurcation cascade the system is unable to jump from one microstate to another, even if it were more energetically favourable to do so. In effect, with ($T > T_f$) a spin glass remains ergodic and given sufficient time can explore all points in phase space, whereas below (T_f) the system becomes non-ergodic. Analogy can therefore be drawn with structural glasses which, on experimental time scales, are also effectively non-ergodic since the maximum relaxation time, although finite, is far larger than is conceivably measurable.

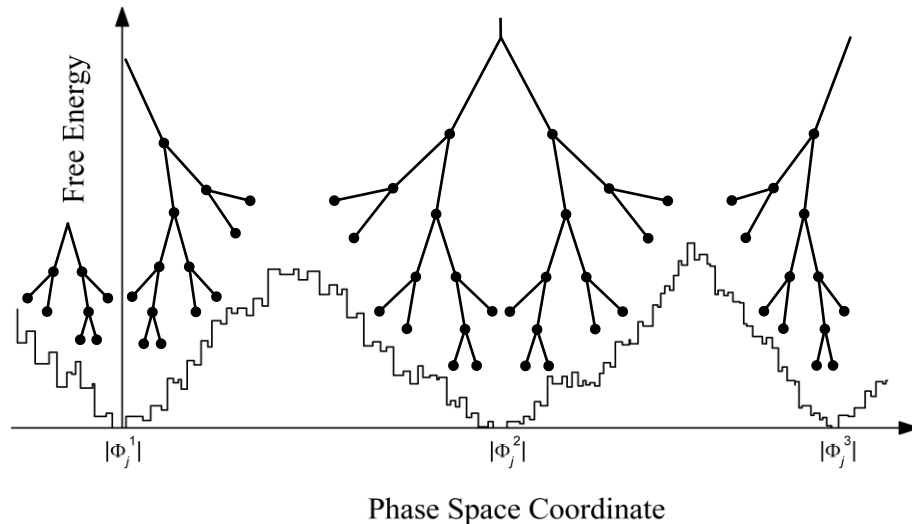


Figure 2:5 Schematic plot of the free energy density as a function of a phase space coordinate for a spin glass at low temperature; partially recreated from³⁵. Note there are many equivalent components or “valleys”, each of which corresponds to a ground state, $|\Phi_j^{(i)}|$, or low-lying excited state.

The fact that these numerous microstates are not related to one another by symmetry, rather appear due to the inherent degeneracy of the system, is a direct consequence of frustration in the system³⁶. Therefore, the broken symmetry between replicas in the Sherrington-Kirkpatrick model is seen as a special case of broken ergodicity³⁷,

and as such any model which attempts to predict the properties of a non-ergodic system must first account for this inherent characteristic.

Palmer approached this by partitioning phase space into a set of mutually inaccessible components (valleys). This transition occurs suddenly; first order in the Ehrenfest sense, although for some structural glasses this need not be the case ³⁸. Ergodicity within each component holds, which leads to a clear distinction between intra- and inter-component relaxation timescales. Intra-component relaxation is that which occurs between the many metastable states within a given valley, and is often so fast as to only be included in the system's entropy. Inter-component relaxation on the other hand occurs on extremely long timescales and is therefore effectively frozen i.e. non-ergodic. Ultimately, if we accept this doctrine we must infer that all glassy systems can break ergodicity if the timescale of the observation is much shorter than the characteristic relaxation time of the system.

2.2.1 Non-exponential Relaxation

With this in mind, three hundred years of empirical evidence including that of mechanical ³⁹, electrical ⁴⁰ and magnetic ⁴¹ relaxation, has shown slow non-exponential behaviour to be a fundamental feature of many diverse materials ⁴². Moreover, for the past 150 years it has been customary to evaluate such anomalous relaxation *via* the so-called *stretched exponential* first suggested by *Kohlrausch* ⁴³, and later derived by *Williams & Watts* ⁴⁴. This behaviour is also observed in the spin relaxation dynamics of spin-glasses, where early measurements above (T_g) quickly reported finding stretched exponential decay in both the remnant magnetisation and spin-spin autocorrelation function ^{45, 46}.

$$\phi(t) \propto \exp\left[-(t/\tau)^\beta\right], \quad 0 < \beta < 1 \quad (2:5)$$

Accordingly, several theories arose in the hope of explaining this ubiquitous behaviour, each based on different interpretations of the physical mechanisms driving it. Each is successful in deriving a stretched exponential of the form given by the equation above, however rather than clarify the situation (as was intended) the

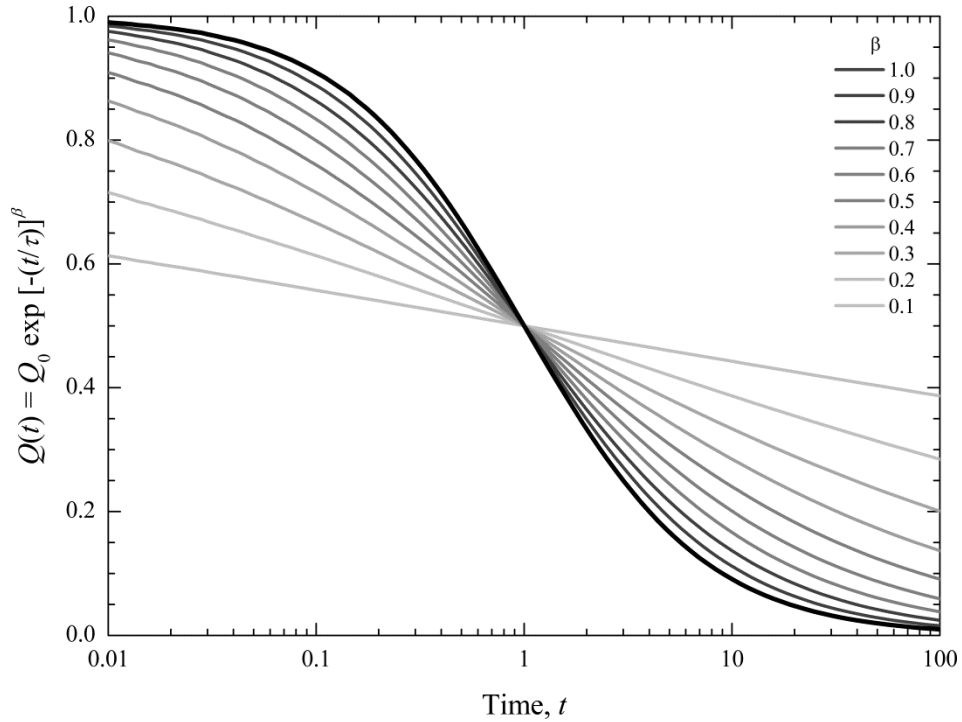


Figure 2:6 The time dependence of the stretched exponential formula, Eq.(2:5), with $\tau = 1$ s, calculated for several (β) values, plotted on a logarithmic time axis.

results caused considerable controversy⁴⁷. In the first instance, it was found the simplest derivation was based on taking a statistical distribution of relaxation times, (τ), representing different atoms, or clusters of atoms. This clearly implies the co-existence of many independent or *parallel* relaxation channels, each with characteristic relaxation time (τ_i). However, it was argued by *Palmer et al.* that such a model was unrepresentative of glassy systems⁴⁸. Any legitimate model would have to incorporate and satisfy three prerequisites: *broken ergodicity*, *interaction constrains*, and *hierarchy*; not simply rely on this statistical and somewhat microscopically arbitrary approach. In short, a hierarchically constrained model was put forward whereby faster degrees of freedom, such as the dynamics of single atoms successively constrain the slower. To some degree this is the antithesis of a parallel picture, but nonetheless still derives at the same functional form. Clearly, equation (2:5) cannot give any physical insight as to the mechanisms involved, and

besides, in many cases the stretched exponential is unable to adequately describe spin glass relaxation at, or close to, the transition temperature.

This was clearly demonstrated by *Ogielski*, who in 1985 performed extensive Monte Carlo simulations, shown in Figure 2:7, from which he was able to show the time dependent spin-spin autocorrelation function is more accurately described by a stretched exponential incorporating a power law pre-factor ⁴⁹,

$$\phi(t) \propto t^{-x} \exp\left[-(t/\tau)^\beta\right] \quad (2:6)$$

This phenomenological result revealed for the first time several interesting features in the time dependence of the exponents, (β) and (x). Firstly, at temperatures relatively far above the glass transition temperature, $\sim 4T_f$, the stretching exponent ($\beta \rightarrow 1$); this essentially means the exponential term is equivalent to simple Debye relaxation (exponential decay). Upon cooling, ($\beta \rightarrow 1/3$) as the transition temperature is approached. At the same time the characteristic relaxation time (τ), diverges. Secondly (x) is predicted to increase from a negligible value at the transition temperature up to approximately 0.5 at high temperatures.

In recent years these predictions have largely been supported by neutron spin echo measurement ⁵⁰, however despite its apparent success *Ogielski's* power law still does not distinguish between parallel or hierarchical relaxation processes and therefore we cannot hope to clarify the fundamental question as to what mechanism, or mechanisms are driving this non-exponential decay. Moreover, the power law pre-factor can lead to unphysical values at short times i.e. ($Q(t) > 1$) as ($t \rightarrow 0$).

A new model is therefore needed to explain this seemingly universal power law response. To this end, the remaining sections of this chapter will present two closely related candidates and discuss how these *general* relaxation equations have recently been extended by *Cywinski & Pickup* to neutron spin echo measurements on several spin glass materials ^{51, 52}.

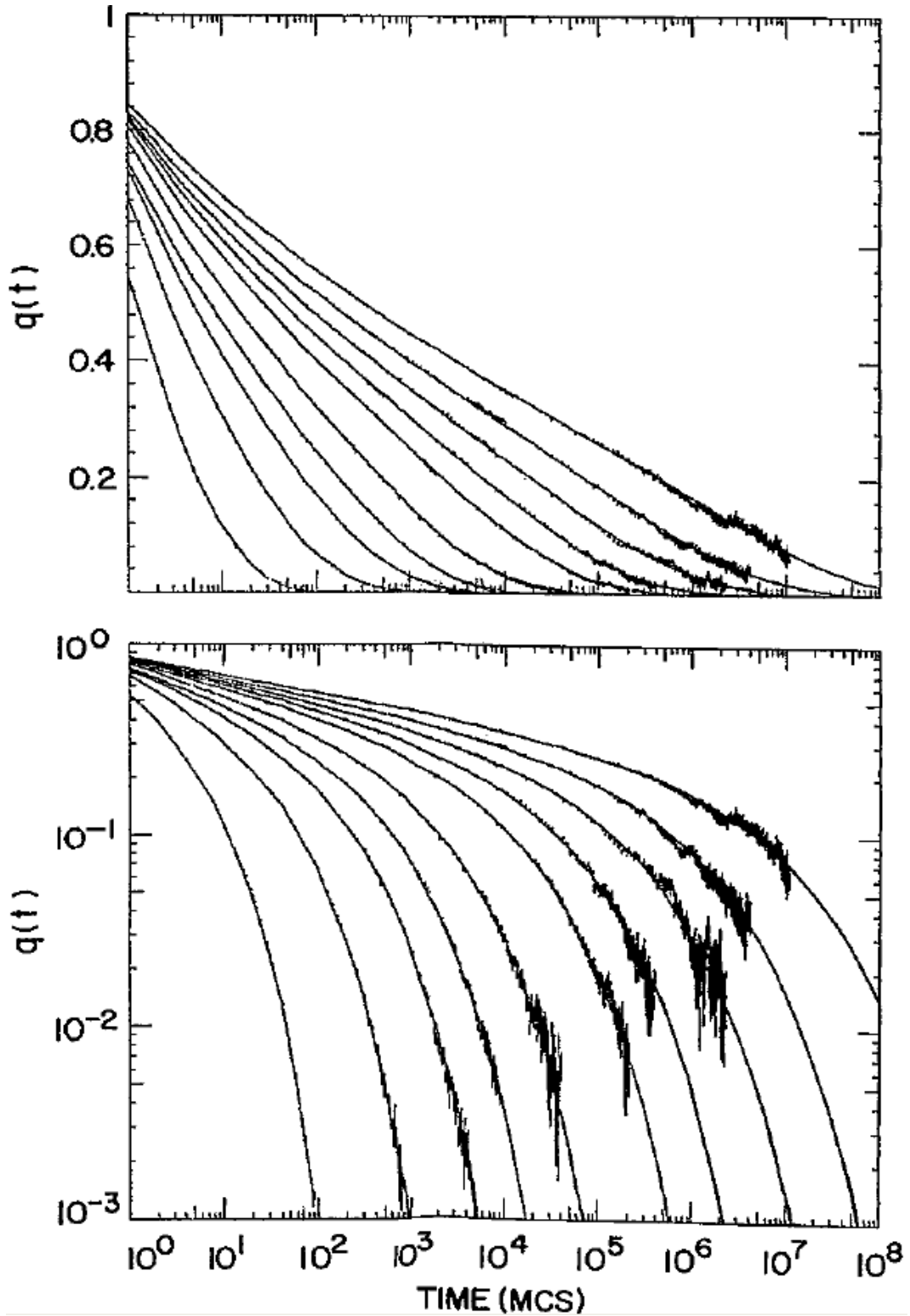


Figure 2:7 Simulated dynamic autocorrelation function above T_f taken from *Ogielski*⁴⁹. From right to left, the temperatures are $T = 2.50, 2.00, 1.80, 1.70, 1.60, 1.50, 1.45, 1.40, 1.35,$ and 1.30 . The solid lines represent least square fits to the data using Eq. (2:6).

2.2.2 A Probabilistic Mechanism

The challenge now for both theoretical and experimental physicists alike is to develop and apply a model which gives physical meaning and indeed an insight to the mechanisms responsible for these peculiar dynamics. In 1991 *Karina Weron et al.* proposed just such a model based on a probabilistic interpretation of dielectric relaxation which, like that of spin-glasses, departs strongly from conventional Debye behaviour⁵³. A schematic representation of the Weron model is offered in Figure 2:8.

Based on the correlated cluster model of *Dissado & Hill*⁵⁴, it is proposed that the relaxation of complex systems originates from co-operative positional or orientational relaxation over portions of spatially limited regions, i.e. clusters of atoms, molecules or aggregates, and that the scale of the relaxation of each individual entity is constrained such that small clusters relax first *via* intra-cluster dynamics. As discussed earlier, it has long been argued that such a framework is physically more realistic, albeit a radical departure from previous derivations. Hence, by depicting a material in terms of cluster-type geometry the model inherently fulfils the requirement of hierarchical constraints on the dynamics.

Although the main motivation of Weron's work was to understand the universal power-law behaviour of dielectric susceptibility the resulting relaxation function was constructed in such a way as to be applicable to any relaxing system where the relaxation of the entire system can be related to a characteristic relaxation rate, ($A = 1 / \tau$). This generality has made it possible to apply this stochastic model to wide range of phenomena, including spin glass relaxation^{51, 52}.

This rigorous probabilistic approach introduces two independent, non-negative random variables: a random waiting time (η_i) and a dispersion rate (β_i). This waiting time is associated with the relaxation rate of each individual entity, whilst the dispersion rate is an adjustment time for the local environment to move back to equilibrium.

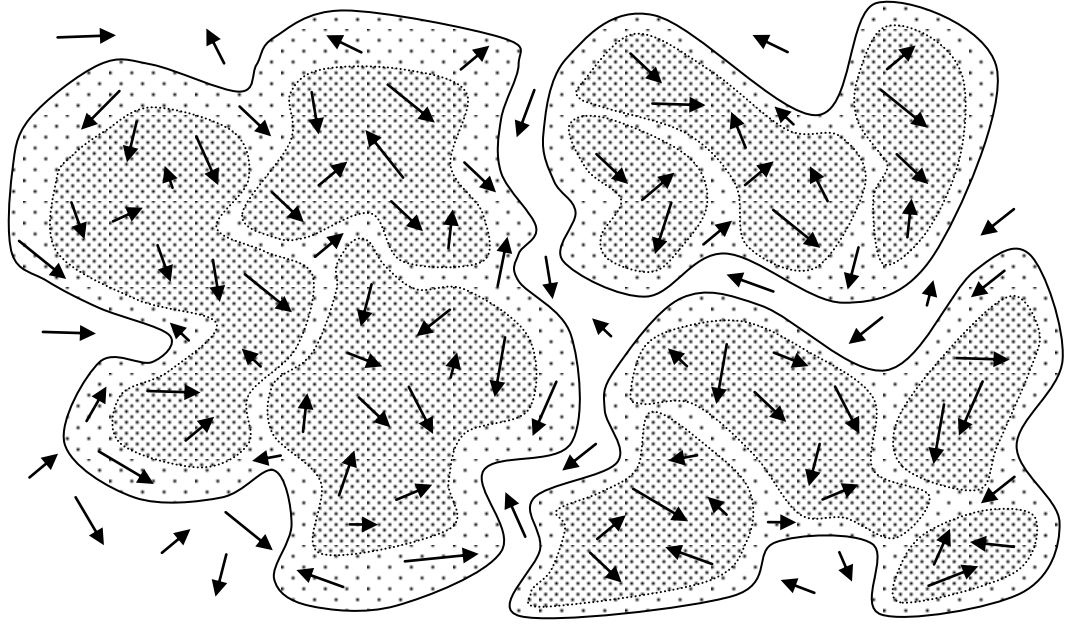


Figure 2:8 2D representation of the cluster geometry used by the Weron Model, possessing both intra- and inter-cluster interactions.

Essentially, their sum describes the time needed to reach equilibrium, and through this Weron derives,

$$\phi(t) = \left[1 + k \cdot \left(\frac{t}{\tau} \right)^\alpha \right]^{-\frac{1}{k}} \quad (2:7)$$

where $(0 < \alpha \leq 1)$ is a measure of the level of self-similarity within the system, and $(k > 0)$ is an effective interaction parameter connected with the waiting time associated with both inter and intra-cluster relaxation processes. Hence the latter expresses the strength of interactions and accordingly the degree of hierarchical constraint on the overall dynamics. Moreover, in the limit $(k \rightarrow 0)$, equation (2:7) reduces to the stretched exponential form, in which case $(\alpha \rightarrow 1)$ reproduces Debye relaxation,

$$\lim_{k \rightarrow 0} \phi(t) \rightarrow \exp \left[-\left(\frac{t}{\tau} \right)^\beta \right] \quad (2:8)$$

This highlights the significance of the interaction parameter (k) in determining the nature of the relaxation process. Furthermore, the relationship between the stretched exponential and Weron model in this limit indicates that the stretching parameter (β) is equivalent to the self-similarity or fractal parameter (α) between the metastable phases within an ergodic valley.

Self-similarity and fractal geometry have received a great deal of attention over recent decades, and the link between this and the complex non-exponential relaxation exhibited in systems of broken ergodicity is attracting more and more interest. Recent research suggests that Boltzmann-Gibbs statistical mechanics can no longer be used to describe the thermodynamic properties of such systems. This departure has led many to consider a model constructed by *Constantino Tsallis*, who has defined a generalised form of entropy commonly referred to as non-extensive. The following section will introduce the salient ideas of his work.

2.2.3 Non-Extensive Entropy

An ever growing catalogue of evidence has, in recent years, led many scientists to apply the ideas of non-extensive statistical mechanics to: computer science⁵⁵⁻⁵⁸; Earth, life and social sciences, geography and climate models⁵⁹⁻⁶⁷; economic and financial patterns⁶⁸⁻⁷¹; and many more complex natural and artificial phenomena. The idea stems from the belief that Boltzmann-Gibbs (BG) statistics, despite apparently being *eternal* (valid always), and *ubiquitous* (valid everywhere) is by no means *universal* (valid for all phenomena)⁷²⁻⁷⁴, and although the precise definition of the domain in which BG-statistic remains valid is as yet an unsolved problem, the current consensus is that it may only be applied when the relevant phase space is smooth⁷⁵. Already from Figure 2:5 we know that this is not the case in broken- or non-ergodic glassy systems which have a multi-fractal nature.

Crucially the definition of standard thermodynamic entropy is not in question, having first been introduced nearly one and a half centuries ago by *Clausius* and later interpreted in the seminal works of *Boltzmann* and *Gibbs* from statistical mechanics. A suitable definition of entropy in non-ergodic systems is however a highly

contentious issue. Nonetheless it should be mentioned how truly remarkable it is that Boltzmann-Gibbs statistical mechanics can bridge a link between microscopic laws and the macroscopic world of classical thermodynamics. Hence *Tsallis* took this construct as his starting point, with entropy being related to the probability, (p_i) , of the total number of possibilities (W) ,

$$S_{BG} = -k_B \sum_{i=1}^W p_i \ln p_i \quad (2:9)$$

In this form entropy is an extensive property, such that for two independent systems, (A) and (B) ,

$$\frac{S_{BG}(A+B)}{k_B} = \frac{S_{BG}(A)}{k_B} + \frac{S_{BG}(B)}{k_B} \quad (2:10)$$

He then constructed a generalisation which considers the possible lack of additivity between these systems by introducing an extensivity parameter (q^*) ,

$$\frac{S_{q^*}(A+B)}{k_B} = \frac{S_{q^*}(A)}{k_B} + \frac{S_{q^*}(B)}{k_B} + (1-q^*) \frac{S_{q^*}(A)S_{q^*}(B)}{k_B k_B} \quad (2:11)$$

Clearly when $(q^* \rightarrow 1)$ this formalisation recovers the usual Boltzmann-Gibbs entropy whereas the other limits, $(q^* > 1)$ and $(q^* < 1)$, both sub-extensive and super-extensive states exist respectively. Hence, equation (2:9) is written in generalised non-extensive form,

$$S_{q^*}(p_i) = k_B \frac{1 - \sum_{i=1}^W p_i^{q^*}}{q^* - 1} \quad (2:12)$$

where (W) is still the number of microscopic possibilities of the system, and (k_B) is still the Boltzmann constant.

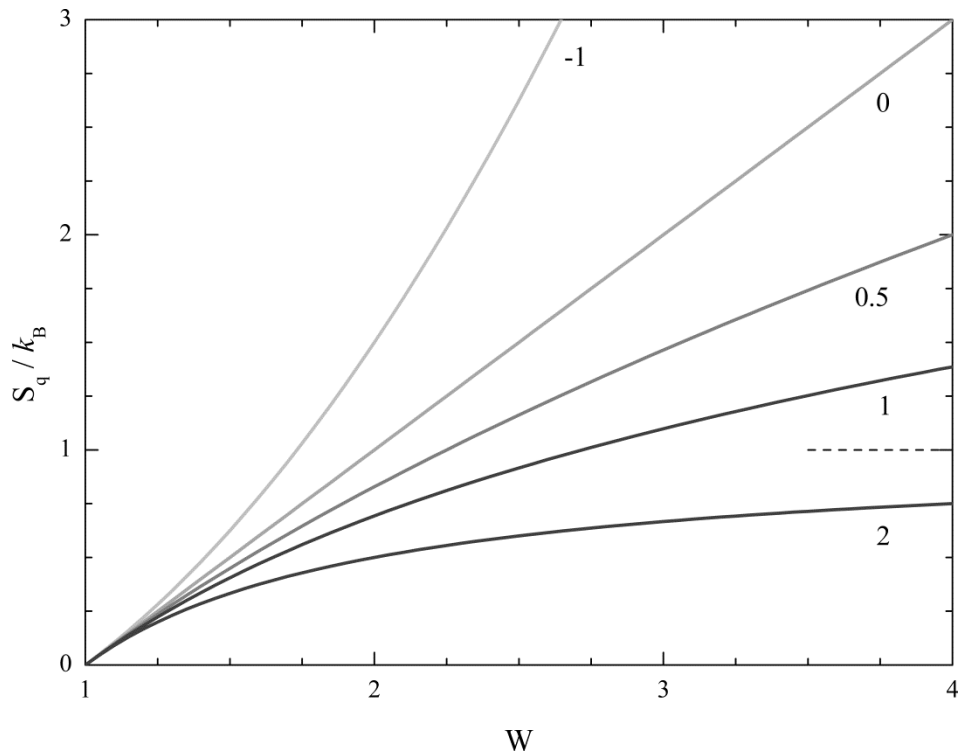


Figure 2:9 Values of the entropy for typical values of q^* extensivity parameter (shown with curve). It can be seen that S_q / k diverges if $q^* \leq 1$, and saturates at $S_q = k_B / (q^* - 1)$ when $q^* > 1$, in the limit $W \rightarrow \infty$.

To grasp this particularly difficult concept it is useful to consider a practical example of non-extensivity. A tornado is perhaps most intuitive. It seems legitimate to assume that the individual air molecules are independent of one another, and they interact only with other molecules in the immediate vicinity (i.e. short ranged interactions); this is the normal extensive statistical mechanics view. However, it is clear that the formation of a tornado is an event that requires the highly correlated motion of trillions of entities over macroscopic distances, ultimately leading to an ordered vortex despite its microscopically disorder nature. With this in mind it becomes easier to appreciate that the entropy of the system as a whole may be less than the entropy of its parts. In such a case the Tsallis extensivity parameter would be ($q^* > 1$), saturating towards $[S_q = k_B / (q^* - 1)]$ in the limit of ($W \rightarrow \infty$), as shown in Figure 2:9.

Using this principle *Brouers & Sotolongo-Costa* derive a two-power-law relaxation function^{73, 76}, identical in form to that of Weron's purely stochastic theory. As such it gives a greater physical meaning to the mathematical parameters, (α) and (k) . In the first instance this phenomenological model begins in the normal way, by taking a weighted average of Debye decay using a distribution of relaxation times, $\omega_\tau(\tau)$,

$$\phi(t) = \int_0^\infty \omega_\tau(\tau) \exp[-(t/\tau)] d\tau \quad (2:13)$$

The relaxation is again assumed to be the collective response of clusters, and as such dependent on their interactions and geometric structure. Smaller clusters relax first, whilst long-range inter-cluster interactions take place on longer time scales. The overall process is seen from a macroscopic perspective and derived in terms of two global parameters, one defining the time and space fractal nature of the relaxation, (α) , and the other, (q) , characterising the hierarchical structure of the cluster geometry through a the maximisation of non-extensive entropy.

The cluster size distribution therefore needs to be related to the relaxation rate distribution in order for it to scale in an appropriate way with the number of relaxing entities within a cluster. To do this the relaxation time is equated to the normalised volume of a cluster (v) via the following expression,

$$\tau = v^{1/\alpha} \quad (2:14)$$

where $(0 \leq \alpha \leq 1)$. Then by maximising the generalised entropy of Tsallis^{77, 78},

$$S_{q^\star}(x) = k_B \frac{1 - \int_0^\infty p^{q^\star}(x) dx}{q^\star - 1} \quad (2:15)$$

the probability, $p(x)$ of the system being in a state between (x) and $(x + dx)$ is obtained. From this the cluster size distribution function can be found,

$$p(v) = \left[1 - \frac{1-q}{2-q} v \right]^{1/1-q} \quad (2:16)$$

where ($1 \leq q < 2$) is the normalised version of (q^*) as derived by *Tsallis et al.* in ^{79, 80}. Together these equations make it possible to write a relaxation function in terms of the distribution of relaxation rates,

$$\phi_{\alpha,q}(t) = \int_0^\infty p_A(\alpha, q) \exp[-(tA)] dA \quad (2:17)$$

where [$A = 1 / \tau$] and,

$$p_\beta(\alpha, q) = \alpha \left(\frac{1}{A} \right)^{(1+\alpha)} \left[1 - \frac{1-q}{2-q} \left(\frac{1}{A} \right)^\alpha \right]^{\frac{1}{1-q}} \quad (2:18)$$

which leads to the relaxation function,

$$\phi(t) = \left[1 + \left(\frac{q-1}{2-q} \right) \cdot \left(\frac{t}{\tau} \right)^\alpha \right]^{-\frac{2-q}{q-1}} \quad (2:19)$$

Through comparison with Weron's function, equation (2:7), it is clear to see that the interaction parameter is equivalent to,

$$k = \left(\frac{q-1}{2-q} \right) \quad (2:20)$$

and therefore must give a direct link to the non-extensivity of the system.

This model has been simulated in Figure 2:10 for typical experimental time-scales to indicate its behaviour as a function of both (q) and (α).

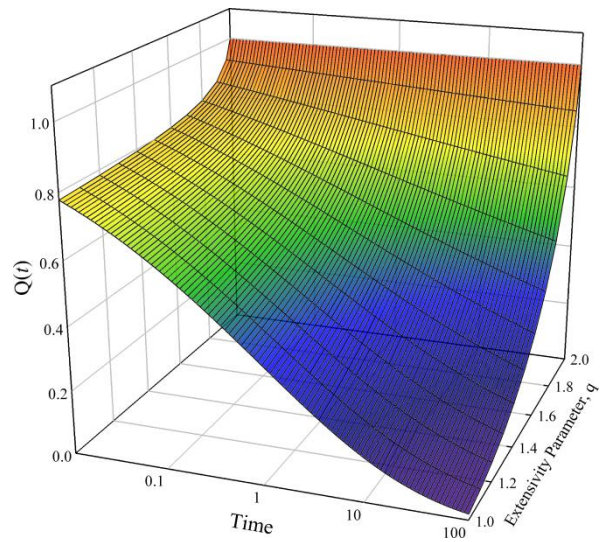
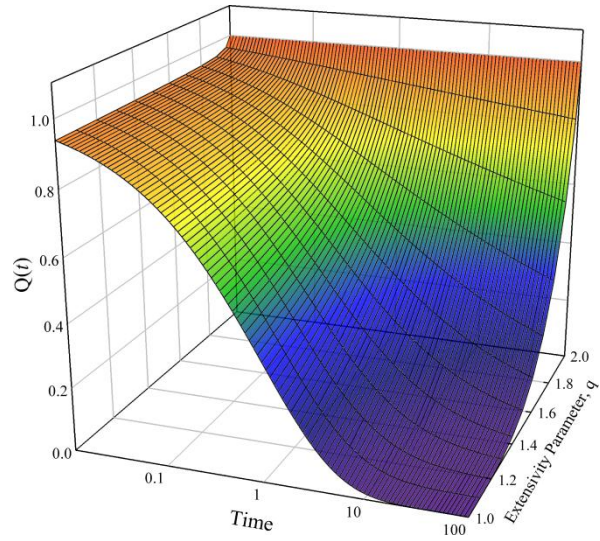
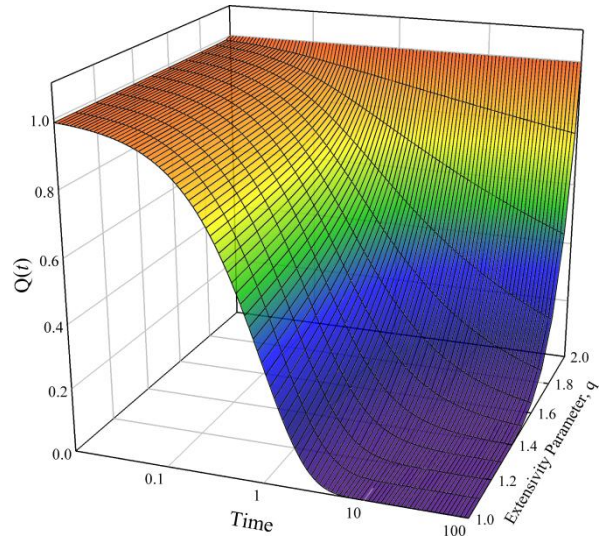


Figure 2:10 Simulated results for the Tsallis relaxation function. Each plot reveals the variation of $Q(t)$ with extensivity parameter for $\alpha = 1.0, 0.6$ and 0.33 ; top, middle and bottom respectively. .

Recently the Weron-Tsallis relaxation function has been applied to Neutron Spin Echo measurements performed on a range of spin-glass, as well Random Anisotropy systems^{51, 52, 81}. It has been found to provide a more accurate and self-consistent description of the evolution of the relaxation dynamics as the transition temperature is approached from above.

A range of canonical systems, such as CuMn and AuFe, have been shown to follow a general pattern, Figure 2:11. At high temperatures the non-extensivity parameter is close to one, which essentially indicates the dynamics are dominated by the parallel relaxation of clusters. Upon a reduction in temperature the non-extensivity parameter is then seen to decrease continually and consistently took a value of ($q = 5 / 3$) at the transition temperature. This value has been shown to mark a transition called the *strong-disorder limit*, where the dynamics are predominantly governed by the power law tails of the cluster size distribution function given in equation (2:16).

Investigations on several Random Anisotropy Magnets have reached quite different conclusions. The non-extensivity parameter is found to be independent of temperature and take a value of approximately 1.5, Figure 2:12. This suggests that in this case the dynamics are not cooperative in nature, and that the behaviour of these systems is dominated by the local random anisotropy axis which causes the random distribution of moments.

2.2.4 Summary

A historical review of the spin glass problem has been presented highlighting many of the important concepts and stages in reaching our current understanding. A general two-power law relaxation function is derived of the form,

$$\phi(t) = \left[1 + \xi \cdot \left(\frac{t}{\tau} \right)^\alpha \right]^{-\frac{1}{\xi}} \quad (2:21)$$

where (α) is associated with the fractal geometry of the system which *Brouers & Sotolongo-Costa* have related to the normalised cluster volume distribution.

Furthermore their model, based on Tsallis entropy, gives a physical interpretation of the mathematical parameters of Weron's purely stochastic theory founded on the survival probability of the initial state in any relaxing non-equilibrium system. Both however can be seen as a derivative of stretched exponential or Kohlrausch decay law in the limit ($\xi \rightarrow 0$), in which case (α) equates to the stretching parameter, ($\alpha \leq 1$), and is said to be a measure of the non-idealness of the relaxing process, i.e. variations in interaction and intra-cluster size ⁷⁶.

Function parameter	Limits
Weron interaction parameter	$k > 0$
Tsallis non-extensivity parameter	$1 \leq q^* < 2$
Normalised Non-extensivity	$1 \leq q < 2$

Given that the functional form of each theory is identical, despite their respective origins being unrelated, it may be assumed the parameter (ζ) is fundamentally equivalent. In essence this parameter provides a measure of the level of constraint on the relaxation dynamics of the system, which for glassy systems is the direct consequence of broken-ergodicity.

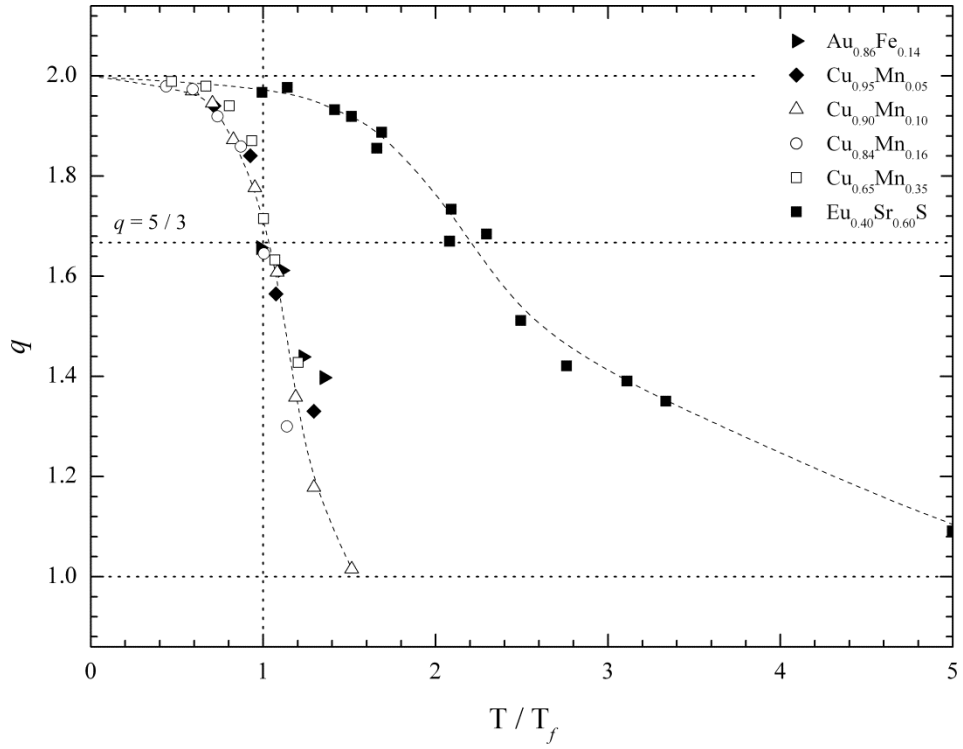


Figure 2:11 The Tsallis non-extensivity parameter obtained by NSE measurements a range of spin glass systems; Recreated from the thesis of *Pickup*⁸¹.

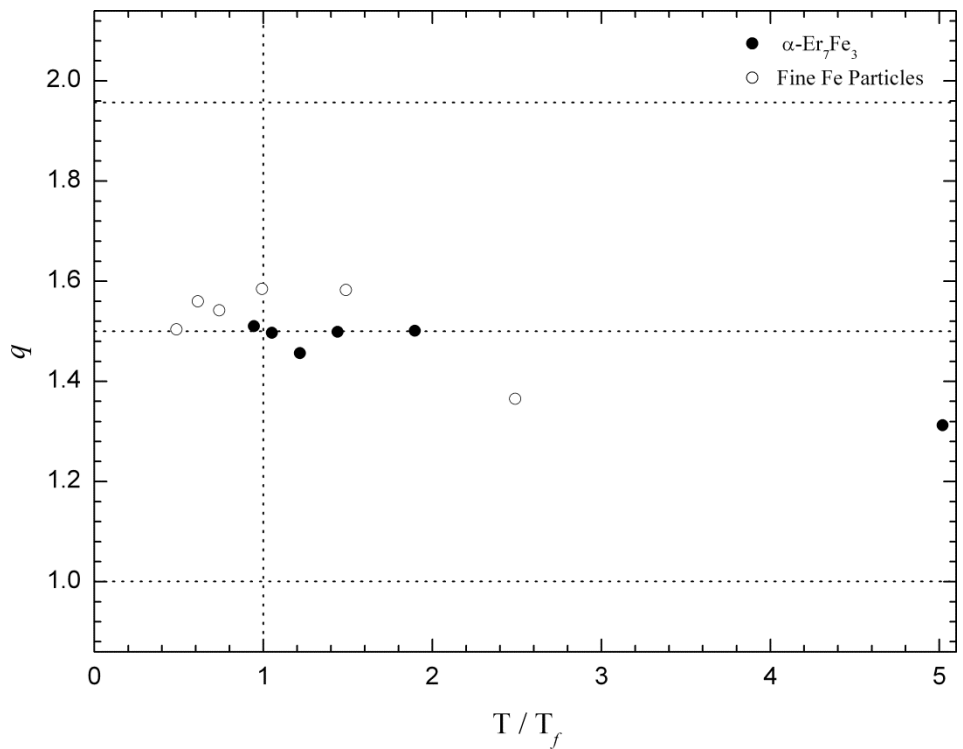


Figure 2:12 The Tsallis non-extensivity parameter for Random Anisotropy Magnets (RAM). Recreated from the thesis of *Pickup*⁸¹.

Chapter 3

EXPERIMENTAL TECHNIQUES & INSTRUMENTS

This final preliminary chapter is presented as a review of the techniques and instruments which have been employed during this project.

3.1 Introduction to Neutron scattering

In order to observe detail on an atomic scale we must use radiation with a wavelength comparable to the interatomic separation of atoms ($\sim 10^{-10}$ m). Visible light is several orders of magnitude too large, and so alternative forms must be sought. Fortunately, electrons, atoms, and x -rays are all suitable candidates; however it is the neutron's unique set of physical properties that make it the outstanding choice for many condensed matter studies:

Energy: using the de Broglie - Einstein postulates we are able to calculate the energy associated with a given neutron wavelength.

$$\lambda = \frac{h}{mv}, \quad k = \frac{2\pi}{\lambda} \quad (3:1)$$

$$\therefore E = \frac{1}{2}mv^2 = \frac{\hbar^2 k^2}{2m} \quad (3:2)$$

Thus we find appropriate wavelengths correspond to the energies of many naturally occurring excitations ($2 \text{ \AA} \approx 25 \text{ meV}$). Ultimately, this makes two distinct *modes* of neutron scattering experiment possible, one in which the positions of atoms are obtained (*diffraction*), and a second to study their dynamics are revealed (*spectroscopy*).

Zero electronic charge: unlike many atomic probes neutrons are able to penetrate deeply into most types of matter. In the first instance this is because a neutron interacts *via* the strong nuclear force ($\sim 10^{-15} \text{ m}$). If we consider that the separation between nuclei (in solids) is in the order of 40,000 times their typical diameter ($\sim 5 \text{ fm}$) it quickly becomes clear that, at least from the neutrons perspective, matter is relatively transparent.

Neutron-nuclei interaction: the strength with which neutrons are scattered or absorbed varies in a non-systematic manner with isotope, as shown in Figure 3:1 and Figure 3:2 respectively. Not only does this allow neighbouring atoms in the periodic table, or indeed isotopes of the same atomic species, to be easily distinguished between, but neutrons often scatter equally strongly from light atoms, unlike *x-ray* scattering.

Magnetic moment: a neutron has a spin of $\frac{1}{2}$ and therefore possesses an intrinsic magnetic moment ($\gamma = -1.913 \mu_N$) which, only four years after *Chadwick's*[§] discovery of the neutron, *Bloch*[§] recognised could be exploited for the study of magnetism⁸². Put simply, in addition to the short-range nuclear potential, magnetic atoms also exert a dipole interaction potential from which neutrons will scatter. Although theoreticians such as *Schwinger*[§]⁸³ and *Halpern & Johnson*⁸⁴⁻⁸⁶ quickly explored the prospects of using neutrons to probe magnetic phenomena, it took over a decade before such an experiment was feasible. *Shull*[§] and his colleagues had by 1951 developed these techniques, and were able for the first time provide experimental proof of anti-ferromagnetic order in MnO ⁸⁷.

[§] Nobel Prize laureate in Physics

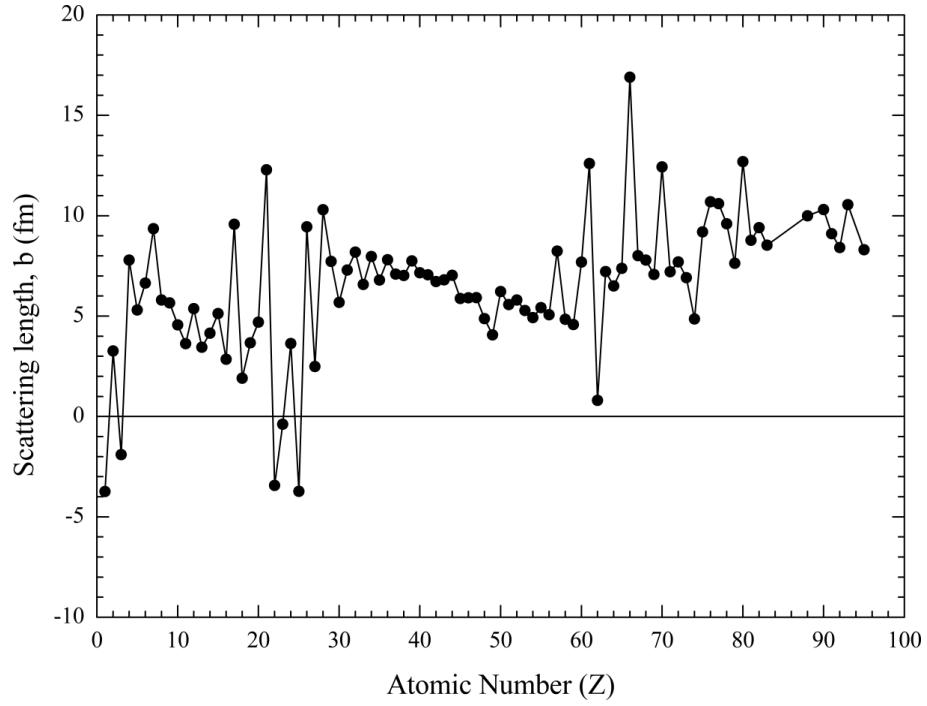


Figure 3:1 Non-systematic variation of the coherent scattering length with atomic number^{88, 89}

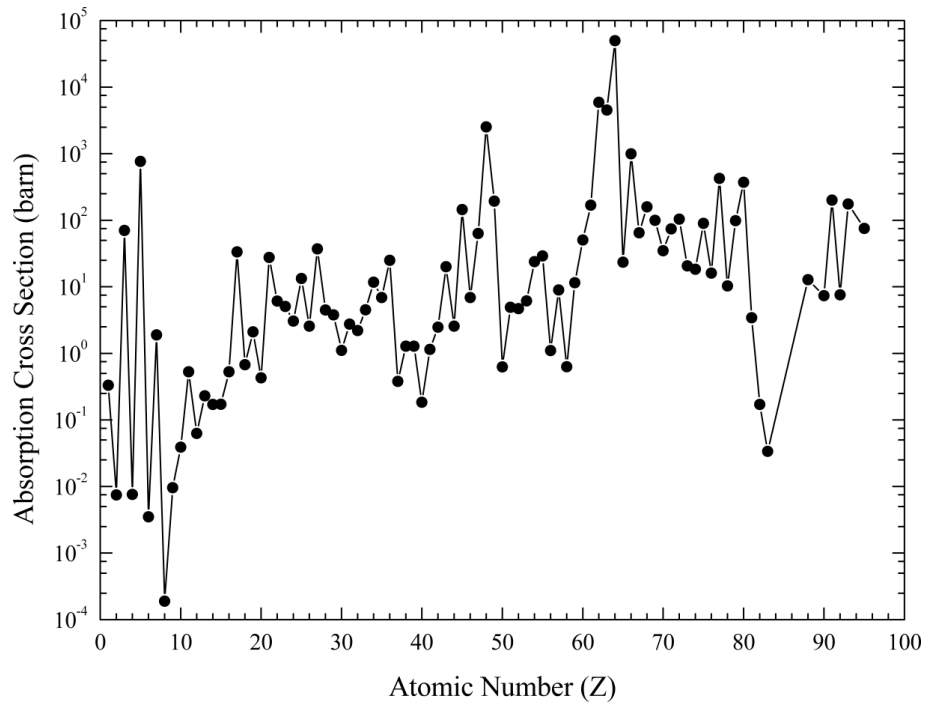
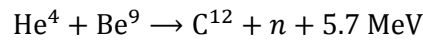


Figure 3:2 Non-systematic variation of the absorption cross section with atomic number in units of barns ($1 \times 10^{-24} \text{cm}^2$)^{88, 89}.

3.1.1 The Production of Neutrons for Science

Famously neutrons were first detected by *Chadwick* in 1932, when he used alpha particles released from Polonium-210 to produce neutrons from nearby Beryllium ⁹⁰:



Today several large scale central facilities operate worldwide dedicated to neutron scattering studies. In general there are three methods through which neutrons are produced: Spallation, Fusion, and Fission. Here the methods employed at ISIS and ILL are presented.

ISIS: Spallation of neutrons at the ISIS facility is driven by a pulsed beam of protons which originate from an ion source feeding negative hydrogen ions into a linear radio-frequency accelerator or LINAC. This accelerator contains four accelerating tanks inside which are a series of drift tubes.

These ions travel through the tanks accelerating between the drift tubes when the field is in the correct direction and being shielded by them when the field reverses. The subsequent 200 μs pulse of ions, at 70 MeV, is then stripped of its electrons by an aluminium oxide foil and injected into a 24 m radius synchrotron. The remaining protons are gathered into two orbiting bunches and are accelerated by voltages reaching 140 kV to energies of 800 MeV. The whole process is repeated 50 times per second producing a double pulsed beam with a mean current of 200 μA on the spallation target.

This target is comprised of thick tungsten plates housed in a water cooled pressure vessel from which 18 beam lines link to the instruments. Neutrons are produced when a proton impinges the target and is absorbed by a target nucleus, elevating it to a highly excited state. This causes the expulsion of high energy nucleons which on the whole are reabsorbed and the process repeated, emitting close to 40 slow neutrons per proton as well as photons and neutrinos. The neutrons' energy is subsequently controlled by moderators placed before the entrance of the beam line.



The ILL research site; credit: Peter Ginter, ESRF

ILL: Fission reactors such as the ILL are usually powered by Uranium-235, an isotope that is present in only 0.7 % of naturally occurring Uranium. By fission with thermal neutrons on average 2.5 fast neutrons and approximately 180 MeV of energy is produced,



The reaction is regulated by boron loaded control rods and becomes self-sustaining when on average $\frac{1}{2}$ a neutron is absorbed by material other than the core, one neutron triggers a further fission event, and one neutron leaves the core for use at an instrument. The energy spectrum of the neutrons produced in this way has three distinct regions, the first being a peak around 1-2 MeV which is referred to as the lamb distribution, these are the fast or high energy neutrons. The next is an intermediate or epithermal region where the energy gradually decreases characterised by a $1/E$ distribution in intensity. Finally the thermal peak which is characterized by a Maxwell-Boltzmann distribution of energies centred on approximately 25 meV. Again the neutron's energy is controlled by moderators prior to entering the beam lines.

3.1.2 Kinematics Approximation

First consider a monochromatic beam of neutrons characterised by an initial wavevector, (\mathbf{k}_i) incident on a solid sample as depicted in Figure 3:3. Since for the reasons already mentioned most samples are largely transparent to neutrons it is unsurprising that a large percentage of the beam's initial intensity is transmitted without being affected. The remaining beam fraction undergoes absorption or scattering.

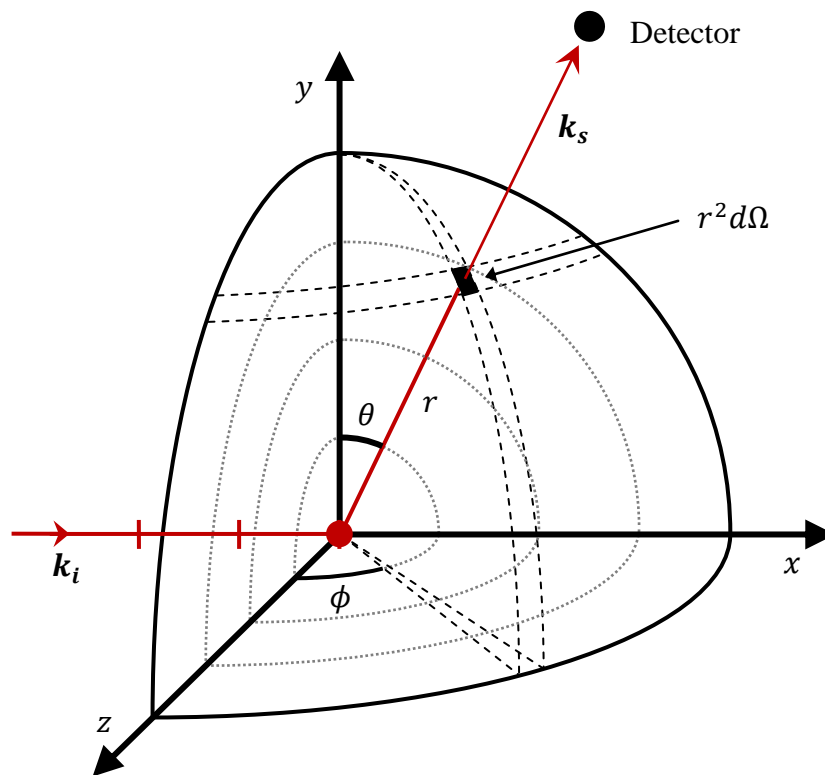


Figure 3:3 The scattering geometry in a generic neutron experiment; the incident beam, travelling in the x-direction, interacts with a scattering system located at the origin. A detector counts the number of neutrons scattered into the solid angle $d\Omega$.

Absorbed neutrons form highly excited compound states with the parent nucleus, which under normal circumstances decay extremely rapidly ($\sim 10^{-14}$ s) expelling nucleons (n, p, α) or, more likely emitting gamma radiation.

Scattered neutrons on the other hand are characterised by a second wavevector (\mathbf{k}_s) and can be counted in a detector a large distance from the sample. The number of

counts per second (C) is proportional to the initial beam intensity (ϕ_o), number of scattering centres at the target (N), and the solid angle subtended by the detector to the scattering system ($d\Omega$).

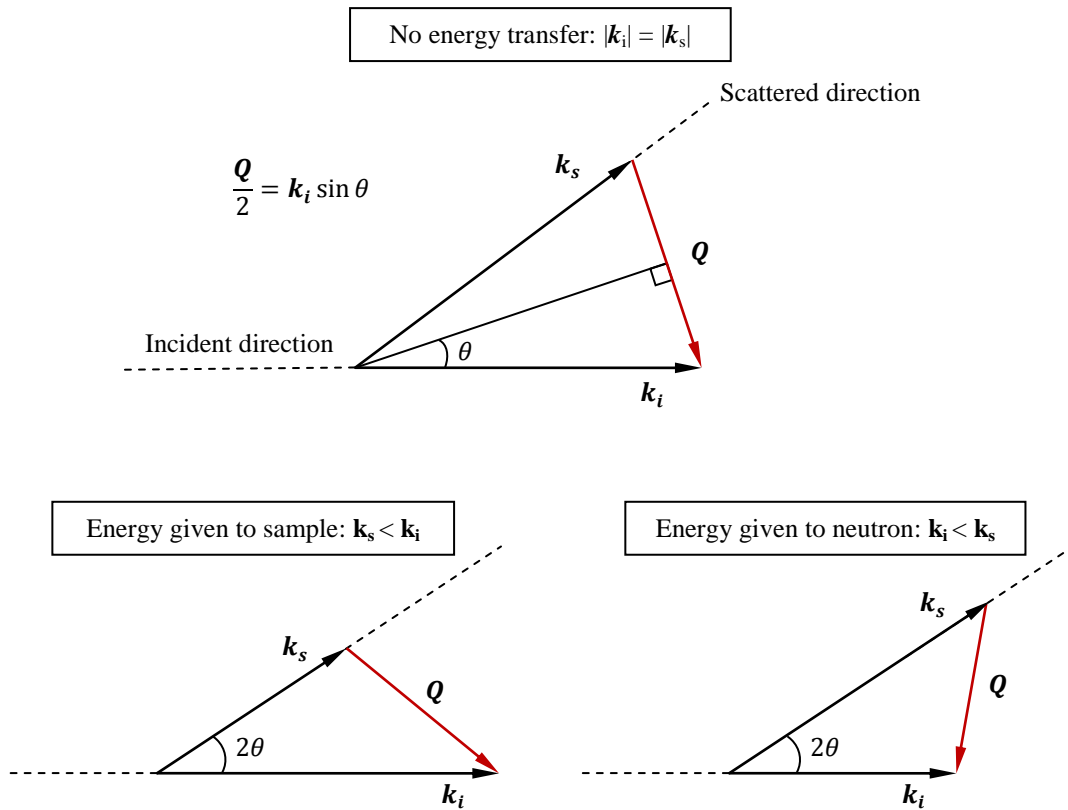


Figure 3:4 Scattering triangles for elastic and inelastic scattering events.

Consequently, a sample specific constant of proportionality known as the differential cross section can be derived,

$$\frac{d\sigma}{d\Omega} = \frac{C}{\phi_o N d\Omega} \tag{3:3}$$

essentially quantifying the number of neutrons scattered into the solid angle ($d\Omega$), independent of any energy being transferred from or to the neutron. Therefore this definition is not applicable to inelastic scattering. The so-called double differential

cross section addresses this by counting neutrons within a given interval of energy exchange (dE),

$$\frac{d^2\sigma}{d\Omega dE} = \frac{C}{\phi N d\Omega dE} \quad (3:4)$$

To quantify the momentum ($m\Delta v$) and energy (ΔE) transferred, equation (3:1) can be rearranged, with (\mathbf{k}_i) and (\mathbf{k}_s) substituted into equation (3:2) to yield

$$m\Delta v = \hbar(\mathbf{k}_i - \mathbf{k}_s) = \hbar\mathbf{Q} \quad (3:5)$$

$$\Delta E = \frac{\hbar^2}{2m}(\mathbf{k}_i^2 - \mathbf{k}_s^2) \quad (3:6)$$

where the scattering vector is defined as,

$$\mathbf{Q} = \mathbf{k}_i - \mathbf{k}_s \quad (3:7)$$

Note that the total number of neutrons scattered by the system every second is defined as the total scattering cross section, and is related to equations (3:1) and (3:4) through integration.

$$\frac{d\sigma}{d\Omega} = \int_0^\infty \left(\frac{d^2\sigma}{d\Omega dE} \right) dE \quad (3:8)$$

$$\sigma_{total} = \int_{4\pi} \left(\frac{d\sigma}{d\Omega} \right) d\Omega \quad (3:9)$$

Returning to Figure 3:3, the scattered beam is isotropic (*s-wave scattering*), expanding in spherical wavefronts or radius (r). This is because neutrons interact with the nucleus at an incredibly short range making the target appear point-like, and also that the neutron wavelength is such that the internal structure of the nucleus is unseen. Accordingly, scattering from a single nucleus may be represented as a plane wave at large distance,

$$\Psi_s = -\frac{b}{r} \exp(ik_s r) \quad (3:10)$$

where (b/r) is the scattering amplitude, characterised by the scattering length constant (b) . Importantly, during the scattering process the target nucleus, with spin (\mathcal{S}) , and neutron combine to form a compound system having spin $[\mathcal{S} + \frac{1}{2}]$ or $[\mathcal{S} - \frac{1}{2}]$. Each of these spin states have a different scattering length denoted by (b_+) and (b_-) respectively, and it is this *spin-dependence* that results in two different *types* of scattering effect when scattering from many nuclei ⁸⁴. The first is coherent scattering, which is due to interference between neutron waves which have a phase corresponding to the interatomic distances between the nuclei. This contribution can be shown to be proportional to the square of the average scattering length,

$$\sigma_{coh} = 4\pi \langle b \rangle^2 \quad (3:11)$$

The second type is incoherent scattering, and is the direct result of there being a distribution of scattering lengths within the sample. This might be due to the spin state of the neutron-nucleus system, or simply the presence of more than one isotope within the sample. Both cause incoherently scattered waves which, since their relative phases are uncorrelated, simply add together and give rise to a flat background signal. This contribution is proportional to the average square deviation of the scattering length constant,

$$\sigma_{incoh} = 4\pi [\langle b^2 \rangle - \langle b \rangle^2] \quad (3:12)$$

Thus, the total scattering cross section is the sum of both terms,

$$\sigma_{total} = \sigma_{coh} + \sigma_{incoh} \quad (3:13)$$

However, this is not strictly the quantity measured during neutron scattering experiments. It is generally the intensity of the scattered beam as a function of

scattering vector (\mathbf{Q}) and energy (ω) which is measured, leading to a function $S(\mathbf{Q}, \omega)$, referred to as the scattering function.

3.1.3 Scattering & Pair Correlation Functions

The scattered neutron measures both the angular dependence and frequency spectrum simultaneously, and so the function $S(\mathbf{Q}, \omega)$ contains all the scattering properties of the system under investigation. What's more, *Van Hove* defined a general expression for the angular and energy dependence of Born approximation** scattering in terms of a pair-correlation function, $G(\mathbf{r}, t)$ which he showed to be the Fourier transform of $S(\mathbf{Q}, \omega)$ ⁹¹. Classically this function can be interpreted as the probability of finding a particle at position (\mathbf{r}) at time (t), and a particle (possibly the same particle) at the space and time origin, ($\mathbf{0}_r, 0_t$).

$$G(\mathbf{r}, t) = \frac{1}{(2\pi)^3} \int d\mathbf{Q} \exp(-i\mathbf{Q} \cdot \mathbf{r}) \int_{-\infty}^{\infty} d\omega \exp(i\omega t) S(\mathbf{Q}, \omega) \quad (3:14)$$

This pair-correlation function can be shown to be equivalent to a density-density correlation function, such that,

$$G(\mathbf{r}, t) = \langle \rho(\mathbf{0}_r, 0_t) \rho(\mathbf{r}, t) \rangle \quad (3:15)$$

where (ρ) is the density operator of all the nuclei, each nucleus given by a δ -function,

$$\rho(\mathbf{r}, t) = \sum_{j=1}^{10^{23}} \delta[\mathbf{r} - \mathbf{R}_j(t)] \quad (3:16)$$

Given equation (3:15), we are able to describe the two *modes* of neutron scattering experiment not only in terms of the scattering law and pair-correlation functions, but also the more intuitive density-density correlation function. Diffraction is the angular dependence of elastic scattering, and is written as the energy-integrated

** Valid when the scattering is weak, the scattered wave is represented by a plane wave.

intensity of $S(\mathbf{Q}, \omega)$, which is the Fourier transform of the density-density correlation function,

$$S(\mathbf{Q}) = \int S(\mathbf{Q}, \omega) d\omega = \langle \int \rho(\mathbf{r} - \mathbf{0}_r) \rho(\mathbf{0}_r) d\mathbf{r} \rangle \quad (3:17)$$

Spectroscopy on the other hand measures the change in velocity of the scattered neutron, leading to the frequency spectrum $S(\omega)$, which is equivalent to the time-dependence of the density function,

$$S(\omega) = \langle \rho(t - 0_t) \rangle \quad (3:18)$$

More rigorous derivation may be found in the following texts ⁹²⁻⁹⁴.

3.1.4 Nuclear Scattering

To make quantum mechanical predictions for the double differential cross section ^{92, 93} the interaction potentials from an assembly of nuclei at positions (\mathbf{R}_j), with scattering lengths (b_j), are substituted by a Fermi pseudo-potential of the form,

$$V(\mathbf{r}) = \frac{2\pi\hbar^2}{m_n} \sum_j b_j \delta(\mathbf{r} - \mathbf{R}_j) \quad (3:19)$$

where (m_n) is the neutron mass and $\delta(\mathbf{r})$ is a Dirac delta function, taking the value of unity at ($\mathbf{r} = \mathbf{R}_j$) and zero everywhere else. Upon scattering both the wavevector and spin state of the neutron change ($\mathbf{k}_i \sigma_i \rightarrow \mathbf{k}_s \sigma_s$). So too does the quantum state of the nuclei from which it scatters ($\lambda_i \rightarrow \lambda_s$). Clearly the detector count rate (C) may be replaced by the rate at which this transition occur (W), and so the differential cross section given by equation (3:4) may be rewritten as,

$$\left(\frac{d\sigma}{d\Omega} \right)_{\mathbf{k}_i \sigma_i \lambda_i \rightarrow \mathbf{k}_s \sigma_s \lambda_s} = \frac{1}{\phi_0 N d \Omega} W_{\mathbf{k}_i \sigma_i \lambda_i \rightarrow \mathbf{k}_s \sigma_s \lambda_s} \quad (3:20)$$

Using Fermi's Golden Rule the transition rate can be expressed as,

$$W_{\mathbf{k}_i\sigma_i\lambda_i\rightarrow\mathbf{k}_s\sigma_s\lambda_s} = \frac{2\pi}{\hbar} |\langle \mathbf{k}_i\sigma_i\lambda_i | V | \mathbf{k}_s\sigma_s\lambda_s \rangle|^2 \rho_{\mathbf{k}_s\sigma_s}(E_i) \quad (3:21)$$

where the probability density of the transition occurring is given by the modulus squared of the matrix element, and $\rho_{\mathbf{k}_s\sigma_s}(E_i)$ is the density of final neutron state ($\mathbf{k}_s\sigma_s$) per unit energy. Setting periodic boundary conditions the incident flux and density of final states can be normalised^{88, 95} to express the differential cross section as,

$$\left(\frac{d\sigma}{d\Omega}\right)_{\mathbf{k}_i\sigma_i\lambda_i\rightarrow\mathbf{k}_s\sigma_s\lambda_s} = \left(\frac{1}{N}\right) \frac{\mathbf{k}_s}{\mathbf{k}_i} \left(\frac{m_n}{2\pi\hbar^2}\right)^2 |\langle \mathbf{k}_i\sigma_i\lambda_i | V | \mathbf{k}_s\sigma_s\lambda_s \rangle|^2 \quad (3:22)$$

By conserving the energy transferred between the neutron and nuclei,

$$E = E_{\mathbf{k}_i} - E_{\mathbf{k}_s} = E_{\lambda_s} - E_{\lambda_i} \quad (3:23)$$

and summing over all final nuclei and neutron-spin states, weighted to the probability of the initial and final states occurring, (ρ_i) and (ρ_s) respectively, we obtain the double differential cross section, or so-called Master equation of neutron scattering,

$$\left(\frac{d^2\sigma}{d\Omega dE}\right) = \left(\frac{1}{N}\right) \frac{\mathbf{k}_s}{\mathbf{k}_i} \left(\frac{m_n}{2\pi\hbar^2}\right)^2 \times \sum_{\lambda_s\sigma_s} \rho_i \rho_s |\langle \mathbf{k}_i\sigma_i\lambda_i | V | \mathbf{k}_s\sigma_s\lambda_s \rangle|^2 \delta(E_i - E_s + E) \quad (3:24)$$

3.1.5 Magnetic Scattering

The magnetic analogue of equation (3:24) is far more complicated to derive, but nonetheless has a very similar form,

$$\begin{aligned} \left(\frac{d^2\sigma}{d\Omega dE}\right) &= \left(\frac{1}{N_m}\right) \frac{\mathbf{k}_s}{\mathbf{k}_i} (\gamma r_0)^2 \\ &\times \sum_{\alpha} \sum_{\lambda_i} \rho_{\lambda_i} \sum_{\lambda_s} \rho_s \langle \lambda_i | \mathbf{D}_{\perp\alpha}^{\dagger} | \lambda_s \rangle \langle \lambda_s | \mathbf{D}_{\perp\alpha} | \lambda_i \rangle \delta(E_i - E_s + E) \end{aligned} \quad (3:25)$$

where (N_m) is the number of magnetic ions in the sample, (r_0) is the classical electron radius which determines the strength of the interaction, (γ) is the

gyromagnetic ratio of the neutron, and (\mathbf{D}) is magnetic interaction operator. For a detailed derivation please consult *Methods of Experimental Physics – Neutron Scattering: Part A* ⁹⁴.

As with the nuclear case however the magnetic double differential cross section is defined by evaluating the matrix element $\langle \mathbf{k}_s | V | \mathbf{k}_i \rangle$, where the interaction potential between a neutron's magnetic dipole moment (\mathbf{B}_n) and the magnetisation density (\mathbf{M}_e) of unpaired electrons is expressed as a dipole interaction potential of the form,

$$V = \frac{1}{4\pi\epsilon_0} \mathbf{M}_e(r) \cdot \mathbf{B}_n(r) \quad (3:26)$$

Furthermore, the magnetisation density at position (\mathbf{R}) for a single electron with momentum (\mathbf{p}), may be expressed as two terms,

$$\mathbf{M}_e = \frac{\mu_0}{4\pi} \left[\left(\text{curl} \frac{\boldsymbol{\mu}_e \times \mathbf{R}}{|\mathbf{R}|^3} \right) - \frac{2\mu_B}{\hbar} \frac{\mathbf{p} \times \mathbf{R}}{|\mathbf{R}|^3} \right] \quad (3:27)$$

the first accounting for the spin angular, and the second orbital angular momentum respectively. (μ_0) is the permeability of free space and (μ_e) is the electron's magnetic moment.

The salient features of magnetic neutron scattering are that the neutron is acted upon by the perpendicular component of the sample magnetisation to the scattering vector (\mathbf{Q}), and secondly, since the volume occupied by a local atomic field is comparable in linear extent to the neutron's wavelength the magnetic scattering amplitude is anisotropic.

Due to the latter, magnetic scattering is \mathbf{Q} -dependent and must therefore include a term referred to as the magnetic form factor $f(\mathbf{Q})$, accounting for this angular dependency. For this purpose, analytical expressions for approximating the atomic form factor in K_α x-ray crystallography ⁹⁶ were adopted by neutron scattering community, which were originally based on a two-term Gaussian expansion, but are currently based on a three term expansion for increase accuracy. In contrast to x-ray scattering however, the magnetic form factor is governed by the unpaired electrons

only, and is expressed as the sum of two independent contributions: one associated with the spin $\langle j_0 \rangle$, and the other orbital $\langle j_2 \rangle$ angular momentum of the magnetic atom. Weighting of these contributions is enabled *via* the Landé-splitting factor (g), such that $f(Q)$ is given by the formula,

$$f(Q) = \langle j_0(Q) \rangle + \left(1 - \frac{2}{g}\right) \langle j_2(Q) \rangle \quad (3:28)$$

which has been calculated for several manganese ions in Figure 3:5

Where the spin contribution follows a form derived by *Forsyth & Wells* in 1959⁹⁷,

$$\langle J_0(s) \rangle = A \exp(-as^2) + B \exp(-bs^2) + C \exp(-cs^2) + D \quad (3:29)$$

and the orbital contribution follows the expansion,

$$\langle J_2(s) \rangle = s^2 [A \exp(-as^2) + B \exp(-bs^2) + C \exp(-cs^2) + D] \quad (3:30)$$

derived by *Lisher & Forsyth* in 1971⁹⁸. In both cases,

$$s = \frac{\sin \theta}{\lambda} = \frac{Q}{4\pi} \quad (3:31)$$

and the coefficients (A, B, C, D, a, b, c) are obtained by least-square fitting to Hartree-Fock calculations of the magnetisation density, (M_e)⁸⁹.

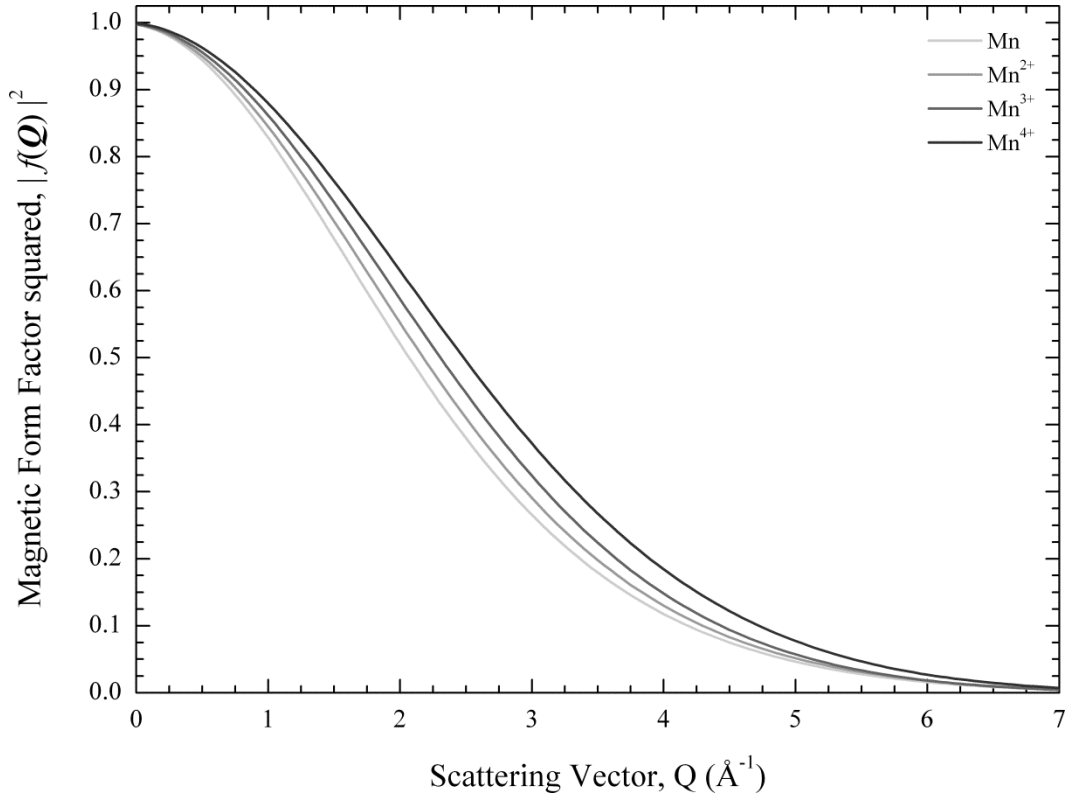


Figure 3:5 The magnetic form factor squared, $f(Q)^2$ of a free manganese atom, as well as several of its ions calculated using equation (3:28). It is clear the magnetic form factor falls sharply with scattering vector, and can vary significantly between ionisation states.

$\langle j_0 \rangle$	A	a	B	b	C	c	D
Mn	0.2438	24.9629	0.1472	15.6728	0.6189	6.5403	-0.0105
Mn ⁺²	0.4220	17.6840	0.5948	6.0050	0.0043	-0.6090	-0.0219
Mn ⁺³	0.4198	14.2829	0.6054	5.4689	0.9241	-0.0088	-0.9498
Mn ⁺⁴	0.3760	12.5661	0.6602	5.1329	-0.0372	0.5630	0.0011
$\langle j_2 \rangle$							
Mn	2.6681	16.060	1.7561	5.640	0.3675	2.049	0.0017
Mn ⁺²	2.0515	15.556	1.8841	6.063	0.4787	2.232	0.0027
Mn ⁺³	1.2427	14.997	1.9567	6.118	0.5732	2.258	0.0031
Mn ⁺⁴	0.7879	13.886	1.8717	5.743	0.5981	2.182	0.0034

Table 3:1 The spin and orbital coefficients calculated by Brown⁸⁹ used to produce Figure 3:5.

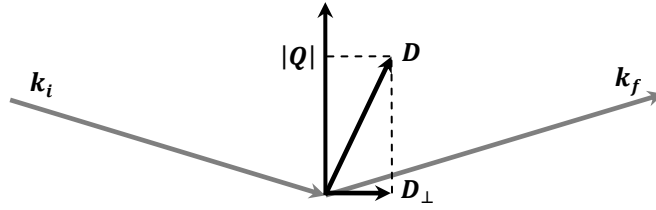


Figure 3:6 Schematic illustration of the relationship between the scattering vector, \mathbf{Q} and the magnetic interaction operator, \mathbf{D} .

3.1.6 Polarisation Analysis

Apart from analysing the wavevector and momentum of a scattered neutron, additional information can be gained through changes in its spin state. This is because, as discussed in the previous sections, neutron scattering is a spin dependent process, and consequently techniques have been developed to exploit this since the early 1960s. This section presents a short overview of xyz -polarisation analysis; a measuring technique which makes it possible to unambiguously separate nuclear, spin-incoherent and magnetic scattering cross-sections.

The polarisation of an ensemble of neutrons is defined as the sum over all polarisation vectors of individual neutrons (j), within the beam.

$$\mathbf{P} = \frac{1}{N} \sum_j^N \mathbf{P}_j \quad (3:32)$$

Subsequently, when ($\mathbf{P} = 1$) the beam is perfectly polarised, and when ($\mathbf{P} = 0$) the beam is totally depolarised. Current technologies permit values of 0.98 and above are routinely achieved.

At this point it is useful to note that coherent nuclear and isotope-incoherent scattering do not change the neutron's spin-state and so are referred to as non-spin flip processes. Nor will it change if the magnetic and nuclear spin components are

parallel to the incident beam polarisation direction. However, when the relative spin components are perpendicular to one another the neutron's spin state will flip.

The “xyz” technique requires the scattering cross sections of spin flip and non-spin flip processes to be measured in all three polarisation directions, leading to six individual components:

Spin flip processes:

$$\begin{aligned}
\left(\frac{\delta\sigma}{\delta\Omega}\right)_{SF}^z &= \frac{2}{3}\left(\frac{\delta\sigma}{\delta\Omega}\right)_{SI} + \frac{1}{2}\left(\frac{\delta\sigma}{\delta\Omega}\right)_{MAG} \\
\left(\frac{\delta\sigma}{\delta\Omega}\right)_{SF}^y &= \frac{2}{3}\left(\frac{\delta\sigma}{\delta\Omega}\right)_{SI} + (1 + \sin^2 \alpha) \frac{1}{2}\left(\frac{\delta\sigma}{\delta\Omega}\right)_{MAG} \\
\left(\frac{\delta\sigma}{\delta\Omega}\right)_{SF}^x &= \frac{2}{3}\left(\frac{\delta\sigma}{\delta\Omega}\right)_{SI} + (1 + \cos^2 \alpha) \frac{1}{2}\left(\frac{\delta\sigma}{\delta\Omega}\right)_{MAG}
\end{aligned} \tag{3:33}$$

Non-Spin flip processes:

$$\begin{aligned}
\left(\frac{\delta\sigma}{\delta\Omega}\right)_{NSF}^z &= \frac{1}{3}\left(\frac{\delta\sigma}{\delta\Omega}\right)_{SI} + \frac{1}{2}\left(\frac{\delta\sigma}{\delta\Omega}\right)_{MAG} + \left(\frac{\delta\sigma}{\delta\Omega}\right)_{NUC} + \left(\frac{\delta\sigma}{\delta\Omega}\right)_{II} \\
\left(\frac{\delta\sigma}{\delta\Omega}\right)_{NSF}^y &= \frac{1}{3}\left(\frac{\delta\sigma}{\delta\Omega}\right)_{SI} + (\cos^2 \alpha) \frac{1}{2}\left(\frac{\delta\sigma}{\delta\Omega}\right)_{MAG} + \left(\frac{\delta\sigma}{\delta\Omega}\right)_{NUC} + \left(\frac{\delta\sigma}{\delta\Omega}\right)_{II} \\
\left(\frac{\delta\sigma}{\delta\Omega}\right)_{NSF}^x &= \frac{1}{3}\left(\frac{\delta\sigma}{\delta\Omega}\right)_{SI} + (\sin^2 \alpha) \frac{1}{2}\left(\frac{\delta\sigma}{\delta\Omega}\right)_{MAG} + \left(\frac{\delta\sigma}{\delta\Omega}\right)_{NUC} + \left(\frac{\delta\sigma}{\delta\Omega}\right)_{II}
\end{aligned} \tag{3:34}$$

By combining these partial differential cross sections it is possible to isolate each of the different forms of scattering, with the only exception being that of isotope-incoherent scattering which cannot be separated from the nuclear coherent scattering cross section.

$$\begin{aligned}
\left(\frac{\delta\sigma}{\delta\Omega}\right)_{MAG} &= 2 \left[\left(\frac{\delta\sigma}{\delta\Omega}\right)_{SF}^x + \left(\frac{\delta\sigma}{\delta\Omega}\right)_{SF}^y - 2 \left(\frac{\delta\sigma}{\delta\Omega}\right)_{SF}^z \right] \\
\left(\frac{\delta\sigma}{\delta\Omega}\right)_{MAG} &= 2 \left[2 \left(\frac{\delta\sigma}{\delta\Omega}\right)_{NSF}^z - \left(\frac{\delta\sigma}{\delta\Omega}\right)_{NSF}^x - \left(\frac{\delta\sigma}{\delta\Omega}\right)_{NSF}^y \right]
\end{aligned} \tag{3:35}$$

The nuclear and spin-incoherent cross section is defined in terms of the total spin-flip (*TSF*) and total non-spin-flip (*TNSF*) partial differential cross sections,

$$\begin{aligned}\left(\frac{\delta\sigma}{\delta\Omega}\right)_{TSF} &= \left(\frac{\delta\sigma}{\delta\Omega}\right)_{SF}^x + \left(\frac{\delta\sigma}{\delta\Omega}\right)_{SF}^y + \left(\frac{\delta\sigma}{\delta\Omega}\right)_{SF}^z \\ \left(\frac{\delta\sigma}{\delta\Omega}\right)_{TNSF} &= \left(\frac{\delta\sigma}{\delta\Omega}\right)_{NSF}^x + \left(\frac{\delta\sigma}{\delta\Omega}\right)_{NSF}^y + \left(\frac{\delta\sigma}{\delta\Omega}\right)_{NSF}^z\end{aligned}\tag{3:36}$$

and so the nuclear and spin-incoherent cross sections are expressed as,

$$\begin{aligned}\left(\frac{\delta\sigma}{\delta\Omega}\right)_{NUC} + \left(\frac{\delta\sigma}{\delta\Omega}\right)_{II} &= \frac{1}{6} \left[2 \left(\frac{\delta\sigma}{\delta\Omega}\right)_{TNSF} - \left(\frac{\delta\sigma}{\delta\Omega}\right)_{TSF} \right] \\ \left(\frac{\delta\sigma}{\delta\Omega}\right)_{SI} &= \frac{1}{2} \left(\frac{\delta\sigma}{\delta\Omega}\right)_{TSF} - \left(\frac{\delta\sigma}{\delta\Omega}\right)_{MAG}\end{aligned}\tag{3:37}$$

There are of course limitations since these equations apply strictly to paramagnetic or disordered static magnets. Non-collinear systems such as helical magnets cannot usually be studied using *xyz*-polarisation analysis.

3.1.7 Polarisation Techniques

The earliest polarised neutron experiments were performed in 1938, only six years after the discovery of the neutron⁹⁹. From these initial experiments stemmed, almost simultaneously, two different methods of producing a beam of polarised neutrons. One based on Bragg scattering¹⁰⁰⁻¹⁰³ the other on total reflection from magnetic surfaces¹⁰⁴⁻¹⁰⁶. Only reflection techniques are implemented on the instruments used during this project, however an excellent and comprehensive review of current polarisation techniques is available in the following reference¹⁰⁷.

As will become clear in the following section, one of the primary purposes of neutron spin echo spectroscopy is to decrease the long counting times generally associated with polarised neutron scattering experiments. Subsequently, these instruments nearly always employ a polarising device known as a supermirror. An example of the efficiency of a supermirror device is given Figure 3:7.

First proposed by *Turchin* in 1967¹⁰⁸, and later rediscovered and successfully

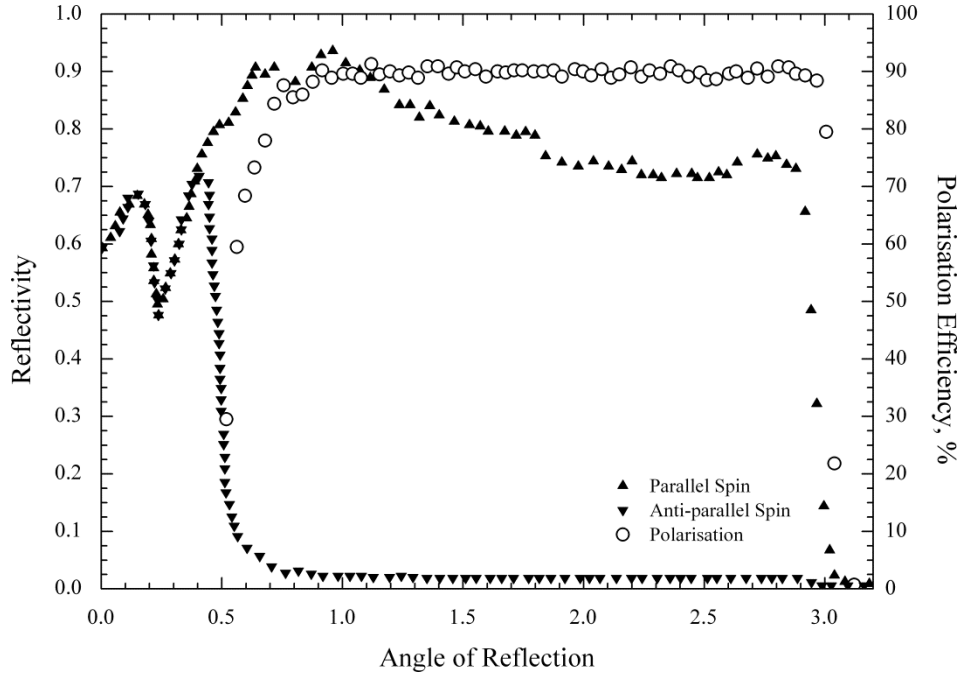


Figure 3:7 Polarised neutron reflectivity measurements for both parallel and anti-parallel spin states of a 900 layer Fe-Si supermirror on a borofloat glass substrate, taken from *Courtois*¹⁰⁹. Angular separation of parallel and anti-parallel spin states is evident, with a critical angle ($\sim 3^\circ$) four times that of Nickel ($m = 4$).

fabricated by *Mezei & Dagleish*^{110, 111}, these are a multilayer (surface) device, which consists of alternating magnetic and non-magnetic layers, saturated by external field (\mathbf{B}), gradually decreasing in thickness (D) towards a substrate^{112, 113}.

This graduation in layer thickness artificially increases the critical angle of incidence or wavelength so that a wider range of neutron energies are polarised. The most crucial element is the choice of materials which make up the magnetic-non-magnetic bi-layers. As discussed, the scattering length density of the magnetic material has two values, dependent on the neutron spin-state, adding to the nuclear potential when parallel, and subtracting when anti-parallel. Therefore a non-magnetic material is chosen which matches the potential seen by the anti-parallel neutron in the magnetic material. While those with spin parallel to (\mathbf{B}) are reflected at the boundary between layers, anti-parallel neutrons pass straight through (not seeing the change in scattering potential between layers). These are eventually absorbed by anti-reflecting / gadolinium doped layers covering the glass substrate¹¹⁴⁻¹¹⁸.

3.2 Neutron Spin Echo Spectroscopy

Conventional polarised neutron experiments demand careful preparation of the neutron beam, and generally employ *parallel* guide fields in order to maintain the beam's polarisation direction (\mathbf{P}) throughout the instrument. As stated, the interaction between the neutron and the sample, and subsequently information on the sample, is gained by discerning the differences between the incident and scattered beams.

Accordingly the instrument resolution is a function of the quadrature sum of the uncertainties in (\mathbf{k}_i) and (\mathbf{k}_s) , and the resolution achievable in $S(\mathbf{Q}, \omega)$ is therefore severely restricted by the precision of their measurement. Unfortunately two problems arise: firstly if we choose to more tightly control the velocity and divergence of the beam, using monochromator and collimating devices, we unavoidably remove more neutrons from the beam and reduce the overall flux. Secondly, even for a theoretically *perfect* instrument, improving the resolution is at best proportional to the square of the number of neutrons counted.

In practical terms this means to improve the resolution by a factor of two we would need to count for four times as long and in view of this a difficult balance must be struck between controlling the physical parameters of the beam and the beam's flux; collecting sufficient quantities of data whilst still maintaining an acceptable resolution. Fortunately, in 1972 a radically different approach was proposed by *Ferenc Mezei* based on labelling each neutron with a unique *time*, allowing for the counting time to be completely decoupled from the resolution¹¹⁹.

Analogous to the NMR spin-echo technique from which its name was derived, neutron spin echo (NSE) uses *perpendicular* fields and static field-inhomogeneities at strategic positions along the neutron's flight-path to carefully control the neutron spin polarisation direction (\mathbf{P}). Ultimately, it provides the highest energy resolution currently attainable using neutrons, whilst at the same time allowing the monochromatization to be broadened substantially ($\Delta\lambda/\lambda = 10 - 20\%$), giving significant gains in flux and therefore reduced counting times. A review of the NSE concept and its implementation is presented at this point.

3.2.1 Principles of NSE: A Classical Description

The most accessible way to visualise the neutron spin echo concept is *via* a classical treatment. In this way a simple pictorial representation can be developed to emphasise the neutron's behaviour as it passes through the individual components of the instrument. A corresponding quantum mechanical treatment can be found in references ^{120, 121}. To aid in this description the initial focus will be on:

- The importance of a guide field, and its relative alignment to (\mathbf{P}),
- the effect of field-inhomogeneities on (\mathbf{P}),
- Mezei flipper coils.

This will provide a framework on which a generalised NSE spectrometer can be described, deriving the so-called NSE equations.

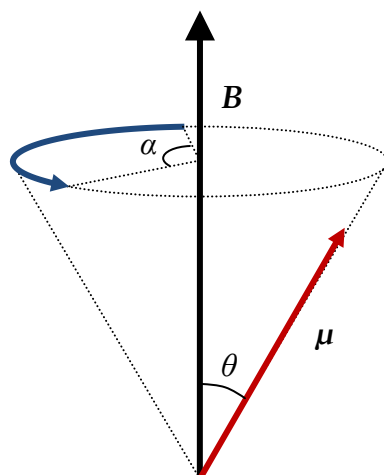


Figure 3:8 Larmor precession for a magnetic moment (μ) placed at an angle (θ) to a magnetic field (\mathbf{B}). The direction in which the moment rotates is shown by the blue arrow.

Guide fields are sometimes generated by permanent magnets but in the case of NSE usually result from current carrying coils. Conventional polarised neutron experiments are set up with the guide fields aligned *parallel* or *anti-parallel* to the beam's polarisation direction. They are required in order to maintain a constant polarisation direction since the neutron's sensitivity to its local magnetic environment is so great that without them (\mathbf{P}) would not only be influenced by the Earth's magnetic field but also inhomogeneities due to nearby magnetic materials.

NSE spectrometers differ, as (\mathbf{P}) has a *perpendicular* component to (\mathbf{B}) so that the neutron's moment $(\boldsymbol{\mu})$ experiences a torque resulting in precession about the field direction. This behaviour is known as Larmor precession, and was first observed in a neutron beam by *Drabkin et al.* in 1965 ¹²².

$$\frac{d\boldsymbol{\mu}}{dt} = -\gamma\boldsymbol{\mu} \times \mathbf{B} = \boldsymbol{\mu}\omega_l \quad (3:38)$$

$$\alpha = \omega_l t \quad (3:39)$$

The Larmor frequency (ω_l) and gyromagnetic ratio (γ) are related by $\omega_l = \gamma\mathbf{B}$, with the total precession angle in radians (α) given by equation (3:39). Since a neutron's angular momentum is constant its precessional frequency (ω_l) , and therefore total precession angle (α) , is independent of (θ) . As such each neutron in the beam will precess with the same frequency and each neutron's total precession angle will depend only on the time it spends in the field i.e. the length of that field (l) , and the exact velocity of the neutron (v) ,

$$\alpha = \gamma \frac{l\mathbf{B}}{v} \quad (3:40)$$

The guide field itself should be constant in magnitude and direction, however to progress further the effects of a change in field direction must be considered. In the first instance we need only consider the rate at which the change occurs by defining an angular frequency,

$$\omega = \frac{d(\mathbf{B}/|\mathbf{B}|)}{dt} \quad (3:41)$$

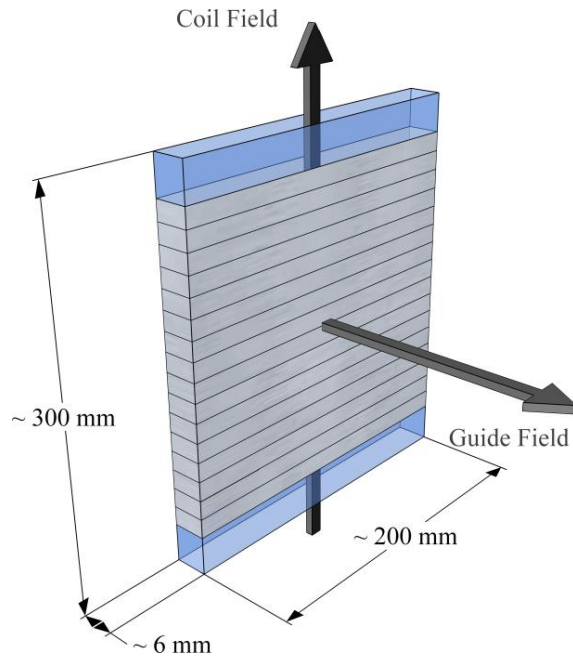


Figure 3:9 Mezei flipper coil.

The change can be considered *slow* if $|\omega| \ll |\omega_l|$, which is known as the adiabatic limit. In this case the neutron polarisation direction simply tracks the change in field direction. On the other hand if $|\omega| \gg |\omega_l|$ the polarisation of the neutron is unable to follow the field, so only their relative alignment changes. This is the so-called *sudden approximation*, which is vital to controlling (\mathbf{P}) on many instruments since it is the basis on which Mezei coils operate.

As shown in Figure 3:9, a Mezei coil is a simple rectangular coil of aluminium wire. The change from field direction outside to that inside occurs over a range approximately equal to that of the wire's thickness ($\varnothing \approx 1$ mm), thus fulfilling the condition for a *sudden* field transition. This in turn means that (\mathbf{P}) can be controlled in an *isolated* and predetermined precession mode inside the coil, making it possible to re-orientate the neutron's spin direction.

In the following discussion the guide field (\mathbf{B}) is parallel to the z -axis, with the field generated by the Mezei coil (\mathbf{B}_π) normal to (\mathbf{B}), in the y -direction. Inside the coil the resultant field direction is labelled (\mathbf{B}_r) in Figure 3:10.

A NSE spectrometer has a velocity distribution significantly wider than normal, thus the spin direction on exiting the Mezei coil will be distributed accordingly. Suppose ($\lambda = \lambda_0 \pm 15$) %, re-orientation through 180° would equate to an angular range of $(180 \pm 27)^\circ$, which corresponds to a reduction of the beam polarisation to ~ 90 %. Nonetheless this is still an acceptable value given the unique way in which the NSE technique performs a measurement.

Using this framework the NSE concept is now very easy to understand. Two identical homogeneous guide fields of length (l) are set up before and after the sample position i.e. [$l\mathbf{B} = l_i\mathbf{B}_i = l_s\mathbf{B}_s$]. A polarised beam of neutrons (in the z -direction) pass through a $\pi/2$ -Mezei flipper coil, orientating (\mathbf{P}) into the xy -plane, Figure 3:10, causing the neutrons to undergo Larmor precession as they traverse the first guide field. This can be seen as an encoding of each individual neutron with a unique *time*, given by the total precession angle which, as shown in equation (3:40), for a constant field of fixed length depends only on the exact velocity of the neutron. If we recall that the beam is only modestly monochromated, it is apparent that the beam polarisation is quickly lost simply due to the distribution of velocities. Crucially however, before entering the second guide field the beam encounters a Mezei π -flipper, rotating the neutrons 180° in the xy -plane, Figure 3:11, and so the second guide field, assuming perfectly elastic scattering with the sample, in effect recovers the initial polarisation,

$$\alpha = \alpha_i - \alpha_s = \gamma \left[\frac{l_i \mathbf{B}_i}{v_i} - \frac{l_s \mathbf{B}_s}{v_s} \right] \quad (3:42)$$

In the quasi-elastic limit, this can be rewritten to provide a direct measurement of the energy transfer ($\hbar\omega$)¹²³,

$$\alpha = \frac{\gamma \mathbf{B} l}{m v^3} \hbar\omega \quad (3:43)$$

Action of a Mezei $\pi/2$ -flipper on a polychromatic beam:

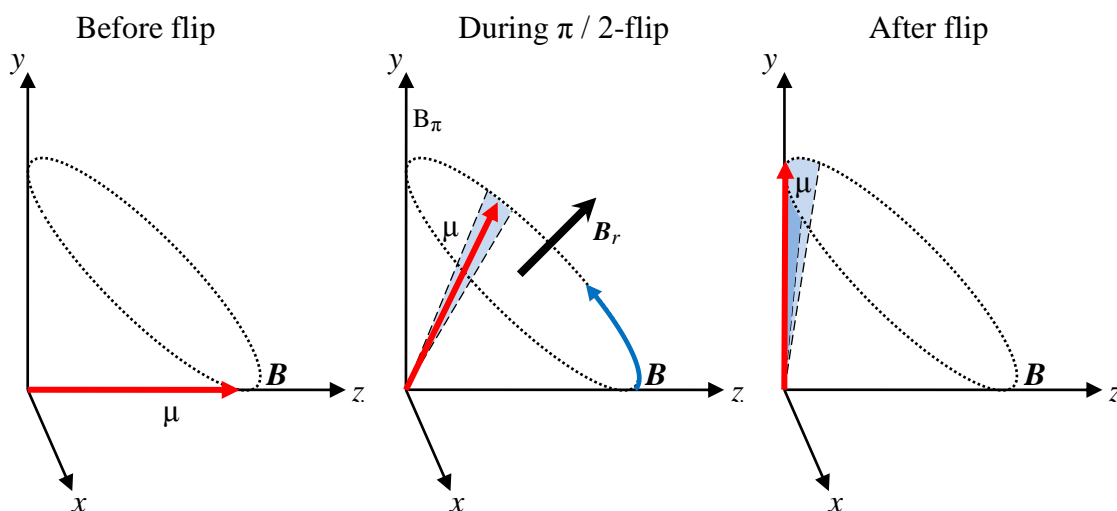


Figure 3:10 The polarisation direction of the neutron beam as it exits the first supermirror is parallel to the field direction of the precession coils (\mathbf{B}). Changing its orientation so that it is perpendicular to z is performed *via* the first of two $\pi/2$ -flipper coils. Its field (\mathbf{B}_π) and that of the precession coils (\mathbf{B}) generate a resultant field (\mathbf{B}_r) orientated at 45° in the y - z plane. The neutrons precess 180° about (\mathbf{B}_r), and so are perpendicular to (\mathbf{B}) as they exit. Note however, that since the beam is polychromatic a distribution of angles is observed (indicated by the blue region).

Action of a Mezei π -flipper in the xy -plane on a polychromatic beam:

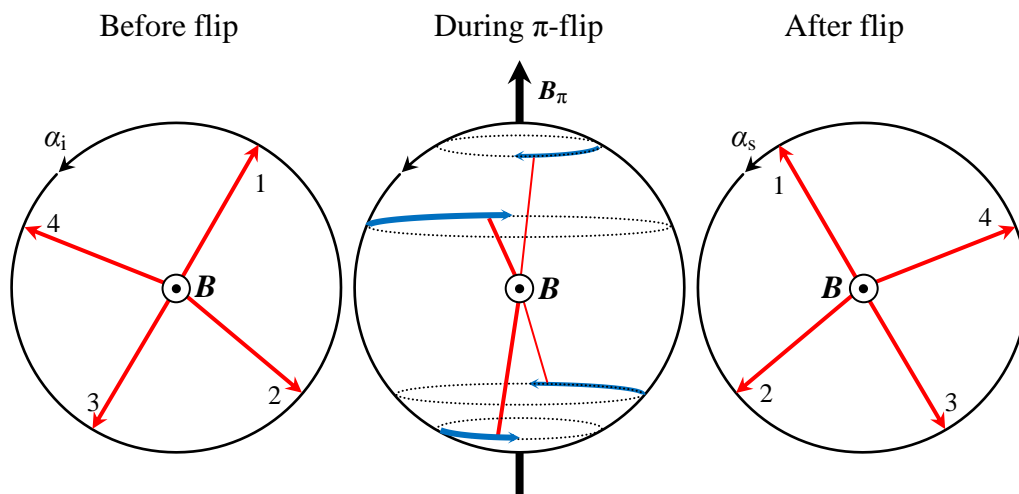


Figure 3:11 Unwinding α_i after scattering is not as simple as reversing the direction of (\mathbf{B}) in the second coil. This approach would generate a zero-field point at the sample position, quickly depolarising the beam. The neutron spin must be rotated 180° about the y -axis using a π -flipper close to the sample. In this way the field in the second precession coil does not need to be altered, and the neutrons precess in the same direction.

The operation of the analyser-detector assembly in a sense measures the distribution of total precession angles (α) in the scattered beam, and as will be shown the resulting signal follows a damped cosine form generally referred to as an *echo*.

$$P_z(\mathbf{Q}, \tau) = \langle \cos \alpha \rangle = \frac{\int \cos\left(\frac{\gamma l \mathbf{B}}{m v^3} \hbar \omega\right) S(\mathbf{Q}, \omega) d\omega}{\int S(\mathbf{Q}, \omega) d\omega} \quad (3:44)$$

This single and direct measurement of the energy transfer can be expressed as a normalised intermediate scattering function, where the numerator is the cosine Fourier transform of $S(\mathbf{Q}, \omega)$. This reveals the time-dependent nature of the correlation function⁹¹, where the constant of proportionality (τ) is referred to as Fourier or *spin echo time*, and is measured in units of seconds.

$$\tau = \frac{\hbar \gamma l \mathbf{B}}{m v^2} \quad (3:45)$$

This can be seen as a measure of the survival time for correlations between atomic spins in the sample. Different Fourier times can then be scanned by varying the field integral ($l\mathbf{B}$), which, using current technologies permits a dynamic range in the order of (0.3 ps – 300 ns). These spectra will therefore be modelled using the Weron-Tsallis relaxation function.

3.2.2 Effects of Sample Scattering

Strictly, the above derivation only remains valid in the case of non-spin flip scattering, that is to say, when the neutron's spin polarisation direction remains unaltered upon scattering from the sample. As stated previously this occurs thorough either nuclear coherent or isotope incoherent processes.

Thus to generalise equation (3:44) to be inclusive of all possible scattering an additional term must be included, (P_s) known as the polarisation factor,

$$P_{NSE}(\mathbf{Q}, \tau) = P_s \frac{S(\mathbf{Q}, \tau)}{S(\mathbf{Q})} \quad (3:46)$$

where, in this form, the scattering function has been integrated over all energies. Clearly ($P_s = 1$) will account for coherent nuclear scattering; however its value must be carefully evaluated for polarisation dependent processes such as nuclear spin incoherent and magnetic scattering.

If the nuclear spins are orientated randomly then spin incoherent scattering has a well defined scattering ratio of 2:1 between spin flip and non-spin flip, irrespective of the scattering geometry. Thus, in addition to the action of the π -flipper, two-thirds of the signal will undergo a second transformation in the xy -plane, reducing the amplitude of the echo signal to one-third. The total transformation between the precession coils therefore reads ($\alpha_i \rightarrow -\alpha_s \pm \pi$); corresponding to ($P_s = -\frac{1}{3}$).

With regard to paramagnetic scattering, if the polarisation is along the scattering vector then all the magnetic scattering is spin flip. However, if it were to be perpendicular to the scattering vector, as is the case with NSE, we know through the partial differentials given in equation (3:35) that the scattered beam is divided equally between spin flip and non-spin flip processes. Therefore the polarisation of the scattered beam, without application of a π -flipper, reads,

$$(P_x, P_y, 0) \rightarrow \frac{1}{2}(P_x, -P_y, 0) + \frac{1}{2}(-P_x, -P_y, 0) \quad (3:47)$$

where only the first term fulfils the echo condition ($\alpha_i \rightarrow -\alpha_s$) and the second term, akin to non-spin flip contributions has opposite phase ($\alpha_i \rightarrow -\alpha_s + \pi$), and therefore does not contribute to the echo signal. Thus, it is possible to measure the paramagnetic spin echo signal separately from nuclear coherent and isotope incoherent scattering so long as the π -flipper is not active and a polarisation factor of ($P_s = \frac{1}{2}$) is included.

The study of ferromagnetic samples by NSE is rather more complicated due to the total beam depolarisation caused by random orientation of multi-domain or powdered samples. To circumvent this an external field sufficient to saturate the sample must be applied in the z -direction. Then with $\pi/2$ -flipper coils place before and after the sample position the spin echo condition can be fulfilled *via*,

$$(P_x, P_y, P_z) \rightarrow (P_z, -P_y, P_x) \rightarrow (0, 0, P_x) \rightarrow (P_x, 0, 0) \quad (3:48)$$

Here, the initial polarisation in the x -direction is transferred to the z -direction, and vice versa, by the first flipper coil. The z and y components of polarisation are then essentially forgotten due to the sample field. The second $\pi/2$ -flipper coil rotates the x -component of polarisation back to the relevant x -direction, which can then be written as,

$$(P_x, 0, 0) = \frac{1}{2}(P_x, P_y, 0) + \frac{1}{2}(P_x, -P_y, 0) \quad (3:49)$$

Clearly, only the second term fulfils the echo condition and accordingly the amplitude is again reduced: ($P_s = 1/2$).

Anti-ferromagnetic NSE spectroscopy can be even more complicated, and formalisation of polarisation analysis is beyond the scope of this review. However, a macroscopically isotropic sample may be treated exactly the same as a paramagnetic sample, where the final polarisation reads,

$$(-P_x, AP_y, 0) = \frac{1+A}{2}(-P_x, P_y, 0) + \frac{1-A}{2}(-P_x, -P_y, 0) \quad (3:50)$$

where (A) is a parameter describing the anisotropy of the sample. A full derivation is given in reference ¹²³. A summary of these results is given in the table below, which lists the sample environments and the polarisation factors needed to account for reduction in the amplitude of the spin echo signal.

Type of Scattering	Flip Coil	Sample Field	Polarisation Factor P_s
Coherent Nuclear	π	<i>small</i>	1
Nuclear Spin Incoherent	π	<i>small</i>	1/3
Paramagnetic	<i>none</i>	<i>small</i>	1/2
Ferromagnetic	$\pi/2 \rightarrow \text{sample} \rightarrow \pi/2$	<i>high</i>	1/2
Anti-ferromagnetic	<i>none</i>	<i>small</i>	$1/2 \leq P_s \leq 1$

Table 3:2 The NSE configurations required for the study of different sample scattering types.

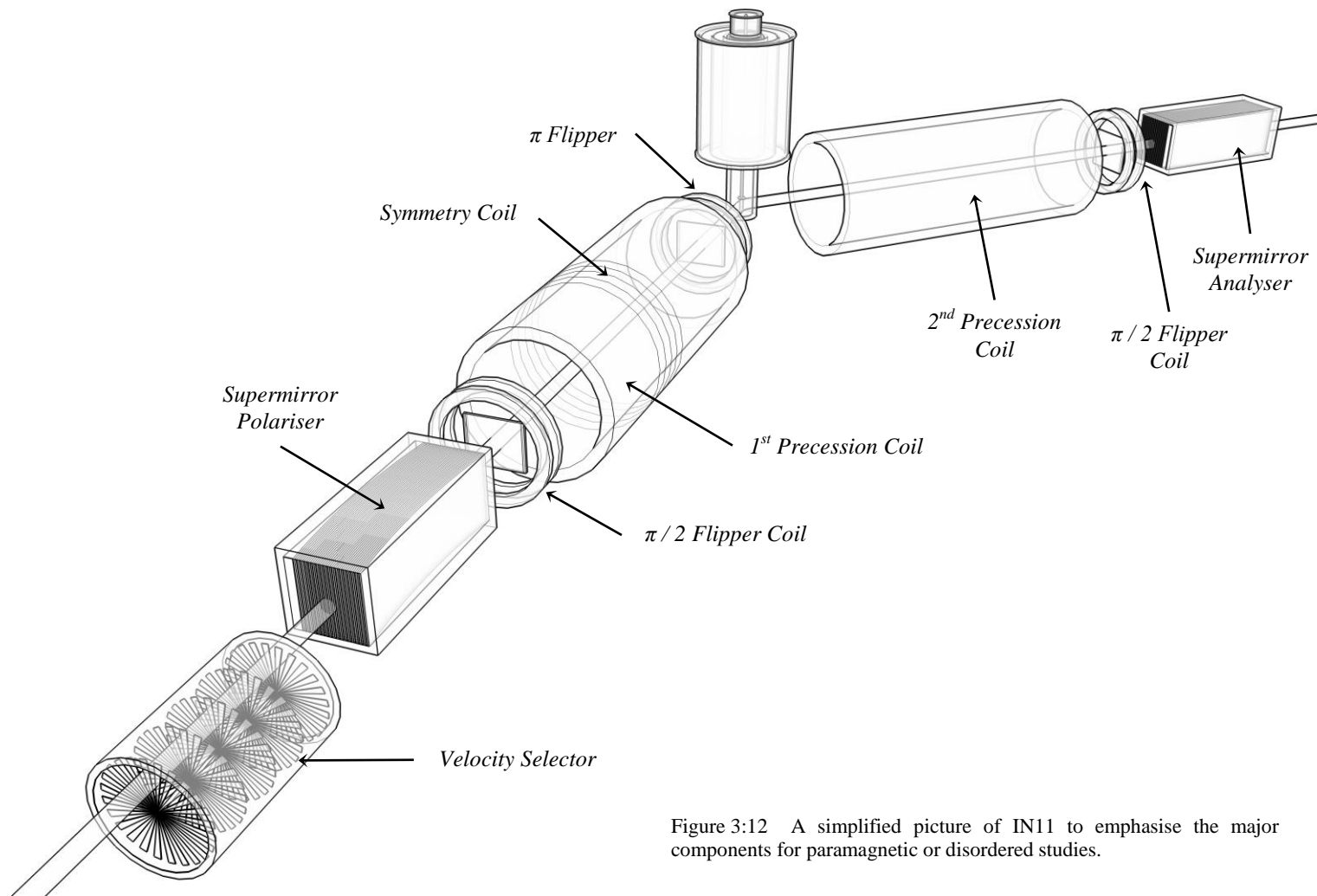


Figure 3:12 A simplified picture of IN1 to emphasise the major components for paramagnetic or disordered studies.

3.2.3 Implementation and Practicalities

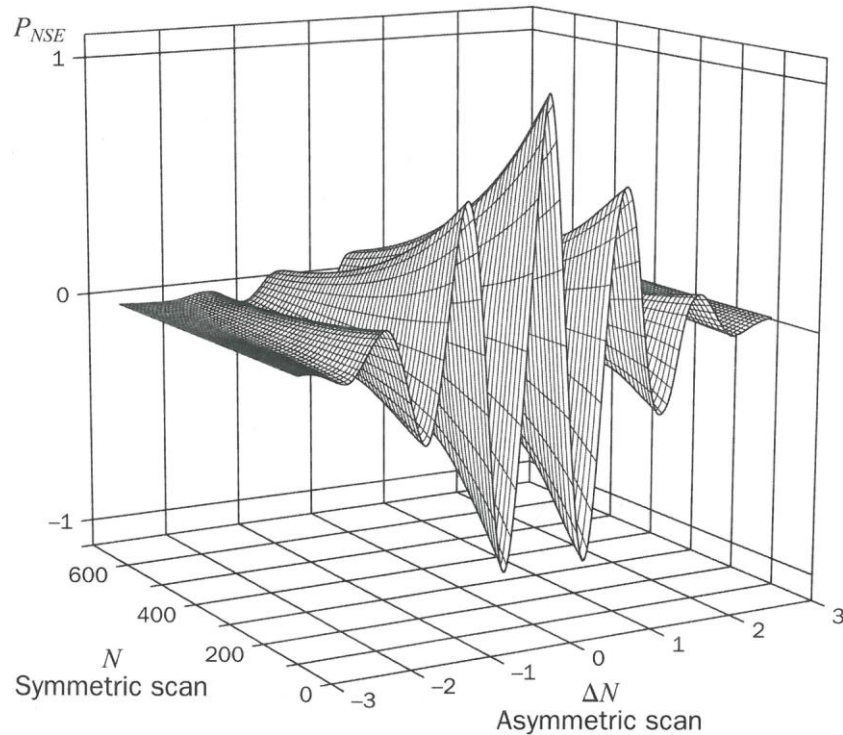


Figure 3:13 Representation of the spin echo group as a function of precession coil (symmetric scan) and symmetry coil (asymmetric scan): image created to *Cywinski*¹²⁴.

From its conception in April 1972 it took only five years to design and build the first NSE spectroscopy, and only one more year for it to be fully deployed to the user community at the Institut Laue Langevin (ILL). This instrument, named IN11, has been in operation ever since and has been used extensively for the purposes of this project. This final section on NSE is intended to give a general overview of performing a measurement on this instrument, which is due to be decommissioned in the near future.

Firstly, from equation (3:45), it can be seen the maximum attainable field integral governs the long-time limit; however the short-time limit is more subtle. Both the Earth's magnetic field and the fields required to control the neutron's spin-polarisation direction play a part, but most importantly the quasi-elastic limit must hold in order for equation (3:43) to remain valid.

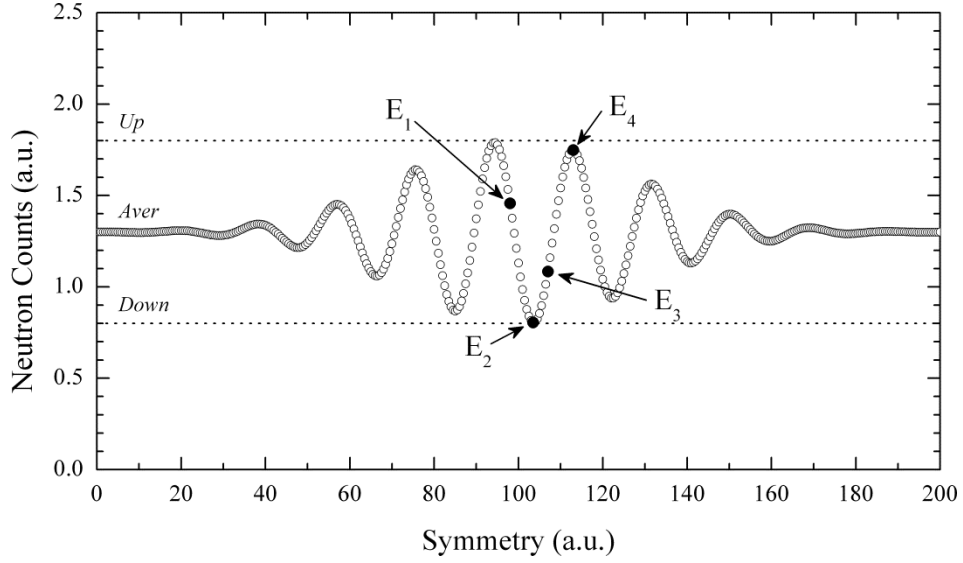


Figure 3:14 Representation of an echo measurement indicating the four measuring points (E_n), average ($Aver$), and maximum amplitude determined by flipper on (up) and flipper off (down) measurements.

Typical spectra consist of approximately thirty echo measurements performed by varying the field integral between these two limits. The echo amplitude contains the information of interests, $S(\mathbf{Q}, \tau)$, and the most common way of determining this is as follows: First the maximum possible amplitude is determined by measuring the difference between the scattered beam polarisation with and without the π -flipper activated - this is used to account for instrumental deficiency and inefficiencies. Then, with precession fields closely matched, a small auxiliary coil (the symmetry coil) is used to find the exact symmetry point where the recovered polarisation is at its maximum,

$$\begin{aligned}
 E_1 &= Aver + A \cdot \sin(\varphi) \\
 E_2 &= Aver - A \cdot \cos(\varphi) \\
 E_3 &= Aver - A \cdot \sin(\varphi) \\
 E_4 &= Aver + A \cdot \cos(\varphi)
 \end{aligned}
 \tag{3:51}$$

This procedure generates the spin echo group, shown in Figure 3:14, however in practise only four symmetry points are measured, placed at 90° steps around the centre of the echo.

At this point it is perhaps relevant to note that the periodicity of the echo is governed by the average neutron energy, and the envelope in which the signal is encompassed is the Fourier transform of the wavelength distribution. Hence, longer wavelengths increase the periodicity of the echo and a more tightly monochromated beam increases the envelope's width.

For equation (3:51), (A_{ver}) is determined simply by taking the average neutron count of the four measurements; as this is the same for all Fourier times it can be determined very precisely. Once the average is known the amplitude (A) and phase (φ) can be determined by taking the differences ($A_{ver} - E_n$). More accuracy can be gained by taking the echo group shape in to account, however its benefit is negligible and generally not included.

The final step is simply to divide the calculated amplitude of the echo group by the maximum. This normalised value is the so-called intermediate scattering function given in equation (3:46).

The NSE experiments presented in the following chapters follow a well-known procedure, generally recognised to be the norm. Once the instrument geometry is set the maximum attainable amplitude is measured using a resolution sample. If the sample under investigation is known to scatter elastically at low temperatures it can also be used, removing any issues associated with maintaining the same sample position. During the course of these studies it was found that a low temperature measurement of the sample consistently gave better data, free from abnormalities such as sudden changes in the autocorrelation function and unphysical values.

The temperature dependence of the autocorrelation function was then measured by cooling the sample in helium reservoir cryostat, allowing the sample to thermalise for between 20 – 30 minutes before recording data. Approximately thirty Fourier times were then measured before the temperature was changed and the process repeated.

3.3 The D7 Spectrometer

Introduced here are the general requirements for a neutron spectrometer dedicated to the study of diffuse scattering, alongside the practicalities of performing such measurements. The causes of diffuse scattering will be discussed in a later section prior to a study of short-range order in the pseudo-binary compound $Y(\text{Mn}_{1-x}\text{Al}_x)_2$.

3.3.1 General Requirements

The review by *Stewart* on the use of neutron polarisation analysis for the study of disordered materials outlines the general requirements of a spectrometer dedicated to diffuse scattering from crystalline materials¹²⁵. Several important design considerations are given,

- i. Diffuse scattering contributions vary smoothly with momentum transfer, and so it is favourable to relax the resolution in Q -space in order to gain higher flux.
- ii. Due to the relative weakness of diffuse scattering, minimisation of the instrument background is vitally important. Normally this is achieved by secondary collimation prior to the detectors which ensures neutrons scattered from the sample environment are not recorded.
- iii. To truly differentiate elastic from inelastic (or thermal diffuse) the instrument should have the ability to analyse the final energy of the neutron.
- iv. Polarisation analysis is also vital so that nuclear coherent, nuclear spin-incoherent and magnetic contributions can be separated.
- v. Lastly, since diffuse scattering contributions generally cover a wide range of Q -space it is also desirable to equip a wide-angle multi-detector array.

D7, being one of the first instruments built in the cold neutron guide hall at the ILL, has had to undergo significant upgrades to achieve each of these requirements. Recently it was completely rebuilt during the first phase of the ILL Millennium Programme which aims to deliver 14 new instruments or radically upgrade existing ones.

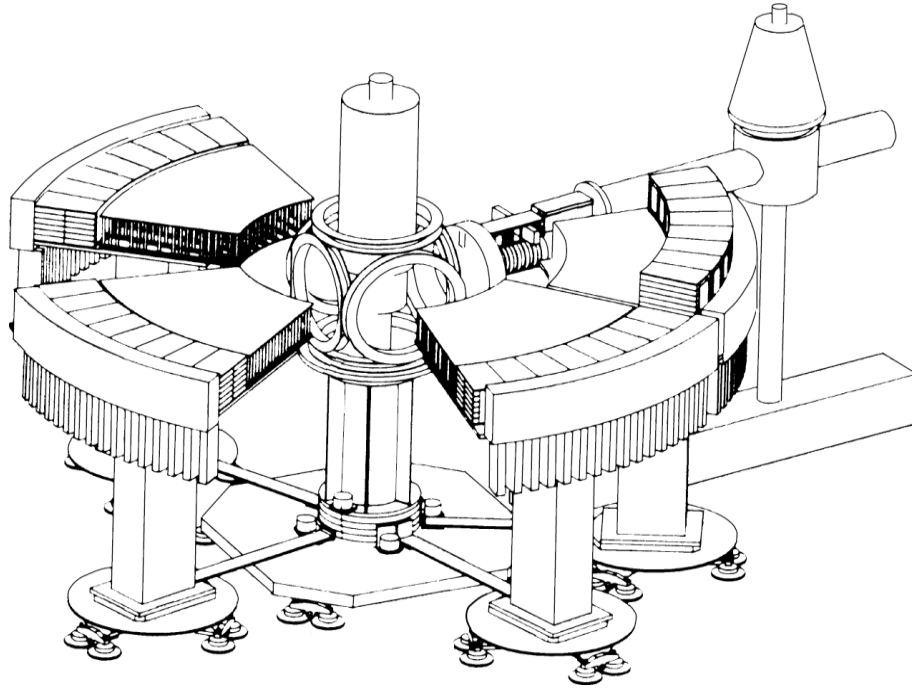


Figure 3:15 D7 has four banks of detectors which have in total over 5000 supermirrors and 132 ^3He detector tubes. Furthermore, the banks rotate about the sample position using pressure pads to give an angular range of ($5^\circ \leq 2\theta \leq 150^\circ$). This image has been taken from Schöpf¹²⁶.

3.3.2 D7 Overview

Neutrons enter the instrument after being monochromated and double focused by a mosaic of pyrolytic graphite crystals before passing through a beryllium filter removing higher order wavelengths (λ/n ; $n = 2, 3, \dots$) of 3.1, 4.8 and 5.8 Å. The beam is subsequently polarised by a supermirror ($m = 2.8$, Co/Ti type) giving a typical polarised beam flux of 1.5×10^6 neutrons $\text{cm}^{-2} \text{s}^{-1}$.

The first stage of the polarisation analysis is a Mezei coil flipper, allowing for the separation of spin and non-spin flip channels. When activated the spin-flip channel is measured and when off the non-spin flip channel is measured. Secondly the sample is centred between three sets of orthogonal coils which rotate the spin polarisation direction by $(\pi / 2)$ before and after scattering, thus allowing measurements to be made alternately in each of the x , y , and z -directions.

The multi-detector array consists of four banks of ^3He tubes covering a horizontal scattering angle of ($5^\circ \leq 2\theta \leq 150^\circ$). In total there are over 5000 supermirrors and

132 detector tubes, with each bank being mounted on pressure pads to allow them to rotate about the sample position and measure the total angular range.

3.3.3 Data Corrections

The first stage is to calculate the relative efficiency of each detector by scattering from a vanadium sample of known mass. The total scattering cross section of vanadium is almost totally incoherent (therefore isotropic over 4π steradian) so it can be said over a sufficient length of time each detector receives an equal number of neutrons to which further measurements can be normalised. Secondly, using amorphous quartz which has a near complete non-spin flip cross section, the flipping ratio of each supermirror can be determined. This is because there is a finite probability neutrons with the wrong spin will pass through the polariser/analysers supermirror. Accurate separation of the flip and non-spin flip cross sections therefore relies on determining the flipping ratios of each supermirror.

The instrument background scattering which is largely due to scattering for the sample environment, sample holder, and air, is separated in to two contributions. Neutrons that pass through the sample position (B_1) and those that do not (B_2). The first is measured by scattering from the empty sample holder, the second by scattering from the sample holder with a rolled sheet of cadmium inside. The following expression is then used to determine the real intensity,

$$I_{real} = \frac{I_{measured} - I_{cadmium}}{T(\theta)} - (I_{empty} - I_{cadmium}) \quad (3:52)$$

where $T(\theta)$ is the angular dependent transmission coefficient, accounting for the self-attenuation of the sample. For a cylindrical holder, as was used, this can be well described by the Blech-Averback formula,

$$T(\theta) = \exp[-(a_1 + b_1 \sin^2 \theta) \mu R - (a_2 + b_2 \sin^2 \theta) (\mu R)^2] \quad (3:53)$$

where $a_1 = 1.7133$, $b_1 = -0.0368$, $a_2 = -0.0927$, $b_2 = -0.3750$ and (μ) is the linear absorption coefficient and (R) is the radius of the cylinder.

Finally, normalisation to an absolute scale in units of barns / steradian / formula unit is achieved by using a known standard. Again vanadium is used since it is known to have a total scattering cross section of precisely 5.07 barns / atom. Thus,

$$\frac{I_V}{N_V} = \frac{5.07}{4\pi} \quad (3:54)$$

where (N_V) is the number density of the vanadium sample. The final absolute scale differential cross-section is therefore given by,

$$\frac{d\sigma}{d\Omega} = \frac{5.07}{4\pi} \frac{I_{real}/N_{sample}}{I_V/N_V} \quad (3:55)$$

3.4 Muon Spectroscopy

The use of muons as a scientific tool, much like the neutron, is based on their fundamental physical properties and how they interact with their microscopic magnetic environment.

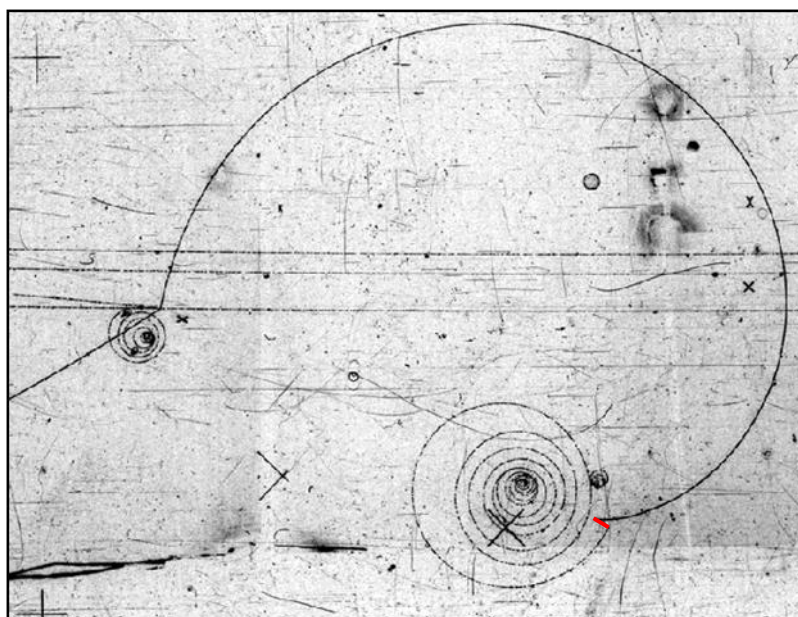


Figure 3:16 Image from the CERN 2m bubble chamber: the incoming beam collides with a hydrogen atom, expelling an electron, spiralling anti-clockwise, and a pion (π^+). The pion decays to a muon (μ^+), which travels ~ 1 cm (red line) before it decays into a positron (e^+), spiralling clockwise.

All muon spectroscopic techniques are referred to under the acronym μ SR which covers three discrete experimental methods: Muon Spin Relaxation, Rotation, and Resonance. These not only provide a uniquely sensitive probe for the internal magnetic fields and the dynamics of such fields within a sample, but also access a range of relaxation times which bridges the gap from bulk magnetisation and susceptibility measurements to neutron scattering methods ¹²⁷.

This section briefly discusses the main historical events and physical properties of the muon, illustrates current methods of producing muons, and eventually introduces the Relaxation technique employed during parts of this work (§ 4.3 and § 7.1). Details of the Rotation and Resonance techniques are available in reference ¹²⁸.

3.4.1 The Muon

The earliest sighting of what we now call the muon was in 1933 using a *Wilson*[†] cloud chamber exposed to cosmic rays^{129, 130}. It was noted that a mystery particle produced ionisation too weak to be a proton, but too strong to be an electron; these results had little impact and a discovery was not claimed. Just three years later whilst performing similar experiments, *Neddermeyer & Anderson*[†] found a particle of unit charge, with mass larger than that of the electron but much smaller than that of the proton; this work is generally accepted to be the true discovery of the muon¹³¹.

	μ^+	μ^-
Mass	206.77 m_e 0.1126 m_p	207.62 m_e 0.1131 m_p
Spin	$\frac{1}{2}$	$\frac{1}{2}$
Charge	+ e	- e
Magnetic Moment (μ_μ)	$4.84 \times 10^{-3} \mu_B$	$4.84 \times 10^{-3} \mu_B$
Gyromagnetic ratio, (γ_μ)	13.55 kHz/G	13.55 kHz/G
Half life (τ_μ)	2.197 μs	2.195 μs

Table 3:3 Currently accepted values of the fundamental muon properties¹³²⁻¹³⁵.

A year earlier the existence of such a particle had been predicted by *Yukawa*[†] which he named the mesotron. In his model this proposed particle was responsible for the strong nuclear force. Understandably it was initially hoped the muon and mesotron were one and the same, however it quickly became apparent it was not¹³⁶; its negligible nuclear interaction disagreed with that required for the mesotron. Shortly afterwards *Tanikawa et al.* worked to resolve this issue, proposing a two meson model whereby a primary strongly interacting particle (the *pion* or π -meson) decays in to a secondary weakly interacting particle (the *muon* or μ -meson)¹³⁷. Indeed it did not take long before this hypothesis was verified experimentally by *Powell*[†] *et al.*¹³⁸.

[†] *Nobel Prize laureate in Physics*

The muon occurs with two charge types (positive μ^+ and negative μ^-), and so interacts with charged particles *via* Coulomb forces. It has a large magnetic moment and is therefore extremely sensitive to magnetic fields. Furthermore, its lifetime is extremely long. Indeed, omitting the proton, electron, and neutrino, which are generally considered to be stable, the muon has the second longest lifetime of any of the unstable particles after the neutron. It also has the second smallest mass after the electron. It can be seen that due to these unique physical properties positively charged muons are often considered comparable to a light isotope of hydrogen.

3.4.2 Pion (Muon) Production

Early experiments relied upon naturally occurring particles produced as the Earth is bombarded by cosmic rays; however such low-intensity high-energy muons are unsuitable for spectroscopic studies. It was not until the 1970's that significant advancements were made; coinciding with rapid developments in accelerator science which enabled intense beams of low-energy muons to be produced with relative ease. All the data presented in this thesis were collected using positive muons at the ISIS Rutherford Appleton Laboratory (RAL) in Oxfordshire. Accordingly the following discussions are tailored to muon production at this facility.

As with all muon facilities the production of an appropriate muon beam begins with the collision of high energy protons on a target of light (low Z) nuclei. At the ISIS facility the 800 MeV proton beam is incident on an intermediate graphite target, with approximately 2 – 3 % of the protons interacting with the carbon nuclei, liberating pions. This particle, with either positive or negative charge, decays with a half-life of 26.03 ns in the following modes,

$$\pi^+ \rightarrow \mu^+ + \nu$$

$$\pi^- \rightarrow \mu^- + \bar{\nu}$$

where (ν) is a neutrino and ($\bar{\nu}$) anti-neutrino. A neutral pion also exists with a much shorter lifetime, however, rather than producing a muon, yields two gamma ray photons.

Bunches of pions are created in the graphite target on every pulse of the synchrotron, which have a wide distribution of kinetic energies. Those with low energy usually come to rest within the target itself, whilst more energetic particles often escape altogether, eventually decaying in-flight. This leads to two distinct channels by which muon beams can be, and indeed are, generated at the ISIS facility.

In the first only the low-energy pions decaying from rest are used. The subsequent muons therefore have a relatively well defined energy (~ 4.1 MeV) since only those close to the target's surface have sufficient momentum to escape. Unsurprisingly, these are known as *surface-muons* which, due to the high pion stopping density of the graphite target, are used to produce highly intense beams of positively charged muons. The rapid absorption of negatively charged muons at rest precludes them from this muon channel.

The second method takes advantage of the high-energy pions which escape the target, directing as many as possible into a region of high longitudinal magnetic field where they decay. Using this method both positive and negative muons can be harvested to produce what is often called a *decay beam*. A detailed description of this was presented in the RAL report on muon facilities and experiments by Eaton¹³⁰ but is outside the scope of this work.

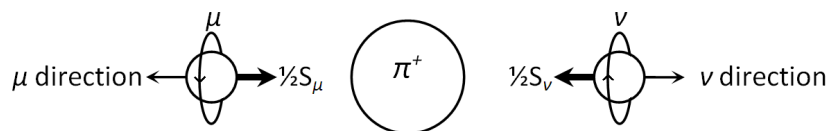


Figure 3:17 Positive pion decay - the relationship between muon and neutrino, propagation vector and spin polarization

The figure above demonstrates how the muon is intrinsically spin polarised so to conserve total angular momentum with, in this case, the neutrino's left-handed

helicity, and its spinless parent. The muon and neutrino therefore always have opposite spin, anti-parallel to their respective propagation vector. This means a high intensity surface beam not only has a narrow distribution of particle energies, but is also naturally 100 % spin polarisation in any chosen direction.

The muon's charge makes transportation from the target to the instrument relatively simple (in comparison to neutrons). Quadrupole doublets are used for focusing the beam, whilst bending magnets are used both to steer and select a momentum. To remove contaminant particles such as positrons, which not only arise due to muon-decay but also gamma ray pair production from neutral pion-decay, a cross field electrostatic separator is employed.

3.4.3 Behaviour of Muons Inside Condensed Matter

Generally there are three states adopted by muons within the atomic lattice of a sample, shown in Figure 3:18. For the purposes of this work however, we need only consider the behaviour of free positively charged muons. Moreover, in line with the above description these muons are of low-energy and therefore thermalise rapidly, generally stopping to occupy an interstitial lattice site.

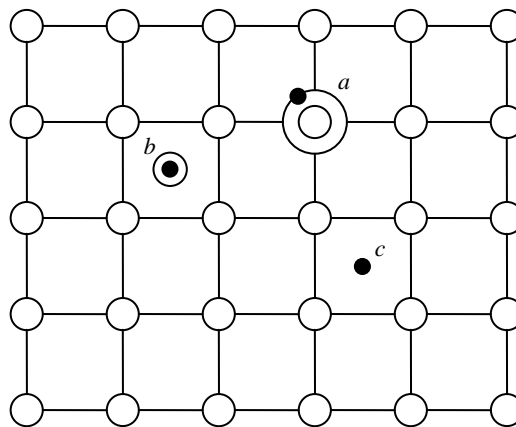


Figure 3:18 Schematic of the three states adopted by muons within the atomic lattice of a sample:
 a) Bound (μ^-) muonic atom, b) Muonium (μ^+), c) Free muon (μ^+)

Several mechanisms are involved in this process, the primary being muon-electron scattering which drops the initial energy from 4.1 MeV down to the keV range

within a nanosecond of being implanted. In the following picosecond electron capture and loss reduces the energy further, down to approximately 200 eV, before scattering from atoms and molecules finally stops the muon completely. Crucially, depolarisation during this process is negligible.

The muon's large moment makes it an extremely sensitive magnetic probe, and from this interstitial position it can survey extremely small local fields, down to $\sim 10^{-5}$ T, produced by the surrounding atomic and nuclear moments. If such a field were to have a perpendicular (*transverse*) component to the muon spin the torque would result in Larmor precession, equation (3:38).

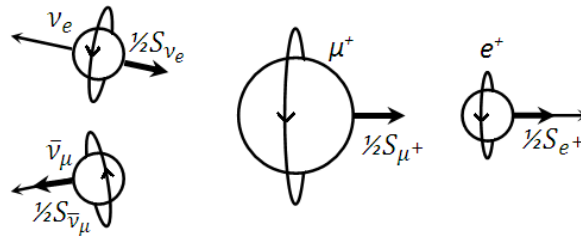
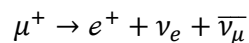


Figure 3:19 Positive muon decay emitting neutrino, anti-neutrino and high energy positron (e^+) preferentially along its spin direction

All Muon Spin Relaxation, Rotation, and Resonance experiments depend on this interaction and the subsequent depolarisation during the muon's lifetime. In the first instance, if the internal magnetic field is uniform in direction and magnitude throughout the sample then the polarization is preserved. Alternatively, if there are a range of fields or temporal fluctuations the muons will correspondingly have a range of precessional frequencies, and the initial polarisation will quickly dephase or be completely lost.

The muon decays with a half-life ($\tau_\mu = 2.197$) μs , emitting a positron (e^+), neutrino (ν) and antineutrino ($\bar{\nu}$),



The angular distribution of the positron emission is highly anisotropic with respect to the spin direction of the muon, Figure 3:20, since the combined spin of the neutrino-pair add to zero, whilst the intrinsic right-handed helicity of the positron itself means it must be emitted along the muon polarisation direction. This asymmetry is seen to be strongest at the maximum positron energy of 53 MeV, and is governed by the probability function,

$$W(\theta) = 1 + A_o \cos \theta \quad (3:56)$$

In this instance (θ) is the angle between muon spin and positron's propagation vector, and the parameter (A_o) is called the asymmetry coefficient which would equal 1/3 if it were possible to detect every positron emitted. For most experiments however it is generally seen to take a value in the region of 0.25.

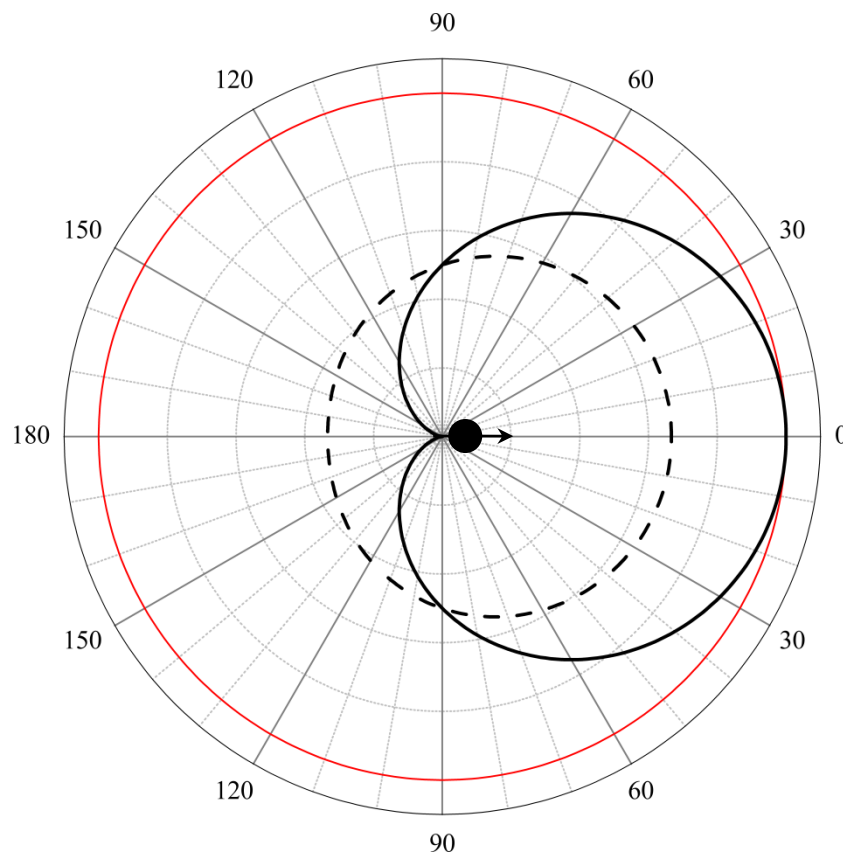


Figure 3:20 Angular distributions of positron emission for: a) the most energetic particles (solid), and b) all energies (dashed), with respect to the muon spin direction (arrow).

3.4.4 Muon Spin Relaxation

Relaxation experiments are performed in longitudinal (parallel to the polarisation direction) or zero field. In both cases however the experimental arrangement is identical, with annular detector rings placed ‘forward’ and ‘backward’ of the sample position, essentially measuring the positron asymmetry in the z -direction.

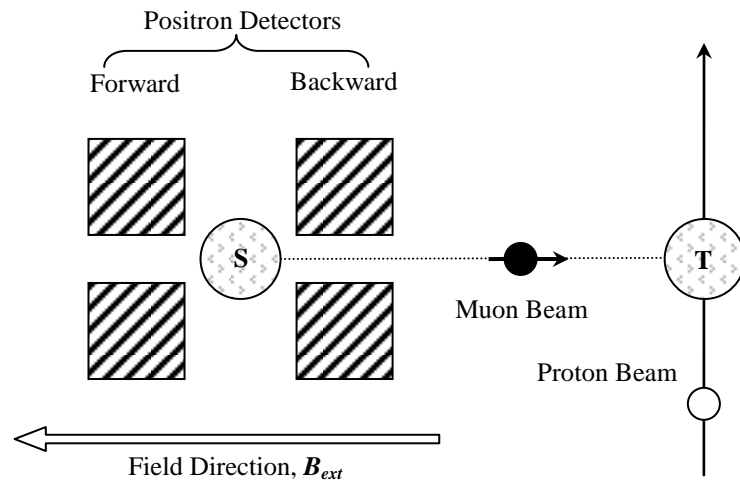


Figure 3:21 The geometry of a typical longitudinal field μ SR experimental: (T) is the target for muon production, the sample (S) is positioned centrally between two annular detector rings, one upstream, and one downstream of the muon beam.

Often, the purpose of studying a sample under a longitudinal field is to obtain the time-evolution of the polarisation due to local atomic field fluctuations within the sample. In zero-field however, the focus is more generally to observe the response due to randomly orientated local fields which produce characteristic spectra, the form of which unambiguously differentiates between dynamic and static behaviours.

The relaxation function is in principle proportional to the normalised time-dependent muon polarisation $P_z(t)$, and is calculated *via* the sum-and-difference ratio of the count rates in the forward (F) and backward (B) detector banks; equations (3:57) and (3:58) respectively:

$$F(t) \propto \exp(-t/\tau_\mu)(1 + A_o P_z(t)) \quad (3:57)$$

$$B(t) \propto \exp(-t/\tau_\mu)(1 - A_o P_z(t)) \quad (3:58)$$

$$G_z(t) = \frac{P_z(t)}{P_z(0)} = \frac{F(t) - \alpha B(t)}{F(t) + \alpha B(t)} \quad (3:59)$$

The elapsed time (t) is taken from the moment the muon pulse enters the sample, (τ_μ) is the muon lifetime, and the parameter (A_o) is the asymmetry coefficient defined in § 3.4.3. The instrumental asymmetry parameter, (α), is used to account for geometric factors, such as the sample not being located in the exact centre of the detector rings, and variation in detector efficiencies. To determine its value a calibration measurement is performed by applying a small (~ 20 G) transverse field. The signal from the spin rotation equates to a damped cosine function, from which an accurate baseline can be determined since the forward and backward asymmetries should add to zero.

At a facility such as ISIS data acquisition must be timed to coincide with the pulse structure of the synchrotron. As stated, timing starts the moment the pulse reaches the sample, however each instrument has a unique time-offset that accounts for the difference between this start time and the middle of the pulse, often referred to as T-zero. It is not until the entire pulse has arrived that useful data can be obtained; the difference between this and T-zero is known as T-good, which can simply be determined from the raw detector count rates.

3.4.5 Muon Spin Relaxation Functions

More than a decade before the Muon Spin Relaxation technique was developed *Ryogo Kubo* and his student *Toru Toyabe* constructed a general stochastic model of zero-field spin relaxation in a system of *static* random local fields¹³⁹. Initially a system of concentrated spins was assumed and accordingly a Gaussian distribution of field strengths, centred on zero, was chosen to describe the average magnetic environment,

$$P^G(\mathbf{B}_i) = \frac{1}{\sqrt{2\pi}\Delta} \exp\left(-\frac{\mathbf{B}_i^2}{2\Delta^2}\right), \quad i = x, y, z \quad (3:60)$$

where (Δ) represents the distribution's width. The subsequent relaxation function is given below, where the relaxation rate $(\sigma = \gamma_\mu \Delta)$. As shown in Figure 3:22, this function initially displays rapid Gaussian-like decay, reaching a minimum-point governed by (Δ) , but subsequently recovers to one third the initial value $(t = 0)$,

$$G_z^{GKT}(t) = \frac{1}{3} + \frac{2}{3}(1 - \sigma^2 t^2) \exp\left(-\frac{\sigma^2 t^2}{2}\right) \quad (3:61)$$

Similarly, for a system of dilute spins a Lorentzian distribution, of width (a) , provides an appropriate representation of the average magnetic environment;

$$P^L(\mathbf{B}_i) = \frac{1}{\pi} \left(\frac{a^2}{a^2 + \mathbf{B}_i^2} \right), \quad i = x, y, z \quad (3:62)$$

The resulting relaxation function is unsurprisingly very similar, Figure 3:23;

$$G_z^{LKT}(t) = \frac{1}{3} + \frac{2}{3}(1 - at) \exp(-at) \quad (3:63)$$

Equations (3:61) and (3:63) do however represent the limiting cases for concentrated and dilute dipole systems respectively, but often spectra exhibit intermediate lineshapes somewhere between the pure-Gaussian and pure-Lorentzian functions. Here a generalised power law is invoked, the so-called Voigtian Kubo-Toyabe, which interpolates between these extremes ¹⁴⁰.

$$G_z^{VKT}(t) = \frac{1}{3} + \frac{2}{3}(1 - (\lambda t)^\beta) \exp\left(-\frac{(\lambda t)^\beta}{\beta}\right) \quad (3:64)$$

where $(1 \leq \beta \leq 2)$, and the parameter (λ) quantifies the relaxation rate, as above.

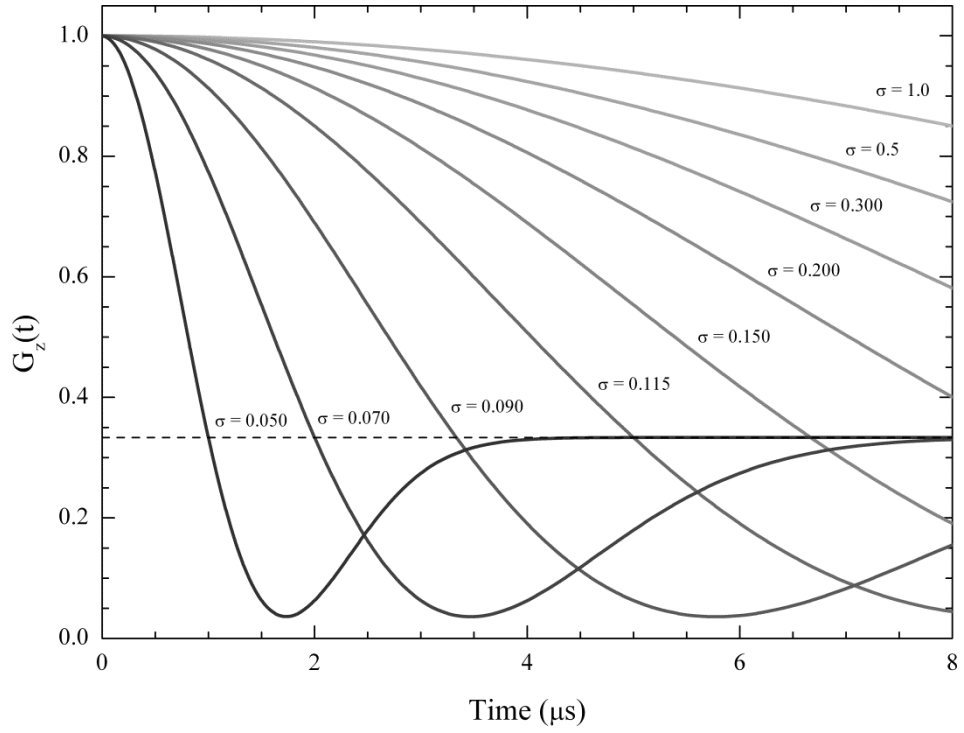


Figure 3:22 Gaussian Kubo-Toyabe relaxation function

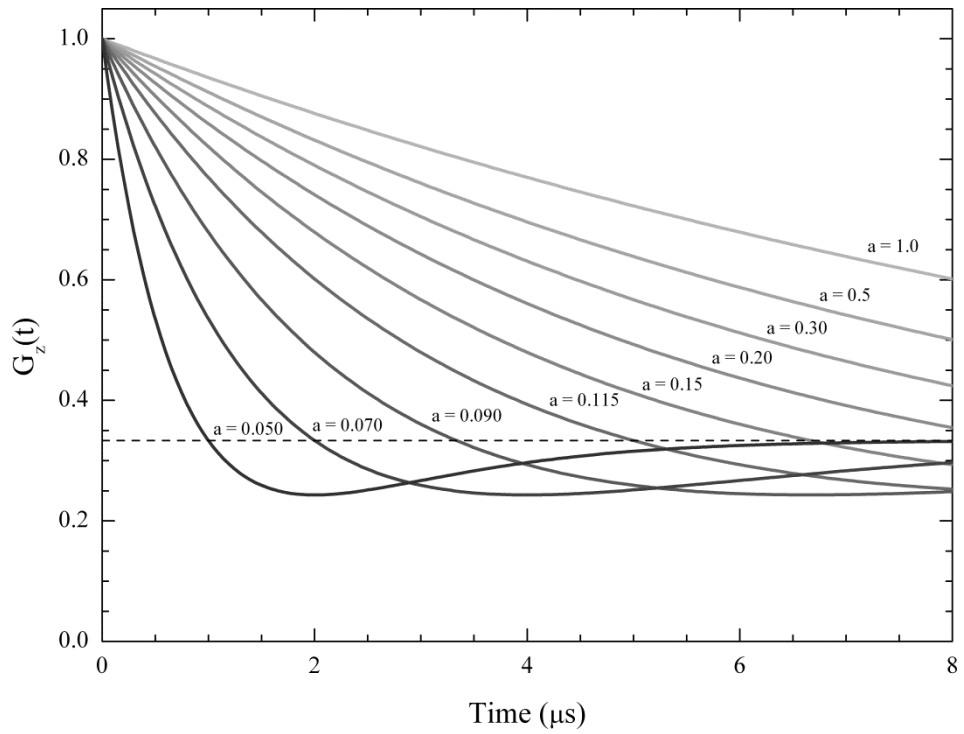


Figure 3:23 Lorentzian Kubo-Toyabe relaxation function

The recovery of the initial distribution-led decay to one third of the initial value can be understood intuitively by considering that for a random distribution of moments one third will have a component orientated in the z -direction, and thus preserve the initial polarisation. However, this is significantly suppressed by the onset of even extremely slow field fluctuations, either from the internal fields themselves or the muon hopping between sites. This behaviour is therefore fundamentally linked to the static (relative to μ_τ) nature of the random internal fields. To account for the presence of such dynamical processes the strong-collision approximation is applied, which assumes:

1. The local field experienced by the μ^+ changes abruptly to a randomly chosen field, taken from the distribution $P(\mathbf{B}_i)$,
2. There is no correlation between the field before and after this change,
3. This change occurs at time (t), with a mean fluctuation rate (ν), according to the probability distribution $P(t) = \exp(-\nu t)$.

However, the resulting dynamical Gaussian Kubo-Toyabe must be evaluated through lengthy numerical calculations¹⁴¹, and so the following three analytical approximations are applied, as shown in Figure 3:25 where ($R = \sigma / \nu$).

Slow fluctuations ($R < 1$): the distinctive recovery to one third the initial value at long times is heavily suppressed leading to a hump at $\sim 3/\sigma$,

$$G_z(t) \approx \frac{1}{3} \exp\left(-\frac{2}{3} \nu t\right) \quad (3:65)$$

Intermediate fluctuation rates ($1 < R < 10$): further stretching the static relaxation function is observed; approximated by the so-called Abragam function,

$$G_z(t) \approx \exp[-\lambda(\exp(-\nu t) - 1 + \nu t)] \quad (3:66)$$

Rapid modulation ($R > 10$): well represented by a simple exponential,

$$G_z(t) \approx \exp(-\lambda t), \text{ where } \lambda = 2\sigma^2/\nu \quad (3:67)$$

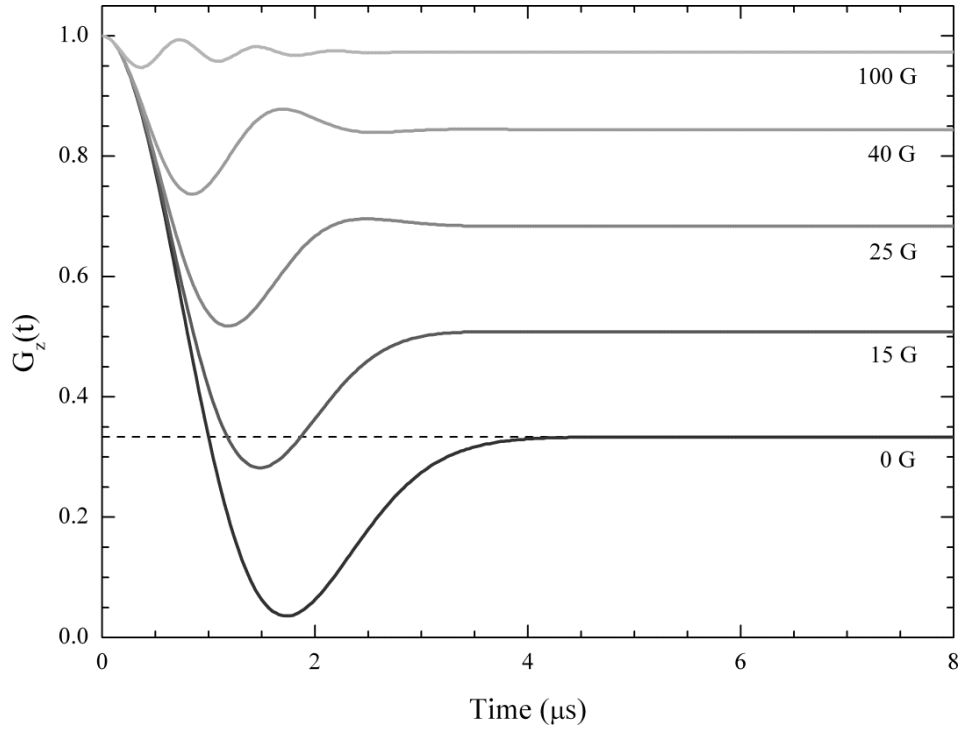


Figure 3:24 Longitudinal field muon spin relaxation spectra for a Gaussian distribution of isotropic random local fields.

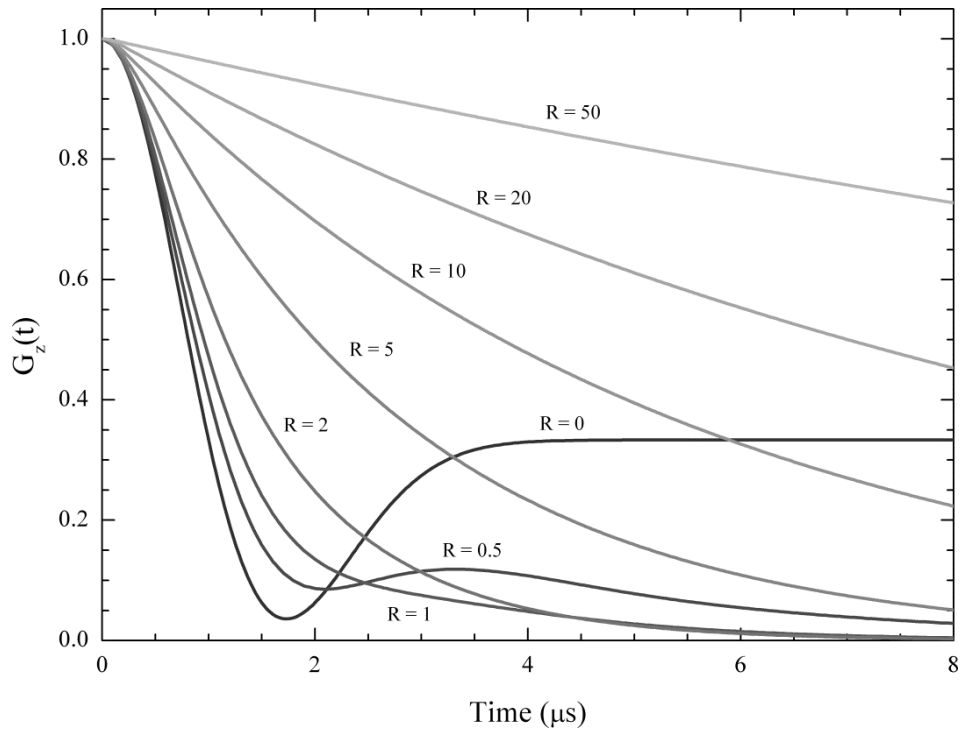


Figure 3:25 The dynamic Gaussian Kubo-Toyabe function, where $R = \sigma/v$

3.5 Sample Preparation

Air sensitive polycrystalline samples are often made using an argon arc-furnace since it can reach the extremely high temperatures required of melting most metals, and inherently does so in an inert atmosphere. Since all the studies performed in this work were on samples prepared in this way a brief description of the technique is presented here.

An arc-furnace is in essence a water-cooled copper hearth housed inside an airtight chamber, which once evacuated is partially refilled with high purity argon. Good practice dictates that this process should be repeating several times to ensure an air free atmosphere prior to melting. The hearth itself features several casting wells, one of which contains a getter; a material that is melted before the sample to absorb any residual reactive gases still present due to outgassing, leaks, or simply inadequate flushing, as it cools. Here the getter was titanium but it is not uncommon to use zirconium or a zirconium alloy.

In operation an arc of plasma passes between a tungsten electrode and the surface of the copper hearth. This is capable of carrying between 100 and 200 amps direct current through ~ 300 mbar of argon.

The predominant heating effect is a result of the potential energy released by the electrons entering the metal anode (sample / hearth), and correspondingly the magnitude of this effect directly relates to the work-function of the particular metal being melted (typically in the region of 4 V). In simple terms, this means a plasma current of 100 A equates to 400 W of highly localised heating under the arc and in this way, provided sufficient current is supplied, temperatures can approach 3000 K^{142, 143}.

In practice however the highly localised nature of the heating restricts the maximum amount of raw material per melt since it is vital that the whole ingot be maintained in a fully molten state for a period sufficient to homogenise the solid solution. Even so, each ingot is melted several times, flipping it once the pool has solidified so that the side in direct contact with the arc of plasma alternates, thus ensuring the raw

materials are indeed thoroughly mixed. In this work the total combined weight of the constituent materials was kept below 12 g, and so to produce the relatively large amounts required for polarised neutron scattering experiments, ~ 30g, several of these ingots were made and then roughly crushed before the full amount was consolidated in a final melt.

All but the (LaEr)Al₂ samples required heat treatments, performed by sealing the ingots in fused quartz ampoules inside which was a reduced (~ 300 mbar) argon atmosphere. To negate the chance of reactions occurring between the sample and SiO₂ all the ingots were first loosely wrapped in tantalum foil, chosen for its exceptionally high melting point.

Sample	T (°C)	Duration (days)
Y(Mn _{1-x} Al _x) ₂	800	7
Y(Fe _{1-x} Al _x) ₂	300 (Al rich)	1
	750 (Fe rich)	7
Cr _{1-x} Fe _x	1000	7
La _x Er _{1-x} Al ₂	NA	NA
Au ₄ V	1000	1
	500	8

Those samples containing yttrium-manganese or yttrium-iron were made slightly off stoichiometry by the addition of 5% excess yttrium. This decision was taken to help avoid the formation of strongly ferromagnetic compounds which often form as a significant impurity phase in these samples. Additionally, once the ingots were crushed the resulting powder was examined with a magnet to removing the remaining trace amounts of these ferromagnetic impurities.

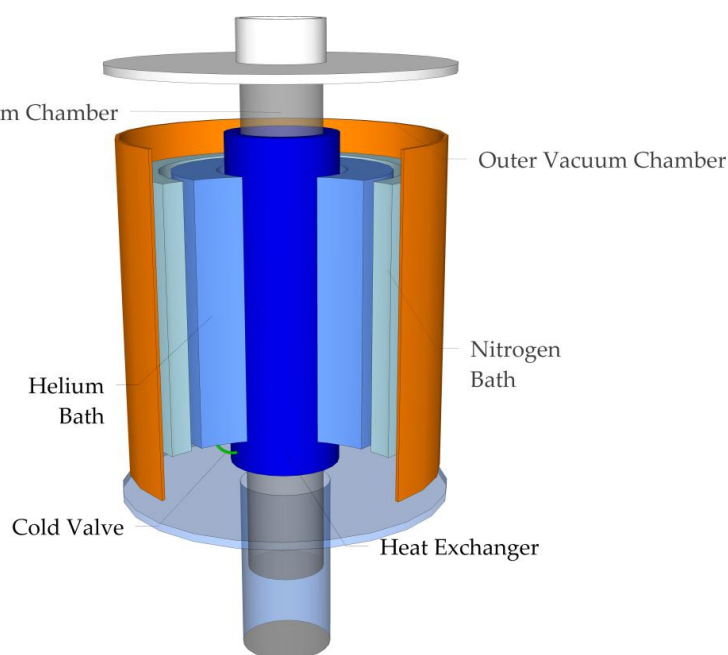


Figure 3:26 Simplified cross-section of an archetypal helium reservoir cryostat used for neutron and muon studies at the ILL and ISIS with labelling of the salient features.

By modern standards achieving the temperature range covered in this work is considered routine (1-300 K), however it is important to have a rough understanding of how these low temperatures are reached and controlled. Therefore a simplified cross-section of the ubiquitous helium reservoir cryostat, optimised for neutron and muon studies is offered in Figure 3:26. As can be seen, the cooling cycle is driven by baths of liquid refrigerant which encompass a long sample chamber reaching into the particle beam. The sample is fixed to a rod and positioned it at the bottom of this well. The influx of external heat is minimised by maintaining the outer chamber under high vacuum, however the inner chamber is partially filled with helium to act as an exchange medium for the flow of heat between sample and exchanger. The helium reservoir is slightly over-pressurised, and a so-called cold valve controls the flow rate of helium vapour into to heat exchanger, with the exhaust helium being drawn by a vacuum pump and recycled.

Temperature changes are governed by a PID controller and small heater positioned close to the sample holder.

Chapter 4

LAVES PHASE SPIN GLASSES

If two metals are alloyed then, broadly speaking there are two possibilities; a solid solution can form in which the resulting material adopts both structural and physical characteristics consistent with the linear interpolation between metal A and metal B, or an intermetallic compound forms. Such compounds have well-defined stoichiometric compositions which, unlike random alloys, regularly possess structural and physical properties different from those of the constituent elements. This chapter presents several investigations of intermetallic compounds with AB_2 stoichiometry.

4.1 Introduction to AB_2 Intermetallic Compounds

Early crystallographic studies of AB_2 intermetallic compounds quickly established the existence of three primary polytypes, the majority of which were performed separately by *Friauf* and *Laves*¹⁴⁴⁻¹⁴⁷. Hence in 1939 *Schulze et al.* coined the term Friauf-Laves phase, colloquially shortened to Laves phase, so that these closely related topologically close-packed structures could be grouped¹⁴⁸. It is important to note that these early studies focused almost entirely on just three compounds: $MgZn_2$, $MgCu_2$, and $MnNi_2$, since these are now widely regarded as the archetype for each polytype or phase. However, in recent years it has become customary to use the Strukturbericht symbols, *C14*, *C15*, and *C36* to refer to each polytype respectively.

The Laves phase structures form the largest of any intermetallic species with well over 1400 entries in ‘*Pearson’s Handbook of Crystallographic Data for Intermetallic Phases*’¹⁴⁹. Geometrically, they are only slight modifications of one another due to differences in the periodicity of their stacking sequence which, along with several other salient properties, are presented in Table 4:1. In the first instance it is generally accepted that the metallic radii of atoms **A** and **B** expand and contract mutually through the hybridisation of the outer electrons in order to approach the ideal space-filling ratio of ($r_A / r_B = 1.225$). However, whilst it is true hexagonal polytypes are most abundant for atomic combinations naturally close to 1.225, the cubic *C15* phase is frequently observed above this critical value¹⁵⁰. Moreover many **AB₂** compounds exhibit an extended range of homogeneity into both the **A**-rich and **B**-rich sides of stoichiometry. These peculiarities are not fully understood but the consensus is that such off-stoichiometric compounds are due to anti-site occupation, vacancies, or a combination of both¹⁵¹. The structure pertinent to this work is the cubic *C15* phase which, it has been reported, can only accommodate anti-site **B** atoms.

Phase Structure	Strukturbericht Symbol	Space Group	Symmetry Type	Stacking Periodicity
MgZn ₂	C14	P6 ₃ /mmc	Hexagonal	AB
MgCu ₂	C15	Fd3m	Cubic	AB ₁ B ₂ (<i>abc</i>)
MnNi ₂	C36	P6 ₃ /mmc	Hexagonal	AB ₁ AB ₂ (<i>abac</i>)

Table 4:1 Listed here are the Strukturbericht designations, space group and crystal symmetry, as well as the AB stacking sequences for each of the founding systems studied by Friauf and Laves circa 1930.

In this lattice structure the larger **A** atoms can be seen to adopt a diamond-like configuration shown in Figure 4:1, whilst the smaller **B** atoms form a sub-lattice of staggered polyhedron constructed from pairs of corner sharing tetrahedra, shown in Figure 4:2. The combined crystal lattice structure is depicted in Figure 4:3, in which the **B** sub-lattice has been extended outside the unit cell to give a fuller depiction of its geometry.

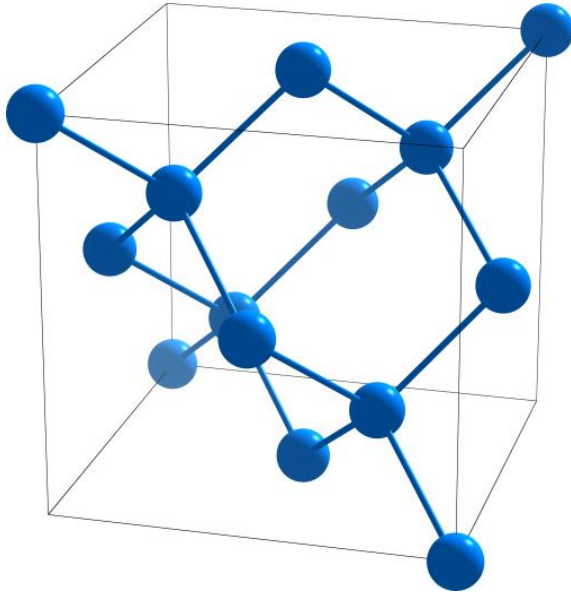


Figure 4:1 This 3D unit cell model illustrates the diamond-like configuration of the **A** lattice in the cubic C15 Laves Phase. These atoms occupy the $8a$ site at $(\frac{1}{8}, \frac{1}{8}, \frac{1}{8})$, but for clarity only the 1st nearest neighbours, at typical interatomic distance $\sim 3.5 \text{ \AA}$ are included.

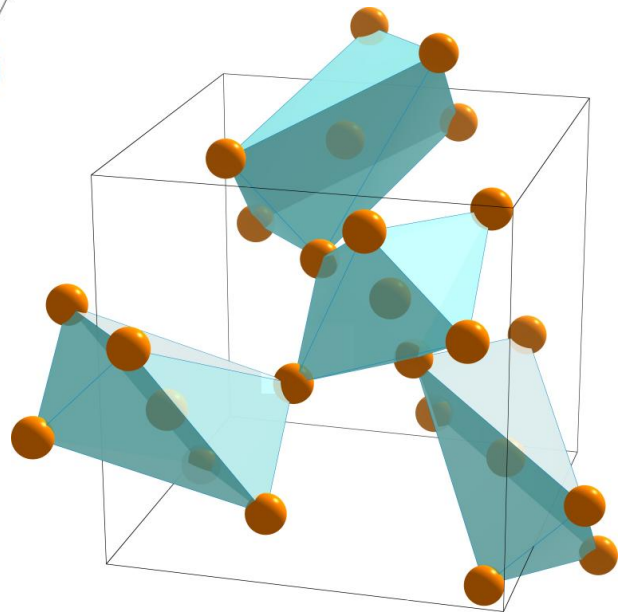


Figure 4:2 The smaller **B** atoms form a complicated array of staggered polyhedron constructed between 1st and 2nd nearest neighbour **B** atoms at typical interatomic distances of $\sim 2.7 \text{ \AA}$ and $\sim 4.7 \text{ \AA}$ respectively. These atoms occupy the $16d$ site at $(\frac{1}{2}, \frac{1}{2}, \frac{1}{2})$ in the unit cell.

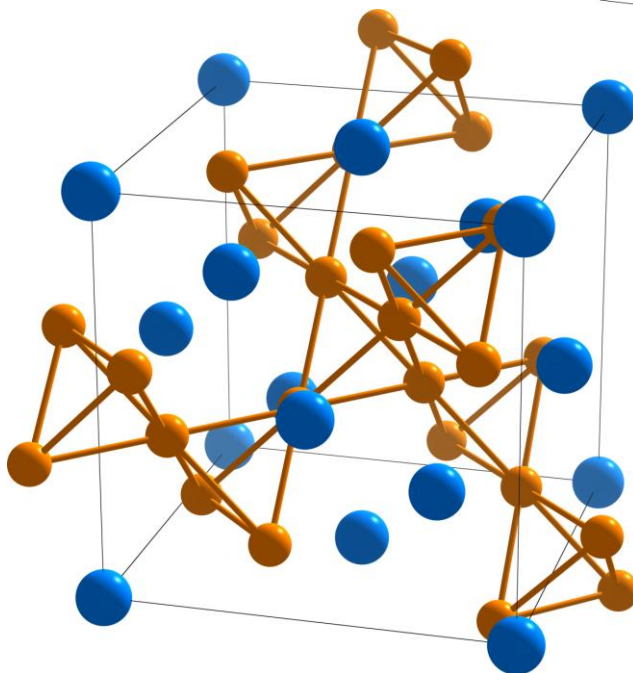


Figure 4:3 The complete MgCu_2 crystal structure, also known as the C15 or cubic Laves phase. The larger Mg sites on the **A** lattice are shown in blue, and the smaller Cu atoms on the **B** sub-lattice in orange. Again, the tetrahedral structure has been extended outside the unit cell boundary in order to give a fuller representation of the **B** sub-lattice.

Unfortunately despite considerable effort being made to construct a model derived from relative atomic sizes, electronegativities, and average valence electron concentration, we currently still lack the understanding necessary to predetermine the most stable polytype for a particular compound ^{151, 152}.

Making such predictions is made even more difficult due to the apparent contradictory behaviour of several well studied systems. For instance, magnesium based Laves phase compounds commonly adopt the *C15* structure at low electron concentration and the *C14* structure at higher concentration, whereas the opposite is true for transition metal based systems. Furthermore, when the **B** atom is nickel or cobalt many **A** atoms with the appropriate diameter to satisfy the space-filling ratio do not adopt any of the Laves structures. What can be said however is that of the three, *C36* is considered an intermediate phase between the more commonly observed *C14* and *C15* phases ¹⁴⁹.

Intermetallic compounds based on Rare earth (Re) *3d* transition metals (T) have been the focus of a particularly large amount of research, with the majority of the literature dedicated to their magnetic properties. The reasons for this are manifold; the well defined crystal structure, and specifically the comparable nearest neighbour distance of the **B** sub-lattice to that of pure transition metals, enables conclusive information to be gained on the nature of *3d* metallic magnetism. Furthermore, due to the chemical similarity^{††} of Re elements it can generally be said if one Re - T combination forms a particular polytype then the same will be true for all other Re combinations. Hence it is possible to study changes in magnetic behaviour as the *4f* - shell is filled ^{153, 154}. Of course this leads to a sub-class where the Re element is non-magnetic (La, Lu, Y) and polarisation of the *3d* moment by the otherwise strong, localised *4f* moment is totally eliminated.

^{††} *By reason of the tightly bound nature of 4f-electrons the outer electronic configuration, and therefore the chemical behaviour of all Rare earth elements is approximately uniform.*

Additionally there exist a extremely large number of ternary systems, for example $A(BC)_2$, through which concentration dependent behaviour is often studied. However it must be stated that all true ternary systems studied up to now adopt the *C14* phase. True ternary systems are those in which the respective binary AB_2 and AC_2 systems do not form Laves phase structures. The systems studied in this project are referred to as pseudo-binary, since their binary systems do crystallise in one of the Laves polytypes. Moreover they often preserve a single structure from one binary extreme to the other, or in other words from pure AB_2 to AC_2 stoichiometry. For this reason they too have been extensively studied since through them we are able to observe evolving behaviours as one atomic species is gradually replaced by another ¹⁵⁵.

4.2 Characteristics of YMn_2

Manganese exhibits four diverse allotropies, referred to as α , β , γ and δ . The magnetic properties of these vary hugely from the non-magnetic β -phase to moments which fluctuate from near zero to $1.8 \mu_B$ in the equilibrium α -phase ¹⁵⁶. Subsequently, several manganese based systems have critically unstable moments, presenting an ideal framework by which the underlying processes of moment localisation can be studied.

One such system is the binary *C15* Laves phase compound YMn_2 . Indeed the remarkable properties of YMn_2 have been the focus of many experimental and theoretical studies, significantly advancing our current understanding of metallic magnetism. The first published work was in 1967, which reported monotonic magnetic susceptibility, suggesting a single Pauli-paramagnetic state to temperatures as low as 10 K ¹⁵⁷. We now know that this measurement was inaccurate, however the report also identified the distinct evolution towards Curie Weiss-like behaviour as the average manganese separation was artificially increased *via* the partial substitution of aluminium onto the manganese sites.

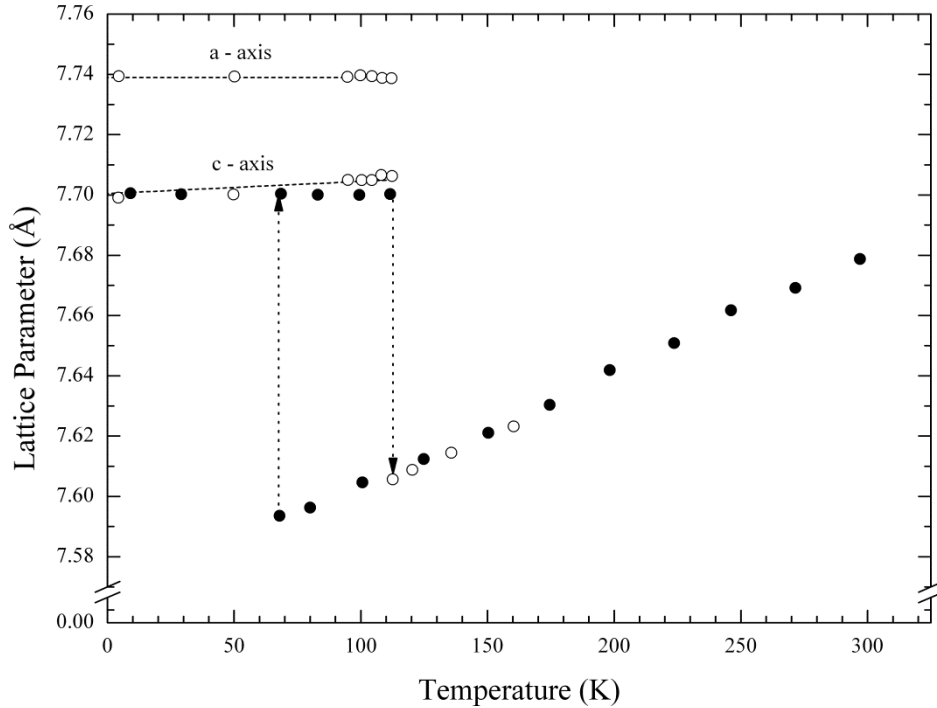


Figure 4.4 The thermal expansion curve of YMn_2 . The original measurements (black) ¹⁵⁴ are presented for comparison with more recent high-resolution measurements (white) ¹⁵⁸.

In 1982 the discovery, *via x-ray* diffraction, of a spontaneous thermal expansion anomaly (*TEA*) indicated the existence of a previously unseen 1st order phase transition at ~ 100 K with a large thermal hysteresis of ~ 40 K ¹⁵⁹. This behaviour is not unusual in Re-T Laves phase intermetallic compounds and often stems from magnetovolume effects ^{153, 160}, however if this were the case it would clearly be inconsistent with the previously reported Pauli-paramagnetism for YMn_2 . Moreover the reported magnitude of this *TEA* equates to a remarkable 5 % expansion in volume.

This unexpected result subsequently sparked a host of new investigations. New magnetic susceptibility measurements confirmed a similar anomaly close to 100 K, and spin-echo NMR spectroscopy revealed two distinct peaks at a 3:1 ratio, which strengthened a growing belief that the *TEA* was driven by a magnetic transition. Moreover, due to the relative population of sites it was suggested that this transition led to localised moments ordered anti-ferromagnetically in the [111] direction ¹⁶¹.

To determine the precise magnetic structure several neutron diffraction investigations were performed in the following years ^{162, 163}, including polarised neutron measurements ^{164, 165}. It was found that in the paramagnetic regime the spin fluctuations are accurately described using an itinerant electron picture within the framework of Moriya's SCR theory. In the expanded phase moments spontaneously localise onto the manganese sites and, due to the topology of the **B** sub-lattice, adopt a complex anti-ferromagnetic spin arrangement, partially relieving the inherent geometric frustration. The spins lay in the (1,0,0) plane and propagate helically in both the [1,0,0] direction with a period of 430 Å, and in the [0,1,0] direction with a much larger period in the order of 2500 Å ¹⁵⁸. Comparison of the nuclear and magnetic peak intensities determined the magnitude of the manganese moment to be in the order of 2.7 μ_B .

Thus the *TEA* is attributed to the difference in atomic volume between manganese sites with and without localised moments, and the Néel temperature correspondingly is taken to be ~ 100 K ¹⁶². At the time of these measurements however it was unclear if the lattice expansion was solely the result of this isotropic magnetostriction or if a second mechanism was also involved ¹⁶⁶. Following further *x*-ray and high-resolution neutron diffraction, Figure 4:4, it was finally discovered that a tetragonal distortion to the *I41/amd* space group was also present at T_N , characterised by a magnetostrictive strain of 5×10^{-3} , acting to further relieve the topological frustration of the **B** sub-lattice.

As has been mentioned, *TEA* are not uncommon for Re-T Laves phase compounds. Indeed investigations across a series of *C14* and *C15* Re-Mn₂ based systems reveal similar behaviour, in which a discontinuous volume expansion at or below 100 K occurs alongside the simultaneous onset of a large (2 - 3 μ_B) magnetic moment ¹⁶⁷; the only exceptions being compounds in which the resulting manganese separation is equal to, or below 2.66 Å, namely HoMn₂, ErMn₂, and DyMn₂. Clearly then for this family of intermetallic compound the lattice parameter plays a crucial role in determining the presence of a localised magnetic moment, and as one might expect the stability and magnitude of this moment is therefore extremely sensitive to both

chemical and mechanical pressure^{168, 169}. For example, the partial substitution of manganese for just a few percent iron or cobalt decreases the lattice parameter sufficiently to prevent moment localisation and subsequent long-range order developing. Similarly the application of external pressure also rapidly reduces the lattice parameter ($\sim 0.016 \text{ \AA /kbar}$) such that 2.7 kbar is again sufficient to fully suppress the magnetic transition^{168, 170, 171}.

4.2.1 Spin Glass Behaviour in $\text{Y}(\text{Mn}_{1-x}\text{Al}_x)_2$

The pseudo-binary intermetallic compound $\text{Y}(\text{MnAl})_2$ has also been extensively characterised using a similar range of techniques^{172, 173}. They have shown that while the value of the ordered moment remains largely unaffected ($\sim 2.7 \mu_B$ per manganese atom) by the substitution of aluminium, both the structural and paramagnetic properties change markedly. Not only does the negative chemical pressure exerted cause a gradual transition from weak itinerant to more localised electron behaviour, Figure 4:5, but also the average lattice parameter increases significantly. In other words the substitution of aluminium onto the **B** sub-lattice effectively stabilises the manganese moments, and simultaneously causes the magnitude of the thermal expansion coefficient to rapidly fall. The volume change steadily becomes less pronounced, as shown in Figure 4:6, and whilst the transition remains 1st order for ($x < 0.03$), higher concentrations results in a more continuous-like transition. By ($x = 0.10$) the volume change has disappeared completely and the high temperature susceptibility has become more Curie Weiss-like. However at low temperature a relatively sharp cusp in the magnetic susceptibility is observed.

Clearly this observation is indicative of a frustrated spin glass-like ground state, due to the apparent total or partial collapse of the long-range anti-ferromagnetic order associated with the parent compound. In 1986 *Motoya* performed neutron diffraction measurements comparing the patterns from YMn_2 with those of $\text{Y}_{1.05}(\text{Mn}_{1-x}\text{Al}_x)_2$; the magnetic contributions being deduced from the difference between the low and high temperature measurements¹⁷⁴. His results showed that even for relatively low concentrations ($x = 0.05$) the magnetic scattering consisted of

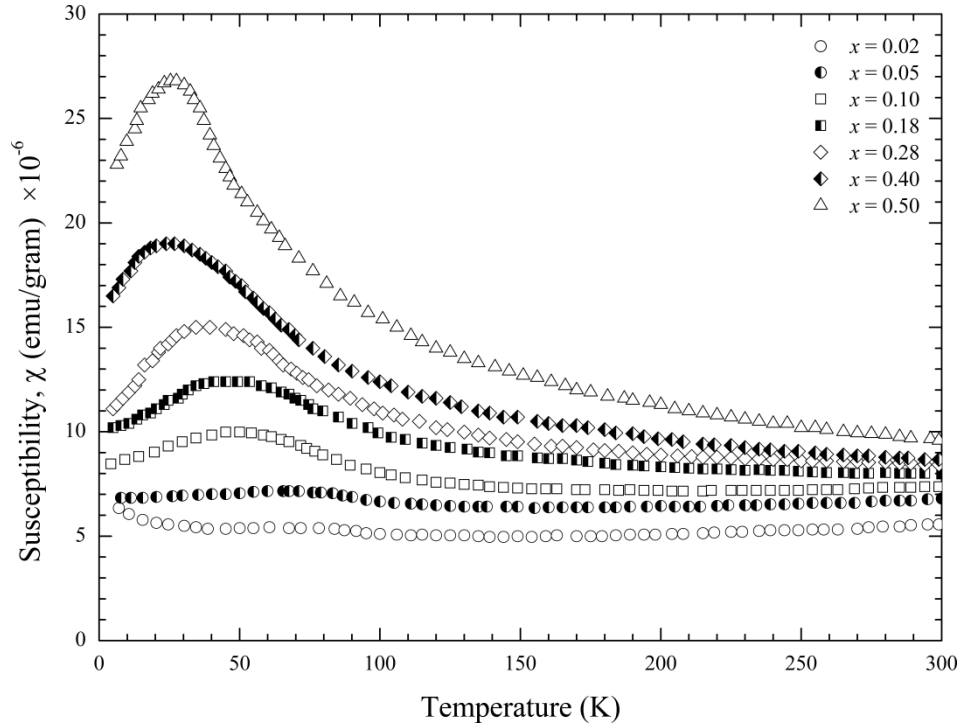


Figure 4:5 Concentration and temperature dependent magnetic susceptibility of $Y(Mn_{1-x}Al_x)_2$ indicating the appearance of Curie Weiss-like behaviour with increasing Al concentration. These results are taken from *Shiga*¹⁷².

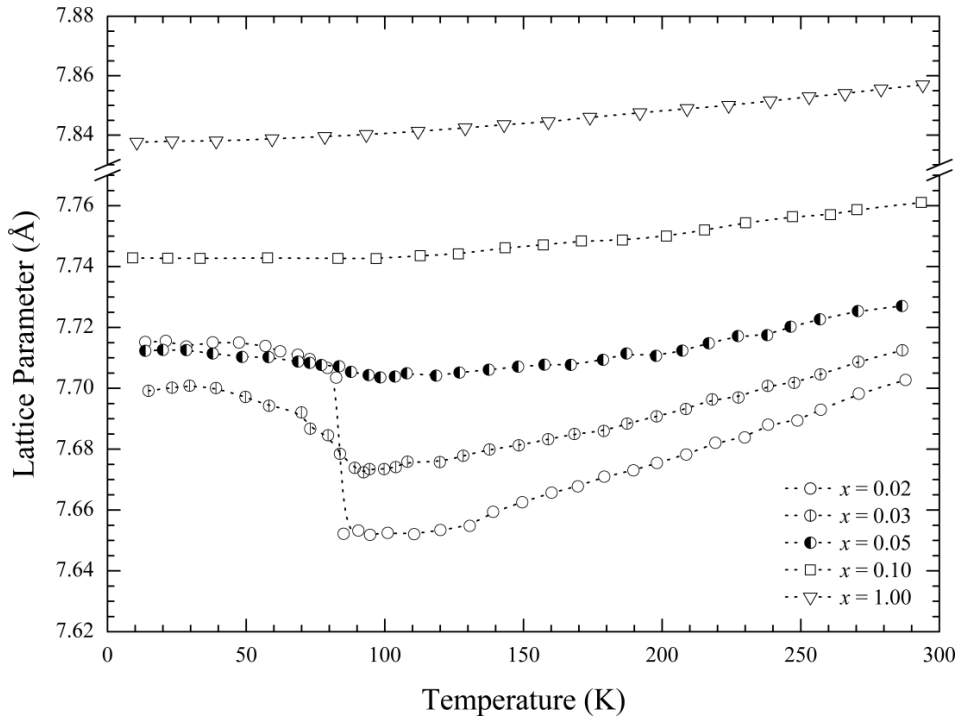


Figure 4:6 Thermal expansion curves suggest a gradual shift towards a 2nd order transition in the range $(0.03 \leq x \leq 0.05)$ and that for concentrations $(x \geq 0.10)$ the volume anomaly is fully suppressed. These results are taken from *Shiga*¹⁷⁵

only diffuse peaks, the largest being centred on the (210) magnetic Bragg reflection of YMn_2 , with secondary diffuse regions at the (110) and (211) peak positions. He concludes that short-range magnetic correlations originating from the underlying anti-ferromagnetic structure clearly persist, and that a short-range correlated spin glass phase forms for concentrations ($x \geq 0.05$.)

4.2.2 Sample Preparation

These samples were made in collaboration with Dr. M. Telling. Samples of the intermetallic compound $\text{Y}_{1.05}(\text{Mn}_{1-x}\text{Al}_x)_2$ with $x = 0.05, 0.10$ and 0.30 were prepared by argon arc melting stoichiometric proportions of 99.995 % pure constituent materials. The off-stoichiometric (1.05 / 2.00) atomic ratio was chosen to avoid the possible formation of manganese-rich ferromagnetic impurities, as discussed in reference ¹⁷⁴. The inability of the *C15* lattice to accommodate anti-site **A** atoms and the general lack of a magnetic moment on the yttrium atom itself means this excess does not have any appreciable effect on the measurements.

The polycrystalline ingots were sealed in quartz ampoules under vacuum and annealed at 800 °C for one week before quenching in liquid nitrogen. They were subsequently crushed into a fine powder in an inert atmosphere.

4.3 Pressure Dependence of Topological Frustration

Previously μSR spectroscopy has proved extremely useful in the characterisation of spin dynamics in YMn_2 ¹⁵⁸, along with the collapse of long-range magnetic order in $\text{Y}(\text{Mn}_{1-x}\text{Al}_x)_2$ ¹⁷⁶. Here I present the results of a further study on $\text{Y}(\text{Mn}_{1-x}\text{Al}_x)_2$ at the concentration ($x = 0.05$) in which external mechanical pressure ($P = 4.5$ kbar) was applied to counteract the chemically induced lattice expansion. It was hoped that in this way the manganese moment could once again be destabilised, and a pure YMn_2 -like state recovered. This stoichiometry was chosen as the recorded magnetic susceptibility exhibited the early stages of a Curie Weiss-like contribution whilst still being beyond the limit of magnetic frustration, as found by *Motoya's* neutron scattering work.

In 1991 *Cywinski et al.* performed transverse field measurements on a sample of YMn_2 over a temperature range of 18 - 300 K, fitting the data to a single exponential relaxation function ¹⁵⁸. It was found that in the paramagnetic regime the characteristic relaxation rate (λ) was extremely small ($\sim 0.025 \mu\text{s}^{-1}$), thus indicating rapidly fluctuating fields about the muon's position. Approaching the Néel temperature a critical slowing of (λ) was observed which reached a maximum of $0.08 \mu\text{s}^{-1}$ below which a broadly stable value of $\sim 0.06 \mu\text{s}^{-1}$ was recorded. In contrast, later measurements on $\text{Y}(\text{Mn}_{1-x}\text{Al}_x)_2$ with ($x = 0.10$) could not be described by as simple a model ¹⁷⁶. For temperatures above 60 K it was necessary for a small rapidly damped contribution ($a_2 = 0.02$, $\lambda \approx 30 \mu\text{s}^{-1}$), possibly due to ferromagnetic Y_6Mn_{23} impurities, to be included, whilst the dominant relaxation process ($t \geq 0.5 \mu\text{s}^{-1}$) was now better described by a stretched exponential term,

$$G_z(t) = a_1 \times \exp(-(\lambda t)^\beta) + a_2 \times \exp(-\lambda t) + a_b \quad (4:1)$$

The temperature dependences of (λ) and the stretching parameter (β) from this experiment are included in Figure 4:10 and Figure 4:11 for comparison with the current work. It can be seen that (β) tends towards a value of 1.5, revealing a progression toward a Gaussian-like distribution of relaxation rates as the temperature increases. Moreover the relaxation rate is considerably slower than that of the undoped compound, increasing from a value of $\sim 0.04 \mu\text{s}^{-1}$ at high temperatures to a maximum of $0.75 \mu\text{s}^{-1}$ at 70 K. Fitting (λ) to the critical form,

$$\lambda(T) = \lambda_0 \left(\frac{T - T_g}{T_g} \right)^{-\gamma} \quad (4:2)$$

it was found ($\lambda_0 = 0.14 \mu\text{s}^{-1}$), ($T_g = 60 \text{ K}$) and ($\gamma = 0.9$).

The high pressure μSR measurements presented here were performed at the RIKEN-RAL muon facility using the ARGUS spectrometer with the sample loaded into a

Copper-Beryllium pressure cell. Pressure was applied using a helium gas intensifier and monitored as the temperature was reduced. Any pressure drop resulting from helium contraction was compensated for above 45 K, ensuring a constant 4.5 kbar below the melting point of helium (~ 40 K at this pressure).

4.3.1 Longitudinal Field μ SR Measurements

When working in longitudinal field geometry it is important to first perform a calibration measurement in a small transverse field (~ 20 G), Figure 4:7. In this way the relative forward and backward detector efficiencies, and thus an accurate asymmetry baseline can be determined. Simplification of the background response from the nuclear dipole relaxation associated with the pressure cell material was achieved by applying a 110 Gauss longitudinal field, as shown in Figure 4:8. The sample was cooled in zero-field and all measurements were taken upon warming from the lowest temperature.

Prior to discussion of these results it is important to consider the position of the muon within the host matrix. It is generally accepted that the muon behaves much like a light isotope of hydrogen, and correspondingly occupies the same interstitial position. At low concentrations hydrogen has been reported to occupy the so-called (2-2) position in YMn_2 ¹⁷⁷, which is at the centre of a tetrahedron surrounded by two manganese and two yttrium sites. This is fortunately the same site thought to be occupied in Re-Al₂ Laves phase compounds, although there is also a second possible, so-called (3-1), site seen at higher hydrogen concentrations. This however is thought to be a highly unlikely position for a μ^+ to occupy¹⁷⁸.

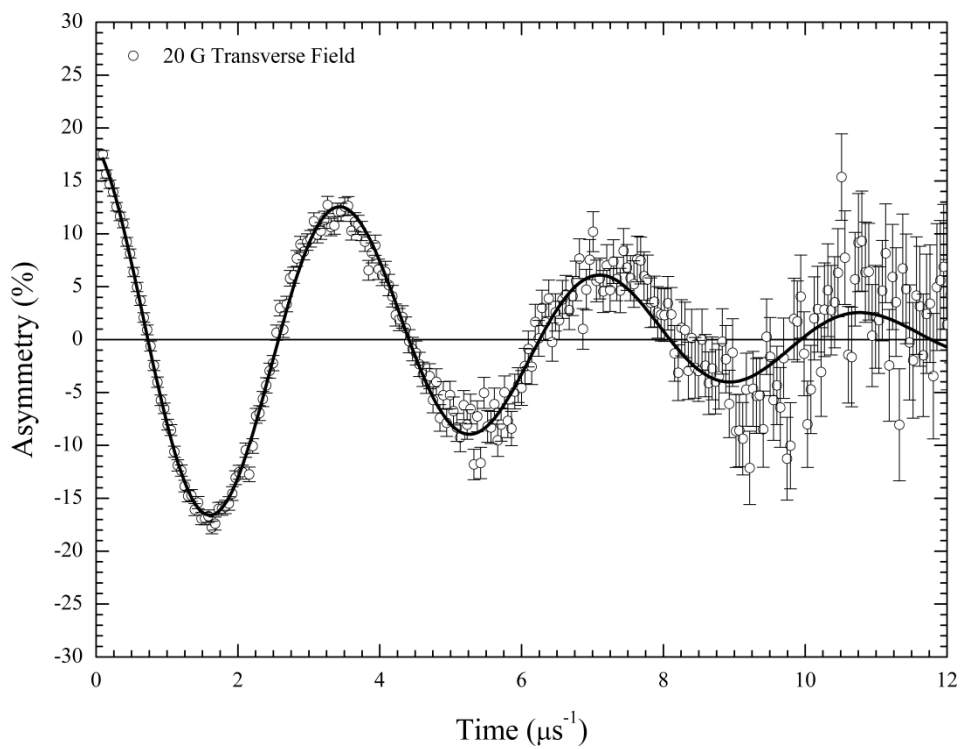


Figure 4:7 Typical instrument calibration measurement performed in a 20 G transverse field. Solid line is a damped cosine fit to the data.

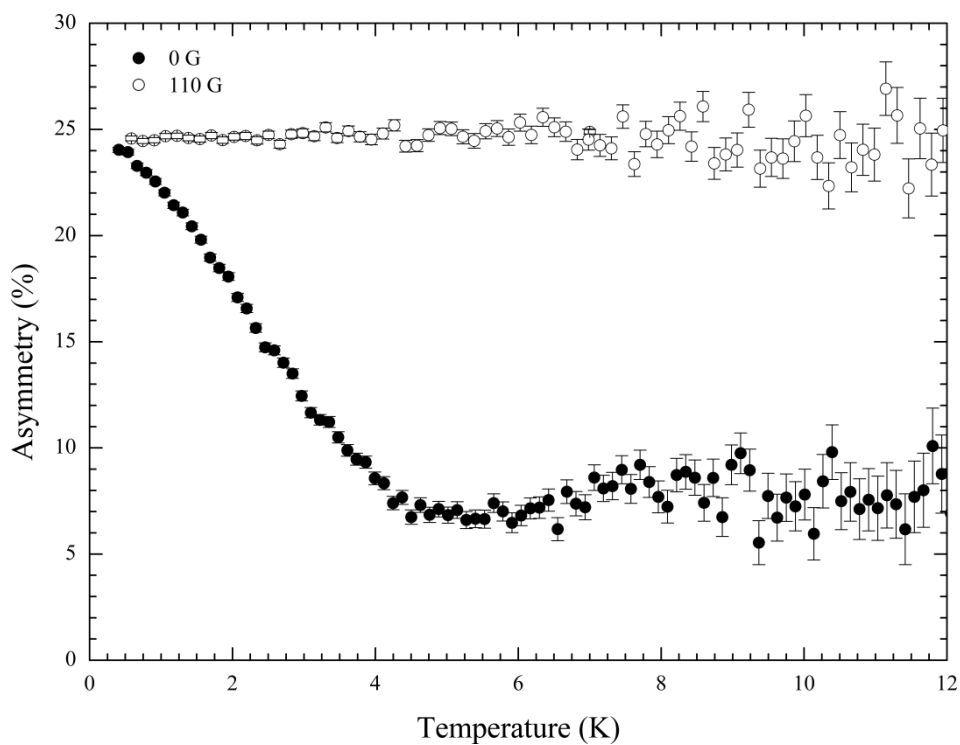


Figure 4:8 Suppression of the background nuclear dipole relaxation from the empty pressure cell *via* the application of 110 G longitudinal field.

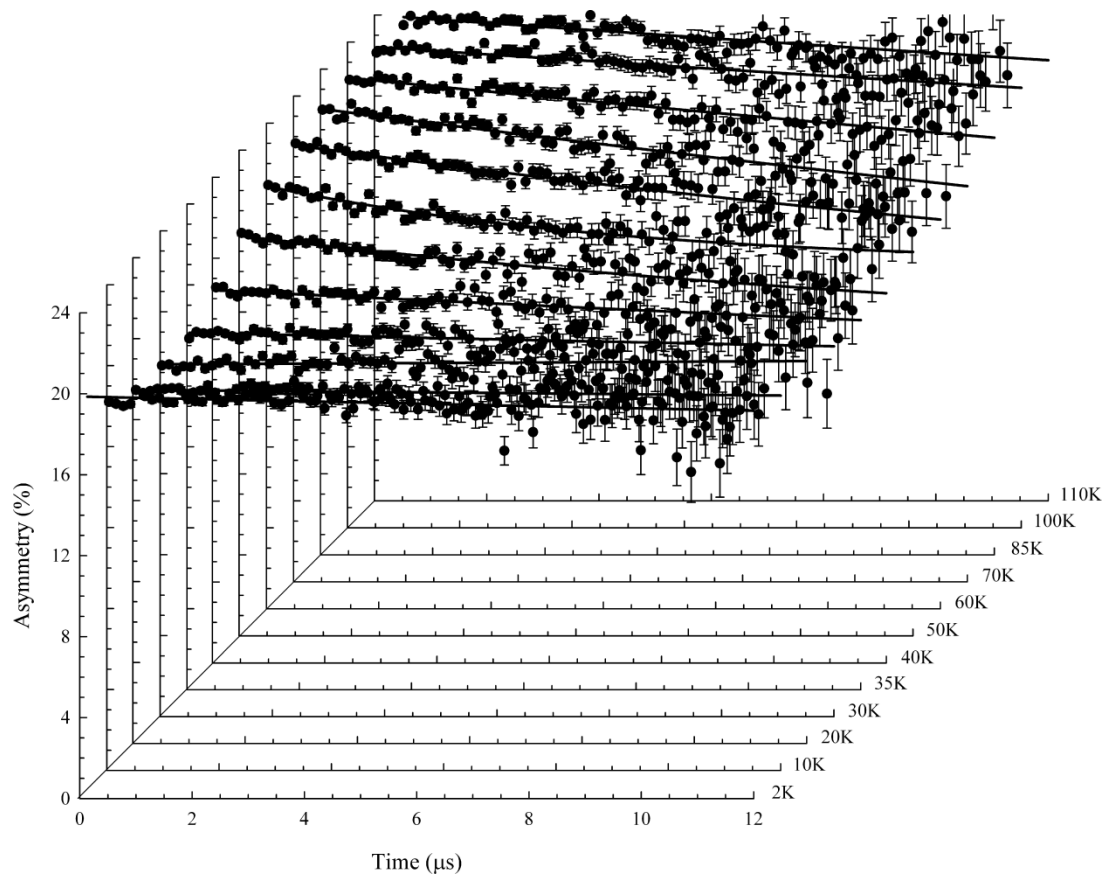


Figure 4:9 The observed muon spin relaxation spectra at 4.5kbar, with 110G longitudinal field; the solid lines represent least square fit to the data.

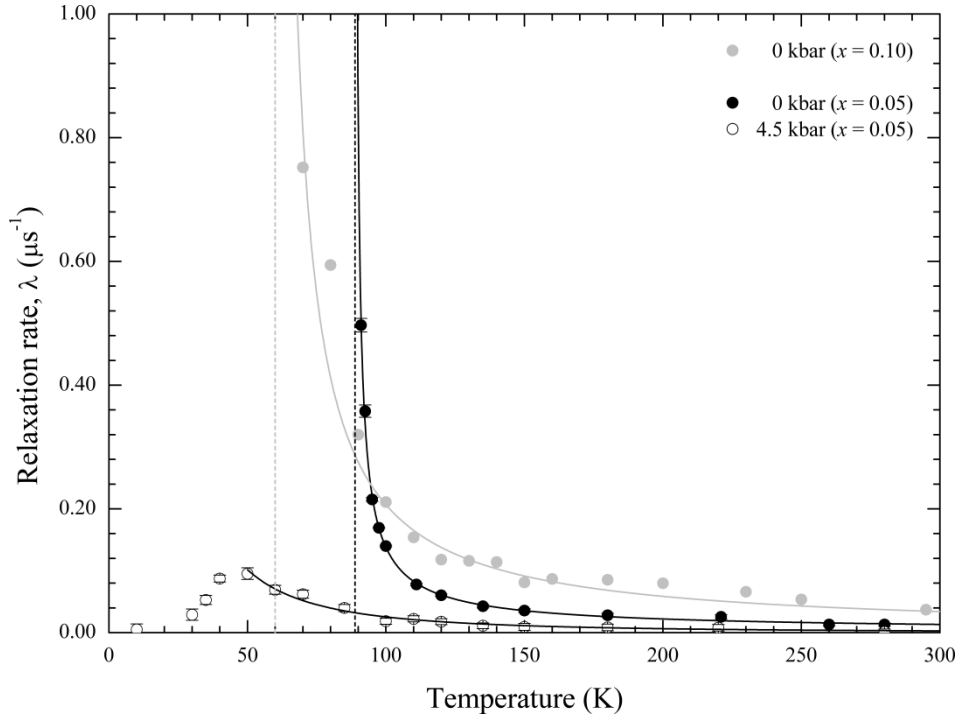


Figure 4:10 Temperature dependence of the muon spin depolarisation rate under ambient and applied pressure conditions with ($x = 0.05$). The ($x = 0.10$) data is from Cywinski¹⁷⁶, and is included for comparison. All solid lines are least square fits to equation (4:2), with vertical dashed lines indicating the position of T_g .

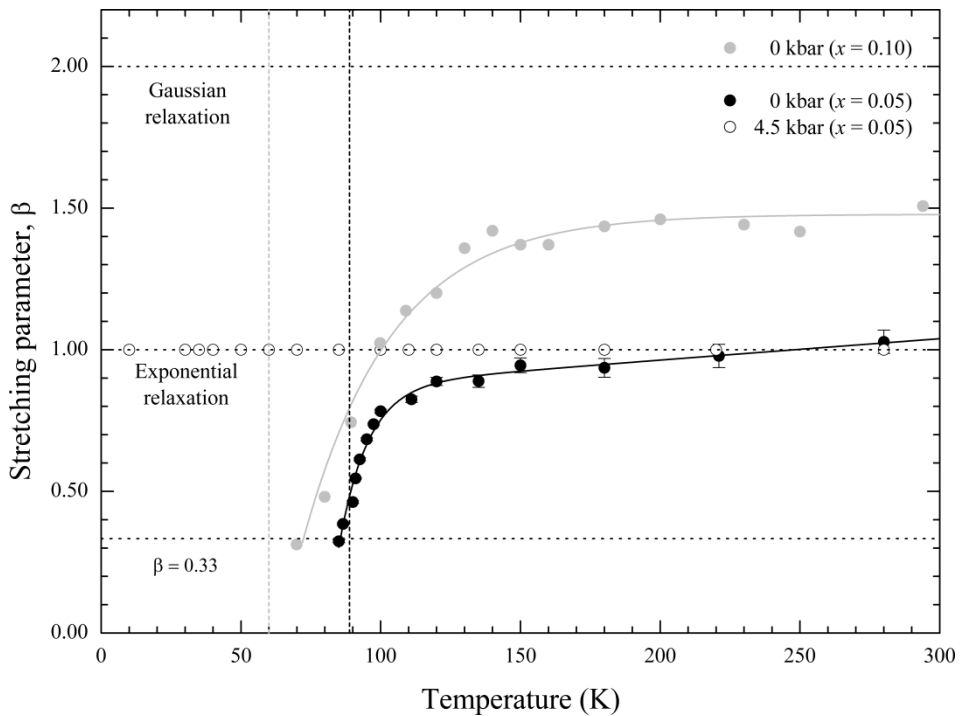


Figure 4:11 Temperature dependence of the stretching parameter (β) under ambient and applied pressure for ($x = 0.05$), with previous measurements for ($x = 0.10$) included for comparison. Solid lines are a guide to the eye.

As with the previous $\text{Y}(\text{MnAl})_2$ measurements, a small rapidly damped contribution was observed at short times, however rather than include an additional exponential alongside the dominant stretched relaxation process the results were truncated at short times, effectively removing this contribution without adversely affecting the results. Thus all fits to the data were performed over the time range ($0.5 \leq t \leq 12$) μs^{-1} using the muon data analysis program WIMDA¹⁷⁹.

Accurate subtraction of the background response associated with the pressure cell material was achieved by characterising the empty cell at each corresponding temperature. It was found that these spectra were well described by a Gaussian relaxation function. However, determining the relative sample to pressure cell signal ratio required characterisation of the sample alone. Therefore the sample was measured under ambient pressure conditions in an external longitudinal field of 110 G across several corresponding temperatures using the MuSR spectrometer. By fixing these relaxation parameters along with those of the empty cell the relative signal ratio was determined to be (1 : 3.4).

Under ambient pressure all spectra collected from the paramagnetic regime are well described using a relaxation function of the form,

$$G_z(t) = \exp(-(\lambda t)^\beta) \quad (4:3)$$

with a (β) parameter that is close to unity at first, then falls rapidly with temperature to approximately 1/3 at 85 K, as shown Figure 4:11. Such behaviour is a characteristic of many concentrated spin glass systems and is generally indicative of the muon experiencing a widening distribution of spin relaxation rates within the sample^{51, 180}.

The associated relaxation rate is seen to increase slowly as the temperature decreases from (290 – 100) K before diverging. Fitting the critical form described by equation (4:2) yields a glass transition temperature of $T_g = (88.0 \pm 0.2)$ K, which is consistent

with previous measurements, and values of $\lambda_0 = (0.026 \pm 0.001) \mu\text{s}^{-1}$ and $\gamma = (0.80 \pm 0.03)$.

In contrast, the application of 4.5 kbar external pressure not only leads to faster relaxation rates but also suppresses the aforementioned magnetic transition temperature, significantly changing the form of the muon spin relaxation function required to describe the data; $G_z(t)$ evolving from stretched to simple exponential form, consistent with the muon sensing a single relaxation rate. Interestingly, the exponent (γ) increases from 0.8 to the unusually high value of 2.0, indicating a significant change in the nature of the spin fluctuations with applied pressure.

The application of external pressure therefore appears not only to have suppressed entirely the magnetic transition, but also to have destabilised the manganese moment, leading to faster spin fluctuations, and eliminating the spin glass-like response associated with the topological and exchange frustration seen at ambient pressure.

4.4 Short-range Order in the Spin Glass Phase

It is clear that the complex underlying anti-ferromagnetic spin arrangement of the parent compound YMn_2 is increasingly perturbed as aluminium is substituted onto the manganese sub-lattice, however little is known on the character of short-range magnetic correlations in the pseudo-binary system. As mentioned, in 1986 *Motoya* performed neutron scattering measurements to compare the diffraction pattern of YMn_2 with those of $\text{Y}_{1.05}(\text{Mn}_{1-x}\text{Al}_x)_2$. This revealed the collapse of long-range magnetic order at concentrations ($x \geq 0.05$), but detailed analysis of the magnetic cross section was not performed. It could only be said that the general features up to and including ($x = 0.20$) were “essentially the same”.

To explore this further nuclear and magnetic diffuse scattering cross sections have now been measured on a range of samples concentrations: ($x = 0.03, 0.05, 0.10,$ and 0.30). The D7 spectrometer was used with an incident wavelength to 3.1 \AA , giving an optimal flux of (1.2×10^6) neutrons $\text{cm}^{-2} \text{ s}^{-1}$ covering a momentum transfer range

in the order of $(0.5 \leq Q \leq 3.7) \text{ \AA}^{-1}$. Powdered samples were packed into a cylindrical thin walled aluminium containers ($\varnothing = 5 \text{ mm}$) and mounted in a helium reservoir cryostat. The nominal beam diameter was set to 30 mm, but collimated to 25 mm slit for these experiments.

4.4.1 Introduction to Diffuse Scattering

Traditional crystallographic analysis of Bragg diffraction is built on the assumption that the crystal lattice is perfectly periodic and as such specific translational symmetry can be used to reduce every atomic position to just a small set of points on a unit cell. However strictly speaking Bragg diffraction only relays information on the average crystal structure since real materials can never truly be perfectly periodic. Even if a sample were to be totally free from so-called *occupational* disorder such as substitutional and interstitial defects, spatial *displacement* from the ideal atomic position is unavoidable due to both thermal and zero-point quantum vibrations.

Ultimately the consequence of any such disorder is a reduction in the Bragg peak intensity^{‡‡}; however this intensity is not lost but instead contributes to a portion of the total scattering cross section appearing beneath the Bragg peaks known as *diffuse scattering*. Frequently this contribution is overlooked despite the valuable information it holds on the degree of deviation away from the prevailing long-range order defined by the unit cell.

Again, there are two distinct categories of local lattice disorder which result in diffuse scattering: *occupational* and *displacement*. To study displacement defects inelastic techniques are necessary which are outside the scope of this work, however the paper by Stewart¹⁸¹ provides a useful introduction in relation to the D7 spectrometer. Static disorder on the other hand results from incomplete *occupation* of the crystal sites due to interstitial or substitutional defects, vacancies, nuclear isotope, and nuclear spin-incoherence; all of which may be studied using a general diffraction technique. If the defects were to be distributed randomly throughout the

‡‡ Crystallographic analysis corrects for this using the Debye-Waller factor.

sample the resulting diffuse scattering signal would appear isotropic and broadly featureless. The presence of correlations between neighbouring atoms however would produce smooth fluctuations in intensity across a wide range of Q -space. The same is true for disordered or mixed magnetic systems which contribute, often far more weakly, through spin correlations. Fortunately with the use of xyz -polarisation techniques these scattering types can be unambiguously separated and analysed independently.

However, interpreting these fluctuations is far from trivial. Prior to 1988 the principal method was to fit an analytic approximation of the diffuse scattering cross section using the least square method but in more recent years it has become increasingly popular to employ Reverse Monte Carlo (RMC) techniques¹⁸².

4.4.2 Nuclear Diffuse Scattering

If the atomic substitution in $Y(\text{Mn}_{1-x}\text{Al}_x)_2$ were truly random the average deviation from the mean scattering length would be distributed randomly across the sample. The diffuse scattering would simply be incoherent and equal to the square deviation from the average scattering length, as discussed in (§ 3.1.2),

$$\begin{aligned} \left(\frac{d\sigma}{d\Omega}\right)_{INC} &= \langle b^2 \rangle - \langle b \rangle^2 \\ &= xb_A^2 + (1-x)b_B^2 - (xb_A + (1-x)b_B)^2 \\ &= x(1-x)(b_A - b_B)^2 \end{aligned} \quad (4:4)$$

where (b_A) and (b_B) are, in this case, the scattering lengths of aluminium and manganese respectively, and x is the concentration of aluminium. Clearly this final expression, called the *Laue Monotonic Scattering* cross section, is directly proportional to the scattering length contrast, $(b_{Al} - b_{Mn})$ and equates to a flat isotropic background. If the occupational disorder were non-random then equation (4:4) would not hold since $[b_A b_B \neq \langle b^2 \rangle]$, and an ensemble average must therefore be taken of individual near-neighbour shells such that,

$$\langle b^2 \rangle_n = x b_A^2 + (1-x) b_B^2 - (1-x) p_A(n) (b_A - b_B)^2 \quad (4:5)$$

where $p_A(n)$ is the probability of finding an aluminium atom in the n^{th} near-neighbour shell around a central manganese atom. For a binary system, the nuclear diffuse scattering cross section, derived independently by *Cowley*¹⁸³ and *Warren*¹⁸⁴, is subsequently given by the sum over all near-neighbour shells,

$$\left(\frac{d\sigma}{d\Omega} \right)_{diffuse} = x(1-x)(b_A - b_B)^2 \sum_{n=0}^{\infty} Z_n \left(1 - \frac{p_A(n)}{x} \right) \exp(i\mathbf{Q} \cdot \mathbf{R}_n) \quad (4:6)$$

where (Z_n) is the coordination number of the n^{th} shell at the position vector (\mathbf{R}) from the central atom. The term in brackets is called the *Warren-Cowley* short range order parameter,

$$\alpha_n = \left(1 - \frac{p_A(n)}{x} \right) \quad (4:7)$$

Regarding this parameter, it must be assumed that the probability of finding an **A** atom (p_A) on the zeroth near-neighbour shell is zero, in which case ($\alpha_n = 1$); this is the first limiting value. Likewise, when a central **B** atom (manganese) is surrounded completely by a shell of like **B** atoms the result is also ($\alpha_n = 1$). On the other hand, when ($p_A = 1$) and a central **B** atom is completely surrounded by **A** atoms the opposite limit is reached, its value being ($1 - 1/x$).

If the occupation of substituent atoms were truly random the probability of finding an **A** atom would be governed by its concentration, thus the Warren-Cowley parameter would be exactly equal to zero. In this case equation (4:6) would then reduce to the *Laue Monotonic Scattering* cross section given in equation (4:4).

For the analysis of polycrystalline samples equation (4:6) must be averaged over all directions of the position vector. The result is an analytical expression for the diffuse scattering cross section,

$$\left(\frac{d\sigma}{d\Omega}\right)_{diffuse} = x(1-x)(b_A - b_B)^2 \left[1 + \sum_n \alpha_n Z_n \frac{\sin QR_n}{QR_n} \right] \quad (4:8)$$

where (R_n) is the radial distance from the origin to the surface of the n^{th} spherical shell. Figure 4:12 shows least square refinement of this equation to the normalised nuclear data measured at 10 K for the concentrations ($x = 0.05, 0.10, \text{ and } 0.30$). Figure 4:13 plots the calculated Warren-Cowley short-range order parameter associated with these fits as a function of radial distance from the central manganese atom.

A simple computer program was written in order to calculate the coordination number and radial distance up to the 32nd shell. Briefly, a ($7 \times 7 \times 7$) supercell model of the *C15* Laves phase **B** sub-lattice was generated from which basic geometric operations could be used to compute the bond lengths between a central atom and all others positions. The lattice parameter used for this calculation was determined *via* the position of the (111) nuclear Bragg peak.

In Figure 4:12 the coherent cross section has been separated *via xyz*-polarisation analysis and the nuclear Bragg peaks removed from the data leaving only a very weak diffuse scattering contribution. The number of shells used to fit the data was chosen in respects to the diffuse magnetic scattering cross section which, as will be shown in more detail later, reveals a peak centred around ($Q = 1.9 \text{ \AA}^{-1}$) with a width approximately equal to 0.5 \AA^{-1} . This value indicates short-range spin correlations are present at length scales of at least 12.6 \AA , pointing to at least 14 near-neighbour shells needed to accurately describe the data. Through trial and improvement this was increased $\sim 18 \text{ \AA}$ (32 shells); constraints were applied to the high order parameters in order to avoid unrealistic values.

Between shell numbers 1-4, the Warren-Cowley short-range order parameter was restricted to ± 0.03 , between 5-13 this was reduced to ± 0.01 and between 14-32 reduced further still to ± 0.05 .

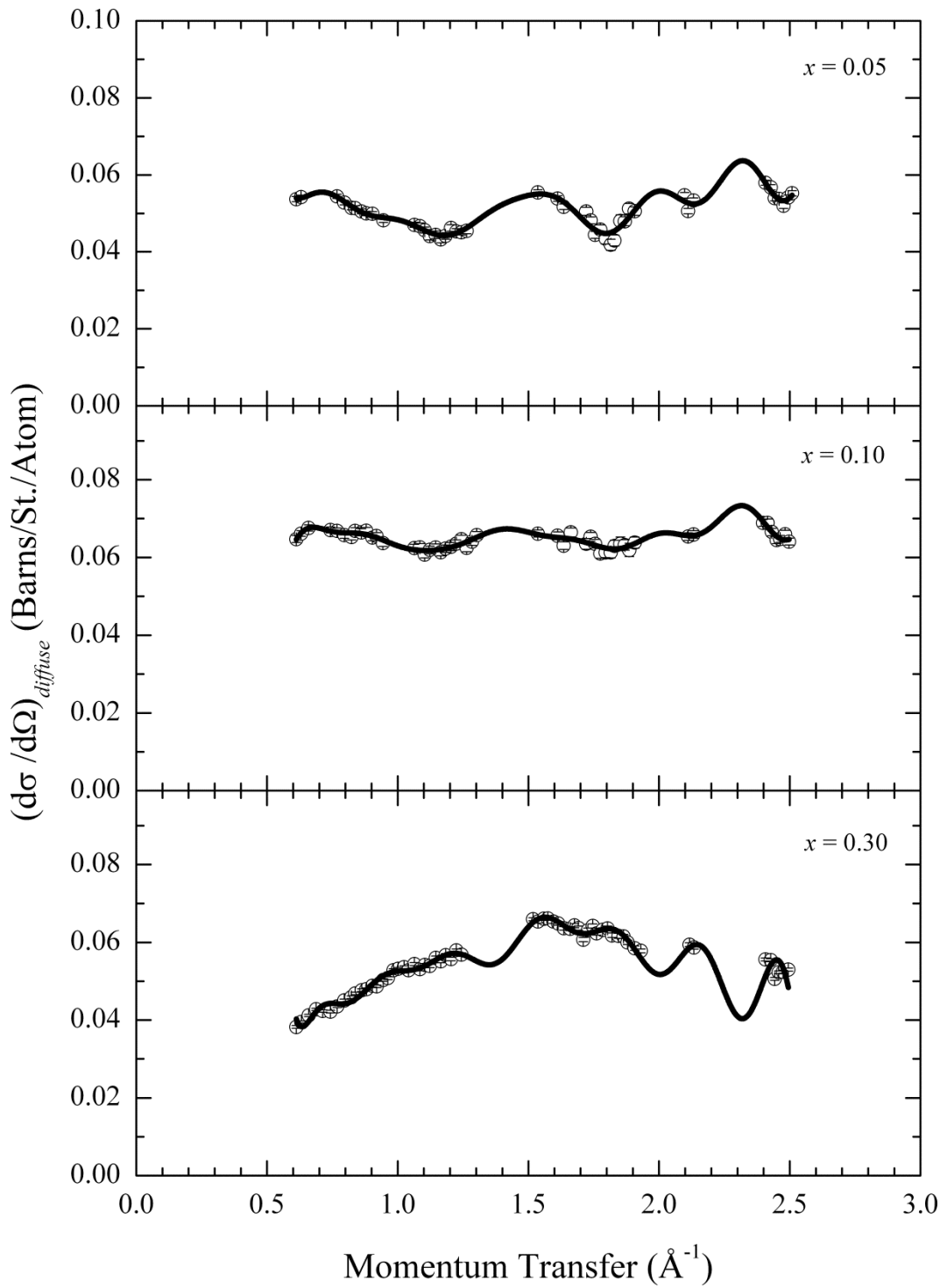


Figure 4:12 Diffuse coherent cross section taken at 10 K for $Y(Mn_{1-x}Al_x)_2$, where $x = 0.05, 0.10, \& 0.30$. Each line represents a least square fit of equation (4:8) to the data.

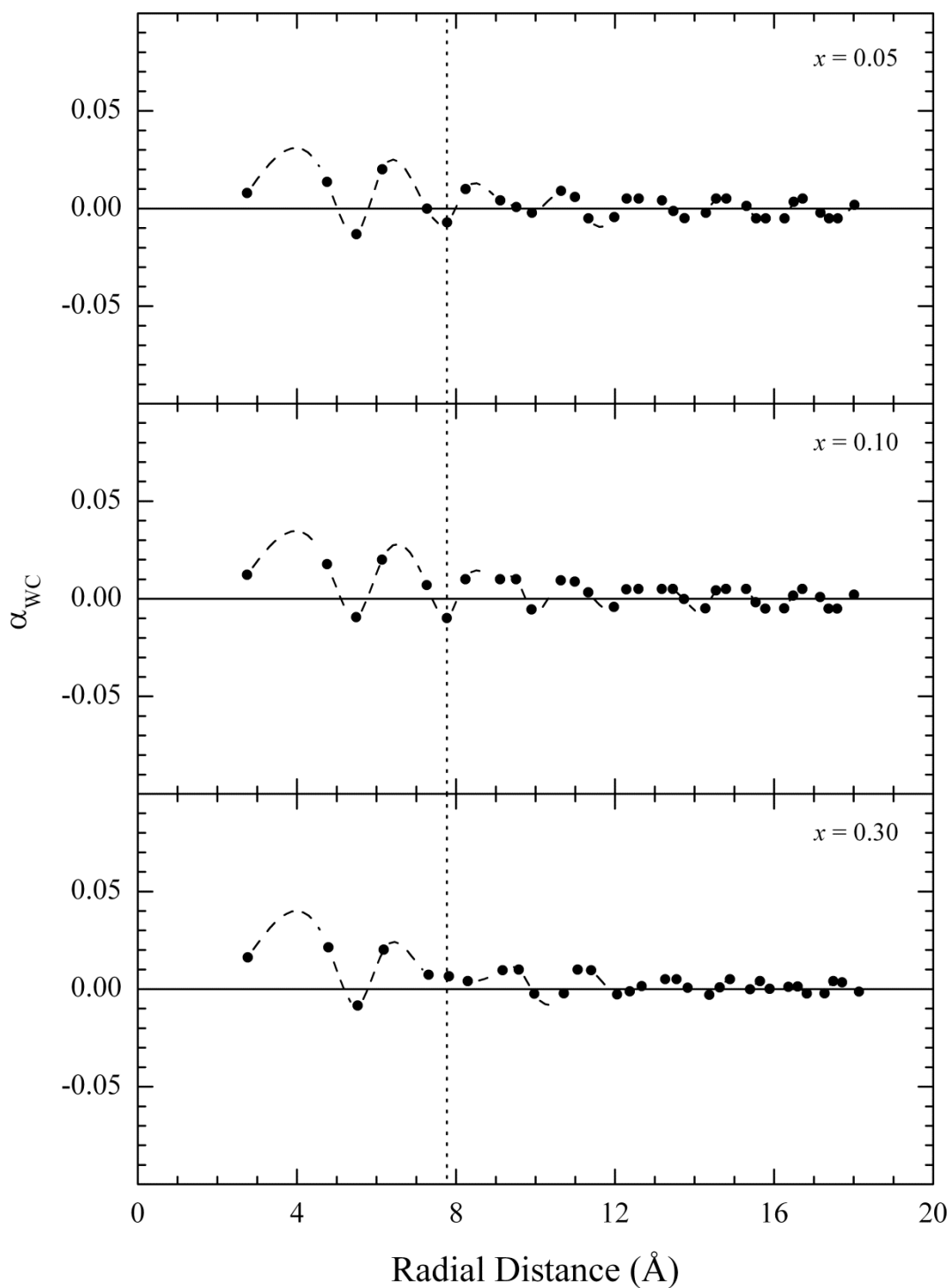


Figure 4:13 The calculated Warren-Cowley short-range order parameter for each aluminium concentration from the fits shown in Figure 4:12. The dashed lines are a guide to the eye; the dotted line indicates the first unit cell distance.

Within the first unit cell, as shown by a dotted line in Figure 4:13, the analysis indicates a greater-than-average probability of finding like atoms on the first, second, fourth, and fifth near-neighbour shell. This would suggest a slight clustering behaviour of the manganese atoms. Furthermore, it appears the aluminium atoms have a propensity to occupy the third and sixth near neighbour shells, after which the short-range order parameter oscillates about zero - suggesting random occupation at large distances. It is interesting to note that the change in diffuse scattering cross section as a function of increasing aluminium concentration appears almost entirely to be the result of occupation on the sixth, and perhaps ninth, near-neighbour shells. In all cases the Warren-Cowley short-range order parameter is seen to oscillate around zero at large distances.

A major disadvantage of this type of analysis is there being no general means of applying non-linear constraints so that the sum of probabilities (p_A) can be normalised. This is due to the least square procedure fundamentally assuming independent variables which is clearly not the case for the Warren-Cowley order parameter.

Despite their relatively subtle nature, the presence of these short-range nuclear correlations would be expected to have an appreciable effect on the magnetic properties of the system.

x_{nom}	$x(1)$	$x(2)$	$x(3)$	$x(4)$	$x(5)$	$x(6)$	$x(7)$
0.05	0.0478	0.0497	0.0497	0.0500	0.0505	0.0503	0.0498
0.10	0.0918	0.0980	0.0989	0.0998	0.0992	0.0999	0.0988
0.30	0.3088	0.2949	0.2961	0.2995	0.2982	0.2970	0.2963

Table 4:2 The calculated aluminium concentrations within the first unit cell i.e. the first seven near-neighbour shells, where x_{nom} is the nominal sample concentration

4.4.3 Magnetic Short-range Order

Figure 4:14 shows a comparison of the neutron diffraction patterns for four sample concentrations with nuclear and magnetic contributions separated. The pattern of the ($x = 0.03$) sample is nearly identical to that of the parent compound YMn_2 , and the Bragg peaks have therefore been indexed in accordance with *Motoya*¹⁷⁴. It is clear that due to increasing aluminium concentration the magnetic scattering becomes progressively more diffuse; the primary peak is centred approximately at ($Q = 1.9 \text{ \AA}^{-1}$), the same position as the (210) magnetic Bragg peak of YMn_2 . Likewise a secondary diffuse region is centred on the (110) magnetic Bragg peak.

All measurements were performed by increasing from the lowest temperature, as previously it has been shown that the (110) magnetic Bragg peak intensity displays a significant thermal hysteresis in YMn_2 ; however this could not be detected in pseudo-binary compounds at the time. Unfortunately due to the time limitations on this experiment such phenomena could not be investigated, however the temperature variation of the ($x = 0.10$) and ($x = 0.30$) patterns are shown in Figure 4:15 and Figure 4:16, respectively, and the integrated intensity between ($0.6 \leq Q \leq 3.7$) \AA^{-1} is shown in Figure 4:17, as a function of temperature.

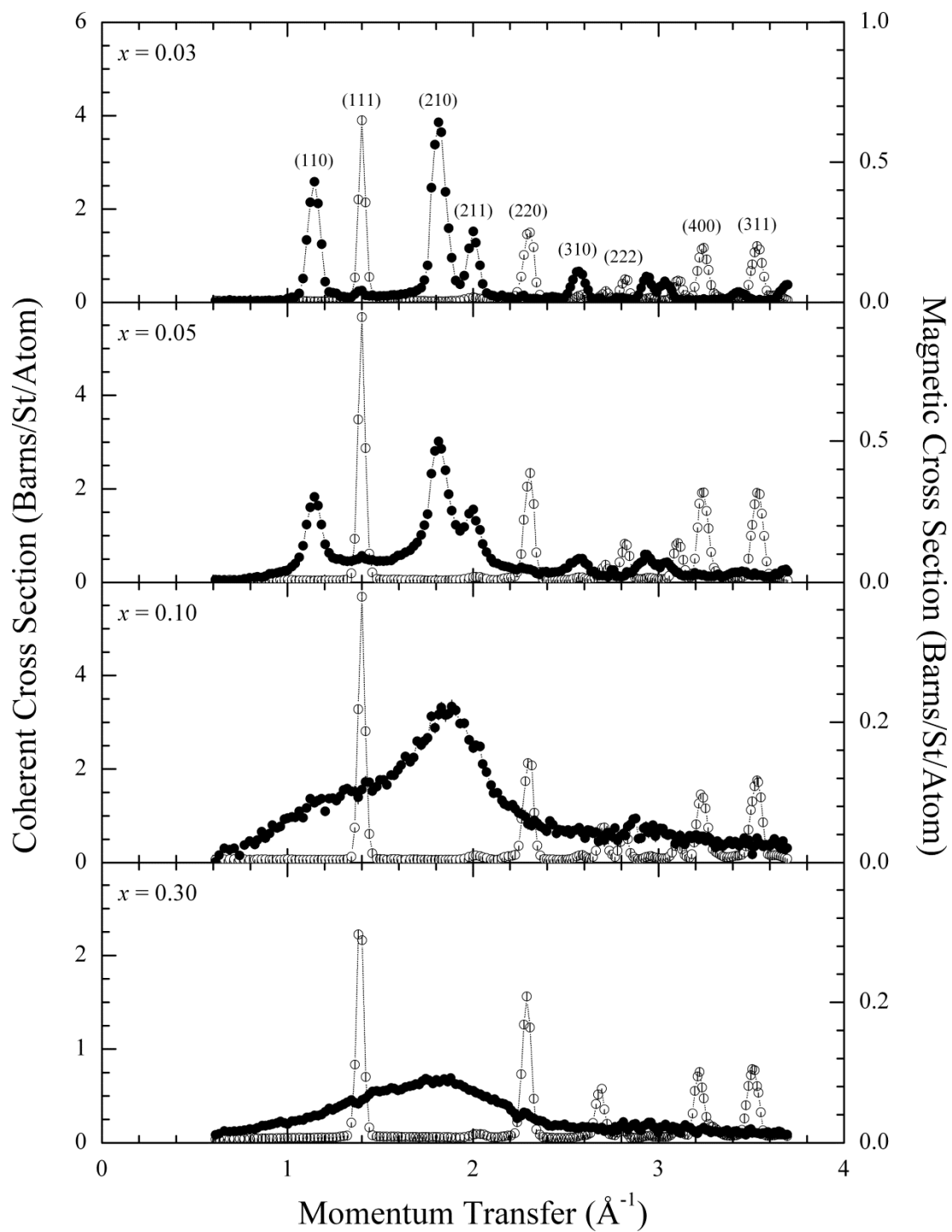


Figure 4:14 Variation in both nuclear coherent (open) and magnetic (closed) neutron scattering cross sections as a function of aluminium concentration measured at 10 K.

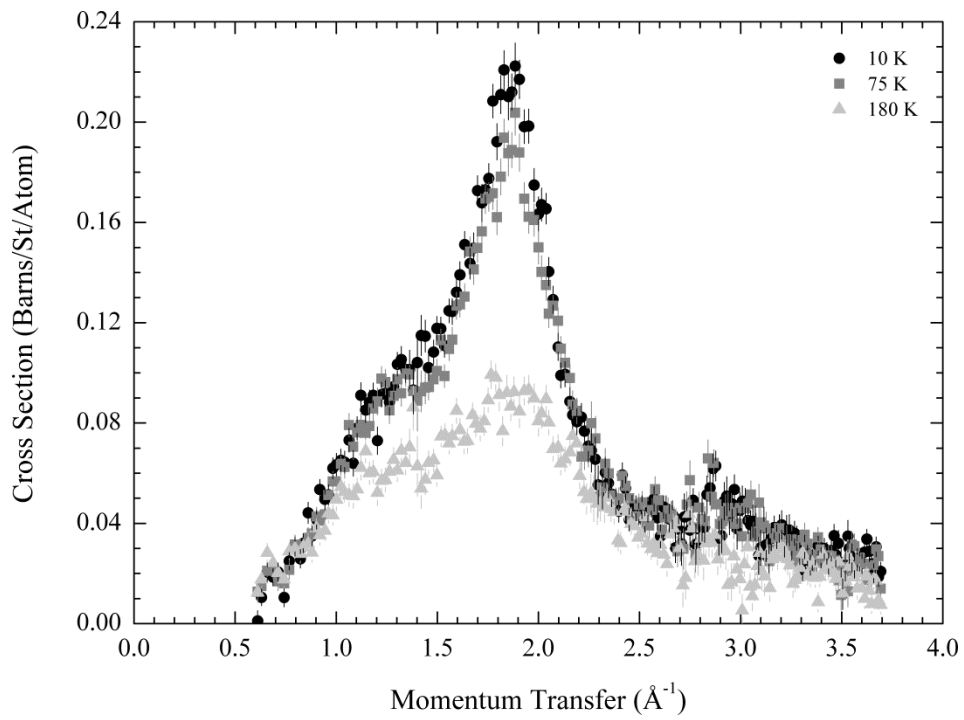


Figure 4:15 The temperature dependence of diffuse magnetic cross section for $x = 0.10$.

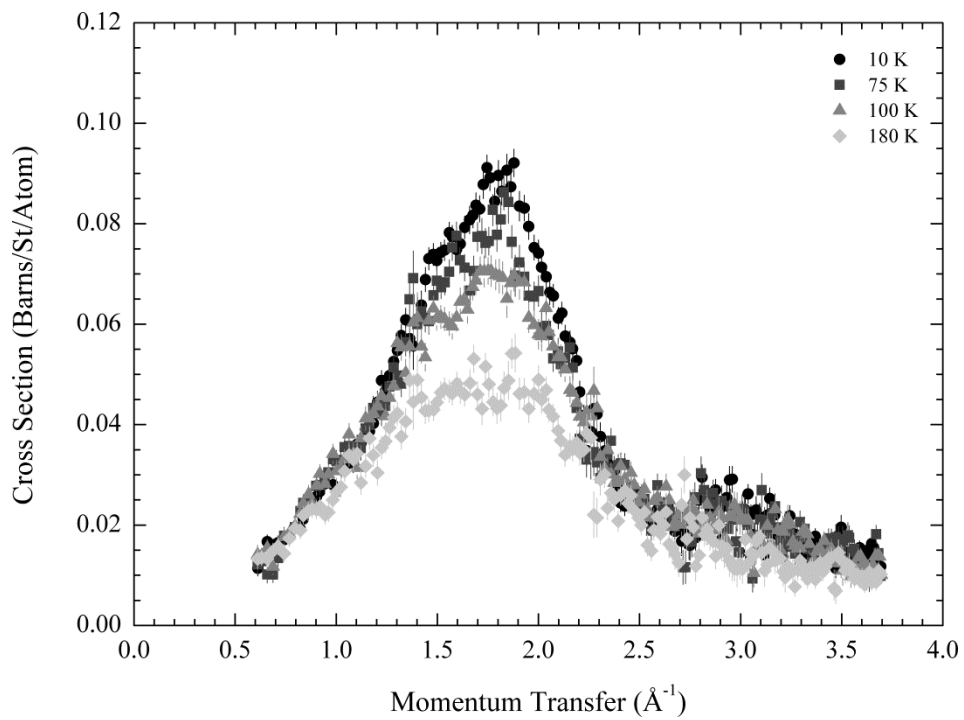


Figure 4:16 The temperature dependence of diffuse magnetic cross section for $x = 0.30$.

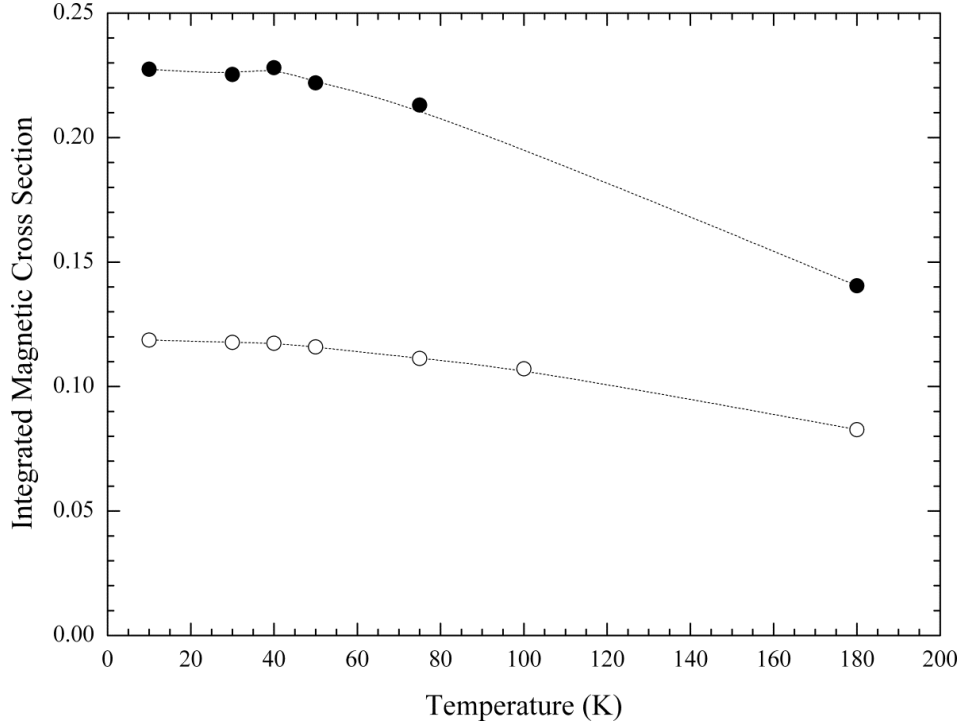


Figure 4:17 Temperature variation of the magnetic diffuse scattering intensities between $(0.6 \leq Q \leq 3.7) \text{ \AA}^{-1}$ for compounds with $(x = 0.10)$ and $(x = 0.30)$ represented by closed and open circles respectively. The intensity is seen to gradually decrease as the temperature increases.

Magnetic neutron scattering from paramagnetic or disordered spin systems is always diffuse. In a system with one magnetic species the diffuse magnetic cross section can be written,

$$\left(\frac{d\sigma}{d\Omega}\right)_{diffuse} = q^2 \left(\frac{\gamma_n r_0^2}{2}\right)^2 f^2(\mathbf{Q}) S(\mathbf{Q}) M^2(\mathbf{Q}) \quad (4:9)$$

where $M(\mathbf{Q})$ is the Fourier transform of the magnetisation density, and $S(\mathbf{Q})$ is the nuclear structure factor. For a randomly orientated magnet the magnetic interaction vector ($q = 2/3$), and,

$$M^2(\mathbf{Q}) = g_s^2 S(S+1) \sum_n \frac{\langle \mathbf{S}_0 \cdot \mathbf{S}_n \rangle}{S(S+1)} \exp(i\mathbf{Q} \cdot \mathbf{r}_n) \quad (4:10)$$

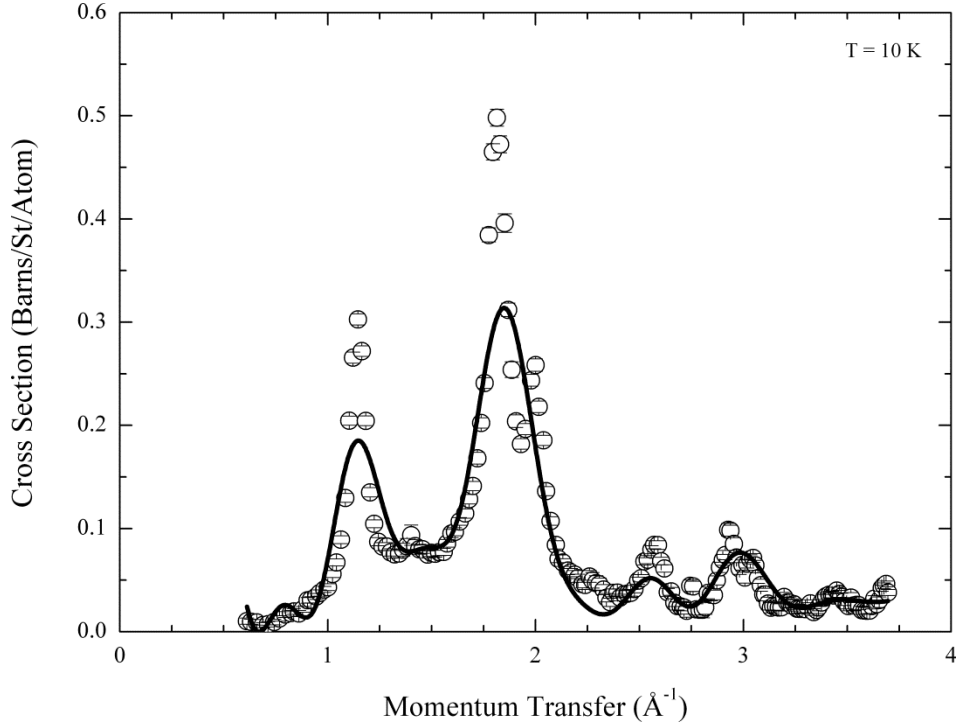


Figure 4:18 Least square fit of equation (4:11), with 32 near-neighbour shells, to sample of concentration ($x = 0.05$).

where (S_0) and (S_n) are the atomic spin vectors at the origin and the n^{th} near-neighbour shell respectively. Thus, equation (4:10) can be factorised into near-neighbour shells, and the powder average taken,

$$\left(\frac{d\sigma}{d\Omega}\right)_{diffuse} = \frac{2}{3} \left(\frac{\gamma_n r_0^2}{2}\right)^2 f^2(Q) g_s^2 S(S+1) \left[1 + \sum_n Z_n \frac{\langle S_0 \cdot S_n \rangle \sin QR_n}{S(S+1) QR_n} \right] \quad (4:11)$$

where (R_n) is the radial distance from the origin to the n^{th} shell, and (Z_n) is the coordination number associated with that shell. To arrive at this expression it is implicitly assumed that $S(Q) = 1$ so that there are no concentration driven fluctuations in the magnetic moment distribution due to nuclear short-range order.

The square magnetic form factor calculation, $f^2(Q)$, is performed using the approximation of *Lisher & Forsyth*, equation (3:30), using coefficients for Mn^{+2} , as this has previously been shown to be more suitable than either Mn^{+1} and Mn^{+3} in this pseudo-binary compound ¹⁶².

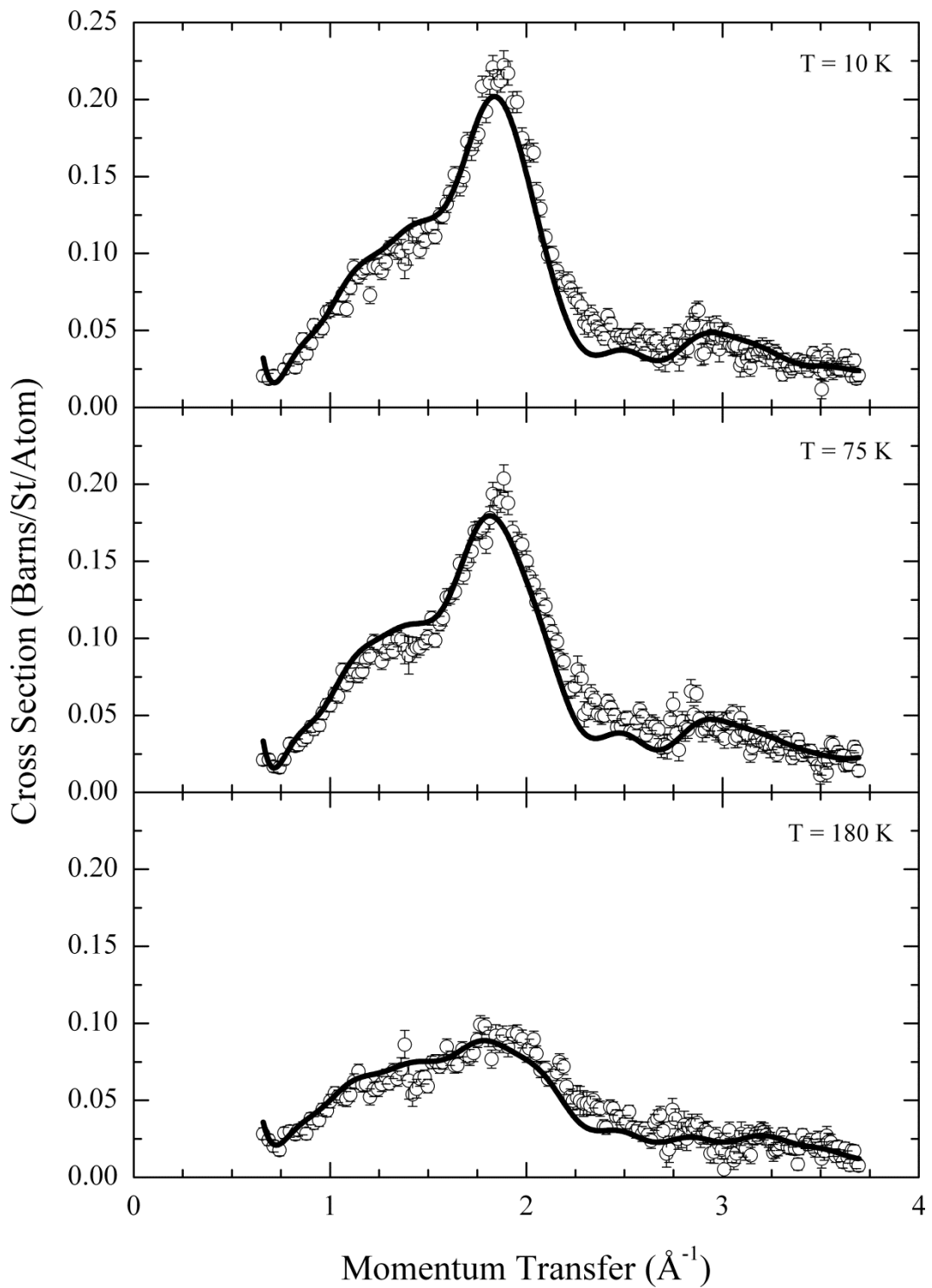


Figure 4:19 Least square fit of equation (4:11), with 32 near-neighbour shells, to sample of concentration ($x = 0.10$).

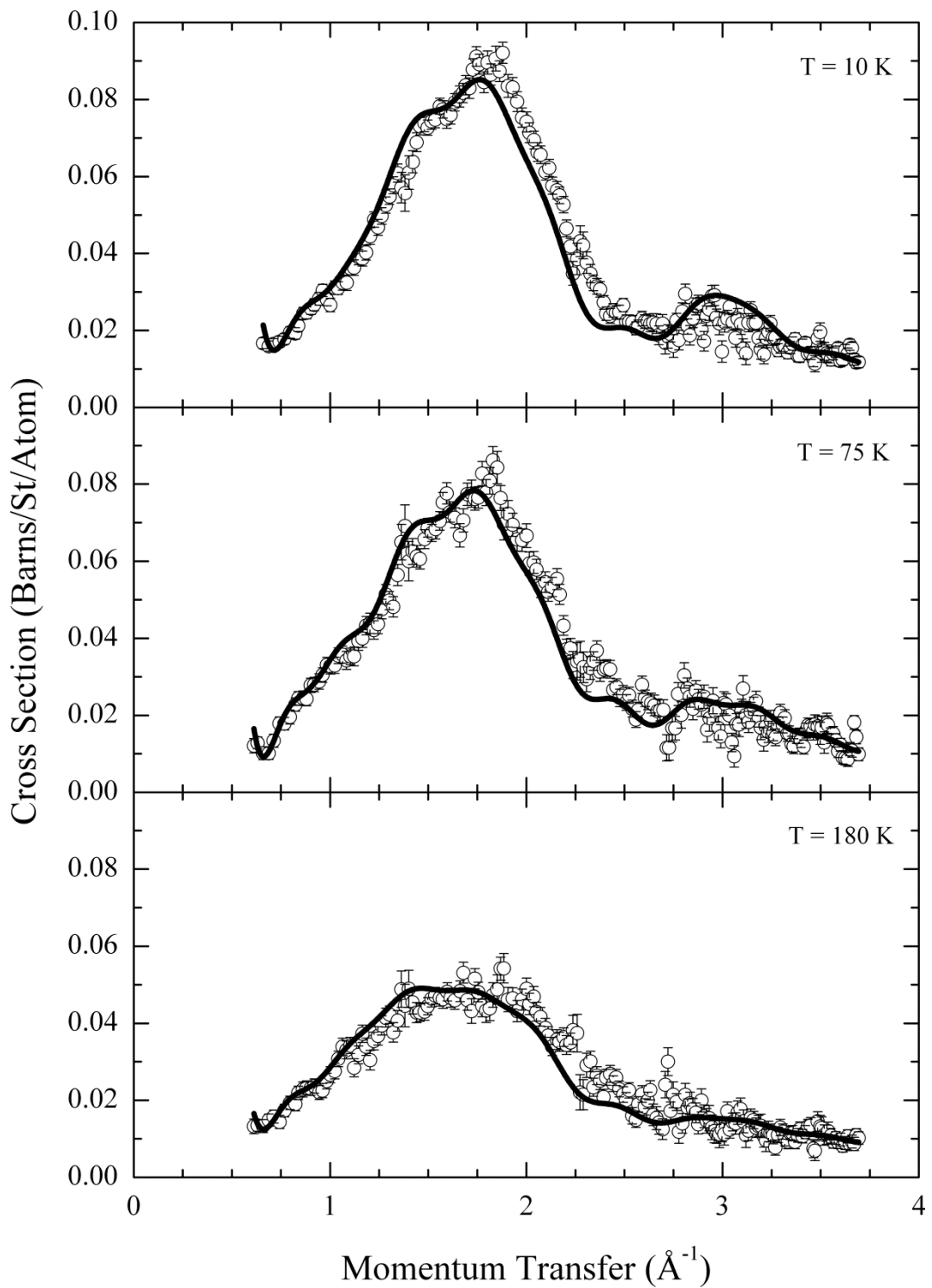


Figure 4:20 Least square fit of equation (4:11), with 32 near-neighbour shells, to sample of concentration ($x = 0.30$).

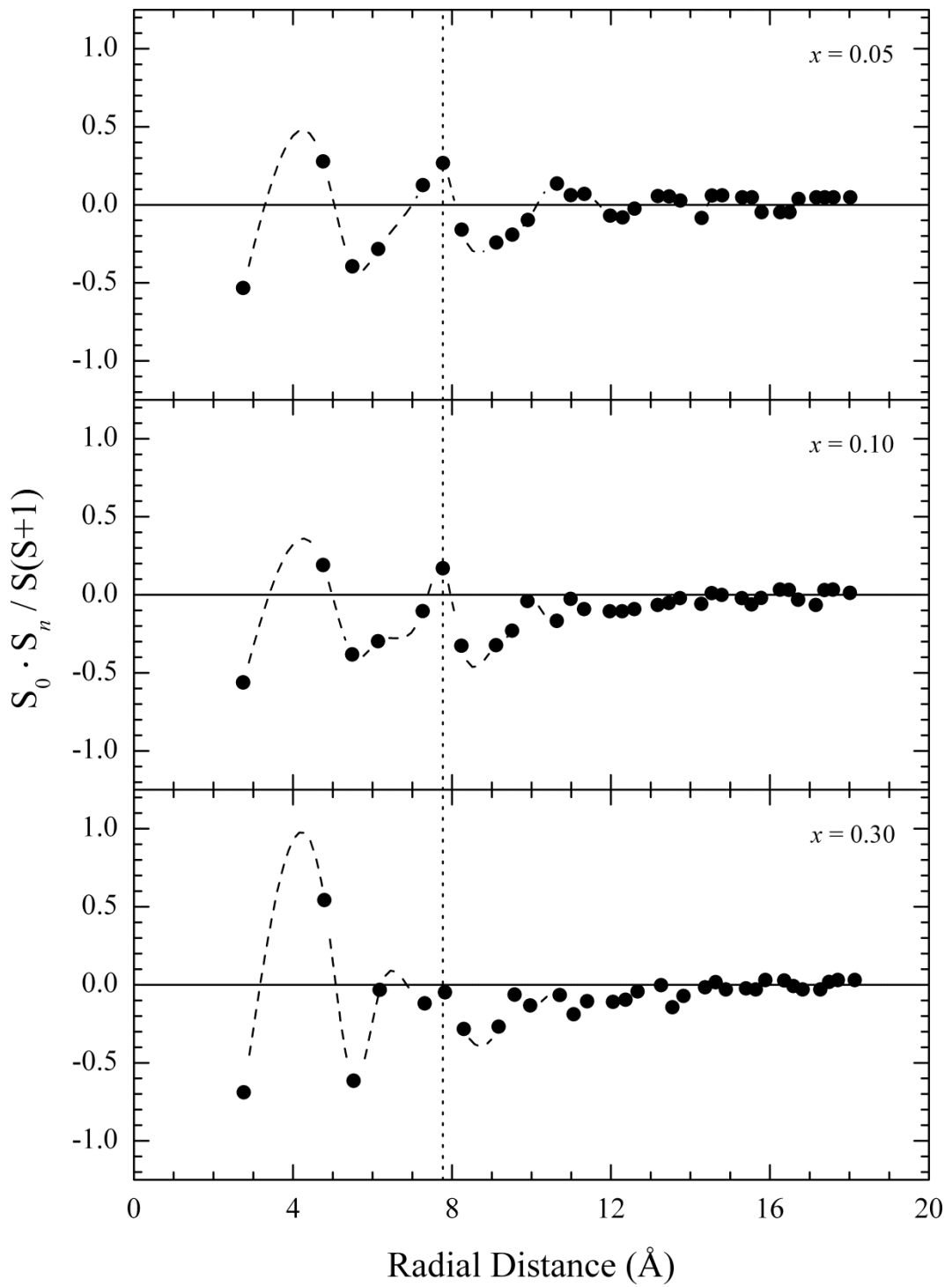


Figure 4:21 Variation of the spin-spin correlation values as a function of radial distance at 10 K.

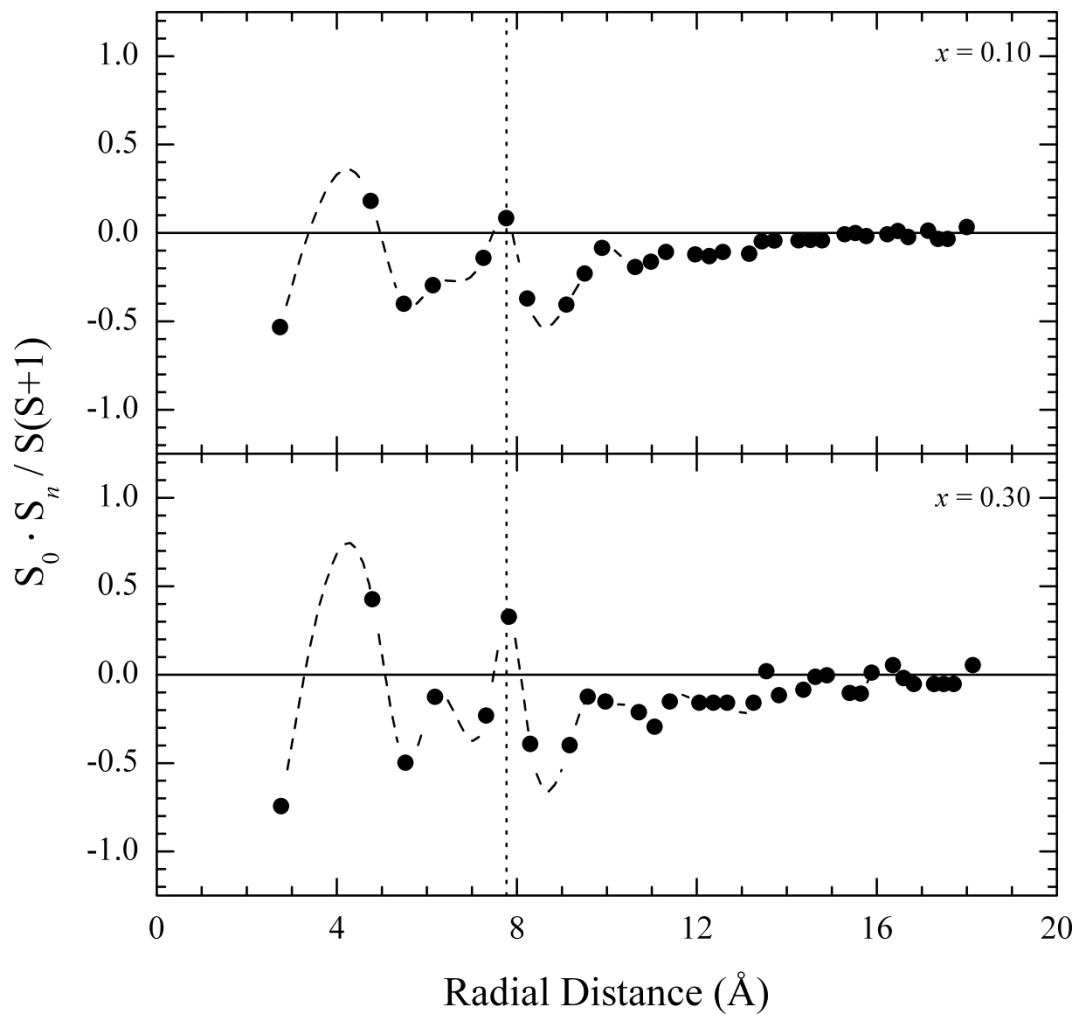


Figure 4:22 Variation of the spin-spin correlation values as a function of radial distance at 75 K.

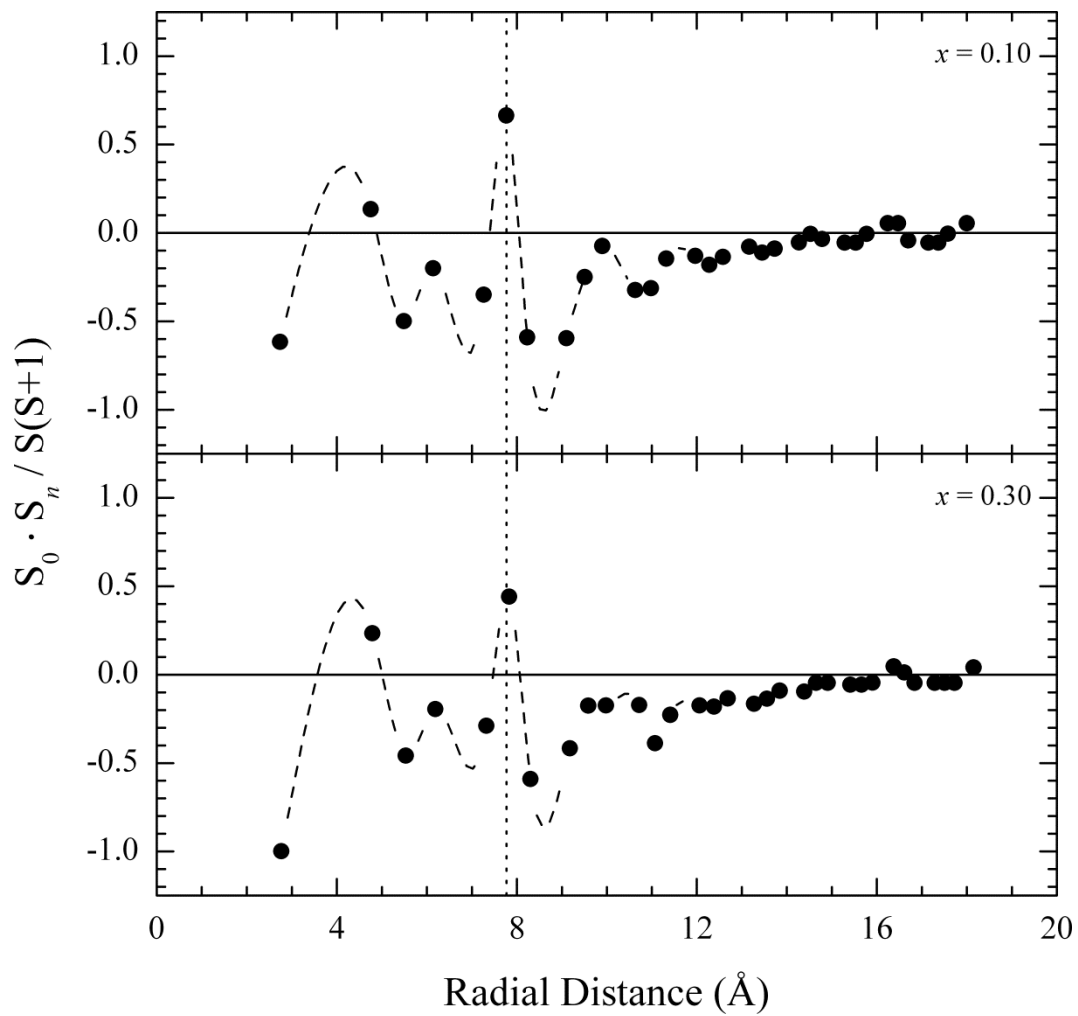


Figure 4:23 Variation of the spin-spin correlation values as a function of radial distance at 180 K.

The normalised spin-spin correlations, $[S_0 \cdot S_n / S(S+1)]$, up to ($n = 32$) have been calculated as a function of radial distance, (R), and plotted to allow comparison between concentrations at three temperatures: 10, 75, and 180 K, (unfortunately there was insufficient time to measure the ($x = 0.05$) sample at temperatures above 10 K). Inspection of the values obtained by least square fitting reveals interesting fluctuations within the distance of the first unit cell.

At all temperatures and all concentrations the first spin-spin correlation tends towards anti-ferromagnetic (*negative*) alignment; ferromagnetic (*positive*) second; anti-ferromagnetic third; and anti-ferromagnetic fourth. With ($x = 0.10$) these appear almost completely unchanged below 75 K, however a distinct shift is observed at 180 K where the fourth spin-spin correlation has a smaller negative value, suggesting atoms at this position tend towards anti-ferromagnetic alignment as the temperature is reduced. A similar observation can be made of the fifth (*negative*), sixth (*positive*), and seventh (*negative*) shells, which are again largely unchanged below 75 K but change dramatically at 180 K. For the concentration ($x = 0.30$) the first near-neighbour shell becomes more negative as the temperature is increased, and the second nearest-neighbour shell approaches zero at 180 K from an initially high positive value. The third shell remains largely unchanged with temperature. In complete contrast to the ($x = 0.10$) sample, here the fourth shell becomes gradually more negative as the temperature is increased, however a similar divergence of the fifth, sixth and seventh spin-spin correlations is observed.

At large distances only the ($x = 0.05$) sample oscillates about zero, both the ($x = 0.10$) and ($x = 0.30$) samples are predominantly anti-ferromagnetic outside the first unit cell distance, and remain so up to ($R = \sim 15 \text{ \AA}$). These calculations suggest relatively strong correlations persist to at least 180 K, however the validity of these fit parameters at this high temperature must be questioned due to the considerably weaker scattering and collapse of significant fluctuations.

Like the Warren-Cowley parameter before, these variables are obviously not independent, and what's more equation (4:11) was derived on the basis that $S(\mathbf{Q}) = 1$; however from (§ 4.4.2) it is clear that this is not the case.

4.5 NSE Measurements of $Y(\text{Mn}_{1-x}\text{Al}_x)_2$

In this section NSE measurements on $Y(\text{Mn}_{1-x}\text{Al}_x)_2$ with ($x = 0.10$) are presented, performed using the IN11 spectrometer at the Institut Laue-Langevin. Since the most intense region of magnetic scattering is flanked by the (111) and (220) nuclear Bragg peaks it was decided that, despite being less intense, the region associated with the (110) magnetic Bragg peak would be used. In this way it was hoped that possible signal contamination could be minimised. To offset the subsequent reduction in neutron count rate a wide-angle multi-detector option was employed, consisting of 41 detector elements covering a (30×1.5) degree solid angle. This however also reduces the accessible Fourier time range due to the difficulty of maintaining a perfectly homogenous field in the wider precession coil.

The neutron wavelength was selected at a mean value of 5.5 \AA , and the detector bank centred on ($Q = 1.055$) \AA^{-1} , thus covering a total momentum transfer range of ($0.781 \leq Q \leq 1.311$) \AA^{-1} . The sample was loaded into a flat thin-walled aluminium container, of dimension ($40 \times 30 \times 2$) mm, which included a cadmium mask. Calculations revealed this thickness to allow approximately 85 % transmission; hopefully reducing multiple scattering effects. Again, the sample was then mounted in a helium reservoir cryostat.

Preliminary analysis of Q -dependence was performed by dividing the multi-detector in to five sub-groups. It was found the spectra from each remained unchanged within experimental error, indicating that the spin dynamic across this range are Q -independent. Furthermore, the eight detectors closest to the (111) nuclear Bragg peak were discarded due to signal contamination, reducing the final momentum transfer range to ($0.781 \leq Q \leq 1.213$) \AA^{-1} .

This experiment began in November 2007, during which time a cryostat failure and reactor shut down greatly limited the time available to complete this investigation. A subsequent continuation proposal was accepted, and the experiment completed in early September 2009.

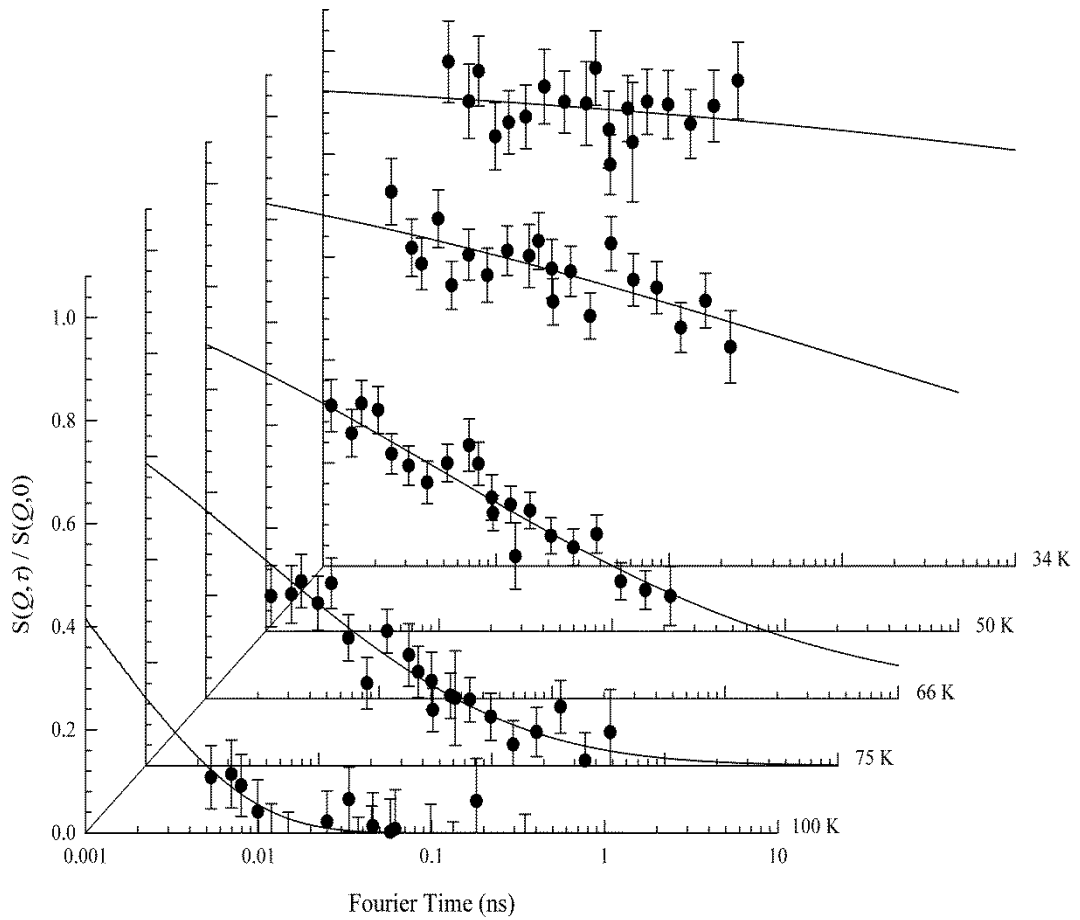


Figure 4:24 Neutron spin echo measurements revealing the temperature dependence of spin dynamics in $\text{Y}(\text{Mn}_{0.90}\text{Al}_{0.10})_2$ over the momentum transfer range $(0.781 \leq Q \leq 1.213) \text{ \AA}^{-1}$. The solid lines indicate fitting of the data to the Weron-Tsallis relaxation function.

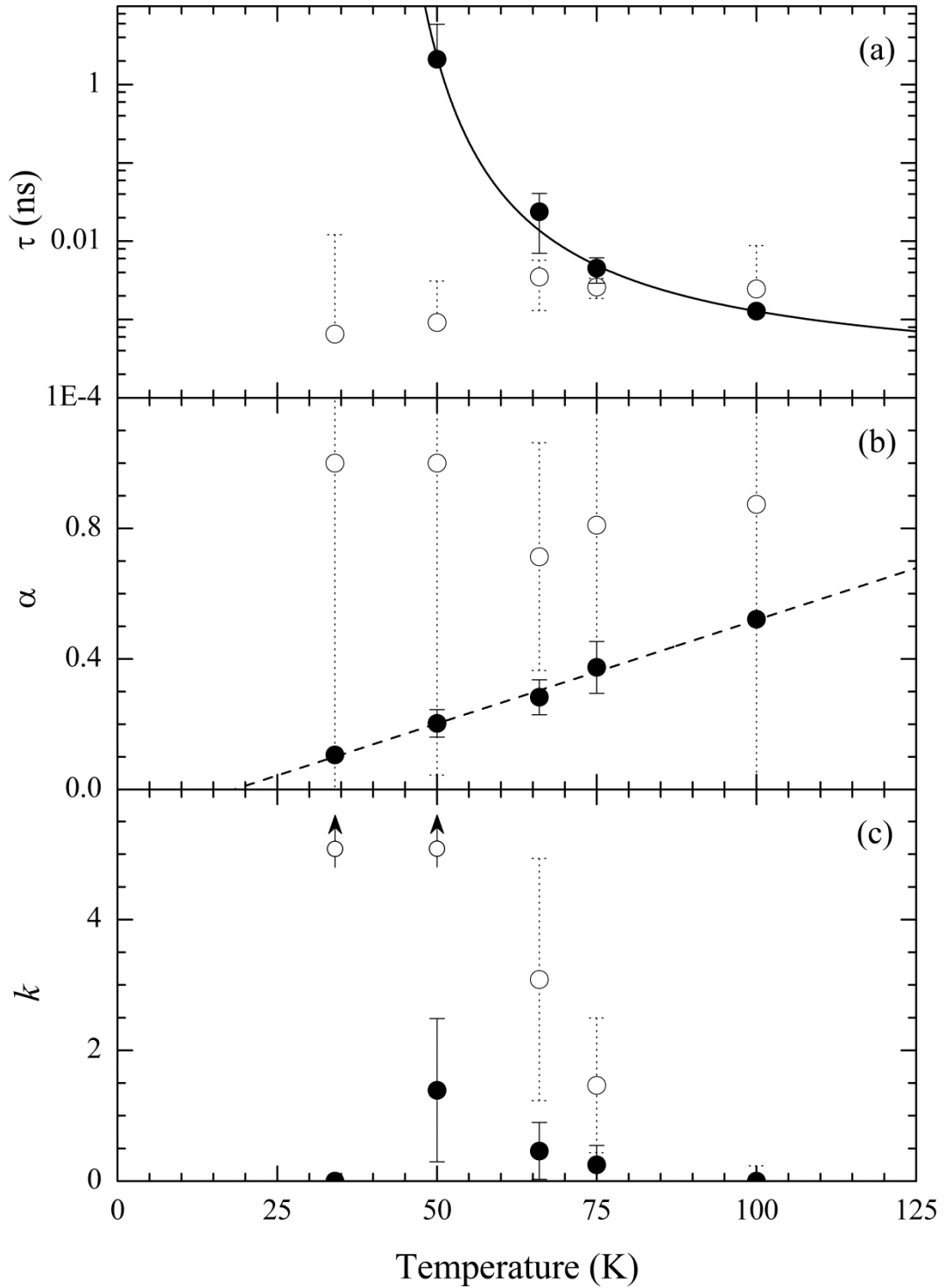


Figure 4:25 Weron parameters for the NSE spectra of $Y_{1.05}(Mn_{0.90}Al_{0.10})_2$ a) temperature dependence of τ , solid line is fit to the Vogel-Fulcher law: $\tau = (1.56 \pm 0.83) \times 10^{-4} \text{ns}$, $E_a/k_B = (134.60 \pm 42.18) \text{K}$ and $T_0 = (35.95 \pm 4.54) \text{K}$. b) fractal parameter, where dashed line is linear fit to data c) the interaction parameter, (k).

The spectra presented in Figure 4:24 have been normalised to $S(\mathbf{Q}, 0)$ measured using the sample at 1.5 K. This, it was found, gave more consistent spectra than were produced when using a dedicated resolution sample, most probably because the sample position was constant. Measurements were performed at several temperatures above and below the glass transition, $T_f \approx 50$ K, but unfortunately a series of malfunctions prevented sufficient statistical accuracy being achieved for a measurement at $T = 58$ K.

It is immediately obvious that the full dynamic range in this, like most disordered systems, covers many decades in Fourier time and the data, at best, reveals only 40 % of the total intermediate scattering function $S(\mathbf{Q}, \tau)$. Hence, initial least square fits of the Weron-Tsallis relaxation function produced inconsistent temperature variation in the fitting parameters, open circles in Figure 4:25, which over emphasised the flatness at low temperatures. Such a result would imply significant relaxation occurring at very short times, $\tau \ll 10^{-15}$ s, which is almost certainly unphysical given the Q -range being studied. Moreover, the data recorded at higher temperatures suggests the system is almost entirely static on this time scale.

For these reasons an artificial data point was added in each spectra at $\tau = 10^{-16}$ s where $S(\mathbf{Q}, \tau) = 0.97$ with an error of ± 0.06 . This point acted to pin the start of the relaxation function at short times, the results of which are shown by closed circles in Figure 4:25. In this way a dramatic change occurs in the values taken by the Weron parameters, which can be seen to follow a more consistent temperature dependent behaviour.

4.5.1 Evaluating the Weron Parameters

At the highest temperatures there is clearly a well defined shape to the spectra, visible despite being largely outside the time window of IN11. Approaching T_f the plots become progressively flatter, particularly evident at 50 K and 34 K, which suggests an extremely wide distribution of relaxation rates.

Furthermore, the relaxation rate (τ) can be seen to diverge approaching the transition temperature, but this divergence did not follow Arrhenius form,

$$\tau = \tau_0 \exp \left[\frac{E_\alpha}{k_B T} \right] \quad (4:12)$$

where (E_α) and (τ_0) are independent fitting parameters characterising the rate of a reaction, and the activation energy (E_α) represents the minimum thermal energy required for the reaction to proceed. The reaction itself being governed by a frequency defined by the characteristic relaxation rate, [$f_0 = 1 / \tau_0$].

Briefly, the Arrhenius Law is often successfully applied to systems of independently relaxing particles, but is usually unable to describe the cooperative motion which sets in during the cooling of glassy systems. Such non-Arrhenius relaxation processes are modelled *via* the empirical Vogel-Fulcher Law^{185, 186},

$$\tau = \tau_0 \exp \left[\frac{E_\alpha}{k_B (T - T_0)} \right] \quad (4:13)$$

with the ideal glass temperature (T_0), defined by the divergence of (τ), being a measure of the *fragility* of the system, and characterising the rate at which the dynamics slow as the glass transition is approached. A *strong* glass is one which approaches Arrhenius-like temperature dependence, ($T_0 \rightarrow 0$), whereas a system that slows over a narrower temperature range is referred to as a *fragile* glass former. For spin glasses systems it has been suggested this parameter measures the interaction strength (dipole, exchange or other) between clusters¹⁸⁷. With ($T_K = E_A / k_B$) two regimes of weak and strong coupling are defined such that weak coupling exists for ($T_0 \ll T_K$) and strong for ($T_0 \gg T_K$)¹⁸⁸.

Fitting the Vogel-Fulcher equation to the relaxation rates calculated by analysis using the Weron-Tsallis relaxation function reveals $\tau_0 = (1.56 \pm 0.83) \times 10^{-4}$ ns, $T_K = (134.60 \pm 42.18)$ K and $T_0 = (35.95 \pm 4.54)$ K, indicating that the spin glass phase of $Y(\text{Mn}_{0.90}\text{Al}_{0.10})_2$ has an intermediate value ($T_0 / T_K = 0.27$) within the weak regime. This result is consistent with many other spin glass systems.

With regards the Weron relaxation function, in the limit ($k \rightarrow 0$) the (α) parameter is equivalent to stretching parameter (β) of the Kohlrausch formula, the temperature

dependence of which has been previously discussed in the context of spin glasses. Starting at 0.55 at high temperature, (α) is seen to decrease gradually, approaching 0.20 at the freezing temperature. It is interesting to note that (α) follows a strict linear temperature dependence. Extrapolating to low temperatures reveals $\alpha = 0$ is reached at approximately 20 K.

The Weron interaction parameter, which indicates the level of hierarchical constraint imposed on the system as the energy landscape evolves during the freezing process, increases as the transition temperature is approached. At the lowest temperature measured, significantly lower than the transition, the interaction parameter falls to zero. However due to the divergence in relaxation rate, and the subsequent difficulty in determining its value, we cannot be confident that this result is real or due to interdependence between (τ) and (k) . The temperature dependence of the interaction parameter will be discussed in more detail in final chapter.

4.6 Spin Dynamics in the Concentrated Spin Glass $Y(\text{Al}_{1-x}\text{Fe}_x)_2$

All known binary intermetallic compounds of type Re-Al_2 or Re-Fe_2 adopt the cubic *C15* structure, regardless of the Rare earth element involved. YFe_2 is believed to be an itinerant electron ferromagnet with a Curie temperature of 554 K. YAl_2 on the other hand has temperature independent susceptibility, and is thought to be Pauli paramagnetic¹⁸⁹. Unlike $\text{Y}(\text{Mn}_{1-x}\text{Al}_x)_2$, several pseudo-binary systems of the type $\text{R}(\text{Al}_{1-x}\text{Fe}_x)_2$ crystallise in the hexagonal *C14* polytype at intermediate stoichiometry. Indeed, *Dwight et al.*¹⁹⁰, and later *Muraoka et al.*¹⁹¹, revealed this to be true of $\text{Y}(\text{Al}_{1-x}\text{Fe}_x)_2$ throughout the concentration range ($0.45 < x < 0.60$).

For this reason two compounds of nominal concentration ($x = 0.25$, and 0.65), both cubic *C15* Laves phase structures, have been studied to further test the Weron-Tsallis relaxation function and scaling relationship of the interaction and non-extensivity parameter.

4.6.1 The $Y(\text{Al}_{1-x}\text{Fe}_x)_2$ System

Partial substitution of aluminium onto the iron matrix not only suppresses the size of the iron moment but also rapidly reduces the Curie temperature. At the concentration ($x = 0.78$) long-range ferromagnetic order collapses, leading to an unusually extended spin glass-like regime within the bounds ($0.1 < x < 0.78$). However, given the geometry of the B sub-lattice, this percolation threshold for long-range ferromagnetic order is unexpectedly high. For this reason the magnetic properties of $\text{Y}(\text{Al}_{1-x}\text{Fe}_x)_2$ have been the focus of much experimental and theoretical effort over the past 40 years, with numerous models proposed in an attempt to explain the anomalous magnetic phase diagram shown in Figure 4:27.

In the first instance, due to the relative electronegativities of iron and aluminium, it is very likely that electron transfer takes place. Accordingly one of the first models proposed took an itinerant electron approach in which it was assumed each aluminium atom donated three electrons to the iron *3d*-band¹⁹². Although in good agreement with the disappearance of the ordered moment, ($x \approx 0.70$), this mechanism alone could not account for the rate at which the moment is collapses.

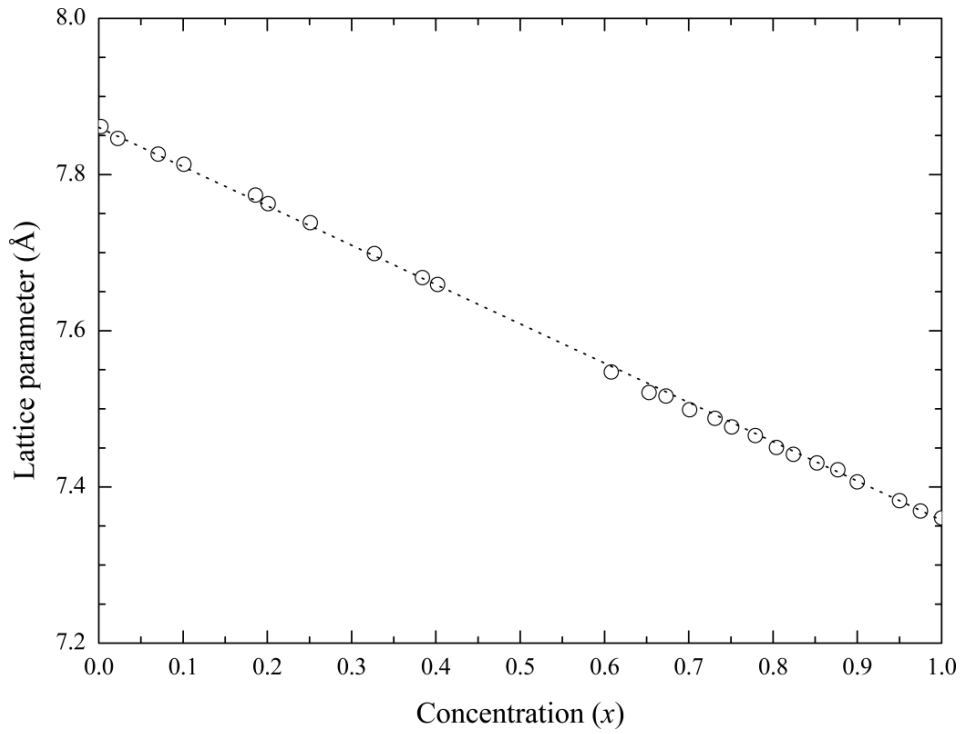


Figure 4:26 Linear concentration dependence of the lattice parameter in the C15 cubic phase of $Y(Al_{1-x}Fe_x)_2$; data taken from *Besnus*¹⁹³.

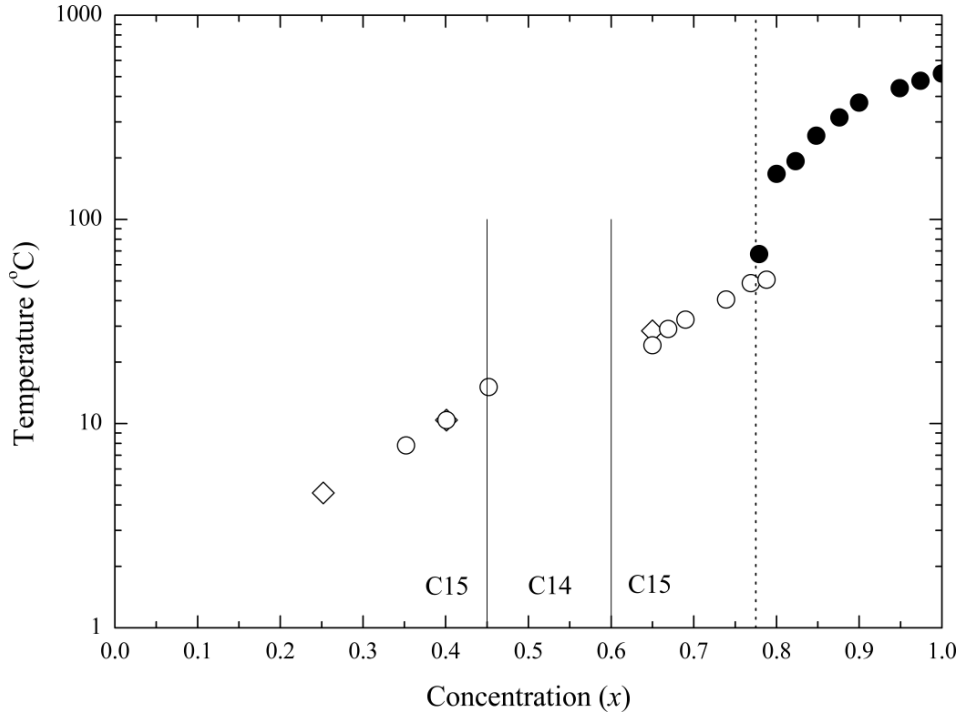


Figure 4:27 The magnetic phase diagram of $Y(Al_{1-x}Fe_x)_2$ where T_g (white circles) and T_c (black circles) were determined *via* DC magnetisation and Mössbauer spectroscopy¹⁹⁴. T_g (diamonds) were determined *via* μ SR¹⁹⁵.

It was suggested that the local atomic environment could also be crucial to determining the magnitude of the iron moment ¹⁹⁶, thus *Besnus et al.* constructed a simple model in which the iron atoms were non-magnetic unless surrounded by a critical number of like atoms in the first and second near-neighbour shells. The key assumption being above this critical number the moment takes the same value as pure YFe₂ ^{193, 197}. Analysis of compounds between ($0.674 \leq x \leq 1$) revealed this critical number to be 15 like atoms (out of a possible 16 B-sites). Unfortunately several discrepancies arose; firstly, ⁵⁷Fe isomer shift revealed the iron site charge density in the iron-rich regime was largely unaffected by the local atomic environment; and secondly, it was demonstrated that the iron atom always carries a magnetic moment even when completely surrounded by aluminium. It was clear that neither of these mechanisms, nor indeed so-called hybrid versions, could account for the collapse of ferromagnetism ¹⁹⁸⁻²⁰⁰, and at this time the magnetic properties of this system are still not fully understood.

More recently the low temperature spin glass state was investigated using Zero-field Muon Spin Relaxation by *Telling et al.* ¹⁹⁵. All spectra collected from three concentrations, ($x = 0.25, 0.40$ and 0.65), were well described by a depolarisation function incorporating a Kubo-Toyabe term multiplied by a stretched exponential; the latter representing a dynamic contribution from atomic fields. The nuclear depolarisation rate was found to be temperature independent, scaling precisely with the concentration of iron. Extrapolating this relationship to ($x = 0$) revealed the muon position to be that of the so-called (2-2) site.

Briefly, at temperature well above the glass transition ($\beta \rightarrow 1$), whilst below ($T \sim 3T_f$) its value decreases, indicating a broadening distribution of relaxation rates (λ) approaching T_f . A critical divergence in (λ) was used to determine the transition temperature of each compound, included in Figure 4:27. Interestingly, below the transition the initial asymmetry falls well below the expected value (1/3 that observed at high temperatures), suggesting spin fluctuations well into the spin glass state.

To explore if the delay in the onset of ferromagnetism was a consequence of topological frustration due to anti-ferromagnetic correlations between spins on the tetragonal B sub-lattice, diffuse neutron scattering measurements were made by *Preston et al.*, again on concentrations ($x = 0.25$ and 0.65)²⁰¹, with the cross sections being analysed using the Reverse Monte Carlo methods.

The calculated Warren-Cowley order parameters indicated a slight anti-clustering of iron atoms in the first and second near-neighbour shells, beyond which ($\alpha_i = 0$). Applying this configuration to the magnetic cross section gave clear evidence that at radial distances ($R \leq 5 \text{ \AA}$) spin correlations were predominantly ferromagnetic for both concentrations. Furthermore these clusters show relatively little temperature dependence up to ($T = 300 \text{ K}$). At larger distances there was evidence of anti-ferromagnetic correlations however these were regarded as too weak to account for the anomalous phase diagram.

4.6.2 Sample Preparation

Polycrystalline samples were prepared by melting the appropriate proportions of spectrographically pure starting materials in an argon-arc furnace. As with $\text{Y}(\text{MnAl})_2$, the compounds were off-stoichiometric ($1.05 / 2.00$) to ensure phase purity; it is reported that this has only negligible effects on the magnetic properties of the system. Weight losses were less than 0.20 % for the iron-rich ingot, and less than 0.37 % for the aluminium-rich ingot.

Both ingots were then loosely wrapped in thin tantalum foil and sealed in quartz ampoules under a reduced ($\sim 330 \text{ mbar}$) argon atmosphere and separate heat treatments performed in accordance with the literature¹⁹². The aluminium-rich ($x = 0.25$) sample was annealed at $300 \text{ }^\circ\text{C}$ for 24 hours whilst the iron-rich ($x = 0.65$) sample was annealed at $750 \text{ }^\circ\text{C}$ for one week. After this time, both samples were immediately quenched in a mixture of water and ice. They were then roughly crushed, and a small piece removed from each for DC susceptibility measurements. The remainder was then crushed into a fine powder in an inert argon atmosphere.

4.6.3 DC Magnetisation

The following measurements were performed using a SQUID magnetometer at the Rutherford Appleton Laboratory. Small, approximately spherical, specimens were taken from the coarsely crushed ingots of each compound. A field of 1 mT was used to calibrate the instrument and centre the sample position. The temperature was first reduced to 2 K in zero field, and measurements taken upon warming at a rate of 10 K per minute in a 0.1 T field for the ($x = 0.65$) sample, and fields of 0.02 T and 0.1 T for the ($x = 0.25$) sample. Before discussing the results it is useful to first consider what has previously been reported.

In 1981 *Hilscher et al.* published a comprehensive review of the magnetic properties of this system, including magnetisation, DC and AC susceptibility measurements. Fourteen compounds were investigated with concentrations between ($0.10 \leq x \leq 0.82$), taking measurements at temperatures as low as 4 K²⁰². The results clearly show three distinct concentration dependent behaviours, broadly categorised as iron-rich, intermediate (*C14* phase), and aluminium-rich regimes. The main features of each can be summarised as follows.

Iron-rich compounds ($x \geq 0.65$) exhibit Curie-Weiss behaviour at high temperatures. The effective moment is nearly concentration independent up to ($x = 0.82$), taking an average value of $\sim 3.7 \mu_B$ per iron atom. Approaching the Curie temperature a significant upturn is observed in the temperature dependence of inverse susceptibility, moving the response away from linear Curie-Weiss behaviour. This is attributed to strong clustering effects which, as discussed, have since been verified by diffuse neutron scattering. Furthermore a distinct peak is observed at low temperatures indicating a spin glass transition.

Due to the structural transition taking place between ($0.45 \leq x \leq 0.60$) a vastly different response is observed. The temperature dependence of inverse susceptibility is significantly steeper, but still follows a Curie-Weiss law, resulting in a sudden drop of the effective moment from 3.7 to $2.4 \mu_B$ per iron atom.

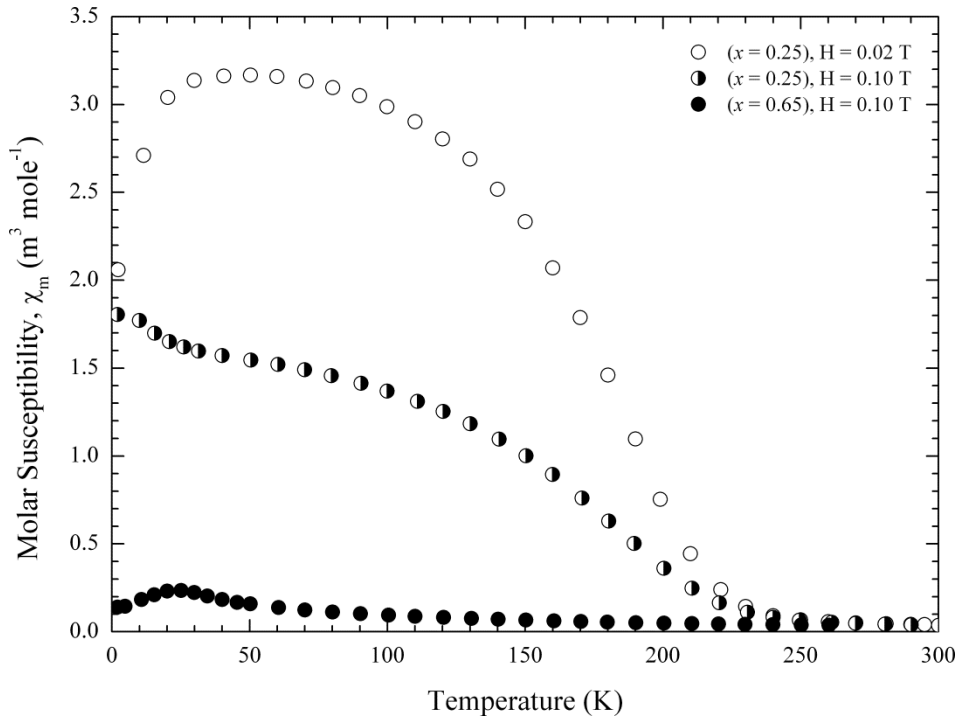


Figure 4:28 Molar magnetic susceptibility against temperature for $Y_{1.05}(Al_{1-x}Fe_x)_2$, where ($x = 0.65$) and ($x = 0.25$). Samples were cooled in zero field and measurements were taken upon warming in fields up to 0.1 T. T_f for the iron-rich sample is approximately 25K.

In the aluminium-rich regime paramagnetic Curie temperatures are observed in the temperature range (80 - 150) K, however no long-range order was detected down to 4 K. Furthermore, in the concentration range ($0.10 \leq x \leq 0.45$) the effective moment per iron atom remains largely constant, having an average value in the order of $2.3 \mu_B$ per iron atom. DC susceptibility in low fields reveals an initial steep increase followed by saturation at low temperatures. *Hilscher* proposed this to indicate the onset of short-range order below the Curie temperature.

Identical behaviour has been observed from these measurements. For ($x = 0.25$) the low field data exhibits this saturation anomaly, shown above, with the effective moment calculated from the Curie constant being identical to that of *Hilscher's* measurements, taking a value of ($\mu_{eff} = 2.05$) μ_B per iron atom. However Figure 4:29 shows that the Curie temperature is ~ 171 K, just outside the accepted range.

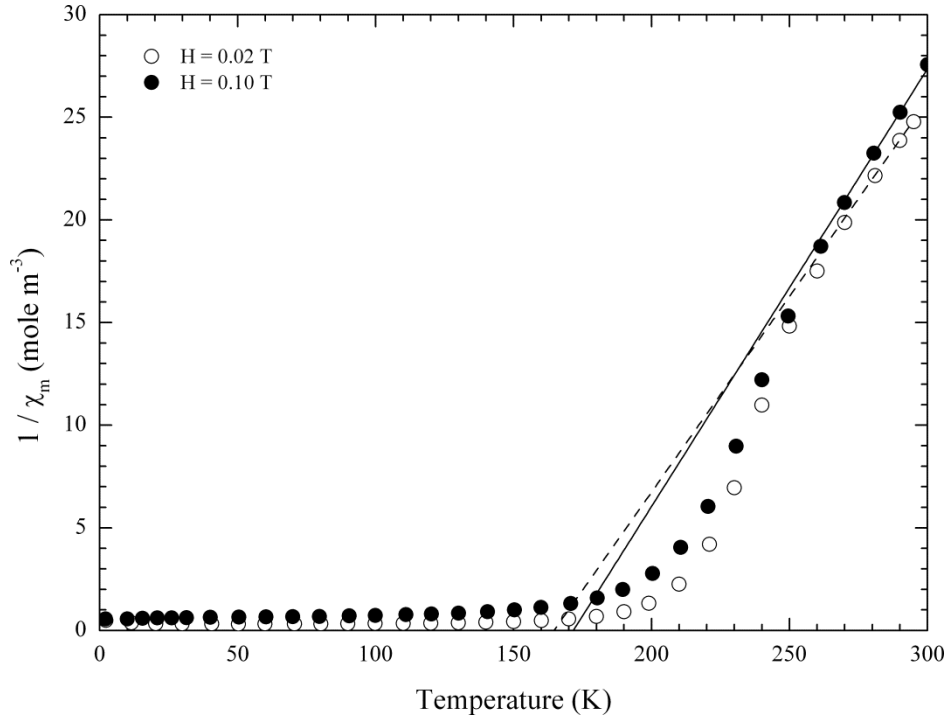


Figure 4:29 Temperature dependence of $1/\chi_m$ for the aluminium-rich ($x = 0.25$) sample fields of 0.02 and 0.10 T. The data has been binned to aid inspection. Lines indicate fits to the Curie-Weiss Law at high temperatures.

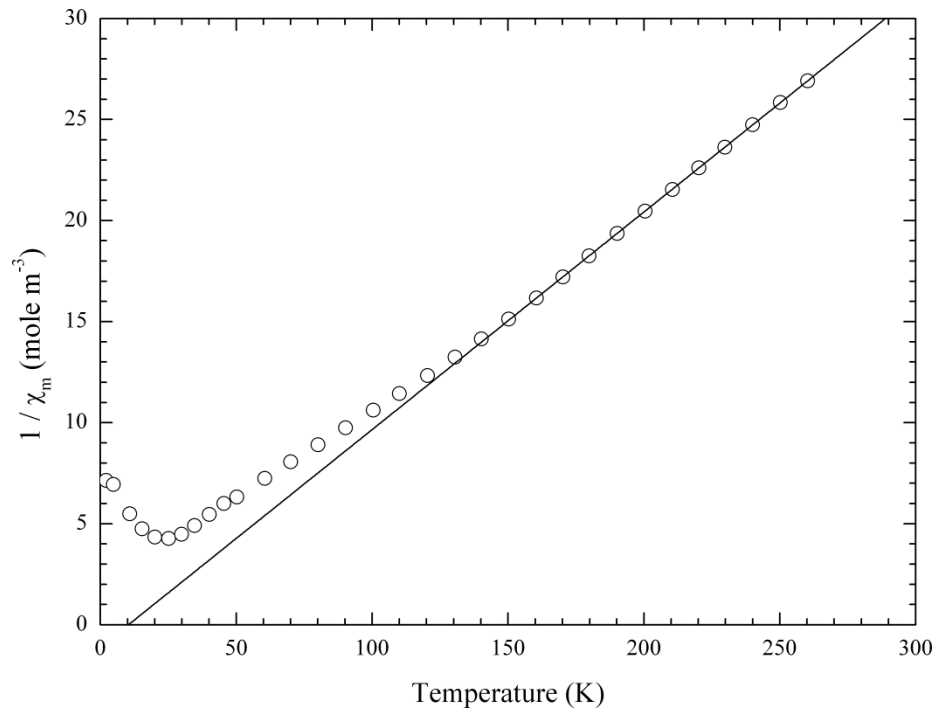


Figure 4:30 Temperature dependence of $1/\chi_m$ for the iron-rich ($x = 0.65$) sample in a 0.1 T field. Solid line indicates Curie-Weiss behaviour at high temperature. Moreover, the predicted upturn at low temperatures and freezing peak are clearly visible.

The iron-rich sample displays both the distinct upturn at low temperature, due to clustering effects, and a freezing peak indicating transition to a spin glass-like state at $T_f \approx 25$ K. However, the calculated effective moment is significantly lower than that of *Hilscher*, taking a value of $(\mu_{eff} = 2.72) \mu_B$ per iron atom compared to $(\mu_{eff} = 3.29) \mu_B$ per iron atom. Even so, this result is consistent with the rapid fall of the paramagnetic moment observed close to this concentration, *Hilscher* reporting a value of $(\mu_{eff} = 2.28) \mu_B$ per iron atom for a compound with $(x = 0.60)$.

4.6.4 Spin Dynamics in $Y_{1.05}(Al_{0.35}Fe_{0.65})_2$

Using IN11 the spin relaxation dynamics have been studied over the momentum transfer range $(0.2 < Q < 0.7) \text{ \AA}^{-1}$ between 1.5 K and 40 K. The lowest temperature was used to normalise the correlation function. The same multi-detector setup was used as for the previous experiment, with an incident neutron wavelength $\lambda = 5.5 \text{ \AA}$, coinciding with the optimum flux. The measurements were performed on powdered sample loaded into a flat 3 mm deep aluminium container; calculations had revealed this to allow ~ 90 % beam transmission.

The detectors were again divided in to five sub-groups for the sample's Q -dependence to be examined. It was found that the spectra were indistinguishable within experimental error, and the dynamics across this range are therefore regarded as Q -independent. Five measurements were then performed above and just below the glass transition temperature, which have been presented in Figure 4:31. Again, the solid lines represent least square fits of the data using the Weron-Tsallis relaxation function. The results, shown in Figure 4:32, display characteristics very similar to those of the previous study on $Y(Mn_{1-x}Al_x)_2$, Figure 4:25. Once again the open circles represent fits to the data without an artificial "pinning" data point at short times.

At the highest temperature measured ($T = 40$ K) much of the dynamics occur outside the time window accessible by IN11. Gradually these dynamics slow as the transition is approached, the spectra become visibly flatter which, as before, indicates a broadening distribution of relaxation rates.

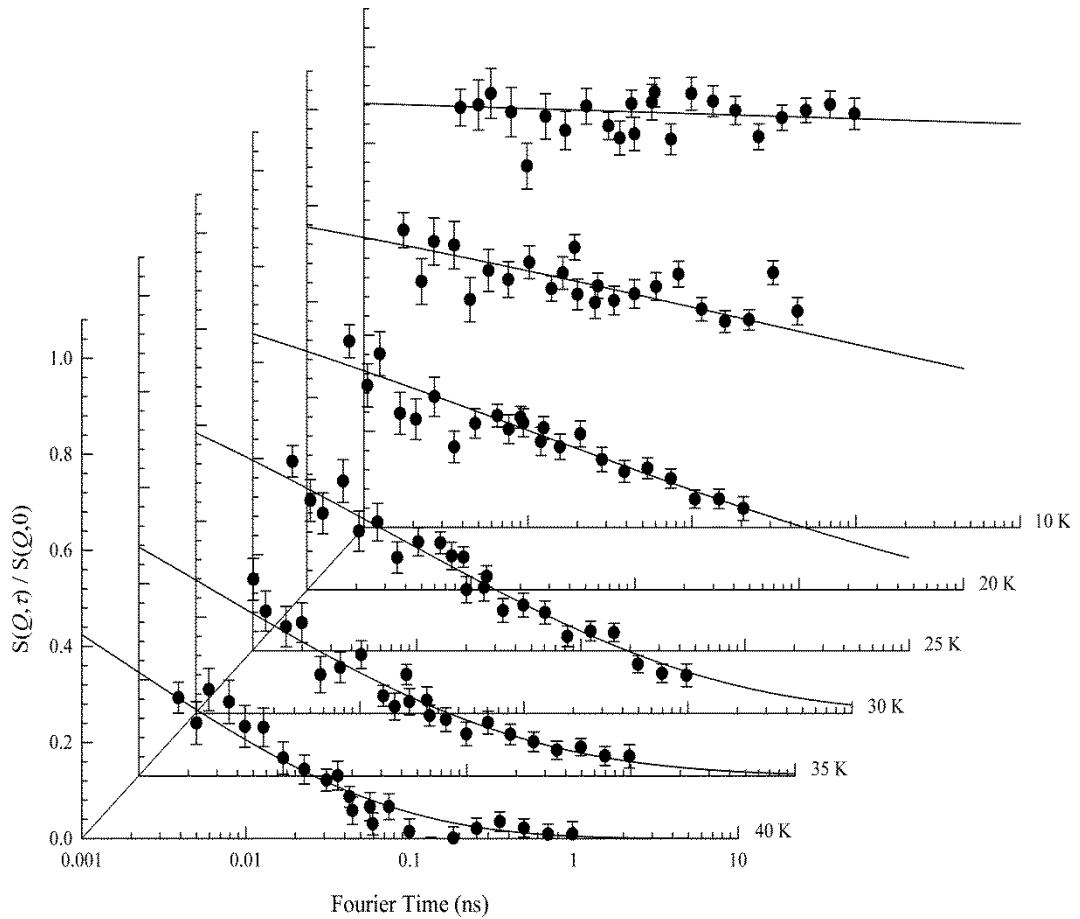


Figure 4:31 Neutron spin echo measurements revealing the temperature dependence of spin dynamics in $Y_{1.05}(Al_{0.35}Fe_{0.65})_2$ over the momentum transfer range ($0.2 \leq Q \leq 0.7$) \AA^{-1} . The solid lines represent least square fit to the data using the Weron-Tsallis relaxation function.

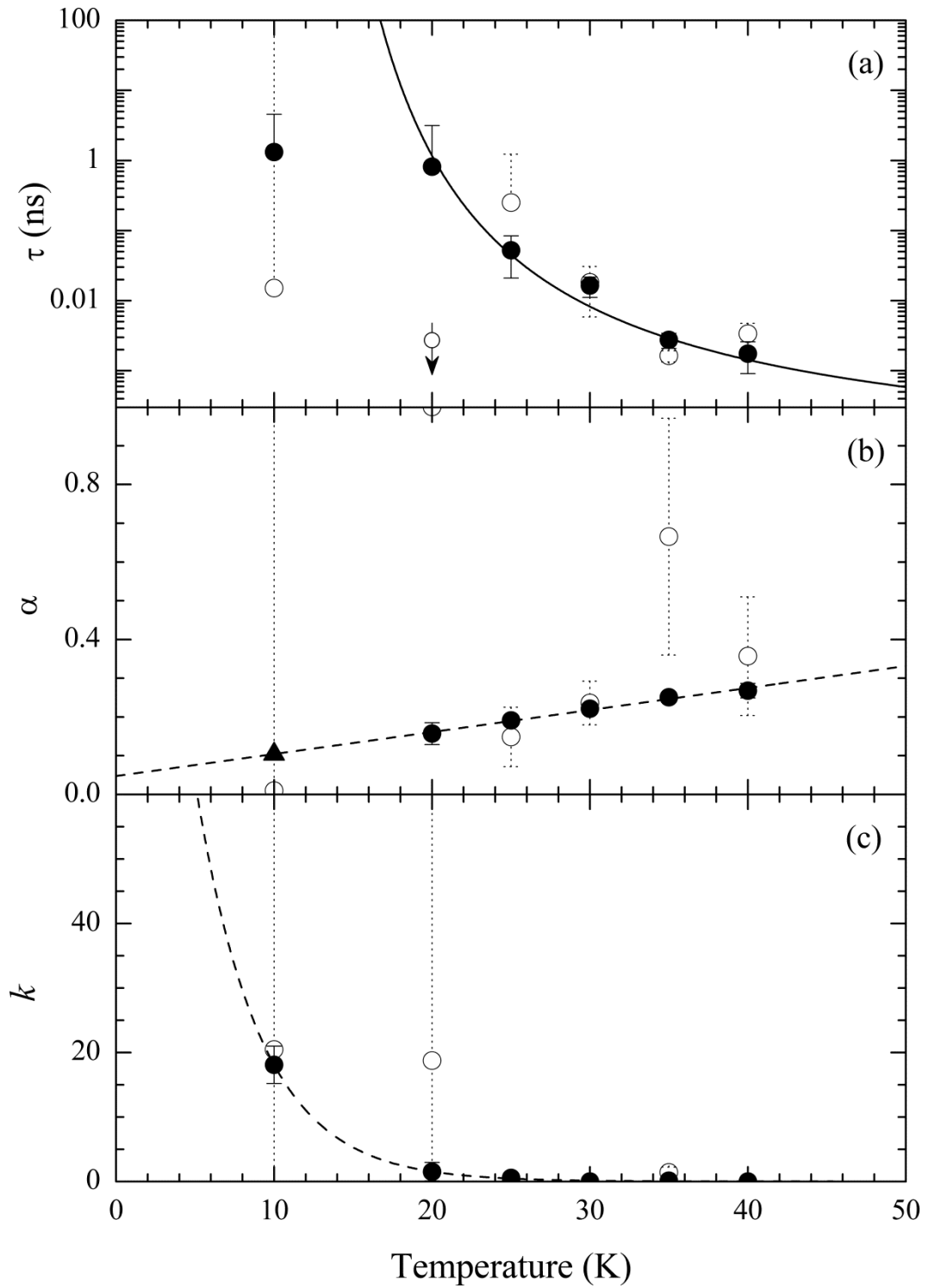


Figure 4:32 The calculated Weron parameters for $Y_{1.05}(Al_{0.35}Fe_{0.65})_2$. a) Temperature dependence of τ , solid line is fit to the Vogel Fulcher law: $\tau_0 = (3.71 \pm 7.05) \times 10^{-6}$ ns, and $E_a/k_B = (112.75 \pm 74.33)$ K, and $T_0 = (9.12 \pm 6.00)$ K. b) Fractal parameter, where dashed line is linear fit to data. c) The interaction parameter, (k); the dashed line is included to guide the eye.

Comparable linear temperature dependence is also observed, however extrapolating this trend reveals (α) does not fall to zero, reaching only a minimum value of approximately 0.05 at zero temperature. The triangular point highlights that α was fixed to follow this linear trend for the temperature $T = 10$ K.

The divergence of the relaxation rate (τ) is again well described by the Vogel-Fulcher law with the parameters: $\tau_0 = (3.71 \pm 7.05) \times 10^{-6}$ ns, $T_K = (112.75 \pm 74.33)$ K and $T_0 = (9.12 \pm 6.00)$ K. Therefore $T_0 / T_K = 0.08$, which implies that the system is again within the weak coupling regime. Moreover the relatively low ideal gas temperature indicates the relaxation processes involved are more Arrhenius-like, and the system therefore less *fragile* than $Y(\text{Mn}_{0.90}\text{Al}_{0.10})_2$.

The interaction parameter (k) tends towards zero for temperatures significantly above the transition temperature, $T_f = 24$ K, increasing slightly at the transition before apparently diverging. Again, due to the difficulty in determining (τ) close to and below (T_0) it is difficult to say if the value calculated for (k) at $T = 10$ K is accurate. It should also be noted that this temperature was not included in the fitting the Vogel-Fulcher Law.

Chapter 5

RAM: RANDOM ANISOTROPY MAGNETS

Random anisotropy is generally associated with amorphous alloys however RAM-like ground states also exist in crystalline Rare earth intermetallic compounds. In this chapter the spin relaxation dynamics of RAM-like C15 Laves phase compound $(La_xEr_{1-x})Al_2$ are investigated using NSE spectroscopy; the recorded spectra are analysed using the Weron-Tsallis relaxation function for comparison with the C15 Laves phase spin glass behaviour already discussed.

5.1 Introduction to Random Anisotropy

The magnetic properties of metallic glasses have been of great interest for many years^{203, 204} since the intrinsic site-disorder results in exchange and anisotropy strengths which vary greatly from site-to-site. The Harris-Plischke-Zuckerman (HPZ) Hamiltonian²⁰⁵ provides the framework for discussing the magnetic properties of such systems,

$$\mathcal{H} = - \sum_{ij} J_{ij} \mathbf{S}_i \cdot \mathbf{S}_j - D \sum_i (\hat{\mathbf{n}}_i \cdot \mathbf{S}_i)^2 - g\mu_B \mathbf{H} \cdot \sum_i \mathbf{S}_i \quad (5:1)$$

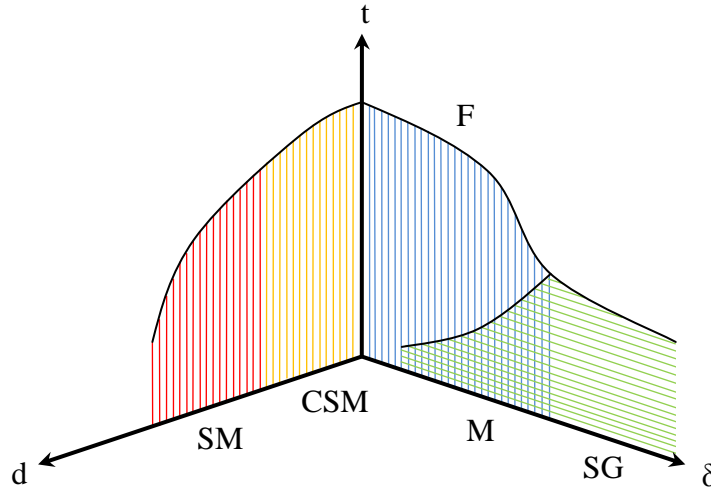


Figure 5:1 Schematic phase diagram of the possible magnetic states in the presence of RAM with average exchange J_0 and exchange fluctuations ΔJ . The axis are defined by $\delta = \Delta J / J_0$, $d = D / J_0$ and $t = k_B T / J_0$.

In the first term (J_{ij}) is the *exchange coupling strength* between the i^{th} and j^{th} spins, the magnitude of which is highly dependent on their separation. The random distribution of spins in an amorphous alloy ultimately leads to a wide distribution of (J) across the system. The second term describes the anisotropy at a single site which has a randomly orientated easy-axis of unit vector length (\hat{n}_i). The parameter (D) is a measure of the *anisotropy strength* along that axis. The final term accounts for the presence of an external magnetic field (H) acting on this spin.

In zero field the HPZ-Hamiltonian has been shown to produce a complex phase diagram, depicted in Figure 5:1, which was introduced by *Sellmyer & Nafis*²⁰⁶. In calculating this phase diagram it was assumed that the exchange coupling strength can be expressed as two separate terms, one defining the average value (J_0), and another the fluctuation (ΔJ_{ij}) about that average. Thus (J_{ij}) was replaced by ($J_0 + \Delta J_{ij}$) in equation (5:1).

The right-hand plane corresponds to a system of negligible anisotropy, where the behaviour is dominated by exchange interactions. This leads to spin glass (SG), mixed (M), and ferromagnetic (F) regimes.

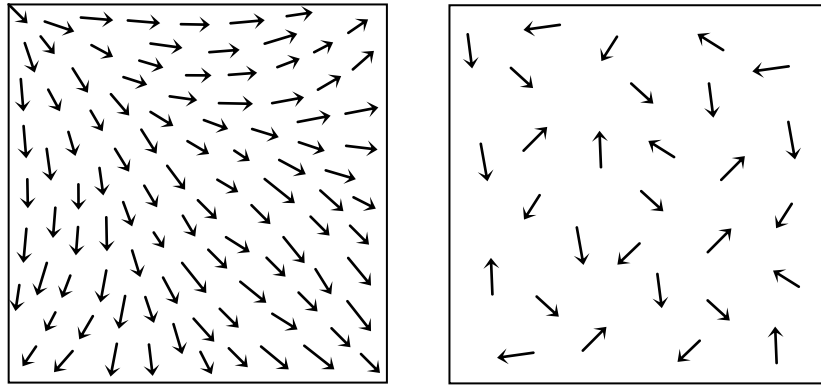


Figure 5:2 Schematic representations of the correlated speromagnetic phase (*left*) and speromagnetic phase (*right*).

The left-hand-side depicts the opposing limit, where exchange fluctuations are weak compared to the coupling strength, ($J_0 \gg \Delta J_{ij}$), and (δ) is therefore negligible. The defining parameter here is the ratio of anisotropy strength to exchange, commonly labelled ($d = D / J$). For very weak anisotropy ($d \ll 1$) the system is on the brink of ferromagnetism; a state referred to as the asperomagnetic phase. However, as the local random anisotropy increases all long-range ferromagnetic order is destroyed²⁰⁷, and the system enters a so-called correlated speromagnetic phase (CSM)²⁰⁸. This state is characterised by a smooth rotation of the local magnetisation, taking place over many interatomic distances. Thus on a local scale ferromagnetic order exists despite the net magnetic moment being zero.

Systems with ($d \geq 1$) enter a frozen random magnetic state at low temperature called the speromagnetic phase (SM), where each spin essentially points along the direction of the local random anisotropy. The magnetic properties are somewhat analogous to those of conventional spin glasses, despite the underlying mechanisms being clearly very different²⁰⁹. For instance, both display a frequency dependent cusp in the magnetic susceptibility. However, for RAM systems the freezing occurs due to significant random anisotropy²⁰⁹⁻²¹¹, not competing exchange interactions (i.e. frustration). Therefore it is of interest to investigate the relaxation dynamics of RAM behaviour for comparison with the previous conventional spin glass systems.

As stated, this phenomenon is usually associated with amorphous alloys, and the majority of literature on this subject pertains to metallic glasses beyond the ferromagnetic percolation threshold. However RAM-like behaviour has also been observed for crystalline Rare earth intermetallics such as $(Y_{1-x}Dy_x)Al_2$ ²¹² and more recently $(La_xEr_{1-x})Al_2$ ²¹³.

5.2 Introduction to $(La_xEr_{1-x})Al_2$

As already stated, Re- Al_2 compounds adopt the *C15* Laves phase structure. However in this system the magnetic spin are situated on the diamond-like A sublattice and are perturbed by a crystal field comparable in magnitude to the RKKY exchange interactions between the localised *4f*-moments²¹⁴. As a result these systems often display a rich variety of magnetic properties²¹⁵.

$ErAl_2$ becomes ferromagnetic below ($T_c = 14$ K) and has an easy axis along the $\langle 111 \rangle$ direction. Magnetisation measurements reveal it to be strongly anisotropic, having a spontaneous moment of $7.9 \mu_B$, significantly smaller than that of the free ion value, $\sim 9.6\mu_B$. It has been discovered that this anisotropy leads to a freezing peak in the pseudo-binary system $(La_xEr_{1-x})Al_2$.

Magnetic susceptibility measurements performed on the compound $(La_{0.8}Er_{0.2})Al_2$ indicate Curie-Weiss temperature dependence with an effective moment approximately equal to $10 \mu_B$ ²¹³. However, in the ground state the erbium ion has been reported to have a moment of approximately $2.7 \mu_B$ in the compound $(La_{0.7}Er_{0.3})Al_2$ ²¹⁶.

A characteristic freezing cusp is observed at ($T_f \sim 3.5$ K), with temperature and frequency dependence closely resembling that of archetypal RAM systems over an extended concentration range, ($0.1 < x < 0.9$). The cusp appears distinctly rounded with a magnitude and temperature that is dependent on frequency, as shown in Figure 5:3. Moreover, the imaginary component is substantially larger than is generally observed in conventional spin glasses²¹³ indicating a speromagnetic-like ground state²¹⁷.

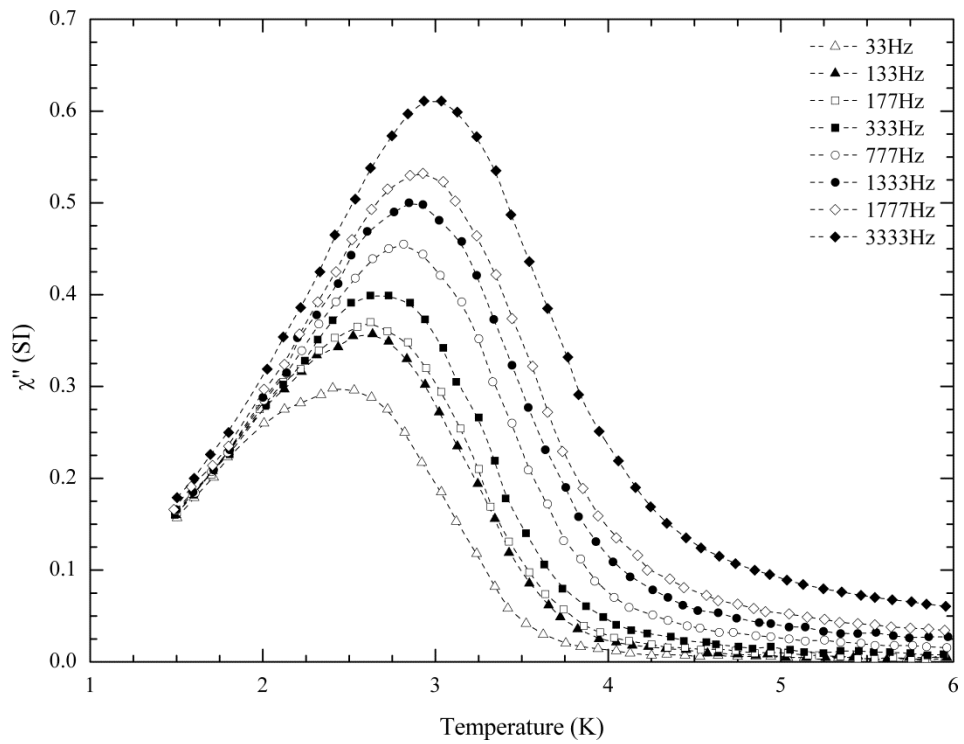
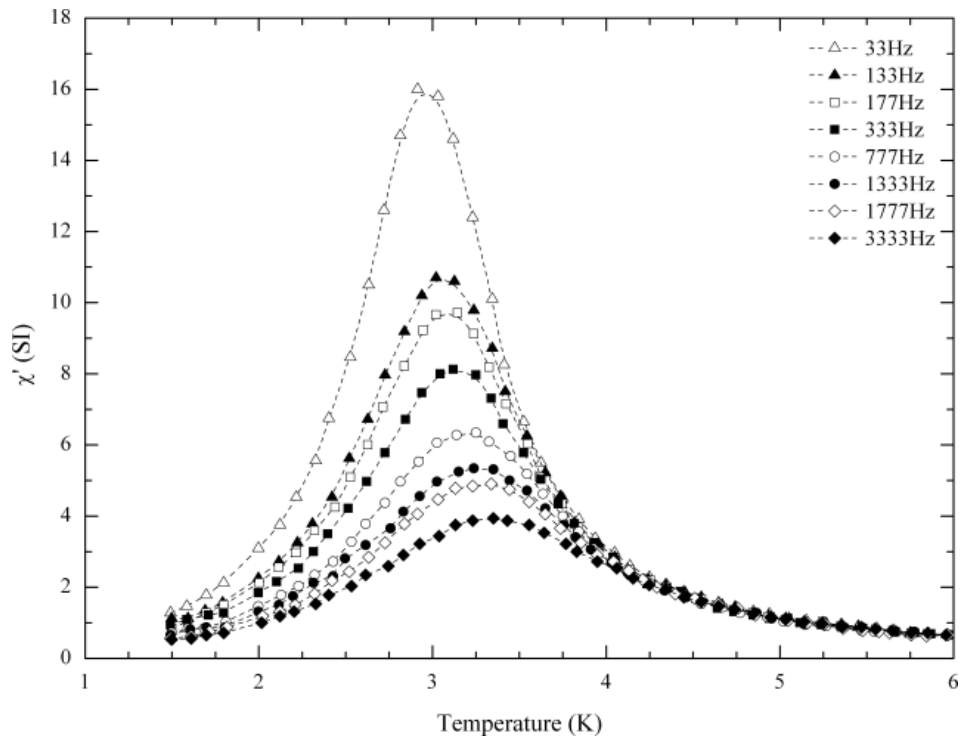


Figure 5:3 The temperature and frequency dependence of χ' (Top) and χ'' (Bottom) for $\text{La}_{0.70}\text{Er}_{0.30}\text{Al}_2$. *Pottinger*²¹⁸.

Recently diffuse neutron scattering was used to study spin correlations within $(\text{La}_{0.8}\text{Er}_{0.2})\text{Al}_2$ via full xyz -polarisation analysis, which has revealed short-range order up to 5.4 K, significantly above T_f , consistent with a system in a speromagnetic state ²¹³.

The question of whether this RAM-like behaviour is due to random anisotropy of individual erbium sites, as is the case for conventional RAM systems, or perhaps shape anisotropy due to the formation of magnetic clusters remains open to debate. However, it can be said that the evolution of these weak correlations is slow approaching the freezing temperature from above, and that below the freezing temperature significant beam depolarisation suggests the onset of either medium to long-range ferromagnetic correlations or clusters.

5.2.1 Sample Preparation

Polycrystalline samples were prepared by melting appropriate stoichiometric proportions of spectrographically pure starting materials in an argon-arc furnace. The ingots were allowed to cool in an inert atmosphere and no further heat treatment was required. Weight losses did not exceed 0.55 % for any of the ingots produced.

5.2.2 NSE Study of $(\text{La}_{0.70}\text{Er}_{0.30})\text{Al}_2$

Re-analysis of the NSE measurements performed by *Mezei et al.* ^{216, 219} in 1984 indicate the Tsallis extensivity parameter, (q), to be temperature independent, taking a value below the strong-disorder limit, ($q = 5/3$). However the temperature range across which these measurements were performed must be extended in order to test the validity of this result.

The sample was crushed in to a fine powder and loaded into a flat 1 mm deep aluminium container allowing for approximately 80 % beam transmission, and mounted in a helium reservoir cryostat. Using IN11 with a small angle multi-detector option and wavelength $\lambda = 7 \text{ \AA}$ it was found that above 5 K the intermediate scattering function, $S(\mathbf{Q}, \tau)$, was Q -independent within experimental error for the range $(0.03 \leq Q \leq 0.46) \text{ \AA}^{-1}$, however the dynamics become strongly Q -dependent below this temperature. This was also reported by Mezei who suggested the spin

relaxation dynamics are therefore not governed by exchange interactions but “by some spin non-conserving effects... this also implies that the spins locally correlated in the SRO, as reflected by $S(q)$, rotate together”.

It should be mentioned that from Figure 5:4 Mezei took the following averages: for $T \geq 10$ K the data represent the averages taken over $Q = 0.045, 0.09, 0.18,$ and 0.36 \AA^{-1} , for $T = 7$ K the points are averaged over $Q = 0.18$ and 0.36 \AA^{-1} , and for $T = 5$ K, only $Q = 0.36 \text{ \AA}^{-1}$ was used.

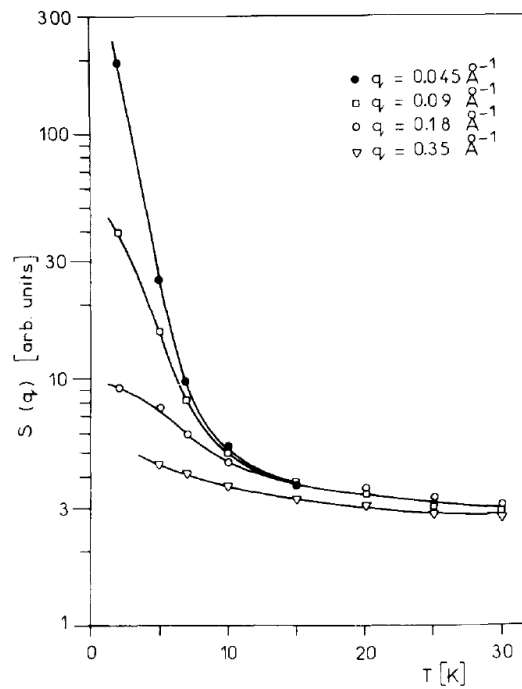


Figure 5:4 The temperature dependence of the total magnetic cross section at various momentum transfer values. This graph has been taken from Mezei²¹⁶.

New measurements were performed at $Q = 0.46 \text{ \AA}^{-1}$ where the enhancement in $S(Q)$ is significantly less, Figure 5:5. The temperature dependence of the Weron fit parameters for spectra recorded during both experiments is shown in Figure 5:6. The divergence in relaxation rate (τ) has again been fitted to the Vogel-Fulcher law: $\tau_0 = (3.58 \pm 2.14) \times 10^{-3}$ ns, $T_K = (29.29 \pm 7.91)$ K and $T_0 = (1.17 \pm 0.68)$ K, which indicates near-Arrhenius, and therefore largely independent, relaxation processes are occurring within the sample.

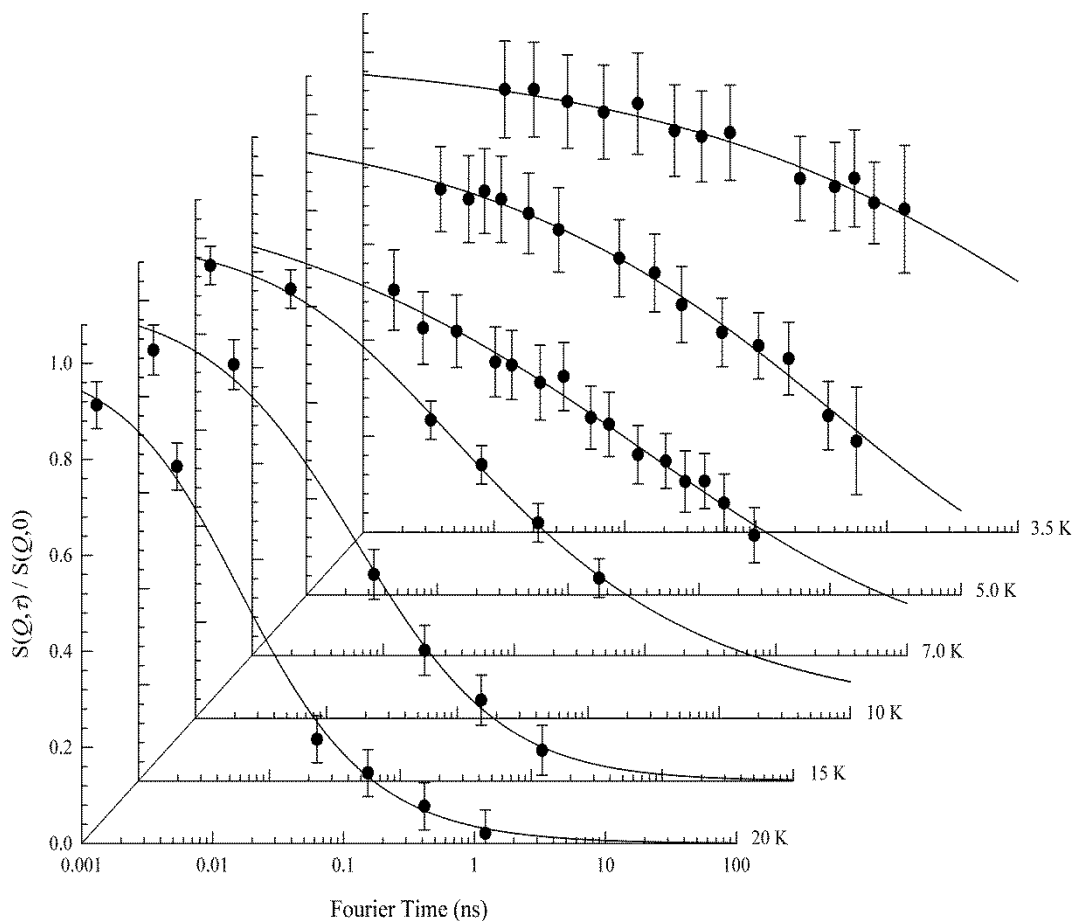


Figure 5:5 Neutron spin echo measurements performed during this investigation ($T = 3.5, 5.0, 7.0$ K, and by *Mezei* ($T = 10, 15, 20$) K) on $(\text{La}_{0.70}\text{Er}_{0.30})\text{Al}_2$. The solid lines indicate fits to the data using the Weron-Tsallis relaxation function.

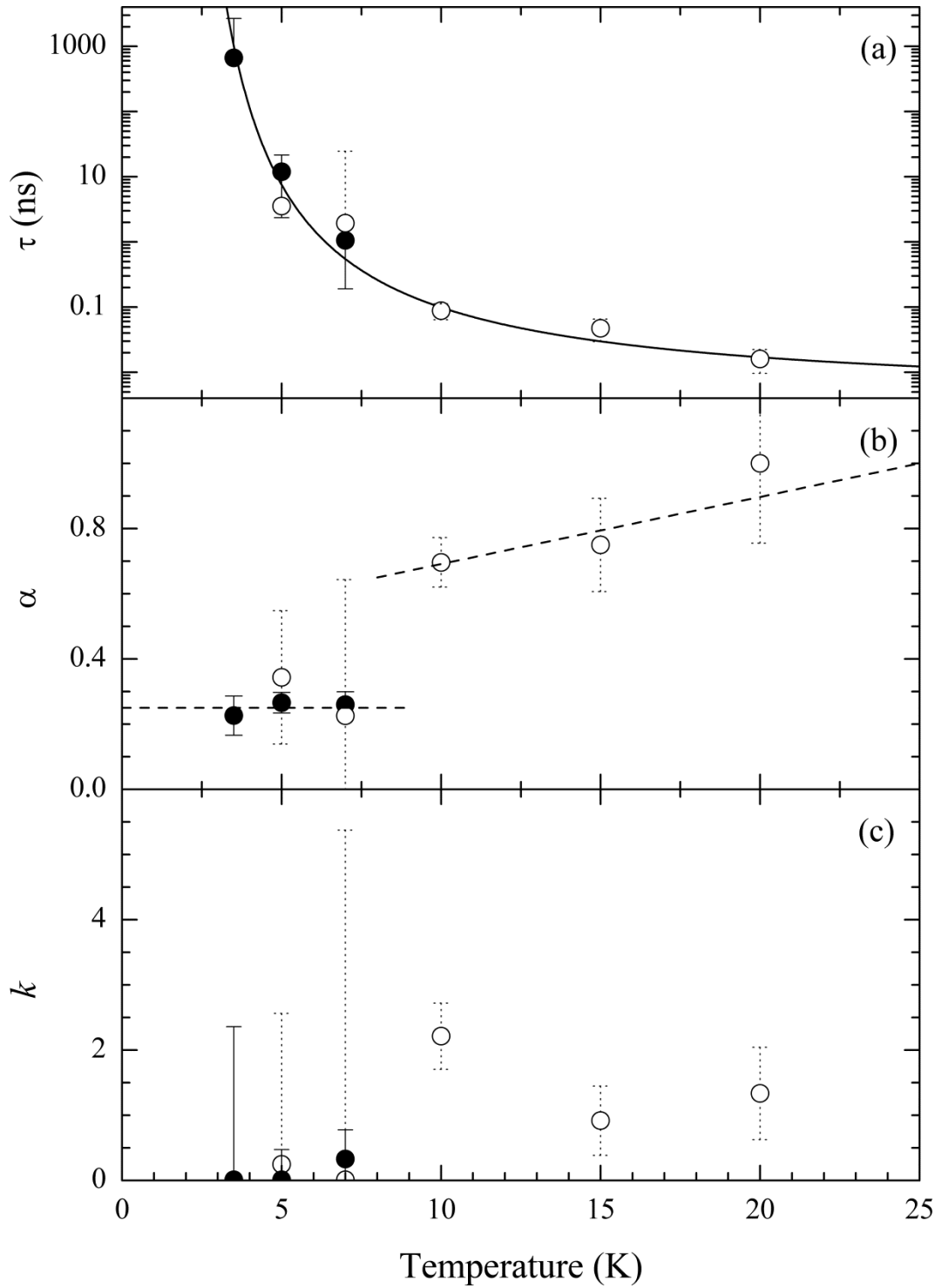


Figure 5:6 Weron parameters for the NSE spectra of $(\text{La}_{0.70}\text{Er}_{0.30})\text{Al}_2$ (a) temperature dependence of τ , solid line is a fit to the Vogel Fulcher law: $\tau_0 = (3.58 \pm 2.14) \times 10^{-3}$ ns, $T_K = (29.29 \pm 7.91)$ K and $T_0 = (1.17 \pm 0.68)$ K, b) fractal parameter; the dashed lines are included to guide the eye c) the interaction parameter, k .

Comparable fits parameters were obtained when analysing these and Mezei's data for $T = 7$ and 5 K, suggesting not only that the desired sample stoichiometry was achieved but that the measurements, performed nearly 30 years apart, are reliable.

Unlike the linear trends of the previous concentrated spin glass systems, the fractal parameter, (α) , appears to fall gradually from an initially high value approaching 10 K, below which a sudden broadening in the distribution of relaxation rates is observed, (α) taking a constant value of 0.25 within error. This could be linked to the onset of short-range order as the system enters a speromagnetic-like state, or perhaps an artefact of the Q -dependence or beam depolarisation observed at these low temperatures.

Preliminary analysis of Mezei's work had suggested the interaction parameter (k) to be largely temperature independent. Indeed the high temperature measurements do not approach zero as was observed in the spin glasses already presented, but instead take values of between $(0.9 \leq k \leq 2.2)$. However, like the fractal parameter, below 10 K the interaction parameter falls sharply towards zero. Hence the Weron function reduces to a stretched exponential suggesting the dynamics in this low temperature regime are largely free from hierarchical constraints.

Chapter 6

SUPERPARAMAGNETIC RELAXATION IN $\text{Cr}_{1-x}\text{Fe}_x$

At low temperatures superparamagnetic materials enter a glassy state which, unlike the spin glass phase, does not depend on the interactions between individual particles, but manifest due to “blocking”. This chapter presents an investigation in which the applicability of the Weron-Tsallis function to model such behaviour has been explored using NSE data recorded on $\text{Cr}_{1-x}\text{Fe}_x$ with ($x = 0.135$ and 0.175).

6.1 Superparamagnetism

As the volume of a ferromagnetic particle is reduced the energy spent in forming domain walls eventually outweighs the demagnetising energy saved by reducing the dipole fields at the surface of the particle. Subsequently, single-domain nano-particles form, the total moment of which is governed simply by the sum of all the atomic moments within it. In such materials strong inter-particle exchange coupled with weak intra-particle interactions gives rise to paramagnetic-like state known as superparamagnetism.

The magnetisation direction of these single-domain particles is often constrained to lie along an easy-axis, either due to the magnetocrystalline anisotropy or shape anisotropy associated with the particle itself. To approximate the energy density of this anisotropy a series expansion is used, which in the uniaxial case takes the form,

$$E = K_1 \sin^2 \theta + K_2 \sin^4 \theta + \dots \quad (6.1)$$

where (K_1) and (K_2) are the so-called anisotropy constants and (θ) is the angle between the magnetisation direction and easy-axis. From this equation it can be seen the energy is minimised at zero or π , where the moments lie parallel or anti-parallel to the easy-axis.

At high temperatures, ($k_B T \gg KV$), the particle's moment fluctuates rapidly behaving much like a paramagnet. The relaxation time associated with this process is governed by the Arrhenius Law,

$$\tau = \tau_0 \exp\left(\frac{KV}{k_B T}\right) \quad (6.2)$$

where the activation energy, ($E_a = KV/k_B$), defines the thermal energy barrier between parallel and anti-parallel directions; clearly this is highly dependent on the particle's volume.

As the temperature is reduced these fluctuations slow until at a critical temperature, known as the blocking temperature (T_B), the system appears static. This occurs when the observation time becomes far smaller than the intrinsic relaxation rate (τ_0), at which point the magnetic particle is frozen or *blocked* on experimental time-scales.

Unlike spin glasses the strength of interactions between magnetic particles is regarded as being weak and consequently superparamagnetic relaxation provides a unique opportunity to study the Weron-Tsallis relaxation function on a relaxation mechanism which is independent of intra-particle interactions.

6.2 The Chromium-Iron System

The first experimental evidence of a magnetic transition in chromium was provided by *Bridgman* in 1932²²⁰, however it took several years before this was identified as a Néel point. Indeed *Néel* himself first suggested that chromium was

anti-ferromagnetic in 1936 based on the observations he made in a dilute solution of gold ¹⁷. The earliest detailed work on chromium's magnetic structure came in the 1950s when *Shull & Wilkinson* presented the results of their neutron diffraction studies ²²¹. However, their result caused considerable confusion as they indicated an anomalously high temperature transition to a commensurate anti-ferromagnetic structure which, it was later discovered, was due to internal strain in their cold-worked sample. Several years later the true transition was identified separately by *Bykov et al.* ²²² and *Corliss et al.* ²²³.

Below the transition, $T_N = 311$ K, atomic moments in the chromium lattice adopt an incommensurate spin density wave (SDW) with a periodicity of 21 unit cells and root-mean-square value of $0.4\mu_B$ per chromium atom. The high temperature phase exhibits a Pauli paramagnetic susceptibility response. A comprehensive review on the physical properties of chromium in relation to its anti-ferromagnetism has been published by *Fawcett* ²²⁴.

When alloyed with elements to its right in the periodic table the Néel temperature usually increases, however for $\text{Cr}_{1-x}\text{Fe}_x$ this is not the case. Not only does the transition temperature decrease but the system is driven into a commensurate state above ($x = 0.02$) ^{225, 226}. At concentrations ($x > 0.10$) the iron atoms begin to form ferromagnetic clusters with 5-10 Å radii suspended within the anti-ferromagnetic host. At high temperature these are superparamagnetic, and appear to enter a re-entrant spin glass-like state below ~ 25 K ²²⁵.

For alloys between ($0.16 \leq x \leq 0.19$) spin glass-like behaviour is displayed at low temperatures, with increased concentration leading to a percolation of the iron clusters and long-range ferromagnetic order being adopted ^{227, 228}. A number of different magnetic measurements have been compiled to reveal the complete magnetic phase diagram for $\text{Cr}_{1-x}\text{Fe}_x$, shown in Figure 6:1.

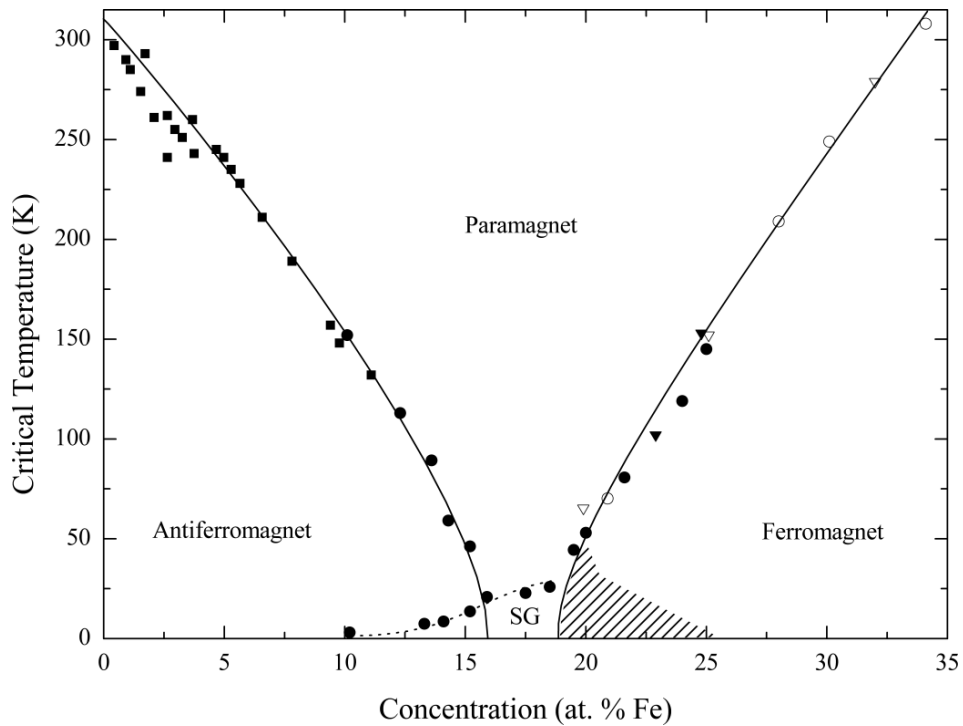


Figure 6:1 Magnetic phase diagram of Cr_{1-x}Fe_x alloys reproduced from ²²⁷. Ferromagnetic boundary determined by *Burke & Cywinski* (filled circle); *Loegel* (open circle); *Aldred & Kouvel* (open triangle); *Shull & Beck* (filled triangle). Anti-ferromagnetic boundary is a compilation of work by *Burke & Rainford*. The spin glass transition temperature was determined by *Burke & Cywinski*. Curved lines are to guide the eye, and the hatching indicates a region of complex magnetic properties.

Neutron scattering measurements in the anti-ferromagnetic regime suggest interactions between the host SDW and ferromagnetic clusters are negligible, but that the strength of interactions between neighbouring ferromagnetic clusters increases rapidly close to the percolation limit ^{225, 226}.

However, whilst small angle neutron scattering measurements taken just below the percolation threshold suggest the onset of long-range ferromagnetic order, susceptibility measurements either side of this critical concentration show very little difference. Such behaviour is often associated with a re-entrant phase, the existence of which has been confirmed *via* inelastic neutron scattering measurements ²²⁷.

More recently μ SR spectroscopy was employed to study the spin dynamics and nature of the phase transitions at the concentrations ($x = 0.135, 0.175, \text{ and } 0.22$). For ($x = 0.135$) it was found that the muon depolarisation rate at room temperature

was small ($\lambda \sim 0.02 \mu\text{s}^{-1}$), indicating an extremely fast field fluctuations. Upon reducing the temperature there was a marked slowing of (λ) as the Néel temperature was approached. However the temperature dependence of signal asymmetry indicated a progressive conversion to a magnetically ordered state. It would therefore seem that the muon was able to sense the condensation of the SDW, not inter-cluster correlations, in the paramagnetic phase and that this muon response was most likely associated with the anti-ferromagnetic host, not the ferromagnetic iron clusters. Upon further cooling towards the freezing temperature, $T_f = 12$ K, the fluctuation rate again slows, however the instrument resolution was insufficient, in regards to the time resolution, to fully characterise these complex spin dynamics at short times. In contrast both the ($x = 0.175$ and 0.22) concentrations are consistent with the typical response of a spin glass system, the muon relaxation spectra being of Kohlrausch form where the stretching parameter falling from unity at high temperatures to $1/3$ at the transition, $T_f = 32$ and 35 K respectively.

6.2.1 Sample Preparation

Two polycrystalline ingots were prepared, of concentration $x = 0.135$ and $x = 0.175$, by argon-arc melting appropriate proportions of the starting materials. Losses during the melting process were minimal and attributed to the evaporation of chromium. These ingots were subsequently sealed in quartz ampoules under a reduced argon atmosphere and annealed at temperatures in excess of 1000°C , after which they were rapidly quenched in an ice-water mixture.

6.2.2 NSE Measurements of $\text{Cr}_{1-x}\text{Fe}_x$

The superparamagnetic spin dynamics of this system have been investigated using the IN11 spectrometer with an incident wavelength of $\lambda = 5.5 \text{ \AA}$, over the momentum transfer range ($0.20 \leq Q \leq 1.31$) \AA^{-1} , using the wide angle multi-detector option discussed previously. The samples was crushed into a fine powder and loaded into thin walled cylindrical aluminium containers. Grouping the detectors, as before, revealed no significant Q -dependence and data was collected across the entire Q -range at six temperatures for each sample concentration.

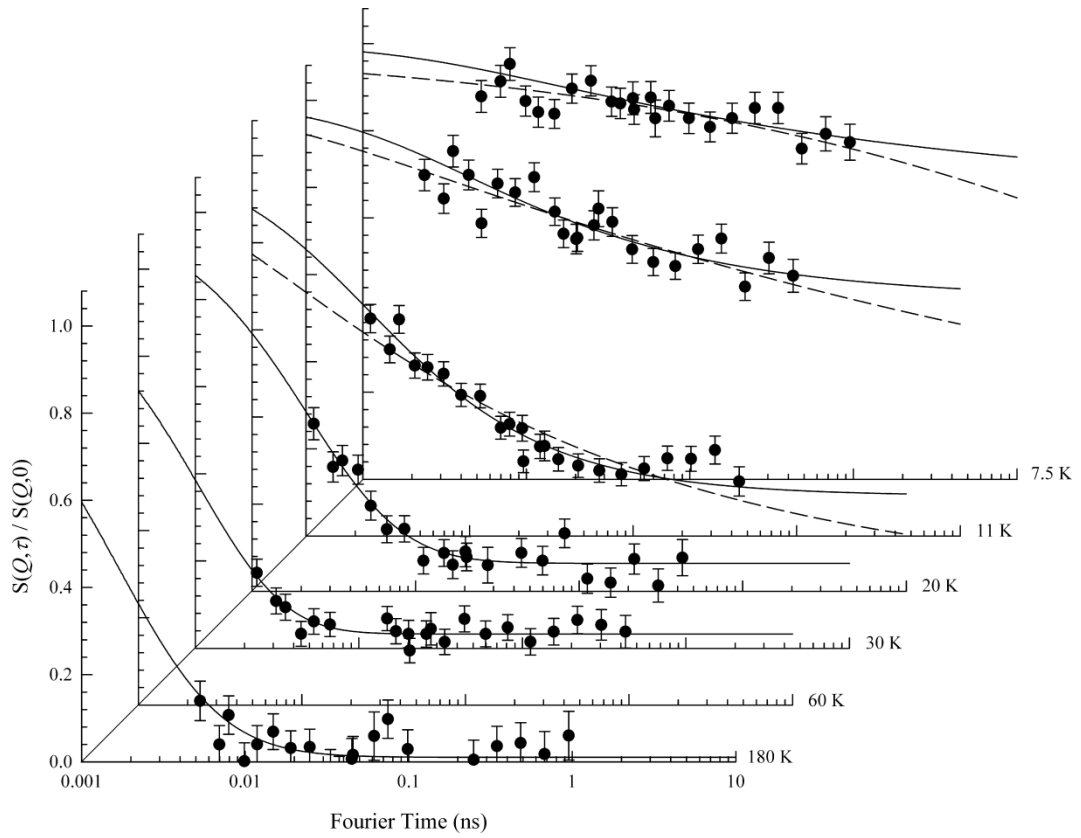


Figure 6:2 Neutron Spin Echo spectra of $\text{Cr}_{0.865}\text{Fe}_{0.135}$; the solid lines are least square fit of a Weron-Tsallis function modified to include a background term, the dashed lines ($T = 20, 11,$ and 7.5 K) represent least square fit to the Weron-Tsallis function.

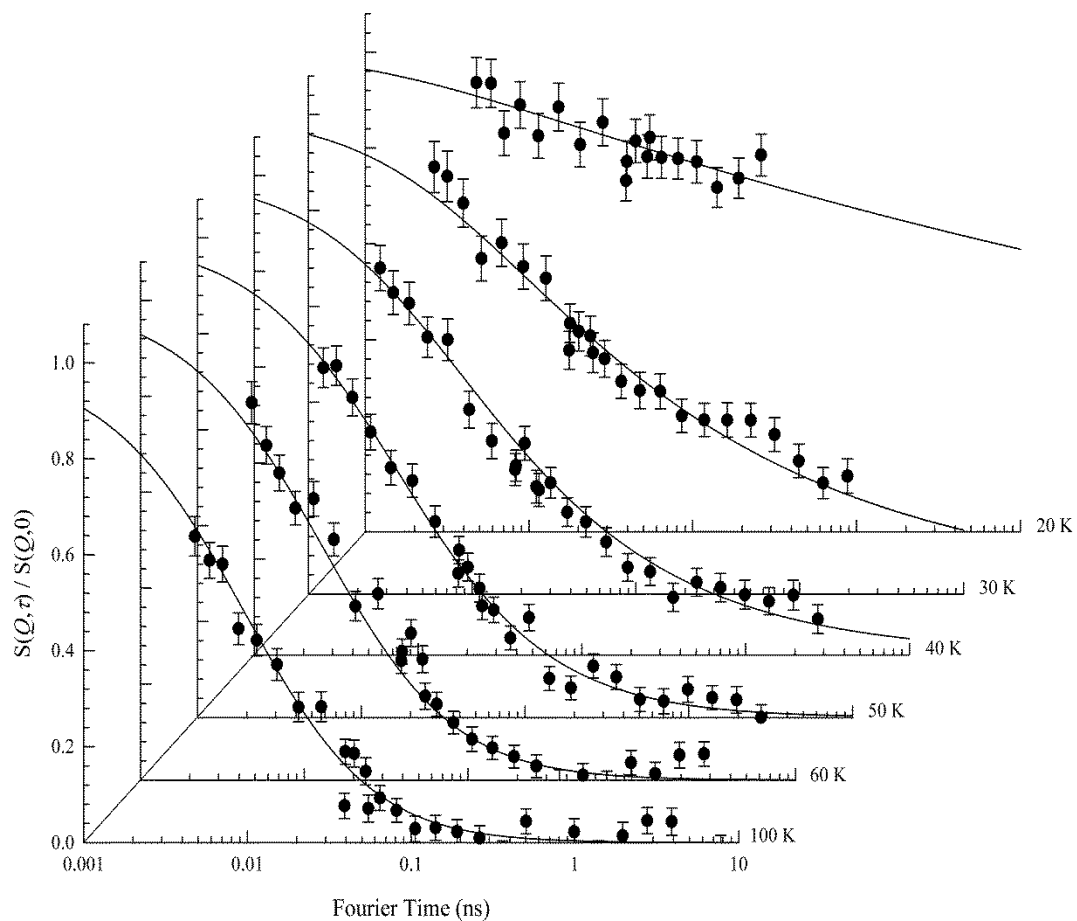


Figure 6:3 Neutron Spin Echo spectra of $\text{Cr}_{0.825}\text{Fe}_{0.175}$; solid lines represent least square fit to the data using the Weron-Tsallis relaxation function.

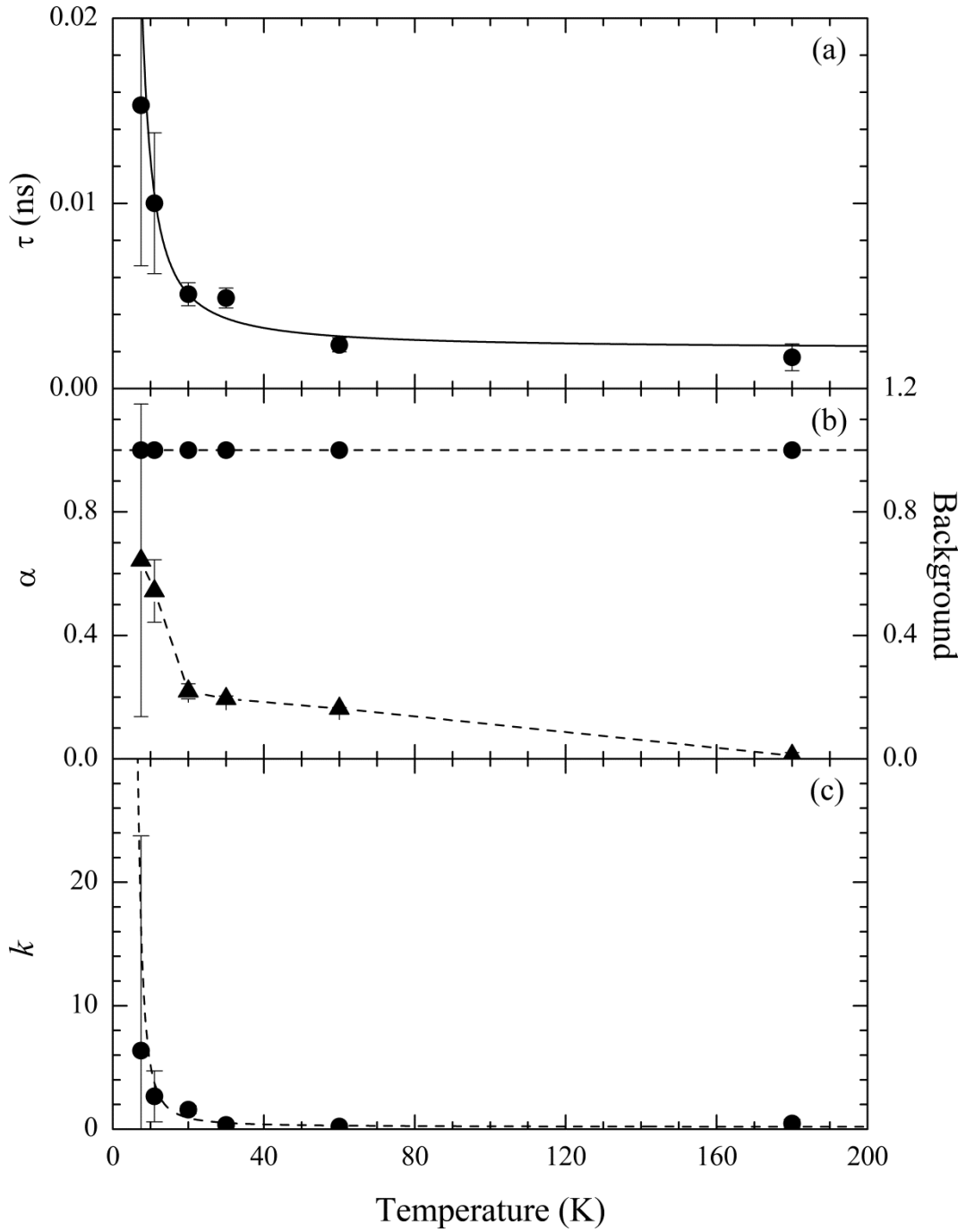


Figure 6:4 The calculated Weron parameters of least square fitting NSE measurements of $\text{Cr}_{0.865}\text{Fe}_{0.135}$. a) the temperature dependence of τ where the solid line is fit to the Arrhenius law: $\tau_0 = (9.46 \pm 1.66) \times 10^{-4}$ ns, $E_a/k_B = (33.51 \pm 2.80)$ K, b) fractal parameter (circle) and background term (triangle), c) the Weron interaction parameter (k); the dashed curve is to guide the eye.

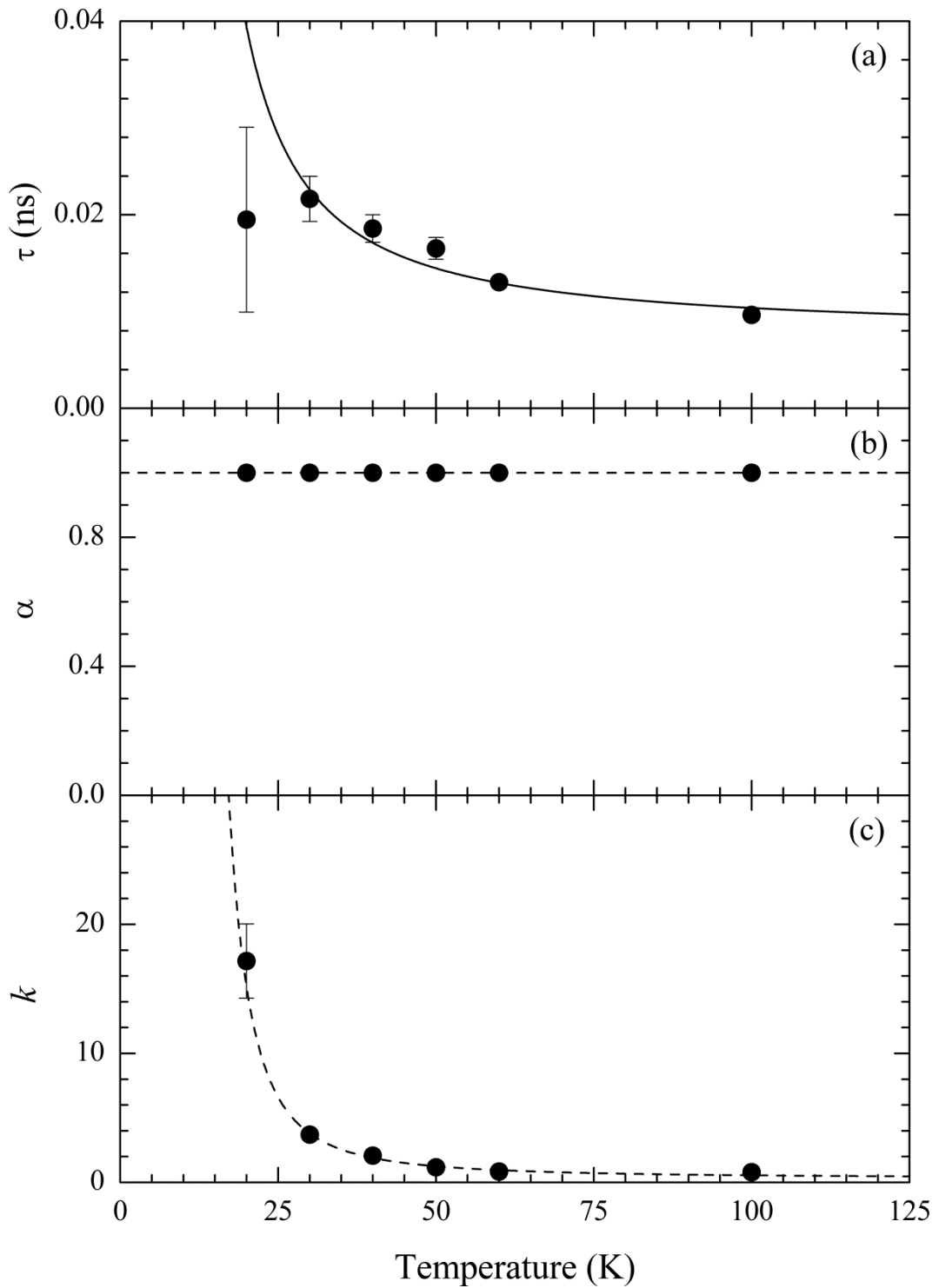


Figure 6:5 The Weron parameters calculated for $\text{Cr}_{0.825}\text{Fe}_{0.175}$. a) the temperature dependence of (τ) where the solid line is fit to the Arrhenius law: $\tau_0 = (7.42 \pm 0.86) \times 10^{-3}$ ns, $E_a/k_B = (33.42 \pm 6.08)$ K, b) fractal parameter (α), c) the Weron interaction parameter (k); the dashed curve is to guide the eye.

Inspection of the different spectra measured for the concentration ($x = 0.135$) immediately reveals a departure from the conventional response; this is particularly evident at the temperatures $T = 20, 30$ and 60 K. Within the time-window of IN11 the data can be seen to fall quickly at short times before reaching a plateau for Fourier times greater than ~ 0.01 ns. This would suggest the presence of an extremely slow relaxing component which is independent of the spin glass-like dynamics associated with the iron clusters. Hence the spectra were fitted to a modified Weron-Tsallis function,

$$\phi(t) = a + (1 - a) \left[1 + \xi \cdot \left(\frac{t}{\tau} \right)^\alpha \right]^{-\frac{1}{\xi}} \quad (6:3)$$

where ($0 \leq a \leq 1$) effectively lifts the function in order to accommodate this plateau. The fits shown in Figure 6:2 reveal the data to be well described by this modification; the values calculated for (a) have been included in the results shown in Figure 6:4b (triangles). At $T = 180$ K this background term is negligible, but steadily increases down to $T = 20$ K where it accounts for approximately 20 % of the intermediate scattering function. Below this (a) increases rapidly, eventually accounting for over 60 % of the spectra at $T = 7.5$ K. In this way it was discovered the fractal parameter of both sample concentrations was equal to one at all temperatures; by fixing this parameter the fitting procedure was then greatly simplified and analogous temperature dependence observed in both concentrations.

With regards the relaxation rate, the data was modelled using the Arrhenius equation, however the $T = 20$ K data for ($x = 0.175$) concentration was not included in the fit. The IN11 spectrometer failed during this measurement and ultimately only half the full Fourier time range was measured. For this reason it was not possible to accurately determine the value of (τ). Within error the activation energy of both is identical, $E_a/k_B = 33.5$ K, which by equating the activation energy to the cluster volume would suggest both samples have very similar cluster volume.

The characteristic relaxation rates (τ_0), however, were found to differ taking a value of $\sim 1 \times 10^{-3}$ ns for the concentration ($x = 0.135$), and 7.5×10^{-3} ns for ($x = 0.175$).

Finally, on a qualitative level, the interaction parameter follows a similar trend to that seen in the Lave phase spin glasses, taking a negligible value at high temperatures, before increasing as the transition temperature is approached. However, due to the narrower time-window over which these dynamics fall, it was not possible to accurately fit spectra just below the transition temperature. This reveals the interaction parameter to continue diverging below T_f .

Chapter 7

SPIN FLUCTUATIONS IN WEAK ITINERANT ELECTRON MAGNETS

Although neither gold nor vanadium generally possess a magnetic moment, the intermetallic compound Au_4V is found to be ferromagnetic below 42 K. In this chapter I report the results of a muon spin relaxation study of the itinerant electron moment fluctuations in Au_4V . The temperature dependence of the muon spin relaxation rate is found to be similar to that of the weak itinerant helimagnet, $MnSi$.

7.1 The Gold-Vanadium System

The first investigations (1959) of magnetism in the gold-vanadium system were performed on disordered alloys ranging from 1-15 at.% vanadium²²⁹, in which the temperature dependent susceptibility closely obeyed a Curie-Weiss law incorporating a temperature independent term, χ_0 , such that

$$\chi = \chi_0 + \frac{C}{(T - \theta)} \quad (7:1)$$

where C is the Curie constant and θ is the critical temperature.

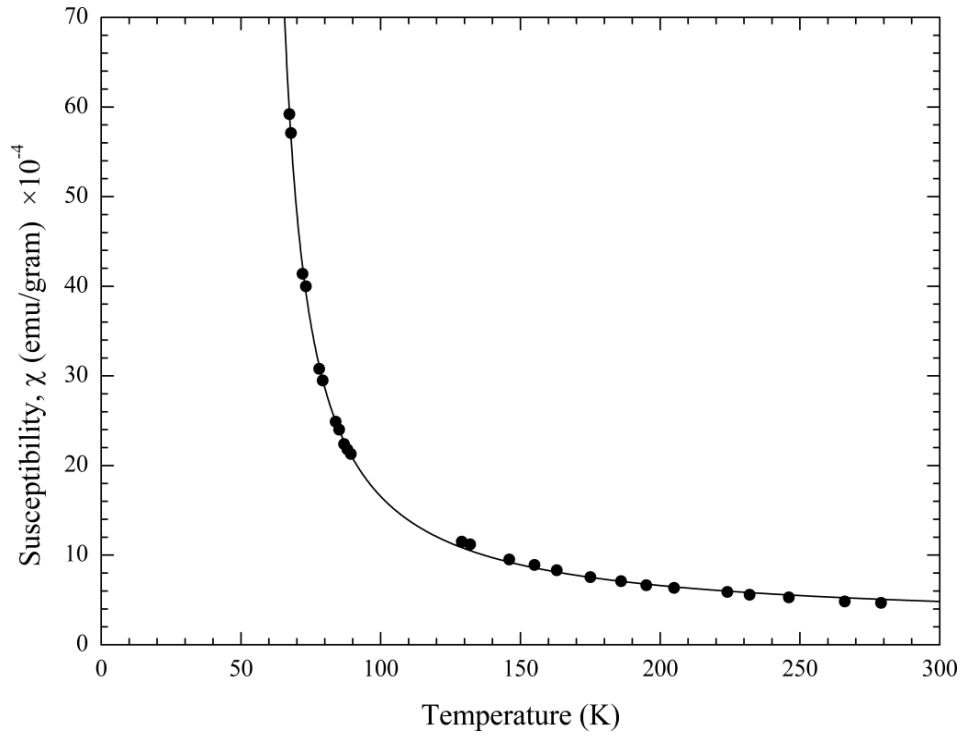


Figure 7:1 Magnetic susceptibility measurements taken from *Creveling*²³⁰, corresponding to a sample which underwent 45 day of annealing at 500 °C followed by 15 days at 300 °C. The solid line is a least square fit to Eq.(6:2); $\chi_0 = 95 \times 10^{-6}$ emu gram, $C = 79.7 \times 10^{-3}$ emu gram, and $\theta = 53$ K.

Interestingly the critical temperature of these relatively dilute alloys was found to be negative, despite there being no evidence of a magnetic transition. To explain this behaviour a model was proposed in which a fraction of *isolated* vanadium atoms i.e. those without other vanadium nearest neighbours, possess a local moment with the remaining fraction contributing to the Pauli-like temperature independent term.

*Creveling et al*²³⁰ extended the study of Au-V to higher concentrations ranging from 17 - 24 at.% vanadium. When annealed at ~ 500 °C, these alloys were found to undergo a structural transition forming an intermetallic compound with the nominal concentration Au_4V with a body-centred tetragonal structure (I4/m). This phase effectively isolates all the vanadium atoms and correspondingly a ferromagnetic transition was found at ~ 45 K. In this ordered phase the susceptibility above T_C obeys the Curie-Weiss law given in equation (6:2). However a large disparity in the magnetic measurements between different samples was noted. It has been suggested that this is due in part to magneto-crystalline anisotropy which is not only the result

of the non-cubic structure but also crystalline imperfections caused by the arbitrary alignment of the tetragonal c-axis.

As generally observed for weak itinerant electron ferromagnets, the ordered moment of Au_4V is substantially lower (approximately half that) of the paramagnetic moment; however, annealing under compression promotes alignment of the c-axis, and increases the ordered moment from the usual value of 0.4 - 0.6 μ_{B} to 0.83 μ_{B} per vanadium atom²³¹. Furthermore, in extremely high pulsed magnetic fields (29 T) the ordered moment saturates to 1 μ_{B} per vanadium atom, indicating a spin- $\frac{1}{2}$ moment²³².

The importance of the vanadium-vanadium distance in establishing a localised moment, and consequently ferromagnetic order, is further emphasised by the observation that when Au_4V is prepared as a disordered solid solution the vanadium moment, and also ferromagnetism, collapses. Au_4V thus appears to belong to the same class of weak itinerant ferromagnets as ZrZn_2 and Sc_3In . However, in marked contrast to systems such as ZrZn_2 , for which the application of external pressure rapidly decreases T_{C} to zero by 20 kbar, the Curie temperature of Au_4V increases with pressure to 90 K at ~ 180 kbar, at which point the magnetic order collapses entirely²³³.

Positive muon spin relaxation has proved to be an invaluable tool in investigating itinerant magnetic systems such as MnSi , as demonstrated in the seminal paper by Hayano *et al.*²³⁴. Therefore zero and longitudinal-field measurements on Au_4V using the MuSR spectrometer (ISIS facility) were performed to follow the evolution of spin fluctuations with temperature between 5 K and 90 K.

7.1.1 Sample Preparation

Polycrystalline Au_4V samples were prepared by argon arc melting stoichiometric proportions of gold and vanadium; weight losses were less than 0.03 %. The resulting 2 g ingots were pressed into disks, approximately 5 mm in diameter and 1.5 mm thick before undergoing two days of homogenisation at 1000 °C under reduced argon atmosphere, followed by annealing at 500 °C for eight days

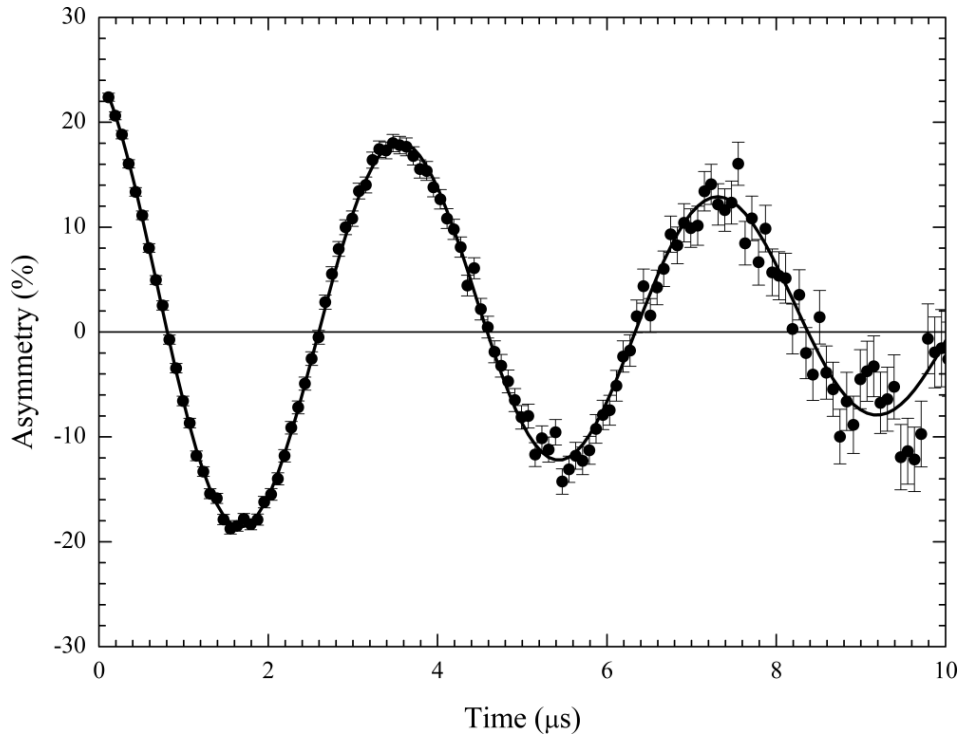


Figure 7:2 Instrument calibration measurement performed in a homogeneous 20 G transverse field. The solid line is a fit to a damped cosine function.

to promote crystallisation to the ordered phase. Several ingots were arranged in a mosaic fashion on a silver sample plate, so as to fill the muon beam as best as possible. Instrument calibration was performed using a small transverse 20 G field, shown above.

7.1.2 Muon Spin Relaxation in Zero-Field

The observed zero-field muon spin relaxation spectra for Au_4V were best modelled by a dynamical Kubo-Toyabe function, $G^{(\text{DKT})}$, representing a nuclear dipole contribution, multiplied by a simple exponential term, representing the contribution from atomic spin fluctuations .

$$A_0 G_z(t) = [a_1 G_z^{\text{DKT}}(t) \times \exp(-\lambda t)] + a_b \quad (7:2)$$

where A_0 is the initial asymmetry, a_1 is the relaxing asymmetry and a_b is a background. In order to determine an accurate value for the background, a_b , which

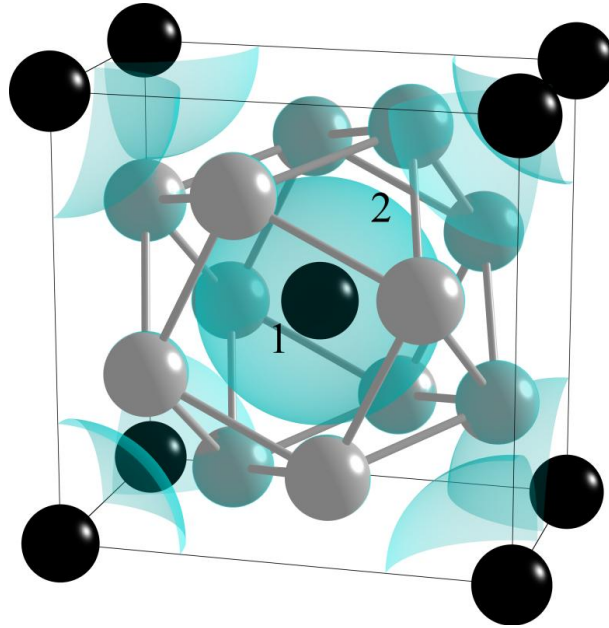


Figure 7:3 The structure of ordered Au_4V in which vanadium atoms are black and gold atoms silver. The isosurface indicates the positions within the unit cell where the nuclear depolarisation rate, $\sigma = 0.34\mu\text{s}^{-1}$. Labels 1 & 2 indicate the likely muon position.

is largely due to those muons which decay from within the silver sample plate, the initial asymmetries from spectra far above and below the reported Curie temperature were examined. By taking the drop in asymmetry to equal $2/3$ of the total relaxing component, simple subtraction yields a good estimate of a_b (9.836 %); this calculated value was subsequently fixed throughout the entirety of the analysis, which was again performed using the muon data analysis program WIMDA.

In the paramagnetic regime, above 50 K, the muon relaxation rate, (σ), from the randomly orientated nuclear dipoles is constant at $0.34\mu\text{s}^{-1}$. Estimates of the nuclear dipole contributions within the unit cell suggest possible muon sites corresponding to this value are at the centres of the $3\text{Au}-1\text{V}$ tetrahedron or the $4\text{Au}-1\text{V}$ octahedron as shown in Figure 7:3. Furthermore, the slow fluctuation rate observed as a damping of the “tail” of the Kubo-Toyabe function, and likely arising from the muon hopping between these interstitial sites, is constant at $\sim 0.25\mu\text{s}^{-1}$ in the paramagnetic regime, but slows significantly below 55 K. At temperatures below 30 K the fluctuation rate once again plateaus, taking a value $\sim 70\mu\text{s}^{-1}$, Figure 7:5b.

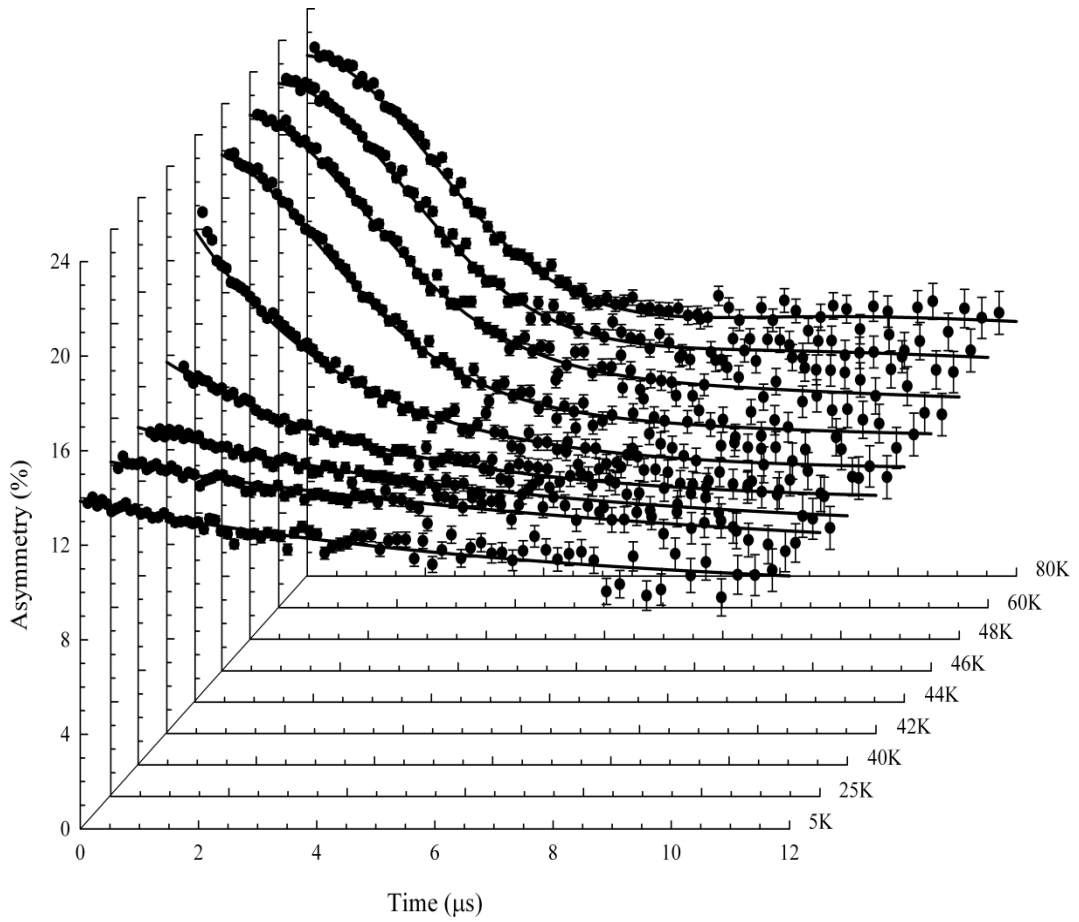


Figure 7:4 The observed zero-field muon spin relaxation spectra of Au₄V; the solid lines represent least square fits using equation (7:2).

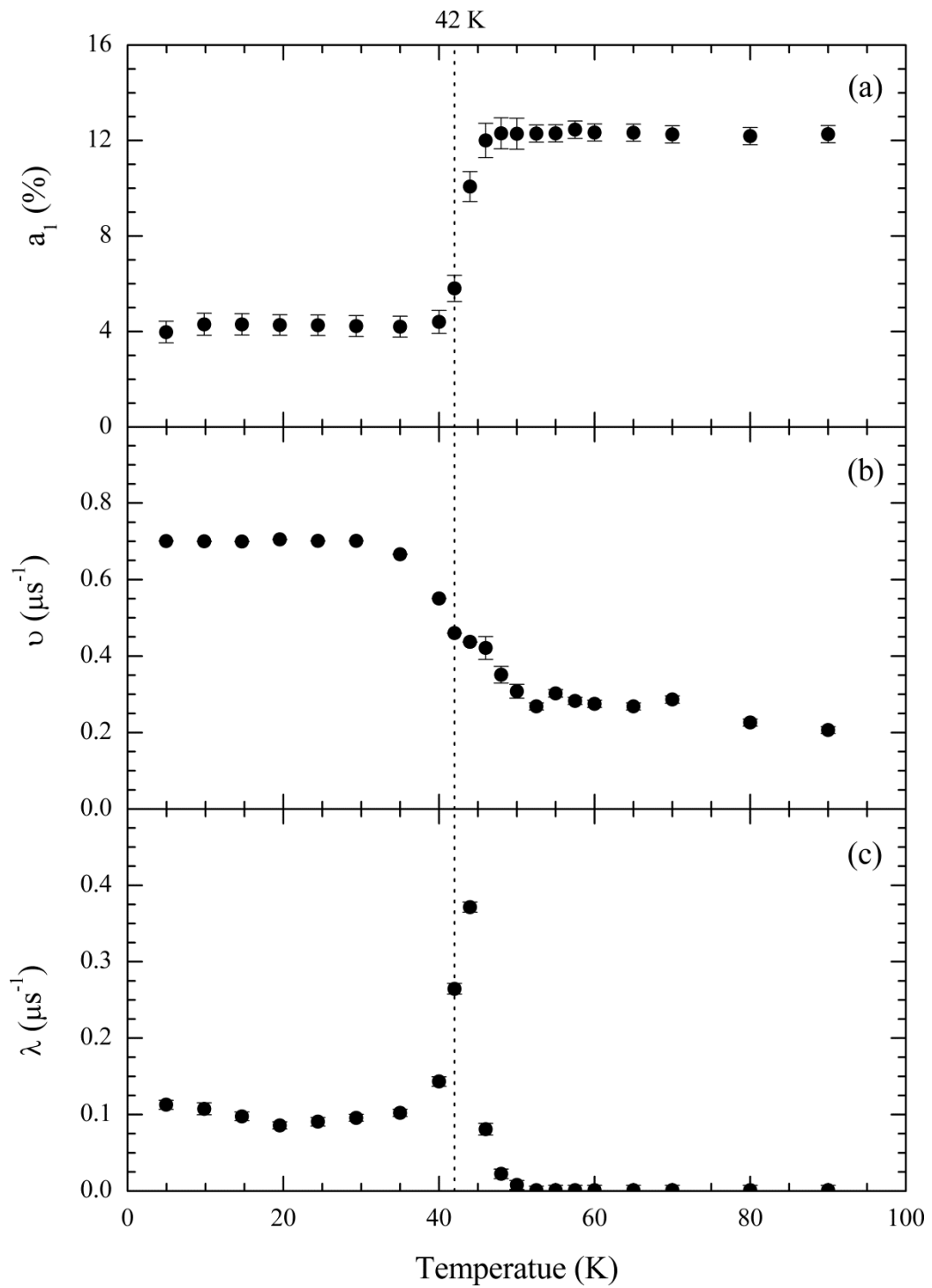


Figure 7:5 Parameter temperature dependence of equation (7:2) from least square fit of the zero-field data; a) the relaxing asymmetry, (a_1) b) the fluctuation rate, (ν) c) the muon spin relaxation rate, (λ).

A sharp drop in asymmetry is observed, falling from $\sim 12\%$ above 46 K to $\sim 4\%$ at 40 K and below. Furthermore the muon's precession decouples from the nuclear dipoles ($\sigma \rightarrow 0$) below 46 K, and the contribution from atomic spin fluctuations dominates the muon spin depolarisation process. These results are entirely consistent with the onset of long range magnetic order, and agree with the reported Curie temperature.

Simultaneously a marked divergence of the muon spin relaxation rate (λ) from a negligibly small value at high temperatures to a maximum at 40 K indicates a critical slowing of spin-lattice relaxation occurs, again at the reported Curie temperature. At lower temperatures (λ) is seen to stabilise at $\sim 0.1 \mu\text{s}^{-1}$. It should be said that the muon spin fluctuation rate in Au_4V is comparable to measurements made by *Hayano et al.* on the weak itinerant system MnSi .

7.1.3 Muon Spin Relaxation in Applied Longitudinal Fields

Spectra were also collected in sufficiently high longitudinal magnetic fields to decouple the muon from the nuclear dipole fields, but sufficiently small to offer negligible perturbation of the atomic spins. In Figure 7:6 the spectra from a range of applied longitudinal-fields above the transition temperature, clearly show a full decoupling at 100 G. Above this field the μSR spectra are well described by a simple exponential function,

$$G_z(t) = \exp(-(\lambda t)^\beta) \quad (7:3)$$

The associated relaxation rate (λ) increases rapidly as the transition temperature is approached until below 50 K a there is a critical divergence. As found for the weak itinerant helimagnet, MnSi ²³⁴ this critical divergence is best described by the simple formula:

$$\lambda = \tau_\infty \frac{T}{T - T_c} \quad (7:4)$$

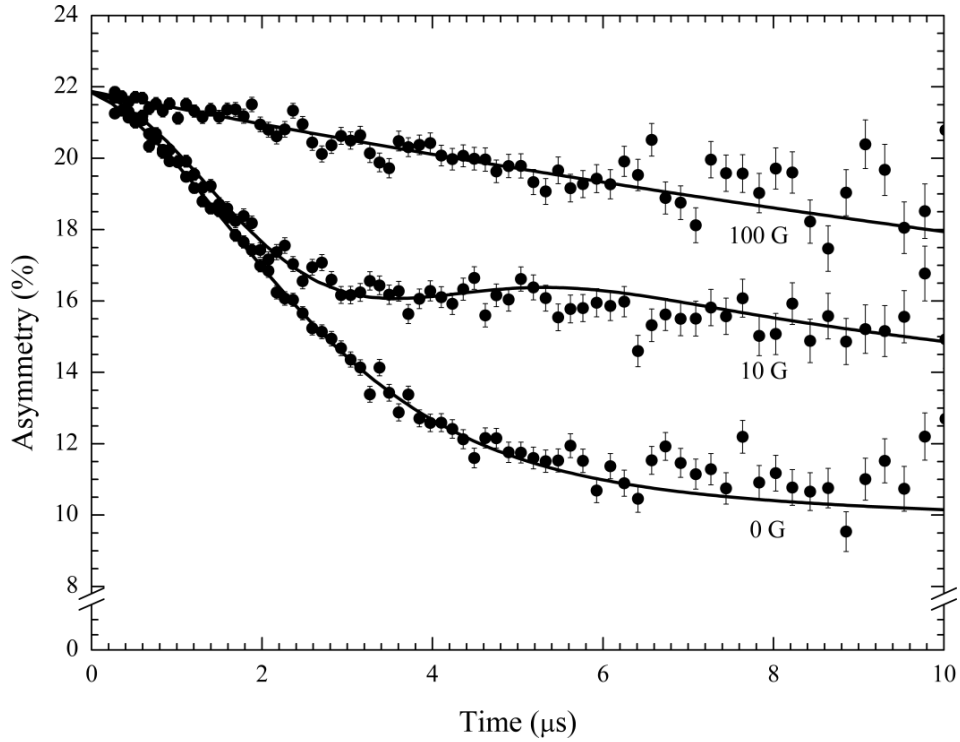


Figure 7:6 The longitudinal field muon spin relaxation spectra from Au_4V observed at 46 K in several applied fields. Eq (7:2) was used to fit both the 0 G and 10 G data. The application of 100 G fully decouples the nuclear dipole fields such that it can be fitted with a single exponential term.

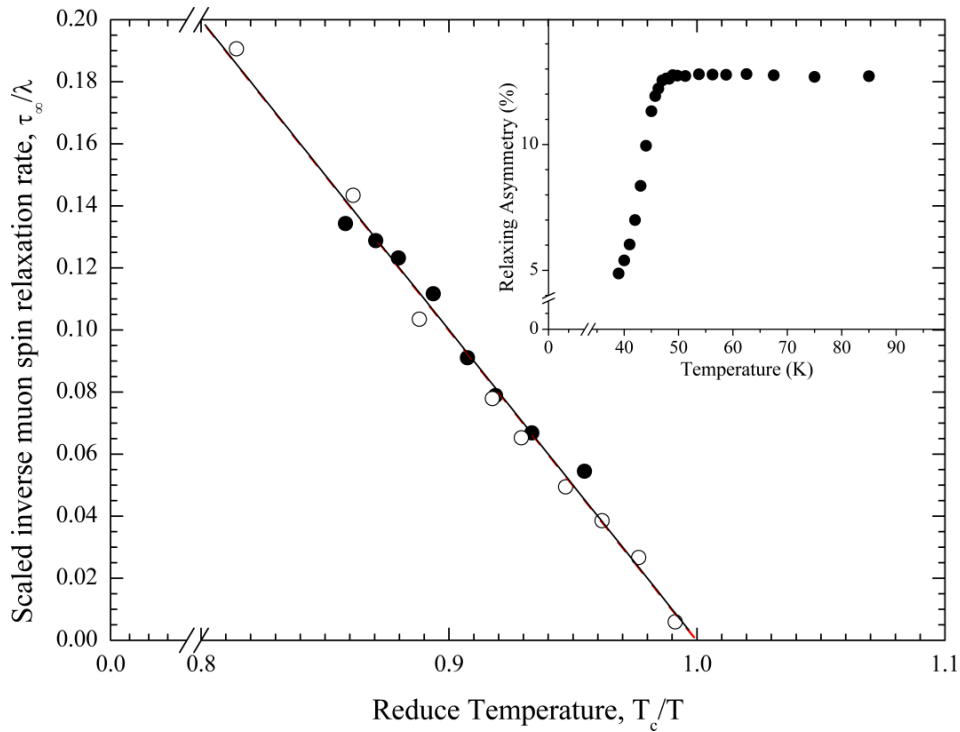


Figure 7:7 The scaled inverse muon spin relaxation rate (τ_∞ / λ) versus reduced temperature for Au_4V (closed circles) and MnSi (open circles). The solid line represents the fit of Eq (7:4) to the data. The experimental points for MnSi are taken from Hayano²³⁴. Inset: The temperature dependence of relaxing asymmetry in Au_4V .

A least square fit of equation (7:4) to the data provides: $T_c = (42.0 \pm 0.2)$ K and $\tau_\infty = (3.17 \pm 0.14) \times 10^{-3} \mu\text{s}^{-1}$. For comparison (τ_∞) for MnSi $T_C = 29.5$ K was found to be $(6.55 \pm 0.13) \times 10^{-3} \mu\text{s}^{-1}$. Figure 7:7 shows the critical scaling of (λ), described by equation (7:4), for both Au₄V and MnSi with the data for the latter taken from *Hayano*²³⁴.

The critical scaling of the muon spin relaxation rate observed for Au₄V shows close similarity with that obtained for the archetypal itinerant electron ferromagnet, MnSi, and correspondingly follows the predications of Moriya's self consistent renormalisation (SCR) theory for itinerant systems²³⁵. In this respect Au₄V may well prove a simpler system with which the mechanisms responsible for moment localisation in itinerant electron magnets can be explored.

Short zero-field measurements were also made on a sample of Au₄V solid solution between 30 K and 5 K. Here all the spectra obtained were identical within experimental error, indicating a stable magnetic environment. However, in contrast to the ordered sample the Kubo-Toyabe function is static, but again seems inclined to take a value of $\sigma \approx 0.34 \mu\text{s}^{-1}$. Thus using equation (7:2) with a fixed fluctuation rate of zero, the muon spin relaxation rate was found to take an almost constant value of $\lambda \approx 0.25 \mu\text{s}^{-1}$.

Chapter 8

CONCLUSION

In this thesis I have presented investigations, using both neutron and muon techniques, concerning the spin dynamics of spin glass, superparamagnet, and random anisotropy magnet systems. To begin with the remarkable magnetic properties of pseudo-binary intermetallic compound $Y(\text{Mn}_{1-x}\text{Al}_x)_2$, due largely to the instability of the manganese moment and topological frustration arising from anti-ferromagnetic correlations on the tetrahedral sub-lattice, were studied by longitudinal muon spin relaxation ($x = 0.05$), diffuse neutron scattering ($0.03 \leq x \leq 0.30$), and neutron spin echo spectroscopy ($x = 0.10$).

Recent neutron diffraction measurements on a sample of ($x = 0.05$) using the OSIRIS instrument at ISIS, had measured the rate at which the lattice parameter contracts under the influence of mechanically applied pressure. It was discovered that 4.5 kbar was sufficient to reduce the value to that of the undoped parent compound, $Y\text{Mn}_2$. The muon is an extremely sensitive local probe of static and dynamic magnetic fields and has previously been used to study the collapse of long-range anti-ferromagnetic order in this system. With this in mind, it was therefore of interest to compare the evolution of the muon depolarisation function with temperature, and therefore the nature of the spin fluctuations, at ambient pressure and 4.5 kbar.

Using the ARGUS spectrometer I have shown at ambient pressure the muon spectra are well described by a depolarisation function of stretched exponential form. This indicates a broadening distribution of relaxation rates as the temperature is decreased, accompanied by a critical slowing of the muon spin relaxation rate. Fitting a critical scaling model to this divergence gives an exponent of $\gamma = 0.8$, which is in close agreement to the value reported previously by *Cywinski et al.* using transverse geometry, $\gamma = 0.9$, for ($x = 0.10$). The calculated transition temperature was also consistent with previous reports, $T_f = 88$ K.

It was found that 4.5 kbar of mechanical pressure induced substantial changes in the depolarisation function, which was described by simple exponential form. The most likely explanation is the muon sensing a single relaxation rate, which is in general wholly uncharacteristic of spin glasses. The relaxation rate is also significantly faster indicating increasing field fluctuations about the muon's position. Lastly, the aforementioned transition at 88 K appears to be totally suppressed.

Based upon these results it can be said that the manganese moment localisation associated with the inverse chemical pressure arising from aluminium substitution is reversible *via* the application of 4.5 kbar pressure but that despite exhibiting a comparable lattice parameter to $Y\text{Mn}_2$ the resulting temperature dependence of the muon spin relaxation rate is altered. This is emphasised all the more by the temperature dependence of the initial asymmetry, which falls rapidly below 100 K. This rapid depolarisation suggests the presence of an additional relaxation process outside the time window of the ARGUS spectrometer.

In §4.4 I have presented for the first time a detailed study of short-range spin correlations in $Y(\text{Mn}_{1-x}\text{Al}_x)_2$ using the D7 diffuse neutron scattering spectrometer at the ILL. Several concentrations were investigated across a wide temperature range, revealing both the initial collapse ($x \geq 0.03$), and progressive decomposition of long-range anti-ferromagnetic order between ($0.05 \leq x < 0.30$). The short-range nuclear correlations were also examined as to include their effects on the diffuse magnetic scattering cross section.

For samples ($x \leq 0.10$) the results indicate the manganese atoms have a propensity to occupy the lower coordination shells, indicating a clustering behaviour which is significantly stronger at ($x = 0.10$). For ($x = 0.30$) however this is reversed, with the occupancy of the first near neighbour shell strongly biased towards aluminium, a phenomenon commonly entitle anti-clustering. The exact cause of such clustering is unknown, but generally forms due to favourable orbital overlaps. This reversal is therefore likely to be associated with the increased unit cell volume.

Inspection of the magnetic scattering cross section revealed it to become progressively more diffuse with increased aluminium substitution, disassembling the long-range anti-ferromagnetic order of the parent compound. This analysis indicates strong anti-ferromagnetic nearest neighbour correlation. It has also been shown that this structure is extremely sensitive to the substitution of non-magnetic aluminium atoms in place of manganese.

The Neutron Spin Echo (NSE) technique has played a vital role during the course this work. What's more these investigations form part of a continuing series of experiments analysing the complex dynamics of disordered magnetic systems: spin glass, RAM, and superparamagnet. Ultimately it is hoped that the Weron-Tsallis function will provide universal physical interpretation of non-exponential relaxation for a wide variety of condensed matter systems. It is vital therefore that the function be tested extensively, not only on a per system basis, but systematically across different relaxation mechanisms and phenomena so that trends (or lack thereof) between individual classes of material can be explored.

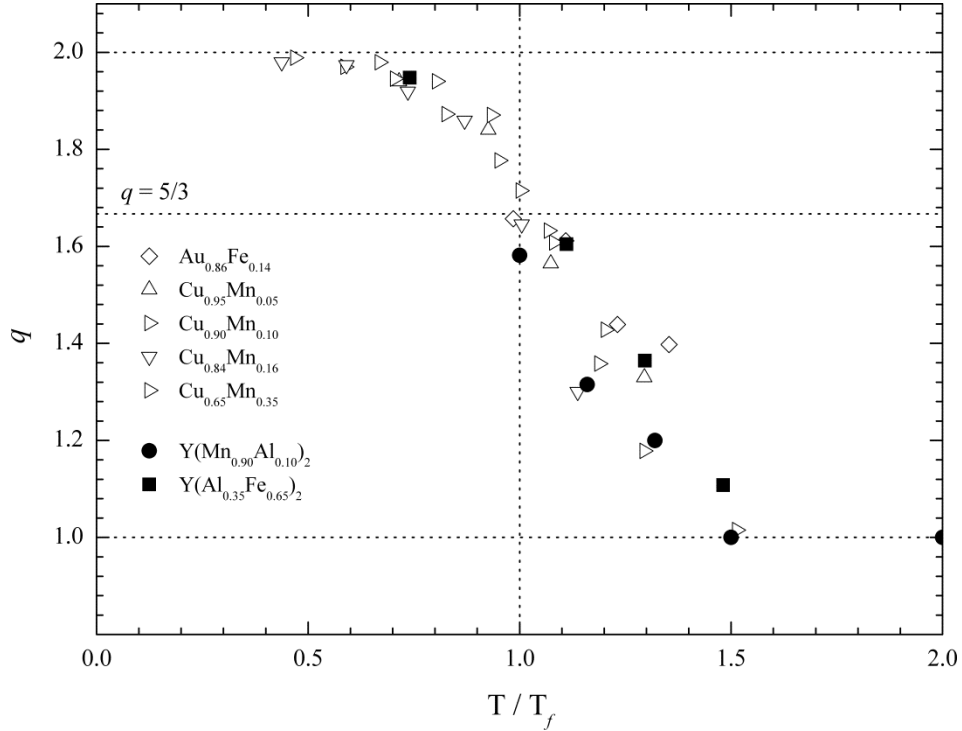


Figure 8:1 Tsallis' non-extensivity parameter calculated from Weron analysis of NSE spectra.

The Weron function has been found to provide a good description of all the NSE spectra measured. This is because the function itself reduced to the stretched exponential in the limit $k \rightarrow 0$, and from stretched exponential to simple Debye relaxation in the limit $\alpha \rightarrow 1$, allowing for a smooth progression from Debye relaxation at elevated temperatures, where the thermal energy is sufficient to overcome all cooperative effects, to the complex response seen at low temperatures where constraints begin to be imposed. It is the Weron interaction parameter (k) which provides a direct measure of the hierarchical constraints imposed on the overall relaxation process.

Brouers & Sotolongo-Costa have related this parameter to Tsallis' non-extensivity parameter, (q), derived from a generalisation of Boltzmann-Gibbs statistics. It has recently been shown by *Pickup & Cywinski* that spin glasses are examples of sub-extensive systems, ($q > 1$), where the entropy of the system as a whole is lower than the sum of its parts. Furthermore, they discovered the temperature dependence of (q) in several dilute spin glass systems to scale very closely. In this thesis I have

extended the investigation to include two concentrated spin glass system, namely $Y(\text{MnAl})_2$ and $Y(\text{AlFe})_2$. The results display temperature dependence of the fractal parameter, (α), consistent with that seen previously for AuFe and CuMn , where a value close to unity was measured at high temperatures, before falling to approximately 0.3 at T_f . However for these systems a smaller initial value at high temperature, indicating a distribution of relaxation rates is present at temperatures significantly higher than the transition. This proved problematic in one respect as that the measured relaxation occurred over time scales significantly wider than the window accessible to NSE instruments. Therefore to aid the fitting process an artificial point was included to pin the spectra at very short times outside the fourier time range of the instrument. The temperature dependence of the non-extensivity parameter, shown in Figure 8:1, offers the clearest indication of a sudden onset of hierarchical constrain close to T_f , which maps directly onto the same q scaling relationship reported for the dilute systems. Analysis of Tsallis relaxation function has shown the transition to be marked by the critical value $q = 5/3$ which is associated with the strong disorder limit, where the macroscopic behaviour begins to be governed by highly improbable collective events.

Prior to this work the Random Anisotropy Magnet (RAM) $\alpha\text{-Er}_7\text{Fe}_3$ had revealed results quite different to those of spin glass systems⁸¹. In short, (q) was found to be temperature independent, suggesting little or no cooperative freezing in RAMs at low temperature. The analysis of RAM-like system $(\text{LaEr})\text{Al}_2$ is unable to corroborate this result. As discussed, such systems are dominated by a large anisotropy to exchange strength ratio, resulting in a random distribution of moments frozen at low temperature. The analysis presented in §5.2.2 reveals a temperature dependent (α) parameter which initially takes a value close to unity falling gradually with decreasing temperature, followed by a discontinuous drop to a constant value of 0.2 below $\sim 3T_f$. The temperature dependence of (q), shown in Figure 8:2, also exhibits a sudden drop at this temperature. Fitting the Vogel-Fulcher law to the relaxation rate reveals $T_0 / T_K = 0.03$, indicating that the system is extremely fragile and the dynamics therefore occur over a very narrow temperature range.

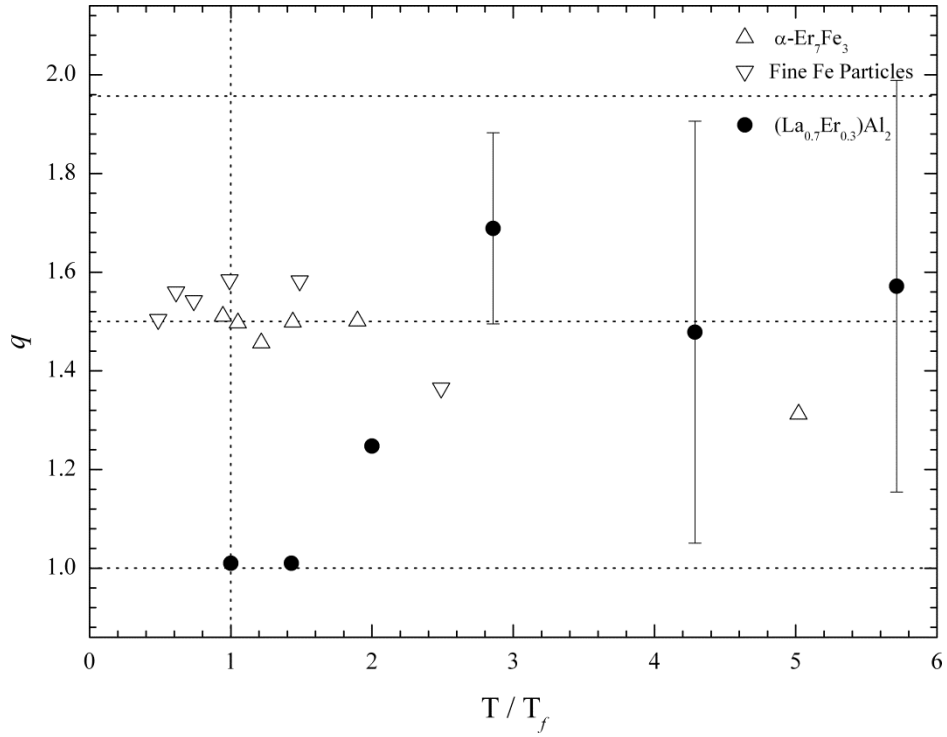


Figure 8:2 Tsallis' non-extensivity parameter for RAM systems investigated using NSE spectroscopy. The q -error for reduced temperatures less than 2 do not fit on this scale, hence are not shown.

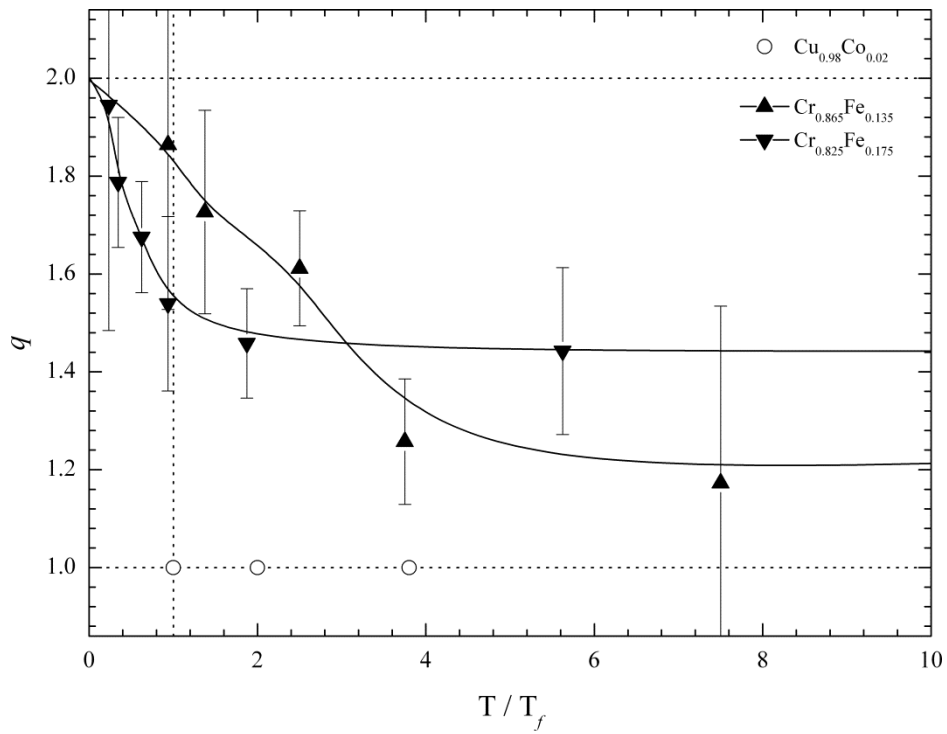


Figure 8:3 Tsallis' non-extensivity parameter for superparamagnetic systems; solid lines are guides to the eye.

The final NSE investigations presented in this work centred on superparamagnet CrFe. Superparamagnetic systems do not display cooperative relaxation behaviour since each paramagnetic cluster is considered to be independent of the others; hence the entropy of the system should equal the sum of its parts and therefore be compliant with Boltzmann-Gibbs statistics. The non-extensivity parameter should therefore be equal to unity, which was the case in a previous study on archetypal superparamagnetic system CuCo. However I have shown $\text{Cr}_{1-x}\text{Fe}_x$ to display quite different behaviour, Figure 8:3. In the first instance a measurements at $x = 0.135$ required a modification to the Weron function due to what appears to be an extremely slow additional “background” relaxation process.

This term was found to be temperature dependent, showing a gradual linear increasing from zero to 0.2 between 180 K and 20 K, before increasing far more rapidly until at $T_f = 11$ K it accounts for approximately half the total measured autocorrelation function. However the Weron function still provides a good description of the non-exponential part of the spectra and what is more the parameters are, in a qualitatively sense, consistent with those calculated for a sample at $x = 0.175$ which did not require this additional background term.

Both concentrations displayed a temperature independent fractal parameter (α) which takes the same value of unity. Assuming the non-exponential term is associated with the superparamagnetic iron clusters this would indicate that the fractal nature of the relaxation is unchanged and the relaxation time, (τ), is directly proportional to the cluster volume, it would therefore seem more likely that the mechanism responsible for the additional background term is due to the chromium which has previously been shown to display an inhomogeneous and progressive conversion to long range anti-ferromagnetic SDW.

Over the temperature range investigated the interaction parameter (k) does not fall to unity, as would be expected for independently relaxing entities, but instead takes a largely temperature independent value of 1.2 for $x = 0.135$ and 1.4 for $x = 0.175$, above $2T_f$, suggesting that there are constraints imposed on this non-exponential relaxation even at elevated temperature. To confirm this behaviour further

measurements are required in this range. Moreover, below $2T_f$ the non-extensivity parameter increases rapidly, showing clearly for the first time that the dynamics of this system are in fact constrained in much the same way as a spin glass. The magnetic nature of the CrFe system is therefore more complicated than first thought, not only due to the iron clusters which may not be truly superparamagnetic but also the distinct possibility of an underlying relaxation mechanism associated with the chromium spin density wave.

Lastly, I have presented a muon spin relaxation study on the weak itinerant ferromagnetic Au_4V , applying the predictions of Moriya's Self Consistent Renormalisation Theory to the critical scaling to the spin relaxation rate, making comparison to the archetypal weak itinerant system MnSi which has led to the discovery that the critical scaling plotted against reduced temperature are near-identical for both systems.

Suggestions: Like YMn_2 , many weak itinerant ferromagnetic (ZrZn_2 , Ni-Pt, Ni-Al) and anti-ferromagnetic alloys (Cr-Fe) display magneto-volume effects. Accordingly, this presents a particularly interesting area of investigation given the results present in this work. Recently high pressure sample environments have been made available on the D7 instrument. During the investigation presented in §4.4 two attempts were made, using different pressure cell equipment, to study the pressure dependence of the diffuse neutron scattering cross sections, however for reasons unknown the results were unusable. Without doubt this new setup will be optimised in the near future, at which time such experiments could reveal crucial information to complement these studies.

The IN11 instrument is due to be decommissioned shortly, and is being replaced by a wide-angle spin echo spectrometer named WASP. Currently scientists must trade count rate for resolution, or vice versa, when using IN11, either choosing a wide angle or conventional setup. The Helmholtz design of the WASP spectrometer is expected to provide 50 times the data rate, whilst achieving the highest resolution currently available on IN11. Given the high expense of neutron spin echo technique

and its high demand amongst scientists, this will provide a remarkable advancement in the field.

It was found that the concentrated spin glass systems exhibit dynamics across a very wide time range leading to difficulty, not in applying the Weron function but in maintaining consistent parameters, particularly in (τ) and (k) , below and far above the transition temperature where the spectra fall outside the window of NSE spectroscopy. This was aided by including an artificial data point in many of the spectra measured during this work; however it would be far more appropriate to use complimentary techniques. AC susceptibility would provide access to longer times, whereas the backscattering instrument IRIS at ISIS would, through Fourier transform of its scattering function, $S(\mathbf{Q}, \omega)$, provide access to shorter relaxation times.

APPENDIX: PUBLICATIONS



12th International Conference on Muon Spin Rotation, Relaxation and Resonance

Pressure Dependent Magnetism in $Y_{1.05}(Mn_{0.95}Al_{0.05})_2$

K.J. Ellis ^{a*}, R. Cywinski ^a, F.L. Pratt ^b and M.T.F. Telling ^{b,c}

^aUniversity of Huddersfield, Huddersfield, HD1 3DH, United Kingdom

^bISIS Facility, Rutherford Appleton Laboratory, OX11 0QX, United Kingdom

^{c†} Department of Materials, University of Oxford, Parks Road, Oxford, OX1 3PH, United Kingdom

Abstract

The Laves phase compound YMn_2 exhibits a discontinuous transition from a spin fluctuating Pauli paramagnetic state above 110 K to an expanded, localised moment helical antiferromagnetic state below 110 K. Substitution of Al for Mn in the pseudo-binary compound $Y(Mn_{1-x}Al_x)_2$ exerts a negative chemical pressure, expanding the unit cell and further localizing the Mn moment. Here we present the results of a μ SR study of spin fluctuations in $Y(Mn_{1-x}Al_x)_2$ ($x = 0.05$) in which external mechanical pressure (4.5 kbar) is applied to counteract the Al induced chemical pressure and destabilize the local Mn moment.

Keywords: $Y(MnAl)_2$; itinerant electron magnetism; muon spin relaxation

1. Introduction

The cubic C15 Laves phase compound, YMn_2 , is Pauli paramagnetic down to 110 K at which temperature a discontinuous 5 % volume expansion occurs and the Mn moment spontaneously localises. Neutron powder diffraction has shown that this transition is accompanied by a tetragonal distortion of the unit cell and the onset of long range antiferromagnetic ordering consistent with a spin arrangement in which the moments lay in the (1,0,0) plane, propagating helically along both the [1,0,0] direction with a period of 430 Å and the [0,1,0] direction with a period in the order of 2500 Å [1]. Further studies have shown that the average Mn-Mn separation in YMn_2 plays a significant role in the localization of the 3d manganese moments and, through the partial substitution of Mn for larger or smaller atoms, the Mn moment can be stabilised or made to collapse entirely [2]. YMn_2 and its ternary derivatives are therefore interesting model systems with which to explore the mechanisms responsible for moment localisation in

* Corresponding author; E-mail address: k.ellis@hud.ac.uk

† Position held: Academic Visitor

3d spin fluctuating systems, for example within the framework of Moriya's Self Consistent Renormalisation (SCR) theory of spin fluctuations [3].

The substitution of Al for Mn in $Y\text{Mn}_2$ increases the Mn-Mn separation and leads to a gradual transition from the itinerant behaviour of $Y\text{Mn}_2$ to more localised behaviour. While the volume expansion and moment localisation remains discontinuous for $x < 0.03$, the increasing Mn-Mn distance resulting from the negative chemical pressure exerted by the Al atoms, together with the disruption of the long range anti-ferromagnetic order caused by the non-magnetic aluminium, leads to a continuous phase change for concentrations greater than $x = 0.03$. Between $x = 0.03$ and $x = 0.10$, a highly frustrated spin glass-like magnetic state is observed [4].

Previously μSR has proved extremely useful in the extensive characterisation of the spin dynamics and the collapse of long range magnetic order resulting from inverse *chemical* pressure on $Y(\text{Mn}_{0.9}\text{Al}_{0.1})_2$ [5]. Here, we present the results of a μSR study of $Y(\text{Mn}_{1-x}\text{Al}_x)_2$ with $x = 0.05$ in which we have applied *external* mechanical pressure ($P = 4.5$ kbar) to counteract the chemically induced expansion of the lattice in order to explore whether the Mn moment can once again be destabilised and a pure $Y\text{Mn}_2$ -like state recovered.

2. Experimental Details

The $Y_{1.05}(\text{Mn}_{0.95}\text{Al}_{0.05})_2$ sample was prepared by melting stoichiometric proportions of pure (99.995 %) constituent materials in a water cooled argon arc furnace. Excess yttrium was added to prevent the formation of the highly ferromagnetic $Y_6\text{Mn}_{23}$ impurity phase. The polycrystalline ingots were sealed in quartz ampoules under vacuum and annealed at 800 °C before quenching in liquid nitrogen. The resulting ingots were then crushed into a fine powder.

The high pressure ($P = 4.5$ kbar) μSR experiments were carried out at the RIKEN-RAL muon facility using the ARGUS spectrometer with the sample loaded into a Copped-Beryllium (CuBe) pressure cell. The pressure was applied using a helium gas intensifier and monitored as the temperature was reduced. Any pressure drop, resulting from helium contraction, was compensated for to ensure that the pressure remained at a constant 4.5 kbar even at the lowest temperatures. Simplification of the background response arising from nuclear dipole relaxation associated with the pressure cell material was achieved by applying a 110 Gauss longitudinal field, as shown in Figure 1(a). As a reference, ambient pressure (i.e. $P = 0$ kbar) measurements were collected using the MuSR spectrometer at the ISIS facility, with the sample loaded onto a silver plate. All spectra were analysed using the data analysis program WIMDA [6].

3. Results and Discussion

Under ambient pressure conditions ($P = 0$ kbar), all spectra collected in the paramagnetic regime are well described using a muon spin relaxation function, $G_z(t)$, of the form,

$$G_z(t) = \exp(-(\lambda t)^\beta) \quad (1)$$

with a stretching parameter, β , that is predominantly less than unity (Figure 1(b) insert); β falling from unity at room temperature to approximately 1/3 by 85K. Such behaviour is a characteristic of many concentrated spin glass systems and, for β values less than 1, generally indicative of the muon sensing a distribution of μ^+ spin relaxation processes within the sample [7, 8]. The associated effective relaxation rate, $\lambda(T)$, is seen to increase slowly as the temperature decreases from 290 to 100 K before diverging.

In contrast, application of 4.5 kbar is seen to produce a marked change in both $\beta(T)$ and $\lambda(T)$. Not only is the magnitude of $\lambda(T)$, which peaks at approximately 50 K, significantly reduced when the system is subjected to high pressure, but β tends to unity at all measured temperatures. Such a simple exponential description of the data suggests that the muon senses a single relaxation process. This simple exponential form of $G_\mu(t)$ is consistent with the response reported for the parent compound, YMn_2 [1]. Figure 1(b) compares $\lambda(T)$ at ambient pressure and 4.5 kbar.

Preliminary analysis of $\lambda(T, P = 0)$, by fitting a critical scaling model to the data, namely,

$$\lambda(T) = \lambda_0 \left(\frac{T - T_g}{T_g} \right)^{-\gamma} \quad (2)$$

yields a transition temperature of $T_g = 88.8 \pm 0.2$ K. Similar parameterisation of the $P = 4.5$ kbar data, however, is compromised by significant uncertainty in the resulting fit parameters. The failure of equation (2) to model, with precision, the high pressure data may suggest a significant change in the nature of the spin fluctuations with applied pressure.

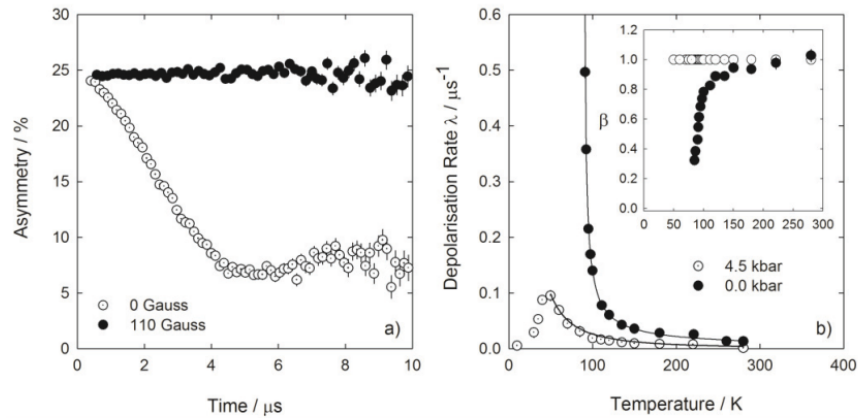


Figure 1: (a) Suppression of nuclear dipole relaxation from the CuBe pressure cell via application of an external longitudinal field of 110 Gauss. (b) Temperature dependence of the muon spin depolarization rate, $\lambda(T)$, with the $Y_{1.05}(Mn_{0.95}Al_{0.05})_2$ sample at (\bullet) ambient pressure and (\circ) under 4.5 kbar. The solid lines are, for the $P = 0$ kbar data, a fit to equation 2 and, for the $P = 4.5$ kbar data, a guide to the eye. Insert: The temperature and pressure dependence of the stretching exponent, β .

4. Conclusions

The stretched exponential description of muon spin relaxation spectra collected from $Y(Mn_{0.95}Al_{0.05})_2$ at ambient pressure, and in the paramagnetic regime, is consistent with that expected from a concentrated, rather than dilute, spin-glass-like system [7]. A glass transition temperature of $T_g = (88.8 \pm 0.2)$ K has been determined by fitting a critical form to the data. T_g determined in this way is consistent with

previously reported values [4]. In contrast, application of 4.5 kbar external pressure not only leads to slower muon spin depolarisation rates, but also suppresses the aforementioned magnetic transition temperature and significantly changes the form of the muon spin relaxation function, $G_z(t)$, required to describe the data: $G_z(t)$ evolving from a stretched to a simple exponential. Such a response is indicative of the muon sensing a single, rather than distributed, relaxation process when the sample is subject to external pressure. It is possible that application of external pressure destabilises the Mn moments, significantly suppressing the spin glass transition and returning the system to a spin fluctuating magnetic state with a simple exponential μ^+ spin relaxation response similar to that observed from the parent compound (YMn_2) under ambient conditions. Based upon the results presented here, it appears that 3d Mn moment localisation, associated with the introduction of inverse chemical pressure arising from Al substitution for Mn, is reversible.

Acknowledgements

The authors would like to thank the UK's Science and Technology Facility Council for access to the ISIS facility, Rutherford Appleton Laboratory. The authors would also like to thank Drs Adrian Hillier, Peter Baker and Steve Cottrell for their help and suggestions during the experiment. KJE wishes to acknowledge EPSRC for financial support through the award of a "Next Generation Facilities User" postgraduate studentship.

References

- [1] R. Cywinski, S. H. Kilcoyne, and C. A. Scott, Magnetic Order and Moment Stability in YMn_2 , *Journal of Physics-Condensed Matter* 1991; **3**: 6473-6488.
- [2] R. Cywinski, S. H. Kilcoyne, and C. Ritter, The Loss of Antiferromagnetism in Fe-substituted YMn_2 , *Applied Physics a-Materials Science & Processing* 2002; **74**: 865-867.
- [3] T. Moriya, and Y. Takahashi, Spin Fluctuations in Itinerant Electron Magnetism, *J. Phys. Colloques* 1978; **39**: 1466-1471.
- [4] M. Shiga *et al.*, Characteristic Spin Fluctuations in $Y(Mn_{1-x}Al_x)_2$, *Journal of Physics F-Metal Physics* 1987; **17**: 1781-1793.
- [5] R. Cywinski, and B. D. Rainford, Spin Dynamics in the Spin-Glass Phase of $Y(Mn_{1-x}Al_x)_2$, *Hyperfine Interactions* 1994; **85**: 215-220.
- [6] F. L. Pratt, WIMDA: A Muon Data Analysis Program for the Windows PC, *Physica B* 2000; **289**: 710-714.
- [7] I. A. Campbell *et al.*, Dynamics in Canonical Spin-Glasses Observed by Muon Spin Depolarization, *Physical Review Letters* 1994; **72**: 1291-1294.
- [8] R. M. Pickup, R. Cywinski, and C. Pappas, A Novel Approach to Modelling Non-exponential Spin Glass Relaxation, *Physica B-Condensed Matter* 2007; **397**: 99-101.

Pressure-dependent spin fluctuations and magnetic structure in the topologically frustrated spin glass alloy $Y(\text{Mn}_{0.95}\text{Al}_{0.05})_2$

M. T. F. Telling,^{1,2,*} K. S. Knight,¹ F. L. Pratt,¹ A. J. Church,¹ P. P. Deen,^{3,4} K. J. Ellis,⁵ I. Watanabe,⁶ and R. Cywinski⁵¹ISIS Facility, Rutherford Appleton Laboratory, Chilton, OX11 0QX, United Kingdom²Department of Materials, University of Oxford, Parks Road, Oxford, OX1 3PH, United Kingdom³Institut Laue-Langevin, BP 156, 6, rue Jules Horowitz, 38042 Grenoble Cedex 9, France⁴European Spallation Source (ESS AB), St Algotan 4, Lund, Sweden⁵School of Applied Science, University of Huddersfield, Huddersfield, HD1 3DH, United Kingdom⁶RIKEN, 2-1 Hirosawa, Wako, Saitama 351-0198, Japan

(Received 19 January 2012; revised manuscript received 29 March 2012; published 17 May 2012)

Longitudinal field (LF = 110 G) muon spin relaxation (μ SR) has been used to investigate the pressure dependence ($P < 4.5$ kbar) of paramagnetic spin fluctuations in the spin glass alloy $Y(\text{Mn}_{0.95}\text{Al}_{0.05})_2$ via observation of the μ^+ spin depolarization. External mechanical force is seen to counteract the Al-induced chemical pressure, fully delocalizing the Mn moment and altering the nature of the spin fluctuation spectrum sensed by the muon. A qualitative change in the functional form of the μ^+ spin depolarization is observed. Complementary ambient and high-pressure neutron diffraction measurements suggest not only pressure-dependent structural transitions but also the instability of the localized manganese moment. The ambient and high-pressure μ^+ spin depolarization results from $Y(\text{Mn}_{0.95}\text{Al}_{0.05})_2$ are likened to $P = 0$ results reported for other $Y(\text{Mn}_{1-x}\text{Al}_x)_2$ alloys. Finally, the possibility of using μ^+ spin depolarization rates to predict experimental inelastic neutron scattering (INS) line widths is considered; the muon having the potential to provide information equivalent to that obtained via INS but with greatly reduced data collection times.

DOI: 10.1103/PhysRevB.85.184416

PACS number(s): 76.75.+i, 28.20.Cz, 75.50.Lk

I. INTRODUCTION

The cubic Laves phase compound YMn_2 ¹ is of interest since it allows theoretical advances that attempt to establish a unified understanding of magnetism to be evaluated.² A member of the RMn_2 ($R = \text{rare earth}$) family of alloys, YMn_2 is best described as a system of well-defined local moments below its antiferromagnetic (AF) ordering temperature ($T_N = 110$ K). In contrast, the paramagnetic phase is more accurately described using an itinerant electron picture within the framework of Moriya's self-consistent renormalization (SCR) theory of spin fluctuations.

At room temperature, YMn_2 supports a cubic C15 structure with a lattice constant of 7.682 \AA ³ ($V_{\text{unit cell}} = 453.34 \text{ \AA}^3$). Upon cooling, the lattice contracts until, at 110 K, a discontinuous, or first order, volume expansion of the unit cell is observed ($\Delta V/V = 5\%$). Correspondingly, the unit cell changes from a cubic (space group: Fd-3m) to tetragonal (space group: $F4_1/d \ 1 \ 2/m$ ($I4_1/amd$)) geometry. Below 110 K, long-range antiferromagnetic (AF) order ensues with the system assuming a helically modulated magnetic structure with a periodicity of about 400 angstroms. Upon warming, marked hysteretic behavior is observed in both lattice parameter and magnetic susceptibility.⁴ These uncommon magnetic properties are a result of i) the proximity of the system to Mn moment instability and ii) topological frustration arising from antiferromagnetic correlations on lattices of corner sharing tetrahedra.⁵ The system exhibits large amplitude spin fluctuations⁶ and a great sensitivity of the magnetic properties to the unit cell volume.

The first-order phase transition in YMn_2 is extremely sensitive to *mechanical* and *chemical* pressure. The Néel point may be fully suppressed by applying 2.7 kbar of external pressure or by inducing "chemical pressure" via, for example,

the substitution of 2.5 at. % Fe for Mn.⁷ Such results indicate that small reductions in the Mn-Mn nearest neighbor distance precipitate a collapse of AF order as the Mn moments revert to a spin-fluctuating state. It is worth mentioning that the existence of a threshold between localized and itinerant magnetism in RMn_2 intermetallic compounds was first observed using NMR.⁸ In brief, Mn moment localization was purported to be governed by interatomic distance after the ⁵⁵Mn hyperfine field was seen to collapse for those RMn_2 alloys with cubic lattice constants less than approximately 7.52 Å (at 4.2 K).

In contrast, partial substitution of aluminium for manganese, i.e., $Y(\text{Mn}_{1-x}\text{Al}_x)_2$, is seen to expand the unit cell.⁴ Here, the magnitude of the volume expansion at the Néel point decreases with increasing Al concentration until, for $Y(\text{Mn}_{0.90}\text{Al}_{0.10})_2$, no volume anomaly is observed. While the phase transition remains first order for $x < 0.03$, percolation of the Al atoms leads to a second-order progression for substituent concentrations greater than $x \sim 0.03$. Moreover, the Mn moments become progressively more localized with increasing Al content. Evidence for this itinerant-local moment crossover comes from the Curie-Weiss-like⁴ appearance of high-temperature bulk susceptibility measurements as well as thermal expansion behavior in accordance with the predictions of SCR theory. Between $x \sim 0.03$ and $x \sim 0.10$, however, a highly frustrated magnetic ground state is observed. The evolution of diffuse magnetic Bragg peaks in neutron diffraction data,⁹ in conjunction with field hysteresis in the susceptibility measurements, suggests short-range spin glass correlations in this compositional range.

Previously, to complement ongoing research into local and itinerant moment magnetism in RMn_2 alloys,^{10,11} we used transverse field (TF) and zero-field (ZF) μ SR to probe spin dynamics, the collapse of long range antiferromagnetic

order and the onset of magnetic frustration in $\text{Y}(\text{Mn}_{1-x}\text{Al}_x)_2$ ($0.0 < x < 0.30$). In C15 compounds, the muon is most likely to reside at the so-called (2-2) site,¹³ with each muon having two Y atoms and two Mn atoms as nearest neighbors. As such, the muon proves itself to be a sensitive local probe of static and dynamic magnetic phenomena. For alloys with $x < 0.03$, we find that in the paramagnetic regime the μ^+ spin relaxation response exhibits characteristics analogous to that of a wholly spin fluctuating ground state. In contrast, muon spin relaxation observed from $\text{Y}(\text{Mn}_{0.90}\text{Al}_{0.10})_2$ favours the Kohlrausch form, as predicted for concentrated spin glass systems.¹⁴ To further this work we have now used longitudinal field (LF = 110 Gauss) muon spin relaxation (μSR) to investigate the pressure dependence ($P < 4.5$ kbar) of paramagnetic spin fluctuations in the spin glass alloy $\text{Y}(\text{Mn}_{0.95}\text{Al}_{0.05})_2$ via observation of the μ^+ spin depolarization; an alloy which exhibits local moment Curie-Weiss-like characteristics but with an Al concentration bordering magnetic frustration.

Complementary neutron diffraction measurements, which illuminate crystallographic anomalies and pressure-dependent manganese moment stability, are also described. In addition, the ambient and high-pressure spin depolarization results from $\text{Y}(\text{Mn}_{0.95}\text{Al}_{0.05})_2$ are likened to μSR measurements (previously unpublished work or reported by other authors) from other $\text{Y}(\text{Mn}_{1-x}\text{Al}_x)_2$ alloys. Our results also add to previous neutron diffraction studies which report the influence of chemical pressure [$\text{Y}(\text{Sc})(\text{Mn}_{1-x}\text{Al}_x)_2$]¹⁵ and applied external pressure [$\text{Ho}(\text{Mn}_{0.9}\text{Al}_{0.1})_2$]¹⁶ on other Al-doped Laves phase RMn_2 alloys.

A. Itinerant electron magnets and μ^+ relaxation: experimental SCR predictions

Qualitative SCR predictions for the temperature dependence of the muon response expected from different 'itinerant' systems in the paramagnetic regime are summarized below. While $\text{Y}(\text{Mn}_{1-x}\text{Al}_x)_2$ is not considered to be a weakly itinerant magnetic system, we report Moriya's findings here since we liken our ambient and high-pressure results to these predictions; application of pressure perhaps inducing a SCR response.

To summarize, the SCR² theory of spin fluctuations (i.e., electron-hole pair excitations) was developed by Moriya in 1985 from earlier self-consistent models by Moriya and Kawabata¹⁷ and Murata and Doniach.¹⁸ SCR was developed to address difficulties encountered using the Hartree-Fock random phase approximation (HF-RPA) method to describe the behavior of itinerant electron magnets. For example, SCR theory explains experimentally observed reduced ordered moment sizes, Curie-Weiss behavior of the uniform susceptibility and reduced transition temperatures. The ability to observe directly the $1/T_1$ relaxation of electron moments via the muon spin depolarization parameter λ ($=1/T_1$) using μSR allows the efficacy of SCR predictions to be tested. The evolution of the temperature dependence of $1/T_1$ expected from different 'itinerant' systems (for example, localized moment magnet (i.e., EuO) \rightarrow itinerant ferromagnet (i.e., Fe) \rightarrow weak itinerant ferromagnet (i.e., MnSi) \rightarrow nonmagnetic metal (i.e., Al)) is given in Ref. 2. With regard to weakly ferromagnetic materials, SCR theory suggests that if the susceptibility, χ , follows

the Curie-Weiss form, then the qualitative prediction for the temperature dependence of the muon spin depolarization above T_c is,

$$\lambda = \frac{1}{T_1} \propto \frac{T}{T - T_c} \quad (1)$$

In contrast, the temperature dependence of λ predicted using the HF-RPA¹⁹ method is $1/T_1 \propto T/(T^2 - T_c^2)$, while a localized moment system usually does not depend upon temperature, except for a narrow critical region near the transition. Equation (1) has been successfully used to describe the temperature dependence of the measured spin-lattice relaxation rate in MnSi (Hayano *et al.*²⁰); MnSi being an itinerant electron system that orders with a long period helical spin structure below a Curie temperature of $T_c \sim 30$ K. The muon measurements were taken with the sample subject to a longitudinal field of 122 Gauss to decouple the dynamical relaxation from the sizable static nuclear dipolar fields arising from ⁵⁵Mn nuclei. While the dynamic fluctuations of electron spins were too fast to observe at room temperature, closer to T_c measurable dynamical relaxation, well described using Eq. (1), became visible. More recently, μSR studies of weak itinerant electron ferromagnetism in Au₄V have also supported SCR predictions.²¹ In contrast, for weak itinerant electron antiferromagnets,

$$\lambda = \frac{1}{T_1} \propto \frac{T}{(T - T_N)^{1/2}} \quad (2)$$

when the susceptibility displays Curie-Weiss behavior. Here, the muon spin depolarisation rate is predicted to increase with temperature as \sqrt{T} for $T \gg T_N$. On the contrary, $\lambda(T)$ predicted using the HF-RPA method is $1/T_1 \propto T/(T^2 - T_N^2)^{1/2}$. To our knowledge, surprisingly few weak itinerant AF systems have been used to test Moriya's theory using muons. Perhaps the most widely studied itinerant electron system displaying strong antiferromagnetic spin fluctuations is YMn_2 itself.

II. EXPERIMENTAL DETAILS

Since μSR ^{13,22} and neutron diffraction^{23,24} are well-established techniques, and described in detail elsewhere, only an overview pertinent to this work is given here.

A. Muon spin relaxation (μSR)

In ZF- μSR experiments, detectors are positioned along the muon beam direction in front of, and behind, the sample. Relaxation spectra are determined from the time-dependent positron count rates collected in the forward $F(t)$ and backward $B(t)$ detectors via the expression,

$$P_z(t) = A_o G_z(t) = \frac{F(t) - \alpha B(t)}{F(t) + \alpha B(t)} \quad (3)$$

where $P_z(t)$ describes the time dependence of the muon spin polarization. A_o is the initial asymmetry (i.e., the asymmetry at time $t = 0$) and α is a calibration term to account for the relative efficiencies of the counters in the forward and backward detectors and for absorption within the sample and sample environment apparatus. α is determined from

a spectrum collected with the sample subject to a small transverse magnetic field of 2 mT (20 Gauss). $G_z(t)$ is the longitudinal muon spin relaxation function.

In a system of concentrated static magnetic dipoles, the resulting internal magnetic field distributions in each of the x , y and z directions are Gaussian centered around zero. Larmor precession of muon spins in such an environment, averaged over all muon sites, leads to, a relaxation function of the form,²⁵

$$G_z(t, \sigma) = \frac{1}{3} + \frac{2}{3}(1 - \sigma^2 t^2) \exp\left(-\frac{\sigma^2 t^2}{2}\right) \quad (4)$$

where σ is the width of the Gaussian distribution. Equation (4) is known as the zero-field static Gaussian Kubo-Toyabe (K-T) relaxation function.²⁵ In contrast, rapid fluctuations of the internal magnetic fields, however, lead to motional narrowing and a simple exponential muon spin relaxation function is observed,

$$G_z(t) = \exp(-\lambda t) \quad (5)$$

where $\lambda = 2\sigma^2\tau_c$ and τ_c is the correlation time of field fluctuations. Fluctuation rates between 10^8 and 10^{13} Hz can be measured using μ SR.

For concentrated spin glasses, numerical simulations of Ising systems by Ogielski²⁶ have shown that above the glass transition temperature, T_g , the local dynamic spin autocorrelation function is proportional to a stretched exponential, $\langle S_x(0)S_x(t) \rangle \propto q(t) \propto \exp(-(\lambda t)^\beta)$, with β' increasing from $1/3$ at the glass transition to unity at $4T_g$. A possible thermodynamic explanation of this behavior in spin glasses based upon the Tsallis concept of subextensive entropy in strongly interacting disordered systems has recently been proposed.²⁷ ZF- μ SR studies by Campbell *et al.*¹⁴ have demonstrated that longitudinal muon spin relaxation measurements are sensitive to such nonexponential, or Kohlrausch, spin relaxation in concentrated spin glass systems. Campbell shows that the corresponding muon relaxation function also takes the form,

$$P_z(t) \propto \exp[-(\lambda t)^\beta] \quad (6)$$

with $\lambda(T)$ diverging at the glass transition and $\beta(T)$ approaching $1/3$.

The high-pressure LF- μ SR measurements presented here were collected using the RIKEN-RAL high-energy muon facility (Port 2) at the ISIS Pulsed Neutron and Muon source, Rutherford Appleton Laboratory, UK.^{28,29} The powdered sample was loaded into a Copper-Beryllium (CuBe) pressure cell. Pressures within the cell were generated using a helium gas intensifier. The relative percentage of signal from the sample to signal from the CuBe cell was $\sim 20\%$; the physical thickness of the CuBe cell limiting sample volume. As a result, the high pressure measurements were performed in 110 G longitudinal field (LF) to greatly simplify the background response from the CuBe [Fig. 1]. The ambient pressure ($P = 0$ kbar) LF- μ SR (LF = 110 G) measurements presented here were collected using the MuSR facility at ISIS. The powdered sample was loaded into a flat plate silver sample holder. All muon relaxation spectra were analyzed using the WIMDA program suite.³⁰ For the high-pressure work ($P = 4.5$ kbar), the background response from the pressure cell was first

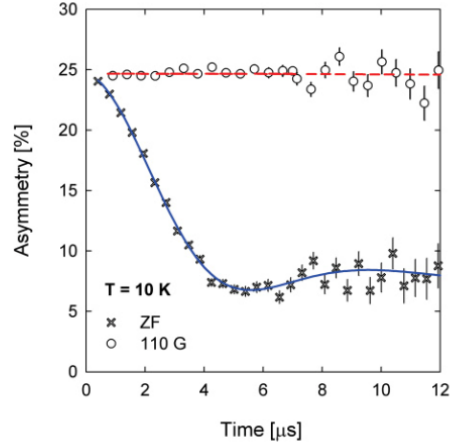


FIG. 1. (Color online) Suppression of nuclear dipole relaxation, associated with the CuBe pressure cell material, via application of an external longitudinal field of 110 G. The dashed line is the result of fitting the LF data (\circ) to a Gaussian relaxation function. The solid line is the result of fitting the ZF data (\times) to a Kubo-Toyabe and a Gaussian relaxation function.

fully characterized as a function of temperature and applied field. This background response was then adjusted, and fixed, temperature point by temperature point during the analysis of spectra collected from the sample. For both pressures ($P = 0$ and $P = 4.5$ kbar), data was collected upon warming with the longitudinal field being applied after the sample had been cooled to base temperature in zero applied field.

B. Nuclear Bragg diffraction

A couple of comments should be made regarding the analysis of neutron diffraction data. First, it is not the purpose of this work to refine the magnetic neutron scattering intensity but to simply observe and characterize its temperature dependence. A detailed study of the evolution of magnetic scattering from $Y(Mn_{1-x}Al_x)_2$ alloys at ambient pressure, as revealed using neutron spin polarization analysis, will be presented elsewhere. An overview of magnetic neutron diffraction can be found in the references given at the start of this section. Second, contamination of the $Y(Mn_{0.95}Al_{0.05})_2$ diffraction data at short d spacing by pressure-dependent Bragg reflections arising from solidified helium, as well as intense Bragg reflections from the Al pressure cell, precludes detailed structural analysis using the Rietveld method. Changes in the volume of the unit cell and/or structural anomalies are therefore gauged by either monitoring the d spacing associated with certain lattice reflections or via peak shape analysis of individual Bragg reflections. Such analysis was performed using the LeBail intensity extraction option coded into the profile refinement package, GSAS.³¹

High-pressure ($0 < P < 4.5$ kbar) neutron diffraction measurements were collected using the backscattering diffraction capabilities of the OSIRIS³² instrument at ISIS. Previous

neutron work³ shows the magnetic reflections from the helical magnetic structure assumed by YMn_2 below T_N to lie between approximately 2 and 5.5 Å. OSIRIS is ideally suited to probe such a d -spacing range and affords both high flux and resolution at the corresponding wavelengths (i.e., 4 – 10 Å). The sample was mounted in an aluminium pressure cell and high pressures were generated using a helium gas intensifier. Lattice spacings were determined using the profile refinement package GSAS.³¹ Instrument-specific parameters necessary for the refinement procedure were determined by analyzing a neutron diffraction pattern collected from a National Institute of Standards and Technology (NIST) reference material; namely silicon (SRM640c).

C. Sample preparation

A 20 g polycrystalline ingot of $\text{Y}(\text{Mn}_{0.95}\text{Al}_{0.05})_2$ was prepared by melting together the appropriate quantities of 99.995% pure constituents using the argon arc melting technique. Losses were less than 2% and attributed to Mn evaporation during the melting process. To avoid formation of the highly magnetic impurity phase, Y_6Mn_{23} , excess Y was added to the level of 5%. The resulting ingot was sealed under vacuum in a quartz ampoule and annealed at 800 °C with subsequent quenching in liquid nitrogen. The alloy was crushed into a fine powder. The same $\text{Y}(\text{Mn}_{0.95}\text{Al}_{0.05})_2$ sample was used for both the neutron and muon work presented here.

III. RESULTS AND ANALYSIS

A. Neutron diffraction: Room temperature (290 K)

At room temperature, $\text{Y}(\text{Mn}_{0.95}\text{Al}_{0.05})_2$ exhibits the same cubic crystal structure (space group: Fd-3m) as the parent compound, YMn_2 . The variation of the Fd-3m unit cell parameter at $T = 290$ K and as a function of (i) increasing external pressure (for the 5 at. % Al alloy) and (ii) increasing Al concentration is shown in Fig. 2. The data is compared to previously reported ambient pressure results.³³ No pressure-induced structural change is observed using OSIRIS. Instead, we find that at 290 K application of external pressure simply results in a linear decrease of the cubic cell parameter until, by 4.5 kbar, the lattice spacing of $\text{Y}(\text{Mn}_{0.95}\text{Al}_{0.05})_2$ resembles that of YMn_2 .

B. Neutron diffraction: Base temperature (10 K)

Analysis of diffraction data collected from YMn_2 at 10 K, using OSIRIS, reveals that the parent compound favors a tetragonal, rather than cubic, unit cell at base temperature. A splitting of the (400) reflection into the (004) and (220) reflections is clearly observed, as shown in Fig. 3. This result is in excellent agreement with work reported by Cywinski *et al.*³ using the high resolution diffractometer, HRPD (ISIS, $\Delta d/d \sim 10^{-4}$). The tetragonal space group $[F4_1/d \ 1 \ 2/m \ (I4_1/amd)]$ proposed by³ for YMn_2 at 10 K was used to fit our OSIRIS data. We find that for YMn_2 in the tetragonal phase $a = b = 7.74$ Å, while $c = 7.702$ Å.

It is not unreasonable to suggest that $\text{Y}(\text{Mn}_{0.95}\text{Al}_{0.05})_2$ also undergoes a similar structural transformation. This hypothesis is supported by the weak structural anomaly observed in the

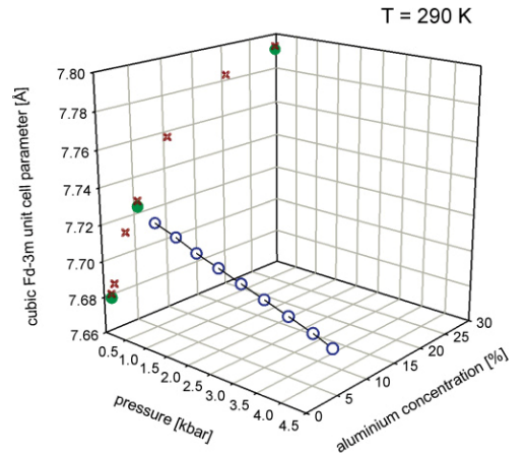


FIG. 2. (Color online) The variation of the cubic Fd-3m unit cell parameter at $T = 290$ K in $\text{Y}(\text{Mn}_{1-x}\text{Al}_x)_2$ as a function of (i) aluminum concentration (\bullet) and, for 5 at. % Al, external pressure (\circ). The variation of cell parameter as a function of Al concentration as reported by Shiga *et al.*³⁴ is shown for reference (\times).

temperature dependence of the (111) nuclear reflection at 100 K [see Fig. 6(c), top]. If correct, and also tetragonal in nature, then as Fig. 3 shows, the resolution of the OSIRIS instrument ($\Delta d/d \sim 10^{-3}$) is clearly not sufficient to resolve splitting of Bragg reflections arising from a tetragonal lattice. While LeBail peak shape analysis of the diffraction data using a tetragonal space group provides an adequate description, higher-resolution diffraction may elucidate subtle structural changes.

It should also be noted that, unlike YMn_2 , comparison of 10 and 250 K data reveals an increase in the intensity of all nuclear Bragg reflections at low temperature, by as much as $\Delta I_{10-250\text{K}}/I_{250\text{K}} = 14\%$ for the (111) reflection shown in Fig. 3. Such a response could suggest long-range ferromagnetic correlations. To test this hypothesis, we collected data from $\text{Y}(\text{Mn}_{0.95}\text{Al}_{0.05})_2$ at 10 K using the neutron polarization analysis technique (D7 diffuse scattering spectrometer, Institut Laue Langevin, Grenoble, France).³⁵ Our results show no evidence of magnetic scattering intensity at the nuclear Bragg positions (Fig. 4). Furthermore, we see no evidence of spin depolarization of the scattered neutron beam. Neutron spin depolarization would imply ferromagnetic correlations within the sample. We therefore attribute the origin of this increased scattering intensity at the nuclear positions to be structural rather than magnetic. It is also worth commenting that since D7 has very coarse instrumental resolution, and a limited Q range, any structural refinement of the nuclear scattering intensity would prove incomplete. A detailed overview of the neutron polarization analysis technique, the D7 spectrometer and complete analysis of magnetic scattering from our neutron diffraction and polarization studies of $\text{Y}(\text{Mn}_{0.95}\text{Al}_{0.05})_2$ will be presented elsewhere.

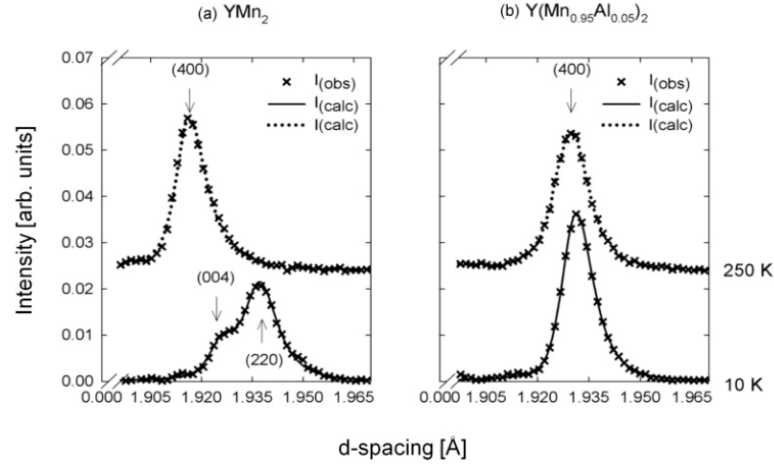


FIG. 3. (a) Tetragonal splitting of the YMn_2 (400) Bragg reflection at 10 K as observed using OSIRIS. The upper dashed line is a LeBail peak fit to 250 K data assuming cubic Fd-3m symmetry. The solid line is a LeBail peak fit to the 10 K data using the tetragonal ($I4_1/amd$) model. (b) Evolution of the (400) Bragg reflection for $\text{Y}(\text{Mn}_{0.95}\text{Al}_{0.05})_2$. The upper dashed line is a LeBail peak fit to 250 K data assuming cubic Fd-3m symmetry. While there is no visible splitting at 10 K, the solid line is a LeBail peak fit using the tetragonal ($I4_1/amd$) model. Peak analysis in this way suggest $a = b = 7.7115(5)$ Å and $c = 7.729(14)$ Å. The high-temperature data has been vertically offset for clarity.

Instead, weak antiferromagnetic satellite reflections are evident at base temperature and at d spacings of approximately 2.45, 3.14, 3.45, and 5.45 Å. These d spacings correspond to momentum transfer (Q) values of 2.56, 2.0, 1.82, and 1.15 \AA^{-1} , respectively. Application of 4.5 kbar, however, is sufficient to completely suppress these magnetic reflections. As an example, the pressure dependence of the (2 0 1) antiferromagnetic Bragg reflection is presented in Fig. 5(b). The decrease in magnetic scattering intensity is accompanied by an anomalous decrease in the peak position of the nuclear (111) lattice reflection for pressures greater than 3.5 kbar, as illustrated in Fig. 5(a).

C. Neutron diffraction: Warming (10–250 K)

Upon warming, and with the $\text{Y}(\text{Mn}_{0.95}\text{Al}_{0.05})_2$ sample at ambient pressure, a structural anomaly is observed at approximately 100 K. The ambient pressure peak position of the (111) nuclear Bragg reflection is plotted as a function of temperature ($2 < T \text{ (K)} < 250$) in Fig. 6(c) [top]. In contrast, application of 4.5 kbar is sufficient to inhibit the volume expansion observed at 100 K when $P = 0$. Instead, we detect a weak structural anomaly closer to 50 K [Fig. 6(c), top].

As stated in the Introduction, Mn moment localization in RMn_2 alloys is reportedly governed by interatomic distance such that the Mn moment collapses for RMn_2 lattice constants less than approximately $d_c = 7.52$ Å at 4.2 K.⁸ In the case of a cubic Laves phase alloy, this corresponds to a critical Mn-Mn distance of approximately 2.66 Å. For $\text{Y}(\text{Mn}_{0.95}\text{Al}_{0.05})_2$, however, collapse of long-range magnetic order below 4.5 kbar

[Fig. 5(b)] does not appear to be a consequence of the unit cell parameter (d) crossing d_c . At room temperature we find that d falls linearly from 7.72 Å at ambient pressure to 7.68 Å by

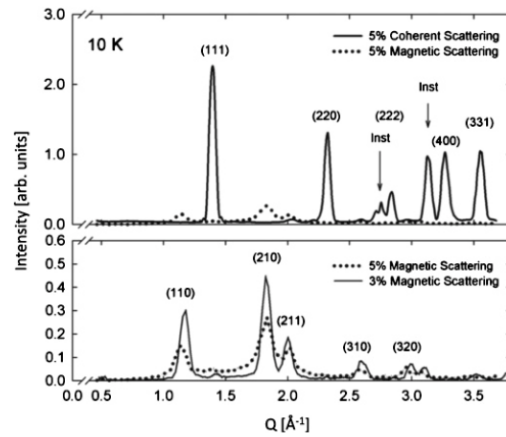


FIG. 4. Nuclear spin coherent (top) and magnetic scattering (bottom) from 5 at. % Al at 10 K. Magnetic scattering from 3 at. % Al is shown to accentuate the diffuse nature of the magnetic scattering from the 5 at. % Al alloy. The data was collected using the diffuse scattering spectrometer, D7, at the Institut Laue Langevin, Grenoble, France. Inst = Bragg reflections originating from the D7 instrument. The nuclear and magnetic peaks have been indexed according to Motoya.⁹

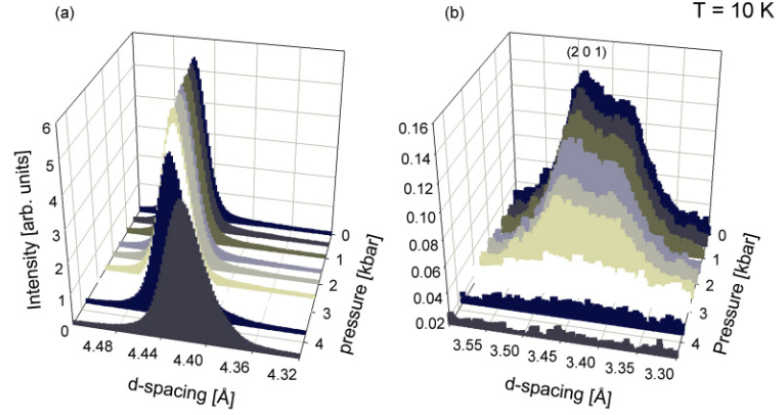


FIG. 5. (Color online) Pressure dependence of the (a) nuclear (111) and (b) antiferromagnetic (201) Bragg reflections at $T = 10$ K. The background from the empty pressure cell has been subtracted from the data.

$P = 4.5$ kbar (Fig. 2). Such a rate of compression corresponds to a bulk modulus, K_0 (GPa) = volume $\cdot \Delta P / \Delta V \sim 29$ GPa. This result is consistent with that reported for the parent compound, YMn_2 .^{36,37} For comparison, at 10 K (and assuming a cubic symmetry due to the limited instrument resolution) two distinct regions of compressibility are observed between ambient and the highest pressure. Below 3.5 kbar, a linear decrease in lattice parameter is observed with d reducing from 7.71 Å ($P = 0$) to 7.68 Å ($P = 3.5$). Such a change corresponds to a $\Delta V_{P=0-3.5} / V_{P=0} \sim 1\%$ and a bulk modulus value of 30 GPa. Above 3.5 kbar, however, an anomalous change in the rate of $d(P)$ is observed [see Fig. 5(a)]. While no meaningful bulk modulus information can be extracted for pressures greater than 3.5 kbar, this point of inflexion does correspond to the collapse of the local Mn moment. Nonetheless, applied external pressures less than 4.5 kbar (0.45 GPa) appear insufficient to drive d below the reported critical point; the cubic unit cell parameter of $\text{Y}(\text{Mn}_{0.95}\text{Al}_{0.05})_2$ at 4.5 kbar and 10 K being 7.64 Å. This may not be so surprising given that at ambient temperature approximately 3.5 GPa of pressure is required to drive the lattice parameter of YMn_2 from 7.68 to 7.52 Å.³⁶

D. Longitudinal field Muon spin relaxation (LF- μ SR)

Longitudinal field- μ SR, in conjunction with the ARGUS CuBe high-pressure cell apparatus,²⁹ was used to investigate the collapse of magnetic order on a *local* level. As previously mentioned, both sample and empty pressure cell spectra were collected upon warming, and at the same temperatures, in a longitudinal field of 110 Gauss to greatly simplify the background response of the CuBe apparatus. We find no evidence to suggest that application of a longitudinal field of 110 G significantly perturbs the spin fluctuation spectrum of $\text{Y}(\text{Mn}_{0.95}\text{Al}_{0.05})_2$. We do observe slight recovery of μ^+ spin depolarization in 110 G compared to ZF. This result suggests a weak static contribution to the μ^+ depolarization measured in zero field. This static contribution most likely arises from nu-

clear dipoles. Application of 110 G is sufficient to suppress this static contribution, leaving only μ^+ depolarization originating from electronic fluctuations.

Depolarization spectra and associated fits to the data collected at ambient pressure and $P = 4.5$ kbar are shown in Figs. 6(a) and 6(b). The resulting fit parameters are compared in Figs. 6(c) and 6(d). We find that between 85 and 300 K, the ambient pressure data is well described by a stretched exponential relaxation function; full asymmetry (0.23) being recovered at short times at all temperatures within this regime. We find that β falls from unity at 280 K to 0.33 at 85 K as predicted for a concentrated spin glass system.¹⁴ Correspondingly, the μ^+ spin depolarization rate (λ) starts to diverge below 120 K.

In contrast, a pressure of 4.5 kbar induces a simple, rather than *stretched*, exponential μ^+ spin relaxation response [Fig. 6(b)] between 50 and 280 K. The depolarization rate increases from $0.002 \mu\text{s}^{-1}$ at room temperature to $0.1 \mu\text{s}^{-1}$ at 50 K. The sudden drop in the asymmetry parameter (A_0) below 100 K indicates the presence of a *second* relaxing component. The rate of this relaxation process, however, is beyond the frequency resolution of the ARGUS instrument. As a result, we are unable to characterize the magnitude and temperature dependence of this additional relaxation term.

The temperature dependence of $\lambda(T, P = 0)$ and $\lambda(T, P = 4.5)$ is highlighted in Fig. 6(c). We find that over the temperature range studied $\lambda(T, P = 0)$ favors a critical scaling model, namely,

$$\lambda(T) = \lambda_0 \left(\frac{T - T_{\text{trans}}}{T} \right)^{-\gamma} \quad (7)$$

which yields a transition temperature, T_{trans} , or in this case glass transition, $T_g = 88.2 \pm 0.2$ K with a critical exponent, γ , equal to 0.92 ± 0.09 . A critical exponent of 0.92 is not unreasonable for a spin glass material. For example, previously reported values of γ range from 0.94 in the cluster glass CrFe (with 17 at. % Fe)³⁸ to 2.6 to 2.9 in the dilute spin glasses CuMn and AuFe .³⁹ Similar parameterization of the $P = 4.5$ kbar

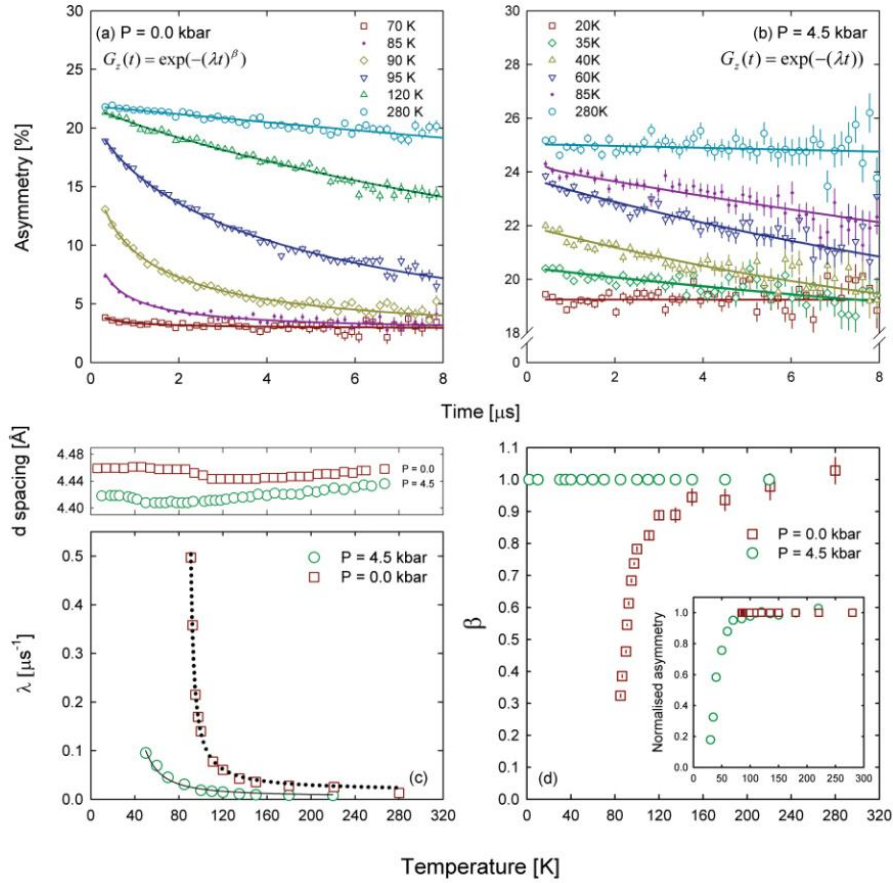


FIG. 6. (Color online) Muon spin relaxation spectra and associated fits to the data collected from $\text{Y}(\text{Mn}_{0.95}\text{Al}_{0.05})_2$ at (a) ambient pressure and (b) $P = 4.5$ kbar. Figure (b) highlights the sizable background signal (bck $\sim 18\%$) originating from the CuBe pressure cell. (c) Comparison of μ^+ spin relaxation rates at ambient pressure and $P = 4.5$ kbar. The solid (Arrhenius fit) and dotted lines (critical form) are fits to the data as described in the text. Top: The temperature dependence of the peak position of the (111) nuclear Bragg reflection at 4.5 kbar and ambient pressure as revealed by neutron diffraction. The data suggests structural transitions at approximately 100 K ($P = 0$) and 50 K ($P = 4.5$). (d) Temperature and pressure dependence of the asymmetry (inset) and beta parameters used to model the observed muon spin depolarization. The asymmetry parameter has had the background component removed and been normalized to $A_a(280\text{ K})$.

data, however, is compromised by significant uncertainty in the resulting, and highly correlated, fit parameters. Instead, $\lambda(T, P = 4.5)$ is better described from 50 to 280 K using the Arrhenius form,

$$\lambda(T) = \lambda_0 \exp\left(-\frac{E_a}{k_B T}\right) \quad (8)$$

with $E_a/k_B = 150 \pm 9$ K. The changing nature of the temperature dependence of $\lambda(T, P)$ is accentuated in Fig. 7(b), where our μ^+ spin depolarization results from $\text{Y}(\text{Mn}_{0.95}\text{Al}_{0.05})_2$ are compared to published, and previously unreported, ambient-pressure relaxation rates from

other $\text{Y}(\text{Mn}_{1-x}\text{Al}_x)_2$ alloys; namely (i) the parent compound, YMn_2^3 (TF measurement, MuSR spectrometer), (ii) an alloy with 10 at. % Al¹² (ZF measurement, MuSR) and (iii) $\text{Y}(\text{Mn}_{0.70}\text{Al}_{0.30})_2$ (ZF, MuSR, previously unpublished). The data points shown have been extracted from the references given. Like $\text{Y}(\text{Mn}_{0.95}\text{Al}_{0.05})_2$ at $P = 0$, the temperature dependence of μ^+ spin relaxation from YMn_2 is well described using Eq. (7). Modeling the data in this manner gives a Néel temperature of 93 ± 7 K. T_N determined in this way is in good agreement with previously reported values.⁴ In contrast, while adequately described using Eq. (7),¹² the temperature dependence of $\lambda(T)$ from $\text{Y}(\text{Mn}_{0.90}\text{Al}_{0.10})_2$, as

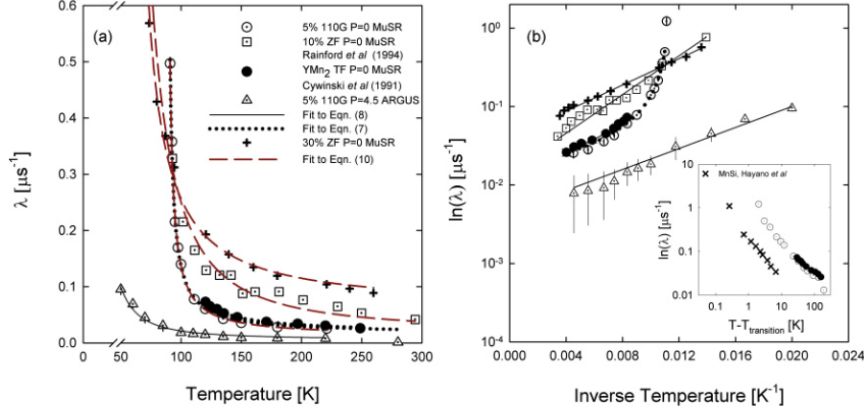


FIG. 7. (Color online) (a) Comparison of μ^+ spin depolarization rates collected from $\text{Y}(\text{Mn}_{0.95}\text{Al}_{0.05})_2$ [$P = 0.0$ (\odot) and 4.5 kbar (Δ)] with other reported, and previously unpublished, $\text{Y}(\text{Mn}_{1-x}\text{Al}_x)_2$ ambient pressure data; namely, YMn_2 ³ (\bullet , TF measurement), $\text{Y}(\text{Mn}_{0.90}\text{Al}_{0.10})_2$ ¹² (\square , ZF), and $\text{Y}(\text{Mn}_{0.70}\text{Al}_{0.30})_2$ ($+$, ZF, unpublished). The lines are fits to the data as described in the text. (b) μ^+ spin depolarization rates plotted as $\ln(\lambda)$ vs. T^{-1} to accentuate the changing temperature, pressure, and concentration dependence of $\lambda(T, P)$. The solid or dotted lines are fits to the data as described in the text. Inset: the magnitude of μ^+ spin depolarization rates from YMn_2 and $\text{Y}(\text{Mn}_{0.95}\text{Al}_{0.05})_2$ compared directly to the response reported for the weak itinerant electron ferromagnet, MnSi, as presented by Hayano in.²⁰

well as $\text{Y}(\text{Mn}_{0.70}\text{Al}_{0.30})_2$, is best described using the Arrhenius form, as illustrated in Fig. 7(b).

IV. DISCUSSION

We have used complimentary longitudinal field (LF = 110 Gauss) muon spectroscopy (μSR) and neutron diffraction techniques to probe the pressure dependence of magnetic order in $\text{Y}(\text{Mn}_{0.95}\text{Al}_{0.05})_2$ on a *bulk* (structure, neutron) and *local* (dynamical, muon) level. The muon spin relaxation results are compared to those reported for other $\text{Y}(\text{Mn}_{1-x}\text{Al}_x)_2$ alloys at ambient pressure.

For $\text{Y}(\text{Mn}_{0.95}\text{Al}_{0.05})_2$, ambient-pressure muon spectra are well described at all temperatures in the paramagnetic regime ($T > 100$ K) using a muon spin depolarization function of stretched exponential form. On a local scale at least, this response is indicative of a broadening distribution of relaxation rates, as witnessed by the tendency of β to fall to approximately 1/3 by 85 K and an accompanying divergence of the μ^+ depolarization rate below approximately 110 K. Over this temperature range (85 K $< T < 110$ K) neutron diffraction measurements suggest that the alloy undergoes a weak structural distortion; a distortion accompanied by the onset of antiferromagnetic (AF) satellite reflections. Considering the diffuse nature of the magnetic structure, and the weak accompanying volume anomaly that signifies the localization of the Mn moments, it is likely that such a distribution arises from regions of well-localized, interacting, but topologically exchange frustrated Mn spins which, at low temperatures, form a concentrated spin glass-like phase. The temperature dependence of $\lambda(T, P = 0)$ is well described using a critical scaling model with a scaling exponent equal to unity. It is interesting to note that modeling $\lambda(T, P = 0)$ from $\text{Y}(\text{Mn}_{0.95}\text{Al}_{0.05})_2$, and YMn_2 , using the critical form gives,

within error, a value for γ equal to unity. For $\gamma = 1$, Eq. (7) reduces to Eq. (1); the SCR prediction for a weak itinerant electron ferromagnet. This result is perhaps not so surprising considering the Curie-Weiss temperature dependence of the local susceptibility displayed by these two alloys.⁴⁰ While we have no reason to describe these materials as weak itinerant electron ferromagnetic systems, the magnitude of the μ^+ spin depolarization rate determined from YMn_2 and $\text{Y}(\text{Mn}_{0.95}\text{Al}_{0.05})_2$ ($P = 0$) is likened [Fig. 7(b), inset] to the response reported for a weak itinerant electron ferromagnet, namely MnSi,²⁰ for comparison.

Application of 4.5 kbar external pressure, however, induces a substantial change in both the observed form of the muon spin depolarization function and the temperature dependence of $\lambda(T)$. Rather than stretched behavior, $G_z(T, 4.5 \text{ kbar})$ is seen to favor a simple exponential form. Such a response suggests that the muon senses a single spin depolarization rate, which is uncharacteristic of a wholly frustrated ground state. Indeed, under 4.5 kbar of applied external pressure, the spin depolarization rate is considerably less than that observed at $P = 0$. For example, at 150 K the ambient pressure relaxation rate is $\lambda(T, P = 0) = 0.0393 + / - 0.002 \mu\text{s}^{-1}$, whereas under 4.5 kbar of applied pressure the system exhibits a depolarization rate of $\lambda(T, P = 4.5) = 0.0169 + / - 0.0026 \mu\text{s}^{-1}$. This result indicates that the application of 4.5 kbar induces *either* substantially smaller internal fields or faster spin fluctuations. In contrast to the ambient pressure response, not only do paramagnetic spin fluctuations appear to exist down to approximately 50 K but the divergence of $\lambda(T, P = 4.5)$ suggests that the muon senses a magnetically driven transition at this lower temperature. Further evidence for a transition is signified by the response of the initial asymmetry parameter, $A_0(T, 4.5 \text{ kbar})$. The temperature dependence of A_0 suggests that this transition is not only discontinuous but that

a second rapid depolarization process, beyond the frequency window of the ARGUS spectrometer, is present. The presence of this additional, yet immeasurable, relaxation process at short times suggests that *below* 100 K, application of 4.5 kbar induces large, initially inhomogeneous, internal fields at the μ^+ site which rapidly depolarize all nearby muons. Indeed, the pressure-induced change in the nature of the spin fluctuation spectrum is further illuminated by the evolution of the temperature dependence of $\lambda(T, P)$; from following a critical scaling model at $P = 0$ to an Arrhenius response by $P = 4.5$.

The changes observed in the muon response at 4.5 kbar can be related to structural changes observed on a bulk level using neutron diffraction. First, it is worth mentioning that at room temperature ($T = 290$ K) application of external pressure results in a linear decrease of the cubic unit cell parameter until, by 4.5 kbar, the volume of the unit cell of $\text{Y}(\text{Mn}_{0.95}\text{Al}_{0.05})_2$ is comparable to that of the parent compound, YMn_2 . Nonetheless, despite exhibiting a unit cell comparable to that of YMn_2 , application of 4.5 kbar does not induce the same spin depolarization rate. Second, neutron diffraction data collected at 10 K shows that application of 4.5 kbar is sufficient to completely inhibit formation of the antiferromagnetic satellite reflections observed at ambient pressure; hence localization of the Mn moments. The pressure dependence of the (201) AF reflection at 10 K suggests that the collapse of the Mn moment begins at approximately 2.5 kbar. Furthermore, the onset of this collapse seems coincident with the structural anomaly seen in the pressure-dependent peak position of the (111) nuclear Bragg reflection. It is likely that the observed reduction in lattice spacing is driven by a magneto-volume effect related to the collapse of the local Mn moments; local moments which, as seen in YMn_2 , serve to expand the unit cell. It is not unreasonable to suggest, therefore, that when subject to an external pressure of $P = 4.5$ kbar, the Mn moment becomes inherently unstable and the system reverts to a wholly itinerant, rather than local moment, state. Maintaining 4.5 kbar, and warming the sample from base temperature to room temperature, results in a weak structural anomaly at ~ 50 K. It is interesting to note that the divergence of the muon spin depolarisation rate, $\lambda(T, P = 4.5)$, is coincident with this structural change. It is likely that the structural change is linked to the magnetic phenomena driving the muon response. On a bulk level, however, no long-range magnetic order is observed in the neutron diffraction data available. It is, of course, possible that the upper working pressure (5.0 kbar) of the CuBe cell is insufficient to fully transform the sample; as suggested by the continuously evolving position of the (111) nuclear reflection in Fig. 5(a). Nonetheless, as we have shown in $\text{Cr}_{1-x}\text{Mo}_x$,⁴¹ the muon is supremely sensitive to weak magnetic phenomena. At this stage, the mechanism driving this structural anomaly, and hence the nature of the transition, is not clear. Nonetheless, considering the qualitative SCR predictions given previously, our results suggest that application of 4.5 kbar does not induce a response in $\lambda(T, P = 4.5)$ indicative of a weak itinerant ferromagnetic or antiferromagnetic ground state.

Muon spin depolarization rates from four $\text{Y}(\text{Mn}_{1-x}\text{Al}_x)_2$ alloys (≤ 30 at. % Al) at ambient pressure are compared in Fig. 7. The magnitude of the transverse field muon spin depolarization rate reported for YMn_2 in the paramagnetic

phase ($T > 110$ K) is comparable to that measured from $\text{Y}(\text{Mn}_{0.95}\text{Al}_{0.05})_2$; despite $G_z(t)$ for YMn_2 favoring a simple, rather than stretched, exponential form. In contrast, the magnitude of $\lambda(T)$ for alloys with 5 at. % Al $< x \leq 30$ at. % Al shows a marked increase with increasing Al substitution. Like $\text{Y}(\text{Mn}_{0.95}\text{Al}_{0.05})_2$, $G_z(t)$ for the 10 at. % Al and 30 at. % Al alloys assumes the stretched form.¹² However, the threefold increase in spin depolarization rate observed from the 10 at. % Al alloy (and which is further accentuated by 30 at. % Al) is likely to arise from larger fields or slower spin fluctuations at the muon site. Of the two scenarios, the latter is deemed more likely considering previously reported inelastic neutron scattering line width, $\Gamma(T)$, studies of spin fluctuations in $\text{Y}(\text{Mn}_{1-x}\text{Al}_x)_2$ alloys.⁴⁰ Such a result is perhaps unsurprising considering the ever more localized nature of the Mn moment with increased Al doping.

Finally, it is worth concluding by commenting that our ambient pressure results from $\text{Y}(\text{Mn}_{0.95}\text{Al}_{0.05})_2$ further support predictions that the temperature dependence of $\lambda(T, P = 0)$, as determined from the muon on a local level, may be directly compared with bulk inelastic neutron scattering line-width measurements, $\Gamma(T)$, via the formalism described by Lovesey.⁴² To summarize,¹² the depolarization rate, $\lambda(T)$, may be related to the neutron line width, $\Gamma(Q)$, using the expression,

$$\lambda(T) = \frac{BT\chi_L}{\Gamma(Q)} \quad (9)$$

Preceding inelastic neutron scattering measurements^{9,43} reveal that in $\text{Y}(\text{Mn}_{0.9}\text{Mn}_{0.1})_2$ not only is the inelastic line width relatively independent of wave vector, Q , but varies with temperature according to the Arrhenius law, i.e., $\Gamma(T) = \Gamma_0 \exp(-E_a/k_B T)$. Moreover, the local susceptibility in this alloy is seen to be Curie-Weiss like, i.e., $\chi_L(T) = C/(T + \theta_w)$. Consequently, the expression for $\lambda(T)$ can be written,

$$\lambda(T) = \frac{cT}{(T + \theta_w) \exp(-E_a/k_B T)} \quad (10)$$

where $c = BC/\Gamma_0$. Here, the activation energy (E_a) and Curie-Weiss (θ_w) temperature parameters are derived from neutron scattering line width analysis. This model assumes (i) that the inelastic line width is relatively insensitive to momentum transfer, (ii) the inelastic line width varies with temperature according to the Arrhenius form and (iii) the T dependence of the local susceptibility, χ_L , of the Mn atoms is Curie-Weiss like. While inelastic neutron scattering has validated these assumptions for 3 at. % Al and 10 at. % Al alloys, they are yet to be tested from a neutron perspective for a 5 at. % Al sample. Nonetheless, it is not unreasonable to hypothesize that these assumptions also hold for alloys in the intermediate compositional range, i.e., 3 at. % Al $< x < 10$ at. % Al. While Eq. (10) does provide a remarkably accurate description of the ambient pressure 5 at. % Al data (fit parameters: $E_a/k_B = 35$ K and $\theta_w = -88$ K), it should be noted that the fit shown in Fig. 7(a) is relatively insensitive to θ_w . Nonetheless, a negative value of θ_w is consistent with the predominately antiferromagnetic exchange interactions expected from this system. Further measurements, using both other $\text{Y}(\text{Mn}_{1-x}\text{Mn}_x)_2$ alloys and other magnetic systems, are necessary to test the full efficacy of Eq. (10) once experimentally determined E_a/k_B and θ_w

parameters derived from inelastic neutron measurements are incorporated. It is worth mentioning, however, that $\lambda(T, P = 0)$ from $\text{Y}(\text{Mn}_{0.70}\text{Al}_{0.30})_2$ is also well described using Eq. (10); the fit suggesting a negative Curie temperature [Fig. 7(a)].

V. SUMMARY

We have used longitudinal field (LF = 110 G) muon spin relaxation (μSR) to investigate the pressure dependence ($P < 4.5$ kbar) of paramagnetic spin fluctuations in the spin glass alloy $\text{Y}(\text{Mn}_{0.95}\text{Al}_{0.05})_2$ via observation of the μ^+ spin depolarization. Compared to ambient pressure measurements, external mechanical force is seen to counteract the Al-induced chemical pressure and significantly alter the nature of the spin fluctuation spectrum sensed by the muon. Complementary high-pressure neutron diffraction measurements show that application of 4.5 kbar is sufficient to fully delocalize the Mn moment and induce a wholly spin fluctuating magnetic ground state. Such high pressure also precipitates a weak structural transition at 50 K coincident with a divergence in the μ^+ spin depolarization rate. Such a response is indicative of a magnetic transition. While the mechanism driving this structural anomaly is unclear, the temperature dependence of $\lambda(T, P = 4.5)$ is not suggestive of a weak itinerant ferromagnetic or antiferromagnetic ground state as predicted by SCR theory.

The ambient and high pressure μ^+ spin depolarization results from $\text{Y}(\text{Mn}_{0.95}\text{Al}_{0.05})_2$ are also likened to ambient

pressure results reported for other $\text{Y}(\text{Mn}_{1-x}\text{Al}_x)_2$ alloys. A distinct change in the magnitude and temperature dependence of the muon depolarization rate is observed with increasing Al substitution; from critical scaling ($x < 5$ at. % Al) to Arrhenius behavior (5 at. % Al $< x \leq 30$ at. % Al). The efficacy of describing μ^+ spin-depolarization data using theory developed to predict inelastic neutron scattering line widths has been further tested and found to provide a realistic description of the muon data. Future effort will test the applicability of the model once experimentally determined parameters from neutron measurements are incorporated. Nonetheless, the results presented here give further weight to complementarities between neutron and muon techniques. The muon has the potential to provide information that is largely equivalent to that obtained from inelastic neutron scattering measurements (at least for systems in which a relatively Q -independent line width is observed) but with greatly reduced sample masses and data collection times.

ACKNOWLEDGMENTS

The authors thank the United Kingdom's Science and Technology Facility Council for access to the ISIS facility, Rutherford Appleton Laboratory. The authors also thank Adrian Hillier, Peter Baker, and Steve Cottrell for their help and suggestions during the experiment. K.J.E. acknowledges EPSRC for financial support through the award of a "Next Generation Facilities User" postgraduate studentship.

*mark.telling@stfc.ac.uk

¹F. Laves, *Naturwissenschaften* **27**, 65 (1939).

²T. Moriya, *Spin Fluctuations in Itinerant Electron Magnetism* (Springer-Verlag, Berlin, 1985).

³R. Cywinski, S. H. Kilcoyne, and C. A. Scott, *J. Phys.: Condens. Matter* **3**, 6473 (1991).

⁴M. Shiga *et al.*, *J. Phys. F* **17**, 1781 (1987).

⁵J. N. Reimers, A. J. Berlinsky, and A. C. Shi, *Phys. Rev. B* **43**, 865 (1991).

⁶B. D. Rainford, in *Muon Science: Muons in Physics, Chemistry and Materials*, edited by S. L. Lee, S. H. Kilcoyne, and R. Cywinski (IOP Publishing, Bristol, 1999).

⁷R. Cywinski *et al.*, *Hyperfine Interact.* **64**, 427 (1990).

⁸K. Yoshimura, M. Shiga, and Y. Nakamura, *J. Phys. Soc. Jpn.* **55**, 3585 (1986).

⁹K. Motoya, *J. Phys. Soc. Jpn.* **55**, 3733 (1986).

¹⁰M. T. F. Telling, C. Ritter, and R. Cywinski, *J. Magn. Magn. Mater.* **177**, 1480 (1998).

¹¹M. T. F. Telling, C. Ritter, and R. Cywinski, *Physica B* **276**, 740 (2000).

¹²R. Cywinski and B. D. Rainford, *Hyperfine Interact.* **85**, 215 (1994).

¹³A. Schenck, *Muon Spin Rotation Spectroscopy* (Adam Hilger, Bristol, 1985).

¹⁴I. A. Campbell *et al.*, *Phys. Rev. Lett.* **72**, 1291 (1994).

¹⁵H. Nakamura *et al.*, *J. Phys. Soc. Jpn.* **65**, 2779 (1996).

¹⁶I. Mirebeau, I. N. Goncharenko, and I. V. Golosovsky, *Phys. Rev. B* **64**, 140401(R) (2001).

¹⁷T. Moriya and A. Kawabata, *J. Phys. Soc. Jpn.* **35**, 669 (1973).

¹⁸K. K. Murata and S. Doniach, *Phys. Rev. Lett.* **29**, 285 (1972).

¹⁹T. Moriya and K. Ueda, *Solid State Commun.* **15**, 169 (1974).

²⁰R. S. Hayano *et al.*, *Phys. Rev. Lett.* **41**, 1743 (1978).

²¹K. Ellis *et al.*, *Physics Procedia* (in press, 2012).

²²A. Yaouanc and P. Dalmas de Reotier, *Muon Spin Rotation, Relaxation, and Resonance: Applications to Condensed Matter* (Oxford University Press, New York, 2011).

²³G. E. Bacon, *Neutron Diffraction* (Clarendon Press, Oxford, 1975).

²⁴C. G. Windsor, *Pulsed Neutron Scattering* (Taylor and Francis, New York, 1981).

²⁵R. Kubo and T. Toyabe, *Magnetic Resonance and Relaxation* (North Holland, Amsterdam, 1967).

²⁶A. T. Ogielski and I. Morgenstern, *Phys. Rev. Lett.* **54**, 928 (1985).

²⁷R. M. Pickup *et al.*, *Phys. Rev. Lett.* **102**, 097202 (2009).

²⁸T. Matsuzaki, K. Ishida, K. Nagamine, I. Watanabe, G. H. Eaton, and W. G. Williams, The RIKEN-RAL pulsed Muon Facility, *Nucl. Instrum. Meth. Phys. Res. A* **465**, 365 (2001).

²⁹I. Watanabe *et al.*, *Physica B: Condensed Matter* **404**, 993 (2009).

³⁰F. L. Pratt, *Physica B* **289-290**, 710 (2000).

³¹A. C. Larson and R. B. Von Dreele, *General Structure Analysis System (GSAS)*, Los Alamos National Laboratory Report LAUR 86-748 (2004).

³²M. T. F. Telling and K. H. Andersen, *Phys. Chem. Chem. Phys.* **7**, 1255 (2005).

³³M. Shiga, *Physica B&C* **149**, 293 (1988).

³⁴M. Shiga *et al.*, *J. Phys. Soc. Jpn.* **57**, 3141 (1988).

- ³⁵J. R. Stewart *et al.*, *J. Appl. Crystallogr.* **42**, 69 (2009).
- ³⁶A. Lindbaum *et al.*, *J. Phys.: Condens. Matter* **11**, 1189 (1999).
- ³⁷H. Sugiura *et al.*, *J. Alloys Compd.* **367**, 230 (2004).
- ³⁸M. T. F. Telling and R. Cywinski, *J. Magn. Magn. Mater.* **140**, 45 (1995).
- ³⁹Y. J. Uemura *et al.*, *Phys. Rev. B* **31**, 546 (1985).
- ⁴⁰B. D. Rainford, R. Cywinski, and S. J. Dakin, *J. Magn. Magn. Mater.* **140**, 805 (1995).
- ⁴¹M. T. F. Telling, S. H. Kilcoyne, and R. Cywinski, *Hyperfine Interact.* **85**, 209 (1994).
- ⁴²S. W. Lovesey, A. Cuccoli, and V. Tognetti, *Hyperfine Interact.* **64**, 321 (1990).
- ⁴³K. Motoya *et al.*, *Phys. Rev. B* **44**, 183 (1991).



12th International Conference on Muon Spin Rotation, Relaxation and Resonance

Au₄V – Moment Stability and Spin Fluctuations in the Ordered Phase

K.J. Ellis^{a*}, R. Cywinski^a, S.H. Kilcoyne^b, A.D. Hillier^c

^aUniversity of Huddersfield, Huddersfield, HD1 3DH, United Kingdom

^bUniversity of Salford, Greater Manchester, M5 4WT, United Kingdom

^cISIS Facility, Rutherford Appleton Laboratory, Didcot, OX11 0QX, United Kingdom

Abstract

Although neither gold nor vanadium generally possess a magnetic moment, the intermetallic compound Au₄V is found to be ferromagnetic below 42K. In this paper we report the results of a muon spin relaxation study of the itinerant electron moment fluctuations in Au₄V above the Curie temperature. The temperature dependence of the muon spin relaxation rate is found to be similar to that of the weak itinerant helimagnet, MnSi.

Keywords: Au₄V; weak itinerant ferromagnet, muon spin relaxation

1. The Gold-Vanadium System

The first investigations (1959) of magnetism in the gold-vanadium system were performed on disordered alloys ranging from 1-15 at.% vanadium [1], in which the temperature dependent susceptibility closely obeyed a Curie-Weiss law incorporating a temperature independent term, χ_0 , such that

$$\chi = \chi_0 + \frac{C}{(T - \theta)} \quad (1)$$

where C is the Curie constant and θ is the critical temperature. Interestingly the critical temperature of these relatively dilute alloys was found to be negative, despite there being no evidence of a magnetic transition. To explain this behaviour a model was proposed in which a fraction of “isolated” vanadium atoms i.e. those without other vanadium nearest neighbours, possess a local moment with the remaining fraction contributing to the Pauli-like temperature independent term.

*Corresponding author. Tel.: +44-1484-471876
E-mail address: k.ellis@hud.ac.uk

Creveling et al [2] extended the study of Au-V to higher concentrations ranging from 17-24 at.% V. When annealed at $\sim 500^\circ\text{C}$, these alloys were found to undergo a structural transition forming an intermetallic compound with the nominal concentration Au_4V with a body-centred tetragonal structure (I4/m). This phase effectively isolates all the vanadium atoms and correspondingly a ferromagnetic transition was found at $\sim 45\text{K}$. In this ordered phase the susceptibility above T_c obeys the Curie-Weiss law given in Eq. 1. However a large disparity in the magnetic measurements between different samples was noted. It has been suggested that this is due in part to magneto-crystalline anisotropy which is not only the result of the non-cubic structure but also crystalline imperfections caused by the arbitrary alignment of the tetragonal c-axis. As generally observed for weak itinerant electron ferromagnets, the ordered moment of Au_4V is substantially lower (approximately half that) of the paramagnetic moment; however, annealing under compression promotes alignment of the c-axis, and increases the ordered moment from the usual value of $0.4\text{-}0.6\mu_B$ to $0.83\mu_B$ per V atom [3]. Furthermore, in extremely high pulsed magnetic fields (29T) the ordered moment saturates to $M_s = 1\mu_B$ per V atom, indicating a spin- $1/2$ moment [4].

The importance of the V-V distance in establishing a localised moment, and consequently ferromagnetic order, is further emphasised by the observation that when Au_4V is prepared as a disordered solid solution the V moment, and also ferromagnetism, collapses. Au_4V thus appears to belong to the same class of weak itinerant ferromagnets as ZrZn_2 and Sc_3In . However, in marked contrast to systems such as ZrZn_2 , for which the application of external pressure rapidly decreases T_c to zero by 20kbar, the Curie temperature of Au_4V increases with pressure to 90K at $\sim 180\text{kbar}$, at which point the magnetic order collapses entirely [5].

Positive muon spin relaxation has proved to be an invaluable tool in investigating itinerant magnetic systems such as MnSi, as demonstrated in the seminal paper by Hayano et al [6]. We have therefore performed zero and longitudinal-field measurements on Au_4V using the MuSR spectrometer, (ISIS Facility, UK) to follow the evolution of spin fluctuations with temperature between 5K and 90K.

The polycrystalline Au_4V samples were prepared by argon arc melting stoichiometric proportions of gold and vanadium. The resulting 2g ingots were pressed into disks, approximately 5mm in diameter and 1.5mm thick before undergoing two days of homogenisation at 1000°C under reduced argon atmosphere, followed by annealing at 500°C for eight days.

2. Muon Spin Relaxation in Zero-Field

The observed zero-field muon spin relaxation spectra for Au_4V were best modelled by a dynamical Kubo-Toyabe function, $G^{(DKT)}$, representing a nuclear dipole contribution, multiplied by a simple exponential term, representing the contribution from atomic spin fluctuations .

$$a_0 G_z(t) = [a_1 G_z^{DKT}(t) \times \exp(-\lambda t)] + a_b \quad (2)$$

where a_0 is the initial asymmetry, a_1 is the relaxing asymmetry and a_b is a background.

In the paramagnetic regime, above 50K, the muon relaxation rate σ from the randomly orientated nuclear dipoles is constant at $0.34\mu\text{s}^{-1}$. Furthermore, these spectra show a marked divergence of λ from a negligibly small value at high temperatures to a maximum at the reported Curie point of Au_4V .

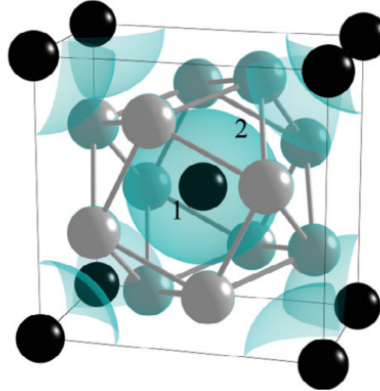


Figure 1: The structure of ordered Au_4V in which vanadium atoms are black and gold atoms silver. The isosurface indicates the positions within the unit cell where the nuclear depolarisation rate, $\sigma = 0.34\mu\text{s}^{-1}$. Labels 1 & 2 indicate the likely muon position.

Estimates of the nuclear dipole contributions within the unit cell suggest possible muon sites at the centres of the $3\text{Au}-1\text{V}$ tetrahedron or the $5\text{Au}-1\text{V}$ octahedron as shown in Figure 1. The slow fluctuation rate ($<1\mu\text{s}^{-1}$) observed as a damping of the “tail” of the Kubo-Toyabe function is likely to arise from the muon hopping between these interstitial sites.

3. Muon Spin Relaxation in Applied Longitudinal Fields

Spectra from Au_4V were collected in sufficiently high longitudinal magnetic fields to decouple the muon from the nuclear dipole fields, but sufficiently small to offer negligible perturbation of the atomic spins. In Figure 2 we present spectra from a range of applied longitudinal-fields above the transition temperature, clearly showing a full decoupling at 100G. Above this field the μSR spectra are well described by a simple exponential function. The associated relaxation rate, λ , increases rapidly as the transition temperature is approached until below 50K a there is a critical divergence. As found for the weak itinerant helimagnet, MnSi [6] this critical divergence is best described by the simple formula:

$$\lambda = \tau_{\infty} \frac{T}{T - T_c} \quad (3)$$

A least square fit of Eq. 3 to the data provides $T_c = 42.0 \pm 0.2\text{K}$ and $\tau_{\infty} = (3.17 \pm 0.14) \times 10^{-3}\mu\text{s}^{-1}$. For comparison τ_{∞} for MnSi ($T_c=29.5\text{K}$) was found to be $(6.55 \pm 0.13) \times 10^{-3}\mu\text{s}^{-1}$. Figure 3 shows the critical scaling of λ , described by Eq. 3, for both Au_4V and MnSi with the data for the latter taken from [6].

4. Conclusions

The critical scaling of the muon spin relaxation rate observed for Au_4V shows close similarity with that obtained for the archetypal itinerant electron ferromagnet, MnSi, and correspondingly follows the predications of Moriya’s self consistent renormalisation (SCR) theory for itinerant systems [7]. In this respect Au_4V may well prove a simpler system with which the mechanisms responsible for moment localisation in itinerant electron magnets can be explored.

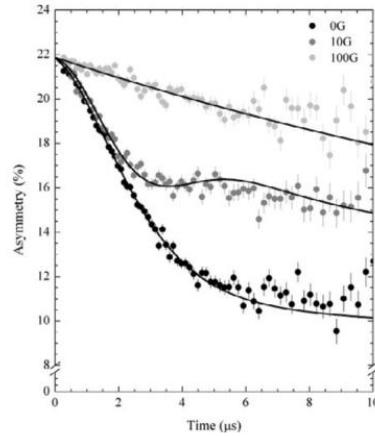


Figure 2: The longitudinal field muon spin relaxation spectra from Au₄V observed at 46K in several applied fields. Eq. 2 was used to fit both 0G and 10G data. The application of 100G fully decouples the nuclear dipole fields such that it can be fitted with a single exponential term.

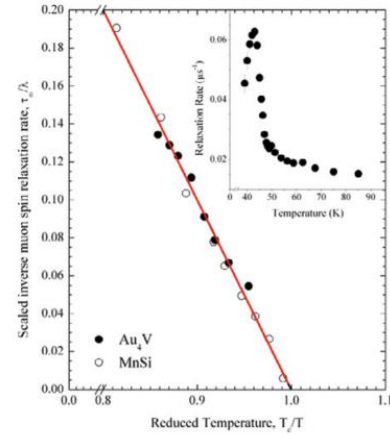


Figure 3: The scaled inverse muon spin relaxation rate (τ_{∞} / λ) versus reduced temperature for Au₄V (closed circles) and MnSi (open circles). The solid line represents the fit of Eq. 3, as predicted by SCR theory [7] to the data. The experimental points for MnSi are taken from [6]. Insert: The temperature dependence of λ in Au₄V.

5. Acknowledgements

KJE wishes to acknowledge EPSRC for financial support through the award of a “Next Generation Facilities User” postgraduate studentship.

6. References

- [1] E. Vogt, and D. Gerstenberg, Magnetische Untersuchungen an Gold-reichen Mischkristallen mit Titan und Vanadium, *Annalen der Physik* 1959; **459**: 145-153.
- [2] L. Creveling, and H. L. Luo, Magnetic Properties of Gold-Rich Gold-Vanadium Alloys, *Physical Review* 1968; **176**: 614-630.
- [3] G. Y. Chin *et al.*, Concentring Vanadium Moment in Ordered Au₄v, *Physics Letters A* 1968; **A 27**: 302-303.
- [4] G. Kido *et al.*, Magnetization Process in Au₄v Single-Crystal under Pulsed High Magnetic-Fields, *Journal of Magnetism and Magnetic Materials* 1983; **31-4**: 283-284.
- [5] D. D. Jackson *et al.*, Structure-dependent ferromagnetism in Au₄V studied under high pressure, *Physical Review B* 2006; **74**: 174401-174408.
- [6] R. S. Hayano *et al.*, Spin Fluctuations of Itinerant Electrons in MnSi Studied by Muon Spin Rotation and Relaxation, *Journal of the Physical Society of Japan* 1980; **49**: 1773-1783.
- [7] T. Moriya, and Y. Takahashi, Spin Fluctuations in Itinerant Electron Magnetism, *J. Phys. Colloques* 1978; **39**: 1466-1471.

REFERENCES

- 1 **P. W. Anderson**, *Science*, **267**, 1609-1618, (1995).
- 2 **W. Heisenberg**, *Zeitschrift für Physik A: Hadrons and Nuclei*, **49**, 619-636, (1928).
- 3 **F. Bloch**, *Zeitschrift für Physik A: Hadrons and Nuclei*, **57**, 545-555, (1929).
- 4 **T. Moriya & A. Kawabata**, *J. Phys. Soc. Jpn.*, **34**, 639-651, (1973).
- 5 **R. Eisberg & R. Resnick**, *Quantum Physics of Atoms, Molecules, Solids, Nuclei, and Particles*, Wiley; 2nd edition, (1985).
- 6 **M. A. Ruderman & C. Kittel**, *Phys. Rev.*, **96**, 99-102, (1954).
- 7 **T. Kasuya**, *Progress of Theoretical Physics*, **12**, 803-805, (1954).
- 8 **K. Yosida**, *Phys. Rev.*, **106**, 893-898, (1957).
- 9 **E. Ising**, *Zeitschrift für Physik A: Hadrons and Nuclei*, **31**, 253-258, (1925).
- 10 **P. J. Weiss**, *Journal de Physique Théorique et Appliquée*, **6**, 661-690, (1907).
- 11 **E. C. Stoner & E. P. Wohlfarth**, *Philosophical Transactions of the Royal Society of London. Series A, Mathematical and Physical Sciences*, **240**, 599-642, (1948).
- 12 **H. Ibach & H. Lüth**, *Solid-State Physics*, Springer, (2002).
- 13 **P. Rhodes & E. P. Wohlfarth**, *Proceedings of the Royal Society of London. Series A. Mathematical and Physical Sciences*, **273**, 247-258, (1963).
- 14 **T. Moriya**, *Spin Fluctuations in Itinerant Electron Magnetism*, Springer, (1985).
- 15 **T. Izuyama, et al.**, *J. Phys. Soc. Jpn.*, **18**, 1025-1042, (1963).
- 16 **T. Moriya & A. Kawabata**, *J. Phys. Soc. Jpn.*, **35**, 669-676, (1973).
- 17 **L. Néel**, *J. Phys. Radium*, **3**, 160-171, (1932).
- 18 **J. Owen, et al.**, *Phys. Rev.*, **102**, 1501-1507, (1956).
- 19 **B. R. Coles**, *Onset of Magnetic Ordering in Random Substitutional Alloys*, Plenum Publishing Corporation, (1973).
- 20 **V. Cannella, et al.**, *J. App. Phys.*, **42**, 1689-1690, (1971).
- 21 **V. Cannella & J. A. Mydosh**, *Phys. Rev. B*, **6**, 4220-4237, (1972).
- 22 **S. F. Edwards & P. W. Anderson**, *J. Phys. F*, **5**, 965-974, (1975).

- 23 **S. F. Edwards & P. W. Anderson**, J. Phys. F, **6**, 1927-1937, (1976).
- 24 **J. A. Mydosh**, J. Magn. Magn. Mater., **7**, 237-248, (1978).
- 25 **D. Chowdhury & A. Mookerjee**, Phys. Rep., **114**, 1-98, (1984).
- 26 **G. Toulouse**, Communications on Physics, 537-542, (1977).
- 27 **D. Sherrington & S. Kirkpatrick**, Phys. Rev. Lett., **35**, 1792-1796, (1975).
- 28 **D. J. Thouless, et al.**, Philos. Mag., **35**, 593-601, (1977).
- 29 **J. R. L. de Almeida & D. J. Thouless**, J. Phys. A, **11**, 983-990, (1978).
- 30 **G. Parisi**, Phys. Lett. A, **73**, 203-205, (1979).
- 31 **G. Parisi & G. Toulouse**, J. Phys. Lett. Paris, **41**, 361-364, (1980).
- 32 **G. Parisi**,
- 33 **D. J. Thouless, et al.**, J. Phys. C, **13**, 3271-3280, (1980).
- 34 **F. T. Bantilan & R. G. Palmer**, J. Phys. F, **11**, 261-266, (1981).
- 35 **K. Binder & W. Kinzel**,
- 36 **K. Binder & A. P. Young**, Rev. Mod. Phys, **58**, 801-976, (1986).
- 37 **R. G. Palmer**, Adv. Phys., **31**, 669-735, (1982).
- 38 **J. C. Mauro, et al.**, J. Chem. Phys., **126**, 184511-184511, (2007).
- 39 **F. Kohlrausch**, Ann. Phys., **204**, 399-419, (1866).
- 40 **R. Kohlrausch**, Ann. Phys., **167**, 179-214, (1854).
- 41 **J. A. Ewing**, Philos. T. Roy. Soc. Lon., **176**, 523-640, (1885).
- 42 **R. V. Chamberlin**, Phase Transit., **65**, 169-209, (1998).
- 43 **R. Kohlrausch**, Ann. Phys., **383**, (1847).
- 44 **G. Williams & D. C. Watts**, Trans. Faraday. Soc., **66**, 80, (1970).
- 45 **R. V. Chamberlin, et al.**, Phys. Rev. Lett., **52**, 867-870, (1984).
- 46 **F. Mezei & A. P. Murani**, J. Magn. Magn. Mater., **14**, 211-213, (1979).
- 47 **J. Klafter & M. F. Shlesinger**, Proc. Natl. Acad. Sci. USA, **83**, 848-851, (1986).
- 48 **R. G. Palmer, et al.**, Phys. Rev. Lett., **53**, 958-961, (1984).
- 49 **A. T. Ogielski**, Phys. Rev. B, **32**, 7384-7398, (1985).
- 50 **C. Pappas, et al.**, Phys. Rev. B, **68**, 054431-054435, (2003).
- 51 **R. M. Pickup, et al.**, Phys. B, **397**, 99-101, (2007).

- 52 **R. M. Pickup, et al.**, Phys. Rev. Lett., **102**, 097202-097205, (2009).
- 53 **K. Weron**, J. Phys.: Condens. Matter, **3**, 9151-9162, (1991).
- 54 **L. A. Dissado & R. M. Hill**, J. App. Phys., **66**, 2511-2524, (1989).
- 55 **S. Abe & N. Suzuki**, Phys. Rev. E, **67**, 016106, (2003).
- 56 **S. Thurner, et al.**, Phys. Rev. E, **76**, 036111, (2007).
- 57 **A. Ziviani, et al.**, Communications Letters, IEEE, **11**, 1034-1036, (2007).
- 58 **C. Tsallis**, Journal of Computational and Applied Mathematics, **227**, 51-58, (2009).
- 59 **T. Takahashi**, Physica A: Statistical Mechanics and its Applications, **386**, 335-338, (2007).
- 60 **C. Tsallis, et al.**, Astrophys. Space Sci., **290**, 259-274, (2004).
- 61 **C. Tsallis & E. P. Borges**, Correlations & Fluctuations in QCD, 326-343, (2003).
- 62 **C. Tsallis, et al.**, Phys. Rev. Lett., **75**, 3589-3593, (1995).
- 63 **C. J. Keylock**, Advances in Water Resources, **28**, 773-778, (2005).
- 64 **M. Ausloos & F. Petroni**, Physica A: Statistical Mechanics and its Applications, **373**, 721-736, (2007).
- 65 **C. Tsallis**, Physics of Life Reviews, **3**, 1-22, (2006).
- 66 **S. Alfarano & M. Milaković**, Journal of Economic Dynamics and Control, **33**, 78-92, (2009).
- 67 **C. Chen, et al.**, Europhysics Letters, **95**, 49001, (2011).
- 68 **S. M. D. Queirós, et al.**, The European Physical Journal B - Condensed Matter and Complex Systems, **55**, 161-167, (2007).
- 69 **S. M. Duarte Queiros, et al.**, Quantitative Finance Papers, (2005).
- 70 **C. Tsallis, et al.**, Phys. A, **324**, 89-100, (2003).
- 71 **C. Tsallis, et al.**, Chaos Solitons & Fractals, **6**, 561-567, (1995).
- 72 **S. Abe & A. K. Rajagopal**, Phys. Lett. A, **272**, 341-345, (2000).
- 73 **F. Brouers & O. Sotolongo-Costa**, Europhysics Letters, **62**, 808-814, (2003).
- 74 **C. Tsallis & J. P. Boon**, Europhys.News, **36**, 185-185, (2005).
- 75 **C. Tsallis**, *Introduction to Nonextensive Statistical Mechanics: Approaching a Complex World*, Springer, (2009).
- 76 **F. Brouers & O. Sotolongo-Costa**, Phys. A, **356**, 359-374, (2005).
- 77 **C. Tsallis, et al.**,
- 78 **F. Brouers, et al.**, Phys. A, **344**, 409-416, (2004).

- 79 **C. Tsallis, et al.**, Phys. A, **261**, 534-554, (1998).
- 80 **D. Prato & C. Tsallis**, Phys. Rev. E, **60**, 2398-2401, (1999).
- 81 **R. M. Pickup**, *Non-Exponential Relaxation in Spin Glasses and Related Systems*, Ph.D., University of Leeds
- 82 **F. Bloch**, Phys. Rev., **50**, 259-260, (1936).
- 83 **J. S. Schwinger**, Phys. Rev., **51**, 544-552, (1937).
- 84 **O. Halpern & M. H. Johnson**, Phys. Rev., **55**, 898-923, (1939).
- 85 **O. Halpern & M. H. Johnson**, Phys. Rev., **51**, 992-992, (1937).
- 86 **O. Halpern & M. H. Johnson**, Phys. Rev., **52**, 52-53, (1937).
- 87 **C. G. Shull, et al.**, Phys. Rev., **83**, 333-345, (1951).
- 88 **R. Celotta, et al.**, *Neutron Scattering: Part A*, Academic Press, Inc. Ltd, (1986).
- 89 **E. Prince**, *International Tables for Crystallography: Volume C Mathematical, Physical and Chemical Tables*, Springer; 3rd edition, (2004).
- 90 **J. Chadwick**, Nature, **129**, 312-312, (1932).
- 91 **L. Van Hove, et al.**, Phys. Rev., **95**, 249-262, (1954).
- 92 **G. L. Squires**, *Introduction to the Theory of Thermal Neutron Scattering*, Dover Publications Inc.; New edition, (1997).
- 93 **S. W. Lovesey**, *Theory of Neutron Scattering from Condensed Matter: Volume I: Nuclear Scattering*, Clarendon Press; New edition, (1986).
- 94 **R. Celotta, et al.**, *Methods of Experimental Physics, Volume 23 - Part A: Neutron Scattering*, Academic Press, Inc. Ltd, (1986).
- 95 **T. Chatterji**, *Neutron Scattering from Magnetic Materials*, Elsevier Science, (2005).
- 96 **V. Vand, et al.**, Acta Crystallogr., **10**, 303-306, (1957).
- 97 **J. B. Forsyth & M. Wells**, Acta Crystallogr., **12**, 412-415, (1959).
- 98 **E. J. Lisher & J. B. Forsyth**, Acta Crystallogr., **27**, 545-549, (1971).
- 99 **P. N. Powers**, Phys. Rev., **54**, 827-838, (1938).
- 100 **C. G. Shull, et al.**, Phys. Rev., **84**, 912-921, (1951).
- 101 **C. G. Shull**, Phys. Rev., **81**, 626-626, (1951).
- 102 **R. Nathans, et al.**, J. Phys. Chem. Solids, **6**, 38-42, (1958).
- 103 **R. Nathans, et al.**, J. Phys. Chem. Solids, **10**, 138-146, (1959).
- 104 **D. J. Hughes, et al.**, Phys. Rev., **75**, 565-569, (1949).
- 105 **D. J. Hughes & M. T. Burgy**, Phys. Rev., **76**, 1413-1414, (1949).

- 106 **D. J. Hughes & M. T. Burgy**, Phys. Rev., **81**, 498-506, (1951).
- 107 **B. Roessli & P. Böni**, eprint arXiv:cond-mat/0012180, (2000).
- 108 **V. F. Turchin**, Atom. Energy Rev., **22**, (1967).
- 109 **P. Courtois, et al.**, Phys. B, **385-386**, 1271-1273, (2006).
- 110 **F. Mezei**, Communications on Physics, **1**, (1976).
- 111 **F. Mezei & P. A. Dagleish**, Communications on Physics, **2**, (1977).
- 112 **J. Schelten & K. Mika**, Nuclear Instruments and Methods in Physics Research, **160**, 287-294, (1979).
- 113 **J. B. Hayter & H. A. Mook**, J. Appl. Crystallogr., **22**, 35-41, (1989).
- 114 **C. F. Majkrzak**, Phys. B, **156-157**, 619-626, (1989).
- 115 **O. Schärpf**, AIP Conf. Proc., 182-189, (1982).
- 116 **O. Schärpf**, Phys. B, **174**, 514-527, (1991).
- 117 **O. Schärpf & I. S. Anderson**, Phys. B, **198**, 203-212, (1994).
- 118 **J. B. Hayter**, J. Magn. Magn. Mater., **14**, 319-324, (1979).
- 119 **F. Mezei**, Zeitschrift für Physik A: Hadrons and Nuclei, **255**, 146-160, (1972).
- 120 **F. Mezei**, Phys. B & C, **151**, 74-81, (1988).
- 121 **R. Gähler, et al.**, Phys. B, **229**, 1-17, (1996).
- 122 **G. M. Drabkin**, Sov. Phys. JETP **20**, 1548, (1965).
- 123 **F. Mezei**, *Neutron Spin Echo: Proceedings of a Laue-Langevin Institut Workshop*, Springer-Verlag, (1979).
- 124 **R. Cywinski**,
- 125 **J. R. Stewart, et al.**, J. Appl. Crystallogr., **42**, 69-84, (2009).
- 126 **O. Schärpf**, Phys. B, **182**, 376-388, (1992).
- 127 **R. Cywinski**, Phys. B, **350**, 17-25, (2004).
- 128 **K. Nagamine**, *Introductory Muon Science*, Cambridge University Press, (2003).
- 129 **P. Kunze**, Zeitschrift für Physik A: Hadrons and Nuclei, **83**, 1, (1933).
- 130 **G. H. Eaton**, RAL Report, **RAL-TR-98-019**, (1998).
- 131 **S. H. Neddermeyer & C. D. Anderson**, Phys. Rev., **51**, 884-886, (1937).
- 132 **W. Liu, et al.**, Phys. Rev. Lett., **82**, 711-714, (1999).
- 133 **I. Beltrami, et al.**, Nuclear Physics A: Nuclear and Hadronic Physics, **451**, 679-700, (1986).

- 134 **H. N. Brown, et al.**, Phys. Rev. Lett., **86**, 2227-2231, (2001).
- 135 **K. L. Giovanetti, et al.**, Phys. Rev. D, **29**, 343-348, (1984).
- 136 **M. Conversi, et al.**, Phys. Rev., **71**, 209-210, (1947).
- 137 **S. Sakata & T. Inoue**, Prog. Theor. Phys., **1**, 143, (1946).
- 138 **C. M. G. Lattes, et al.**, Nature, **159**, 694, (1947).
- 139 **R. Kubo & T. Toyabe**, *Magnetic Resonance and Relaxation*, Amsterdam: North-Holland, (1967).
- 140 **M. R. Crook & R. Cywinski**, J. Phys.: Condens. Matter, **9**, 1149-1158, (1997).
- 141 **R. S. Hayano, et al.**, Phys. Rev. B, **20**, 850-859, (1979).
- 142 **A. E. F. Gick, et al.**, J. Phys. D, **6**, 1941-1949, (1973).
- 143 **M. B. C. Quigley, et al.**, J. Phys. D, **6**, 2250-2258, (1973).
- 144 **J. B. Friauf**, J. Am. Chem. Soc., **49**, 3107-3114, (1927).
- 145 **J. B. Friauf**, Phys. Rev., **29**, 34, (1927).
- 146 **F. Laves & H. Witte**, Metallwirtschaft, **14**, 645, (1935).
- 147 **F. Laves**, Naturwissenschaften, **27**, 65-73, (1939).
- 148 **G. E. R. Schulze**, Zeitschrift für Elektrochemie und Angewandte Physikalische Chemie, **45**, 849-865, (1939).
- 149 **P. Villars, et al.**, *Pearson's Handbook of Crystallographic Data for Intermetallic Phases*, American Society for Metals, (1985).
- 150 **D. J. Thoma & J. H. Perepezko**, J. Alloy. Compd., **224**, 330-341, (1995).
- 151 **F. Stein, et al.**, Intermetallics, **12**, 713-720, (2004).
- 152 **R. L. Johnston & R. Hoffmann**, Z. Anorg. Allg. Chem., **616**, 105-120, (1992).
- 153 **M. Brouha, et al.**, IEEE Trans. Magn., **10**, 182-185, (1974).
- 154 **W. Hussen, et al.**, J. Magn. Magn. Mater., **84**, 281-287, (1990).
- 155 **F. Stein, et al.**, Intermetallics, **13**, 1056-1074, (2005).
- 156 **H. Nakamura, et al.**, J. Phys.: Condens. Matter, **9**, 4701-4728, (1997).
- 157 **S. A. Marei, et al.**, J. Less Common Met., **13**, 391-398, (1967).
- 158 **R. Cywinski, et al.**, J. Phys.: Condens. Matter, **3**, 6473-6488, (1991).
- 159 **M. Shiga, et al.**, J. Magn. Magn. Mater., **31-4**, 119-120, (1983).
- 160 **Y. Nakamura**, J. Magn. Magn. Mater., **31-34**, 829-834, (1983).
- 161 **K. Yoshimura & Y. Nakamura**, J. Magn. Magn. Mater., **40**, 55-60, (1983).

- 162 **Y. Nakamura, et al.**, Phys. B & C, **120**, 212-215, (1983).
- 163 **R. Ballou, et al.**, J. Magn. Magn. Mater., **70**, 129-133, (1987).
- 164 **J. Deportes, et al.**, J. Phys. Paris, **48**, 1029-1034, (1987).
- 165 **K. Motoya, et al.**, J. Phys. Soc. Jpn., **56**, 885-888, (1987).
- 166 **I. Y. Gaidukova, et al.**, J. Magn. Magn. Mater., **72**, 357-359, (1988).
- 167 **M. Shiga**, Phys. B & C, **149**, 293-305, (1988).
- 168 **S. Mondal, et al.**, Phys. B, **180**, 108-110, (1992).
- 169 **R. Hauser, et al.**, Phys. B, **199**, 662-664, (1994).
- 170 **G. Oomi, et al.**, J. Magn. Magn. Mater., **70**, 137-138, (1987).
- 171 **R. Cywinski, et al.**, Hyperfine Interact., **64**, 427-433, (1990).
- 172 **M. Shiga, et al.**, J. Magn. Magn. Mater., **54-7**, 1073-1074, (1986).
- 173 **K. Yoshimura, et al.**, J. Magn. Magn. Mater., **54-7**, 1075-1076, (1986).
- 174 **K. Motoya**, J. Phys. Soc. Jpn., **55**, 3733-3736, (1986).
- 175 **M. Shiga, et al.**, J. Phys. F, **17**, 1781-1793, (1987).
- 176 **R. Cywinski & B. D. Rainford**, Hyperfine Interact., **85**, 215-220, (1994).
- 177 **K. Fujiwara**, J. Phys. Soc. Jpn., **57**, 2133-2142, (1988).
- 178 **O. Hartmann & et al.**, J. Phys. F, **16**, 1593, (1986).
- 179 **F. L. Pratt**, Phys. B, **289**, 710-714, (2000).
- 180 **I. A. Campbell, et al.**, Phys. Rev. Lett., **72**, 1291-1294, (1994).
- 181 **T. Eqami & S. J. L. Billinge**, *Underneath the Bragg Peaks: Structural Analysis of Complex Materials*, A Pergamon Title, (2003).
- 182 **R. L. McGreevy & L. Pusztai**, Molecular Simulation, **1**, 359-367, (1988).
- 183 **J. M. Cowley**, Phys. Rev., **77**, 669-675, (1950).
- 184 **B. E. Warren, et al.**, J. App. Phys., **22**, 1493-1496, (1951).
- 185 **H. Vogel**, Viskosität von Flüssigkeiten Phys. Z., **22**, 645, (1921).
- 186 **G. S. Fulcher**, Journal of the American Ceramic Society, **8**, 339-355, (1925).
- 187 **C. N. Guy, et al.**, J. App. Phys., **50**, 7308-7317, (1979).
- 188 **S. Shtrikman & E. P. Wohlfarth**, Phys. Lett. A, **85**, 467-470, (1981).
- 189 **A. Pösinger, et al.**, Journal of Physics: Condensed Matter, **5**, 7277, (1993).
- 190 **A. E. Dwight, et al.**, J. Less Common Met., **40**, 285-291, (1975).

- 191 **Y. Muraoka, et al.**, Phys. Status Solidi A, **42**, 369-374, (1977).
- 192 **R. Grössinger, et al.**, J. Magn. Magn. Mater., **2**, 196-202, (1975).
- 193 **M. J. Besnus & et al.**, J. Phys. F, **8**, 191, (1978).
- 194 **M. Reissner, et al.**, J. Phys. F, **14**, 1249-1259, (1984).
- 195 **M. T. F. Telling, et al.**, Phys. B, **289-290**, 213-216, (2000).
- 196 **K. H. J. Buschow**, J. Less Common Met., **40**, 361-363, (1975).
- 197 **M. J. Besnus, et al.**, Phys. B & C, **86-88**, 85-86, (1977).
- 198 **M. Aoki & H. Yamada**, Solid State Commun., **72**, 21-24, (1989).
- 199 **A. Pösinger, et al.**, J. Phys.: Condens. Matter, **5**, 7277-7288, (1993).
- 200 **P. Blaha, et al.**, J. Magn. Magn. Mater., **104-107**, 683-684, (1992).
- 201 **J. M. Preston, et al.**, Appl. Phys. A: Mater., **74**, S689-S691, (2002).
- 202 **R. Grössinger, et al.**, J. Magn. Magn. Mater., **23**, 47-58, (1981).
- 203 **J. D. Patterson, et al.**, Phys. Rev. B, **18**, 1377-1390, (1978).
- 204 **J. R. Cullen**, J. Magn. Magn. Mater., **73**, 167-170, (1988).
- 205 **R. Harris, et al.**, Phys. Rev. Lett., **31**, 160, (1973).
- 206 **D. J. Sellmyer & S. Nafis**, J. App. Phys., **57**, 3584-3588, (1985).
- 207 **Y. Imry & S. Ma**, Phys. Rev. Lett., **35**, 1399-1401, (1975).
- 208 **E. M. Chudnovsky & R. A. Serota**, J. Phys. C, **16**, 4181, (1983).
- 209 **B. Diény & B. Barbara**, Phys. Rev. Lett., **57**, 1169, (1986).
- 210 **M. J. O'Shea, et al.**, Solid State Commun., **46**, 313-316, (1983).
- 211 **O. V. Billoni, et al.**, Phys. Rev. B, **72**, (2005).
- 212 **A. del Moral, et al.**, J. App. Phys., **76**, 6180-6185, (1994).
- 213 **R. Cywinski, et al.**, Phys. B, **385**, 363-365, (2006).
- 214 **H. B. Stanley, et al.**, Physica B+C, **130**, 355-359, (1985).
- 215 **K. Buschow**, Reports on Progress in Physics, **42**, 1373, (1979).
- 216 **F. Mezei, et al.**, Solid State Commun., **45**, 411-415, (1983).
- 217 **R. I. Bewley & R. Cywinski**, Phys. Rev. B, **54**, 15251, (1996).
- 218 **M. J. Pottinger**, *Spin Dynamics and Superconductivity in some Rare Earth Intermetallics*,
Ph.D., University of Leeds
- 219 **F. Mezei**, J. Magn. Magn. Mater., **31-4**, 1327-1330, (1983).

- 220 **P. W. Bridgman**, Proceedings Of The American Academy Of Arts And Sciences, **68**, 27, (1933).
- 221 **C. G. Shull & M. K. Wilkinson**, Rev. Mod. Phys, **25**, 100-107, (1953).
- 222 **V. N. Bykov, et al.**, Doklady Akad Nauk Minerologia USSR, **128**, 1153, (1959).
- 223 **L. M. Corliss, et al.**, Phys. Rev. Lett., **3**, 211-212, (1959).
- 224 **E. Fawcett**, Rev. Mod. Phys, **60**, 209-283, (1988).
- 225 **S. K. Burke & B. D. Rainford**, Journal of Physics F: Metal Physics, **13**, 441, (1983).
- 226 **R. Cywinski & T. J. Hicks**, Journal of Physics F: Metal Physics, **10**, 693, (1980).
- 227 **S. K. Burke, et al.**, Journal of Physics F: Metal Physics, **13**, 451, (1983).
- 228 **S. K. Burke & B. D. Rainford**, Journal of Physics F: Metal Physics, **13**, 471, (1983).
- 229 **E. Vogt & D. Gerstenberg**, Ann. Phys., **459**, 145-153, (1959).
- 230 **L. Creveling & H. L. Luo**, Phys. Rev., **176**, 614-630, (1968).
- 231 **G. Y. Chin, et al.**, Phys. Lett. A, **A 27**, 302-303, (1968).
- 232 **G. Kido, et al.**, J. Magn. Magn. Mater., **31-4**, 283-284, (1983).
- 233 **D. D. Jackson, et al.**, Phys. Rev. B, **74**, 174401-174408, (2006).
- 234 **R. S. Hayano, et al.**, J. Phys. Soc. Jpn., **49**, 1773-1783, (1980).
- 235 **T. Moriya & Y. Takahashi**, Journal de Physique Colloques, **39**, 1466-1471, (1978).